UHPFRC Strengthening of Reinforced Concrete Flexural Members subjected to Static and Blast Loads

by

Chuanjing Li

Thesis submitted to the University of Ottawa
in partial fulfilment of the requirements for the degree of
Doctor of Philosophy
in Civil Engineering

uOttawa

Department of Civil Engineering
Faculty of Engineering
University of Ottawa

Abstract

Ultra-high performance fiber-reinforced concrete (UHPFRC) is an advanced cement-based composite with enhanced compressive strength, tensile resistance and toughness when compared to conventional concrete. Interest in the application of UHPFRC as a retrofit material has been rapidly increasing, and a few existing studies have examined the ability of UHPFRC to retrofit and strengthen existing reinforced concrete (RC) structures under static loading; however, very limited studies have examined the effectiveness of UHPFRC to improve the response of RC members under blast loading. This thesis aims at filing this research gap and investigates the behavior of UHPFRC retrofitted RC flexural members under both static and blast loads. A total of twenty-one (21) specimens, in two different series are tested. Series 1 includes nine (9) singly-reinforced beams built with high-strength concrete (HSC) and strengthened by UHPFRC to improve shear and flexural behaviour. Series 2 includes a further twelve (12) doubly-reinforced beams/columns built with normal-strength concrete (NSC), and strengthened by UHPFRC to improve response under blast, or combined blast-axial loading. Various test parameters are examined including the effects of varying retrofit types (full jacket, U-jacket or T-sided), surface roughening methods, longitudinal steel reinforcement ratio, single vs. repeated blasts, and the effects of axial loading.

The results from this thesis are presented in six journal articles. Papers 1 and 2 study the effects of UHPFRC jacketing on the static and blast behaviour of the singly-reinforced HSC beams in Series 1, while Paper 3 discusses the effects of additional parameters such as: the effect of retrofit type, roughening method and steel detailing on blast behaviour. Under static loading (Paper 1), the UHPFRC jacketing was found to be effective in increasing shear resistance (by preventing shear failure), and improving flexural behaviour (by increasing strength, stiffness, ductility and overall toughness) when compared to control beams built without UHPFRC. Similarly, under blast loads (Paper 2) the use of UHPFRC jacketing prevented shear failure, and improved flexural behaviour by reducing displacements at equivalent blasts, increasing overall blast capacity, and improving damage tolerance. On the other hand, the results show that UHPFRC-retrofitted beams with low longitudinal steel ratios may be vulnerable to brittle bar fracture failures. As part of the numerical research, finite element (FE) modelling is used to predict the static and blast behaviour of the test beams using software LS-DYNA (Papers 1 and 2). The results from Paper 3, provide further insights into the effects of retrofit type (FJ, UJ and T) and roughening method on blast performance; both the UJ and FJ retrofits were found to be effective in increasing shear resistance, reducing blast-displacements and increasing blast capacity, while the benefit of the T-sided retrofit was limited by the crushing capacity of HSC concrete. The effect of roughening method was found to be negligible, except at the very late stages of blast loading.

Papers 4, 5 and 6 present the experimental results from the doubly-reinforced NSC beams tested in Series 2, with a focus on the effect of UHPFRC jacketing, UHPFRC retrofitting type and Axial loading, respectively. Paper 4 shows that the UHPFRC jacketing increased the stiffness and strength of the beams under both static and blast loading, however the high bond capacity of the UHPFRC and relatively low tension steel ratio increased the vulnerability of bar rupture failure. The numerical parametric study investigates the effects of steel ratio and blast load scenario, jacket thickness and interface location on blast performance and failure model. Paper 5 confirms that the blast performance of the beams is influenced by the retrofit type, with optimal performance obtained when using full- or U-jacketing. The efficient use of localized “hinge” retrofits was also found to be effective, and reduced the vulnerability to bar rupture. The numerical parametric study investigates the effects of steel ratio and blast load scenario (single vs. repeated) on the blast performance of the beams. Paper 6, studies the effect of UHPFRC jacketing in columns tested under combined axial and blast loading. The retrofit is shown to increase blast capacity and reduce blast-induced displacements and damage, though the final failure of the columns was governed by bar rupture. As part of the numerical parametric study the effects of axial load ratio, boundary conditions, steel ratio, jacket thickness and jacket design are studied numerically and found to have significant effects on blast behaviour and failure mode.

Keywords: UHPFRC; Retrofit; RC structures; Blast loading; LS-DYNA;

Acknowledgement

There is a saying "Never forget why you started". I think I still remember it. During my master's study, I was deeply attracted by research and developed an enthusiasm for it. Hence, I was lucky enough to start my Ph. D for a clear reason: curiosity and interest. It is well-known that "curiosity and interest" tend to push people forward, but hard-working is necessary for success. My Ph.D. journey started in a completely unfamiliar country when I landed in Toronto on August 25th, 2018. I can imagine this journey is not going to be easy while it is full of challenges and opportunities. Time flies, it has been almost 5 years since I realized that this journey is going to the end. During this period, many things happened, either happy or sad, but they all made me better. Nowadays, I would like to acknowledge the support and assistance of the following individuals.

Foremost, I would like to sincerely thank my supervisor, Dr Hassan Aoude, associate professor at the University of Ottawa. Without his continuous patience, encouragement and support, I am not confident to face and get through all the challenges. I would also like to thank my supervisor for setting an example of being an excellent supervisor and being positive whenever facing troubles. It is my great honor to work with him, and the experience is invaluable.

My thesis focuses on experimental research which was conducted in the structural lab at the University of Ottawa. The work in the lab was challenging and laborious, so I spent more than 1 year in "casting-roughening-testing" with the help of technical officers. Now, I would like to express my acknowledgement to Dr. Muslim Majeed and Dr. Gamal Elnabelsya for their assistance in the lab.

I would also like to express my appreciation to my friends, Dalu Xing (helper), Yanqi Huang (helper), Guo Chen (driver) and Yupeng Liu (cook), etc. Without their help and support, my life would have been much tougher.

Finally, I would like to thank my parents and my sister for their continuous support and encouragement. The financial assistance provided by China Scholarship Council (CSC) was also highly appreciated.

Now, I am ready for the next adventure…

Chuanjing Li - April 18, 2023 (Midnight)

Table of contents

Lists of Figures

Lists of Tables

Chapter 1: Introduction

1.1 General

In recent years, the vulnerability of structures to accidental explosions or blast threats from terrorist attacks has increased. While rare, events such as the Beirut Explosion, Lac-Mégantic Disaster and Oklahoma City Bombing and demonstrate the significant damage and devastation that can be caused by blast loads on structures (**Figure 1 - 1**). As a result, there is a need to increase the blast resistance of critical and vulnerable structures such as government buildings, corporate offices, strategic bridges, and industrial facilities such as gas, petroleum and nuclear installations.

Recently, ultra-high performance fiber-reinforced concrete (UHPFRC) has been proposed to strengthen or retrofit existing reinforced concrete (RC) structures. UHPFRC is a novel cement-based composite which shows superior properties when compared to conventional concrete, including: high compressive strength, improved tensile resistance, and impressive durability, which make it an ideal solution to retrofit or strengthen existing structures. Indeed, as shown in **Figure 1 - 2**(a-b), UHPFRC shows a dense, compact and optimized matrix, which when combined with fibers, allows for its high strength, high durability and crack-free behaviour under service conditions. The provision of fibers in UHPFRC also allows for remarkable toughness and fragmentation resistance, which make it an attractive material for the protection of structures against impact and blast loads.

Brühwiler [1] first proposed UHPFRC for the rehabilitation and retrofit of existing structures, in which the material's advanced properties could be exploited in bending, combined bending/shear, and under fatigue loading, with the concept applied in numerous field applications in viaducts, bridges, building slabs and tunnel linings (see **Figure 1 - 2** (c-d)). A number of research studies have examined the behaviour of UHPFRC strengthened beams and slabs under static loading [2], with the UHPFRC either applied as a retrofit (to replace part of the existing substrate concrete) [3-8], or as an overlay (as an additional layer) [4, 5, 7, 9-14], and in various configurations (Tension or Compression-sided, or as U or full-jackets) (see **Figure 1 - 3**). Among these studies most demonstrate the ability of tension-sided (T-sided) UHPFRC overlays to improve flexural or shear capacity, while studies on UHPFRC jacketing retrofits are limited.

While a few experimental studies have investigated the ability of UHPFRC to increase the flexural capacity of existing RC beams and slabs under static loading, limited research has been conducted on the blast resistance of UHPFRC strengthened structures. Research on the use of UHPFRC for shear-strengthening or in higher strength concrete beams is also limited. Accordingly, this project examines the ability of UHPFRC strengthening to improve the performance of existing reinforced concrete beams under both static and blast loading conditions. Both normal and high-strength concrete beams are tested, and the ability to improve shear and flexural behaviour in shear-deficient and flexural-dominant beams is studied.

(a) Oklahoma Bombing (Intentional explosion) (b) Beirut explosion (accidental explosion)

Figure 1 - 1 Previous blast disasters

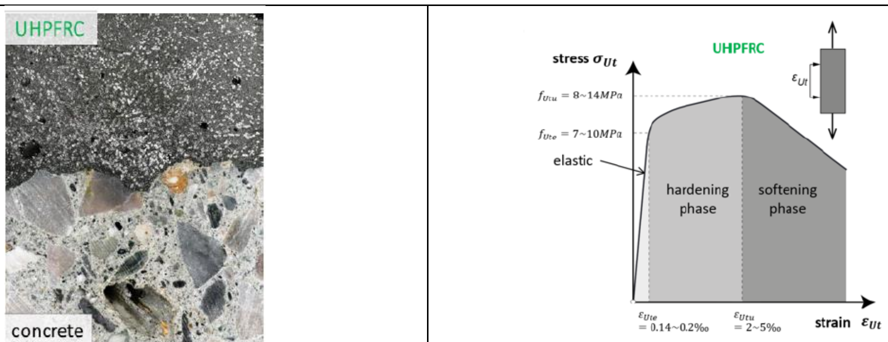

(a) Comparison of UHPFRC and concrete (b) UHPFRC response in tension

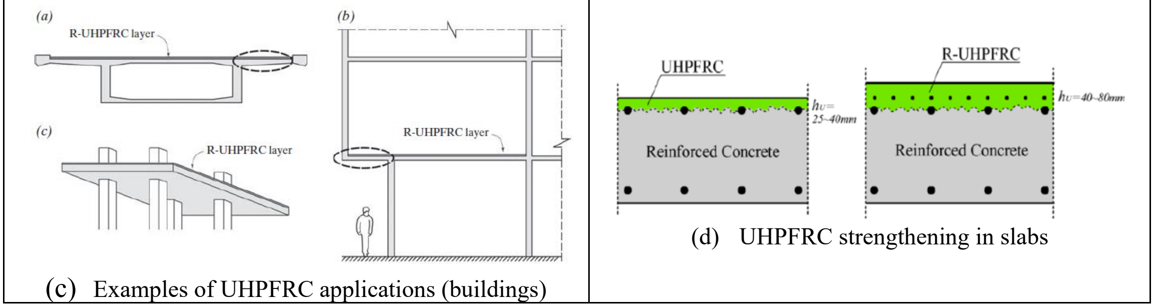

(c) Examples of UHPFRC applications (buildings) (d) UHPFRC strengthening in slabs

Figure 1 - 2 UHPFRC properties and applications (Eugen Brühwiler et al)

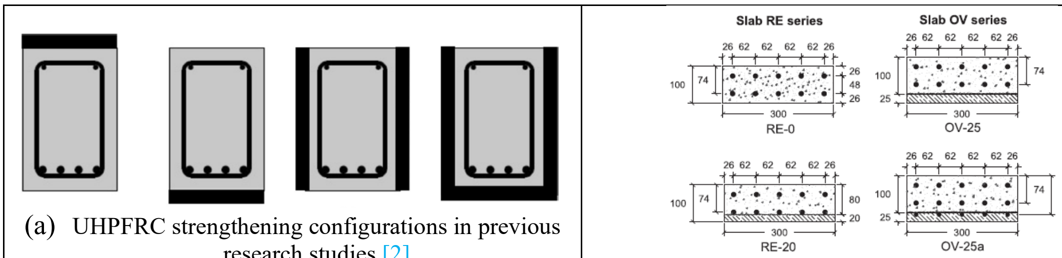

(a) UHPFRC strengthening configurations in previous research studies [2] (b) UHPFRC applied as a retrofit or as an overlay [4]

Figure 1 - 3 UHPFRC strengthening configurations

1.2 Research Objectives

The thesis aims at examining the ability of UHPFRC strengthening to improve the shear and flexural behaviour of existing reinforced concrete beams under blast loading. Beams are selected to study fundamental behaviour of RC members in shear and flexure. Two series of tests on normal-strength concrete (NSC) and high-strength concrete (HSC) beams are conducted. Both singly-reinforced and doubly-reinforced RC members are considered, with various retrofits applied in shear-deficient and flexural-dominant members. Tests are conducted on selected beams under quasi-static loading, with blast testing simulating far-field explosions conducted using a shock-tube. The tests investigate the effects of important parameters such as the influence of UHPFRC retrofit type, interface preparation method, and the longitudinal and transverse steel ratio in the as-built beams. The effect of axial load on blast performance is also studied. In the numerical phase, the thesis aims at developing numerical (finite element) models that can reliably predict the blast response of the tested UHPFRC-strengthened beams. The validated numerical models are then used to conduct extensive parametric studies on variables not considered in the experiments.

1.3 Scope

The scope of the experimental program includes, a total of twenty-one (21) specimens, in two series. The tests examine the effects of retrofit type, interface preparation method, longitudinal and transverse steel ratio, and axial loading on the static and blast behaviour of singly-reinforced and doubly-reinforced HSC and NSC members.

Series 1 includes nine (9) singly-reinforced beams built with high-strength concrete (HSC) and strengthened by UHPFRC to improve shear and flexural behaviour. The HSC beams are singly-reinforced with two different tension steel ratios, and include specimens with and without stirrups. Various UHPFRC retrofits are considered including: T-sided layer, U-jacket (UJ) and Full-jackets (FJ). Two (2) beams are tested under static loading, while seven (7) beams are tested under repeated blast loads using a 4PT bending setup. The results are compared to a set of control HSC beams tested in a previous study. The following specific parameters are investigated in three papers:

- The effects of UHPFRC FJ-jacketing and steel ratio on the behaviour of shear-deficient and flexural-dominant HSC beams under quasi-static loading (Paper 1);
- The effects of UHPFRC FJ-jacketing and steel ratio on the behaviour of shear-deficient and flexural-dominant HSC beams under blast loading (Paper 2);

- The effects of various UHPFRC retrofits (T-sided, FJ, UJ), interface preparation methods, and steel detailing (steel ratio and presence of stirrups) on the blast behaviour of shear-deficient and flexural-dominant HSC beams under blast loading (Paper 3);

Series 2 includes twelve (12) doubly-reinforced beams built with normal-strength concrete (NSC), and strengthened by UHPFRC to improve flexural response. All specimens are doubly reinforced, with closed ties throughout the beam span. Various retrofits are considered including: T-sided, UJ, FJ, as well as localized retrofits in the middle hinge region. Two specimens are tested under static loads, while the remaining beams are tested under either single or repeated blast loads using a UDL setup. The following specific parameters are investigated and the results are presented in three papers:

- The effects of UHPFRC FJ-jacketing on the flexural response of the doubly-reinforced RC beams under static and blast loading. The effects of single and repeated blast loading on the as-built and retrofitted beams are also studied (Paper 4);
- The effect of various UHPFRC retrofits (T-sided, UJ, FJ and Localized-Hinge retrofits) on the flexural response of the double-reinforced RC beams under single and repeated blast loading (Paper 5);
- The effects of axial loading and UHPFRC FJ-jacketing on the response of doubly-reinforced RC beam-columns under blast loading (Paper 6);

The numerical phase consists of finite element (FE) modelling of the control (as-built) and UHPFRC-retrofitted members in Series 1 and 2 using software LS-DYNA. The validated numerical models are further used to conduct extensive parametric study on the effects of variables not considered in the experiments. Specifically, the following aspects are studied:

- Paper 2 presents FE simulations of the UHPFRC-jacketed HSC beams under blast loading;
- Paper 4 presents FE simulations of the UHPFRC-jacketed NSC beams under blast loading. The effects of longitudinal steel ratio, jacket thickness, jacket interface location are studied numerically under single and repeated blast loading;
- Paper 5 presents FE simulations of the UHPFRC-retrofitted NSC beams having various retrofit types under blast loading. The effects of longitudinal steel ratio, retrofit type and blast load scenario (single vs repeated) are studied numerically;

- Paper 6 presents FE simulations of the UHPFRC-jacketed NSC beam-columns under blast loading. The effects of axial load ratio, boundary condition, longitudinal steel ratio, jacket thickness and jacket design are studied numerically;

1.4 Thesis breakdown

This thesis is composed of ten chapters and is divided as shown below (see **Figure 1 - 4**). The experimental results of Series 1 and 2 are presented in the form of six papers:

Chapter 1: Introduction

- Introduces the thesis topic and clarifies the thesis objectives and scope.

Chapter 2: Literature Review

- Summarizes existing research on the behavior of UHPFRC-retrofitted members under static, impact and blast loading.

Chapter 3: Experimental Program

- Presents the experimental program, including the overall test matrix, the specimen designs, material properties, construction sequence, test setups and loading protocols.

Chapter 4: Results of static tests in Series 1 (effect of jacketing) – Paper 1

- Summarizes the results of the UHPFRC-jacketed and singly-reinforced HSC beams (without stirrups) tested under quasi-static loading, and discusses the effects of the FJ retrofit on shear and flexural behaviour.

Chapter 5: Results of blast tests in Series 1 (effect of jacketing) – Paper 2

- Summarizes the results of the UHPFRC-jacketed and singly-reinforced HSC beams tested (without stirrups) under blast loading, and discusses the effects of the FJ retrofit on blast performance in terms of blast-displacements, blast capacity and failure mode. Presents numerical FE simulations of the tested beams under blast loading.

Chapter 6: Results of blast tests in Series 1 (effect of retrofit type) – Paper 3

- Summarizes the results of UHPFRC-retrofitted and singly-reinforced HSC beams (with and without stirrups) tested under blast loading, and discusses the effects of the retrofit type (T-sided, FJ, UJ), interface preparation method, and steel detailing (steel ratio and stirrups) on blast performance in terms of displacements, blast capacity and failure mode.

Chapter 7: Results of static and blast tests in Series 2 (effect of jacketing) – Paper 4

- Summarizes the results of the UHPFRC-jacketed and doubly-reinforced NSC beams tested under static and single/repeated blast loading, and discusses the effects of the FJ retrofit and load type on flexural and blast performance in terms of load capacity, ductility, blast-displacements, blast capacity, post-blast resistance and failure mode. Presents numerical FE simulations of the tested beams under blast loading, and presents a numerical parametric study on the effects of steel ratio, jacket thickness and jacket interface location under single and repeated blast loads.

Chapter 8: Results of blast tests in Series 2 (effect of retrofit type) – Paper 5

- Summarizes the results of the UHPFRC-retrofitted and doubly-reinforced NSC beams tested under single or repeated blast loading, and discusses the effects of the retrofit type on blast performance in terms of blast-displacements, blast capacity, post-blast resistance and failure mode. Presents numerical FE simulations of the tested beams under blast loading, and presents a numerical parametric study on the effects of steel ratio and loading scenario (single and repeated) under blast loading.

Chapter 9: Results of blast tests in Series 2 (effect of axial loading) – Paper 6

- Summarizes the results of the UHPFRC-jacketed and doubly-reinforced NSC columns under combined axial and blast loading, and discusses the effects of axial loading and the FJ-retrofit on blast performance in terms of blast-displacements, blast capacity, post-blast resistance and failure mode. Presents numerical FE simulations of the tested columns under blast loading, and presents a numerical parametric study on the effects of axial load ratio, boundary conditions, steel ratio, jacket thickness and jacket design under blast loading.

Chapter 10: Conclusions

- Summarizes the overall thesis conclusions from the experimental tests and numerical FE simulations presented in the previous chapters, and provides suggestions for future investigations.

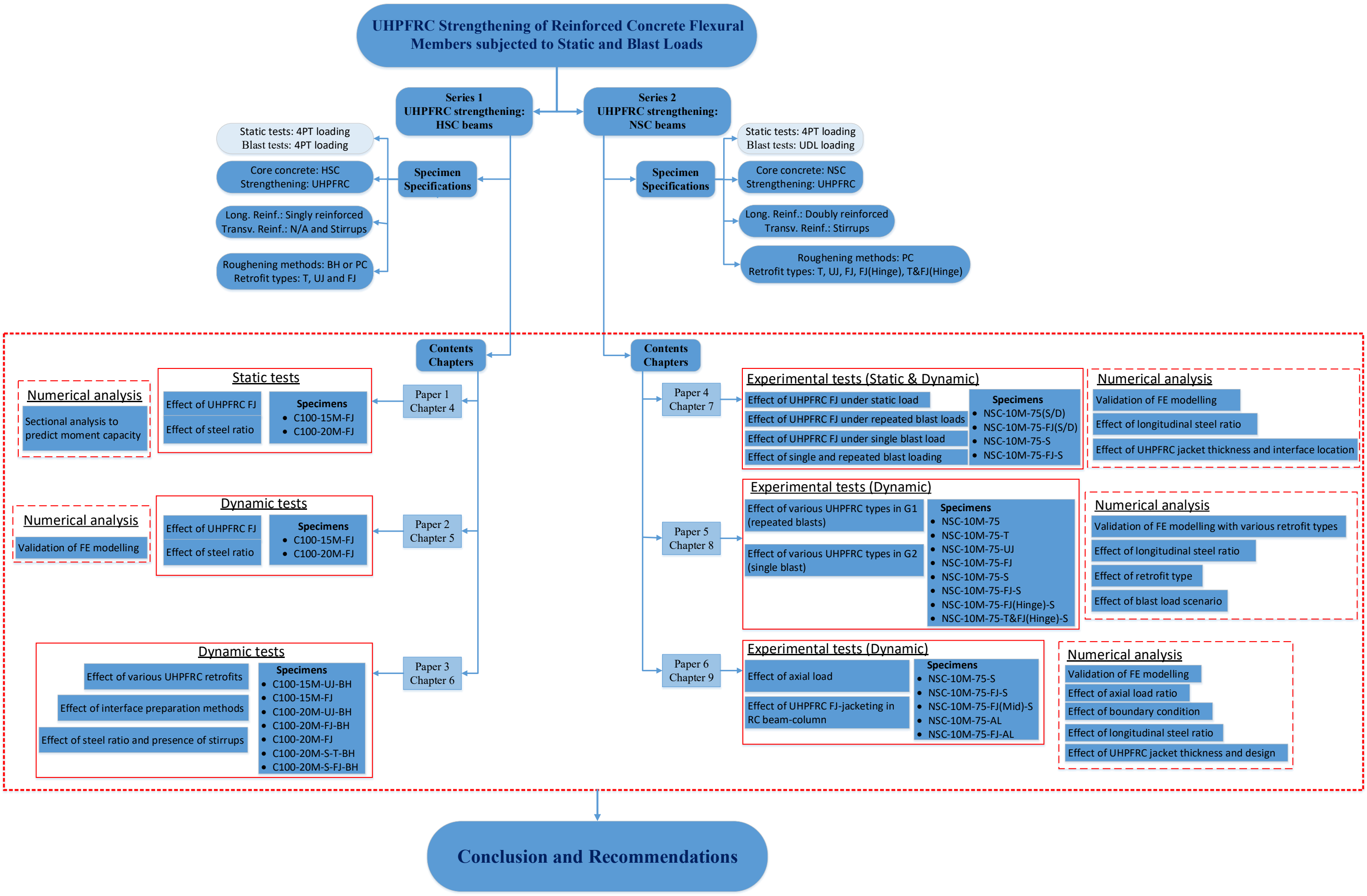

Figure 1 - 4 Thesis organization

References

[1] Brühwiler E. UHPFRC is ready to revolutionize existing and new structures. IABSE Symposium Prague 2022 - Challenges for Existing and Oncoming Structures. Prague, Czech Republic: Zürich, Switzerland, IABSE; 2022. p. 67-79.

[2] Zhu Y, Zhang Y, Hussein HH, Chen G. Flexural strengthening of reinforced concrete beams or slabs using ultra-high performance concrete (UHPC): A state of the art review. Engineering Structures. 2020;205.

[3] Yuan TF, Hong SH, Shin HO, Yoon YS. Bond Strength and Flexural Capacity of Normal Concrete Beams Strengthened with No-Slump High-Strength, High-Ductility Concrete. Materials. 2020;13.

[4] Yin H, Teo W, Shirai K. Experimental investigation on the behaviour of reinforced concrete slabs strengthened with ultra-high performance concrete. Construction and Building Materials. 2017;155:463-74.

[5] Moon J, Reda Taha MM, Kim JJ. Flexural Strengthening of RC Slabs Using a Hybrid FRP-UHPC System Including Shear Connector. Advances in Materials Science and Engineering. 2017:1-7.

[6] Safdar M, Matsumoto T, Kakuma K. Flexural behavior of reinforced concrete beams repaired with ultra-high performance fiber reinforced concrete (UHPFRC). Composite Structures. 2016;157:448-60.

[7] Hussein L, Amleh L. Structural behavior of ultra-high performance fiber reinforced concrete-normal strength concrete or high strength concrete composite members. Construction and Building Materials. 2015;93:1105-16.

[8] Noshiravani T, Brühwiler E. Experimental Investigation on Reinforced Ultra-HighPerformance Fiber-Reinforced Concrete Composite Beams Subjected to Combined Bending and Shear. ACI Stuctural Journal. 2013;110:251-61.

[9] Sakr MA, Sleemah AA, Khalifa TM, Mansour WN, Beushausen H, Dehn F, Moyo P. Behavior of RC beams strengthened in shear with ultra-high performance fiber reinforced concrete (UHPFRC). MATEC Web of Conferences. 2018;199:09002.

[10] Ramachandra Murthy A, Karihaloo BL, Priya DS. Flexural behavior of RC beams retrofitted with ultra-high strength concrete. Construction and Building Materials. 2018;175:815-24.

[11] Paschalis SA, Lampropoulos AP, Tsioulou O. Experimental and numerical study of the performance of ultra high performance fiber reinforced concrete for the flexural strengthening of full scale reinforced concrete members. Construction and Building Materials. 2018;186:351-66.

[12] Tanarslan HM, Alver N, Jahangiri R, Yalçınkaya Ç, Yazıcı H. Flexural strengthening of RC beams using UHPFRC laminates: Bonding techniques and rebar addition. Construction and Building Materials. 2017;155:45-55.

[13] Al-Osta MA, Isa MN, Baluch MH, Rahman MK. Flexural behavior of reinforced concrete beams strengthened with ultra-high performance fiber reinforced concrete. Construction and Building Materials. 2017;134:279-96.

[14] Lampropoulos AP, Paschalis SA, Tsioulou OT, Dritsos SE. Strengthening of reinforced concrete beams using ultra high performance fibre reinforced concrete (UHPFRC). Engineering Structures. 2016;106:370-84.

Chapter 2: Literature Review

2.1 Chapter Overview

This chapter presents a literature review on the use of UHPFRC to retrofit and strengthen reinforced concrete beams and slabs under static loading, with a focus on flexural and shear studies. Existing studies on UHPFRC retrofitted members under blast and impact loading are also reviewed. UHPFRC is typically always reinforced with fibers in practice; therefore, in this thesis, the term UHPFRC is used but also refers to ultra-high performance concrete (UHPC).

2.2 Previous research on RC-Beams retrofitted by UHPFRC under Static Loading

2.2.1 Flexural studies

Table 2 - 1 provides an overview of previous flexural studies. The table reports the loading type (4PT or 3PT bending, cantilever, FEM); element type (beam or slab); specimen dimensions, properties of the reference elements (concrete strength and steel ratio); and UHPFRC retrofit details (type, thickness, strength, fiber content).

Murthy et al. (2018) [1] conducted a series of tests on the flexural behavior of normal-strength RC beams (f_c' = 35 MPa) strengthened by precast T-sided UHPFRC strips (t_U = 10 mm) which were applied below the existing concrete section as seen in **Figure 2- 1**. To improve bond, the concrete surface was roughened and the strips were glued using an epoxy adhesive. The application of the UHPFRC strips improved the stiffness and load carrying capacity of the beams, and the pre-dominant failure mode was similar to that of the conventional RC beams, consisting of steel yielding followed by concrete crushing.

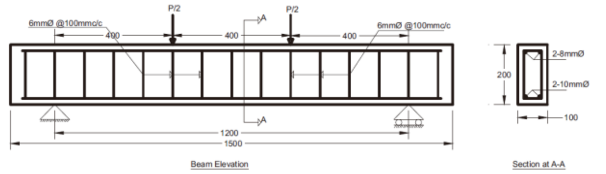

(a) Geometry of the RC beam and details of reinforcement

(b) UHPFRC strip

Figure 2- 1 Dimensions of specimens (Murthy et al. (2018))

Paschalis et al. (2018) [2] conducted a series of experimental and numerical analyses on RC beams strengthened by UHPFRC in tension (t_U= 50mm) shown in **Figure 2- 2**, with or without embedded steel bars, applied below the existing concrete section, and found that the use of UHPFRC T-sided layers significantly improved stiffness and delayed crack formation; however, the load carrying capacity was just slightly increased, while specimens with additional bars resulted in a greater increase in the load capacity.

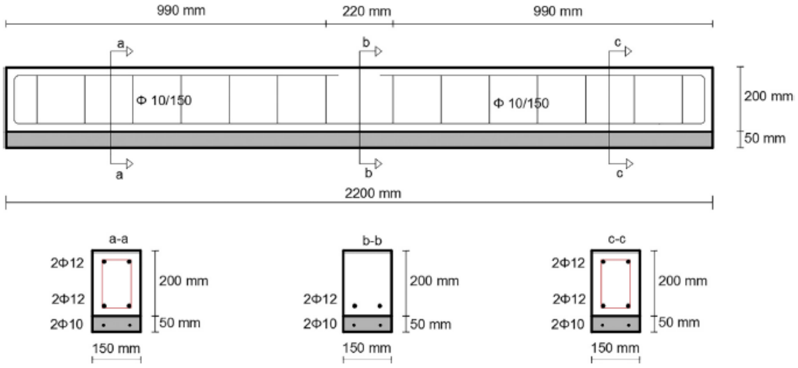

Figure 2- 2 Geometry of retrofitted specimens (Paschalis et al. (2018))

Tanarslan et al. (2017) [3] presented a further study on the use of T-sided UHPFRC laminates to strengthen conventional RC beams (f_c' = 20.4 MPa) in flexure (as shown in **Figure 2- 3**). The precast laminates were 30 mm thick, and were cast either with or without embedded steel bars. Two bonding techniques were considered (epoxy resin and mechanical anchors). Crack localization and fracture of the laminates limited the ability of the UHPFRC to increase ultimate load carrying capacity. Adding internal steel bars increased the ultimate load by a minimum of 73%. Anchored and glued beams had similar ultimate loads, but the ultimate deflection was reduced in the glued specimen with embedded reinforcement.

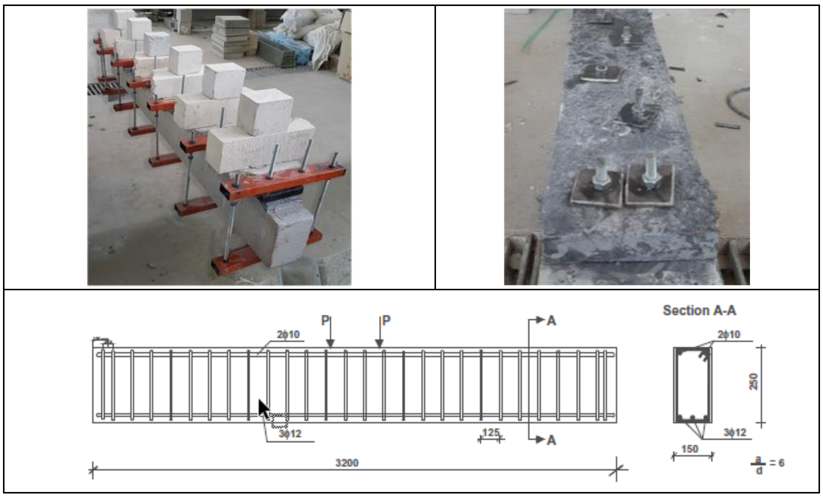

Figure 2- 3 Bonding procedure and beam dimensions (Tanarslan et al. (2017))

Al-Osta et al. (2017) [4] presented another series of tests on eight conventional RC beams (f_c' = 54 MPa) strengthened by UHPFRC. Two different bonding techniques (sand-blasting/cast in-situ, and epoxy adhesive) and three different strengthening configurations (T-sided, 2-sided and UJ) were considered shown in **Figure 2- 4**. The 30 mm UHPFRC was used to increase the existing section dimensions. Good bonding was obtained irrespective of bonding technique, and the use of UHPFRC increased the stiffness and load carrying capacity of the beams. Beams with the 3-sided (UJ) retrofit showed the highest capacity enhancement, but resulted it an unfavorable compromise in ductility. An index, consisting of the ratio of beam steel reinforcement to the UHPFRC used as retrofit, was found to play an important role in defining the ductility of the retrofitted member, with ductility reducing as this ratio reduced.

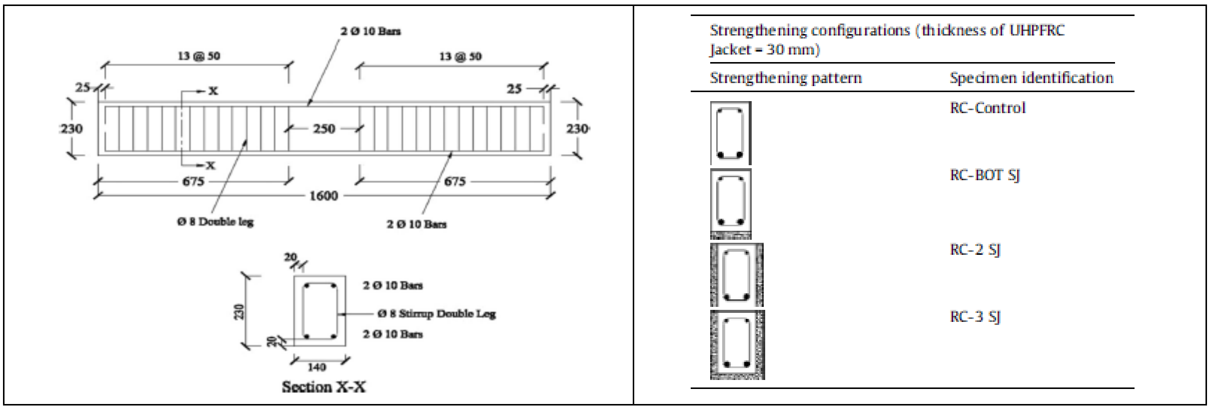

Figure 2- 4 Dimensions and Retrofitting configurations (Al-Osta et al. (2017))

Safdar et al. (2016) [5] examined the effects of compression and tension-sided UHPC retrofits, with varying thickness (t_U) from 20 to 60 mm, on the flexural behavior of normal-strength RC beams (f_c' = 29.7 MPa) presented in **Figure 2- 5**. The existing concrete was removed by high pressure water-jet and replaced by UHPC in either the tension or compression zones (within the cover, up to the mid-level of the bars, and above the bars). The addition of UHPC improved the stiffness, moment capacity, and delayed crack formation under service conditions when compared to the reference beam. In both retrofit types, the load-capacity increased with the increase in UHPC thickness, however the maximum deflection (ductility) was reduced when using the T-sided retrofits, with bar fracture in the beam with 40 mm UHPC applied up to the mid-level of the bars.

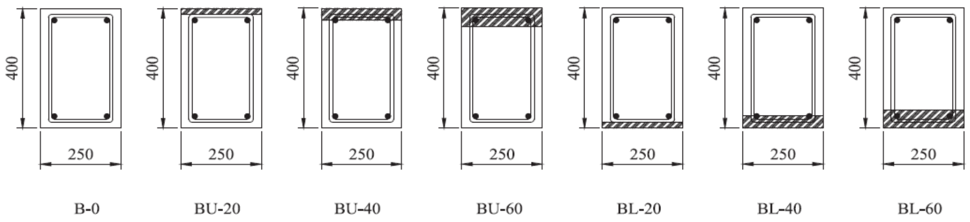

Figure 2- 5 Dimensions and Retrofitting configurations (Safdar et al. (2016))

Lampropoulos et al. (2016) [6] numerically studied the effects of UHPFRC retrofit type (T-sided, C-sided and UJ) and UHPFRC material properties on the flexural behaviour of normal-strength RC beams (f_c' = 39.5 MPa). The 50 mm UHPFRC was applied as an overlay to increase the existing section dimensions. All retrofit types increased flexural capacity, however much greater increases were achieved when using the three-sided (UJ) jackets. Doubling the UHPFRC tensile strength (from 8 to 12 MPa) did not significantly affect the results for the T or C-sided retrofits but resulted in a 50% increase in moment-capacity for the UJ type. The three-sided retrofit also showed the greatest improvement in moment capacity when compared to traditional strengthening with RC layers. In general, the authors noted that superior performance can be achieved by using three-sided UHPFRC jackets.

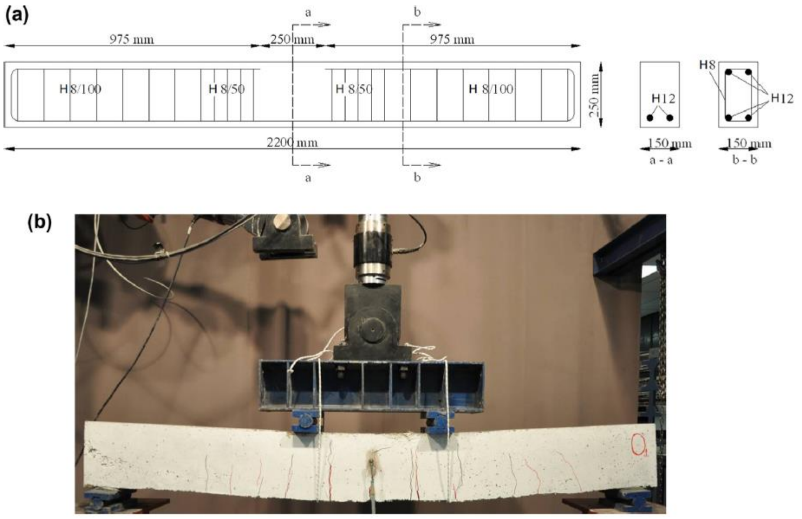

Figure 2- 6 (a) Geometry and (b) testing setup (Lampropoulos et al. (2016))

Moon et al. (2017) [7] proposed a hybrid system (seen in **Figure 2- 7**), consisting of CFRP laminates, UHPFRC and shear connectors, for the flexural strengthening of RC slabs (f_c' = 54 MPa), which was applied to the top surface of the slabs. The results showed that the hybrid combination of UHPFRC and CFRP obviously improved the stiffness, load carrying capacity and toughness, while the use of shear connectors ensured ductile behavior in the retrofitted slabs.

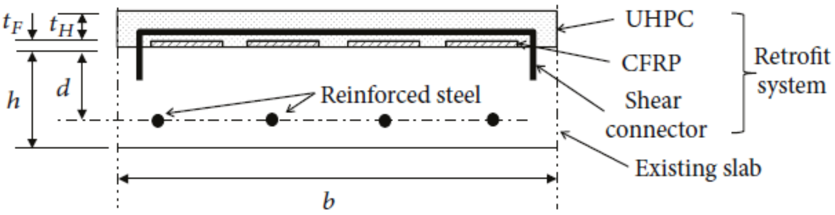

Figure 2- 7 HPC-CFRP retrofit systems for flexural strengthening (Moon et al. (2017))

From the above research, it is clear that further studies are required to examine the benefits of UHPFRC to improve the flexural behaviour of HSC beams having $f_c' \geq 60$ MPa. The benefits of implementing full-jacket retrofits, which can simultaneously increase shear and flexural resistance, also requires further study. Finally, as shown in **Table 2 - 1**, few studies have investigated the effects of longitudinal steel ratio in UHPFRC-retrofitted members. Previous research indicates that the steel ratio affects the ductility and failure mode of conventional UHPFRC beams [8-10]; thus, further data on the influence of this parameter in UHPFRC-retrofitted members is needed.

2.2.2 Shear studies

Table 2 - 1 also provides an overview of previous shear studies. The table reports the loading type (4PT or 3PT bending, cantilever, FEM); element type (beam or slab); specimen dimensions, properties of the reference elements (concrete strength and steel ratio); and UHPFRC retrofit details (type, thickness, strength, fiber content).

Research on the use of UHPFRC to increase shear capacity in shear-deficient RC members is limited. **Noshiravani and Brühwiler (2013)** [11] studied the flexure-shear behavior of composite beams, consisting of a thin layer of UHPFRC with embedded steel bars (R-UHPFRC) applied on the tension side of the normal-strength RC beams (f_c' = 41.6 MPa) shown in **Figure 2- 8**. The application of the R-UHPFRC retrofit significantly increased stiffness and ultimate resistance, and allowed beams with wide stirrups to reach their maximum bending resistance, without shear failure. Accordingly, the addition of tension R-UHPFRC was demonstrated to be an effective shear-strengthening method.

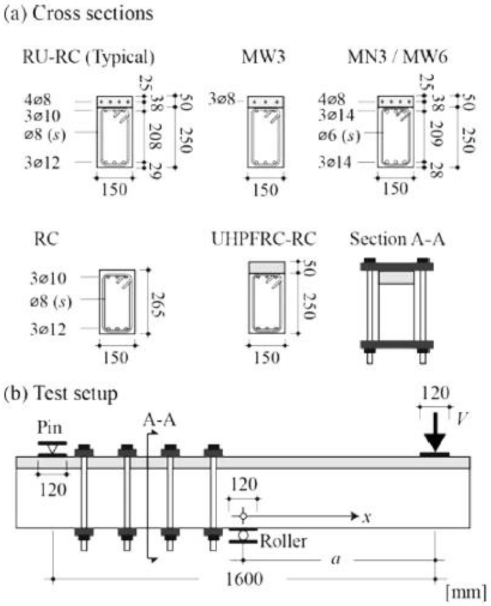

Figure 2- 8 Dimensions and retrofitting (Noshiravani and Brühwiler (2013))

Hussein and Amleh (2015) [12] investigated the flexural and shear capacity of composite UHPFRC-RC beams, with UHPFRC applied below the neutral axis in tension. Both NSC and HSC beams were tested (f_c'= 51 and 70 MPa). Each specimen had constant section dimensions of 150mm × 300mm, shown in **Figure 2- 9**. Although all beams failed in shear, the UHPFRC increased the load capacities and ductility in both the NSC and HSC beam types. Also, the bond strength between the NSC/HSC and UHPFRC was remarkably high, so shear connectors were not necessary.

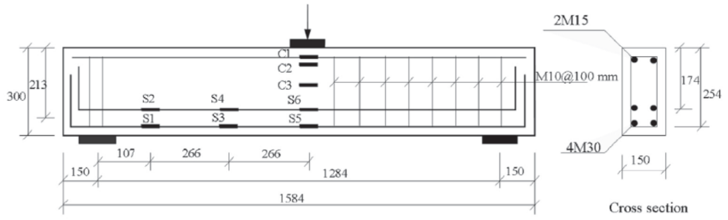

(a) Series 1

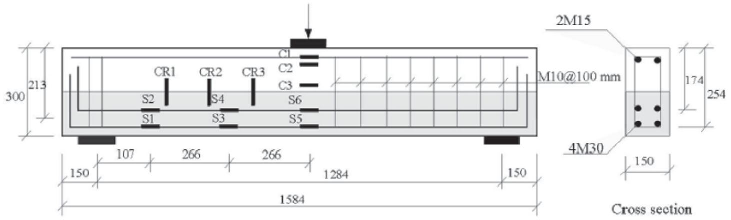

Figure 2- 9 Dimensions and retrofitting configuration (Hussein and Amleh (2015))

Sakr et al. (2018) [13] investigated the effectiveness of two different retrofitting types (2-sided, and 1-sided, applied on the web faces, with t_U = 30 mm or t_U = 60 mm, respectively) for shear improvement of RC beams (f_c' = 30 MPa) seen in **Figure 2- 10**, and showed that the specimens retrofitted by 2-sided UHPFRC had a greater increase in load capacity when compared to the single-sided retrofit (145% vs. 34%). Failure in the 2-sided retrofit occurred due to rupture of the UHPFRC plates, while debonding was observed in the beam with single-side UHPFRC plates.

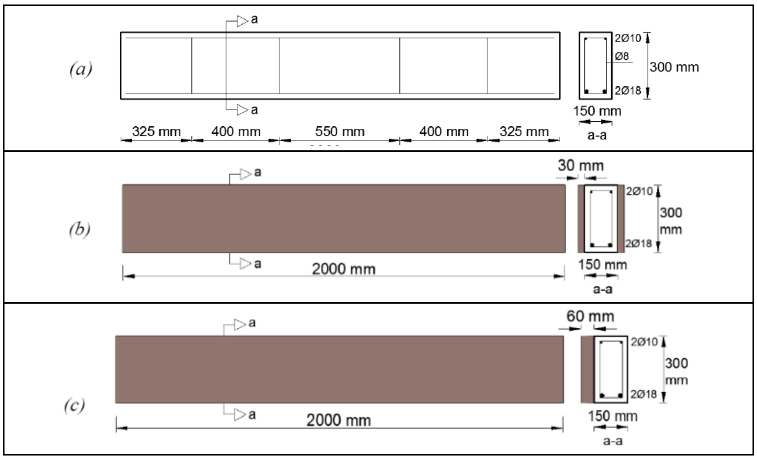

Figure 2- 10 Dimensions of specimens and retrofitting configuration (Sakr et al. (2018))

Yin et al. (2017) [14] studied the UHPFRC strengthening of RC slabs (f_c' = 23 MPa) in two series, namely: a rehabilitation (RE) series and a UHPFRC overlay (OV) series shown in **Figure 2- 11**, with the UHPFRC applied on the tension side. In the RE series, the use of UHPFRC changed the failure patterns from shear to ductile flexural failure with the increase in UHPFRC thickness (32 or 50 mm), although no improvement in ultimate strength was observed. In the OV series, shear failure was not prevented, although overall stiffness was improved, and development of shear cracks was delayed.

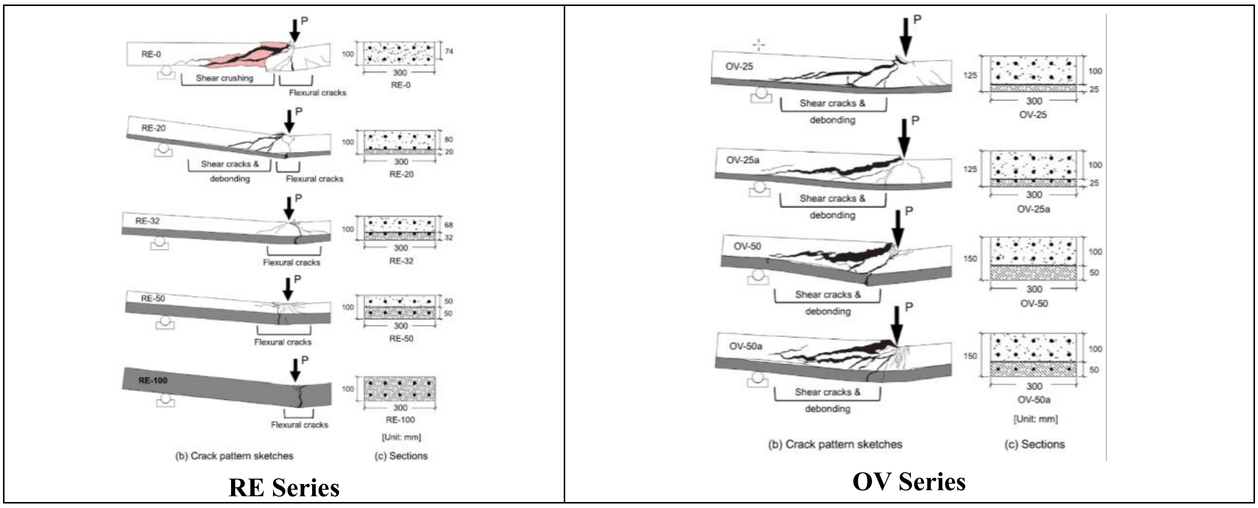

RE Series

OV Series

Figure 2- 11 Retrofitting types and failure modes (Yin et al. (2017))

Finally, **Yuan et al. (2020)** [15] studied the flexural responses of normal-strength RC beams (f_c' = 45 MPa) retrofitted by NSHSDC (no-slump, high-strength, high-ductility concrete) using T-sided (BJ), T+C-sided (2J), UJ (3J) and FJ (4J) configurations (see **Figure 2- 12**). Shear failure was not prevented in the BJ and 2J beams, however the 3J and 4J retrofits changed the failure from shear to flexure, and improved the stiffness and ductility. The flexural strength and ductility were more significantly improved when using the 4J full-jacket retrofit.

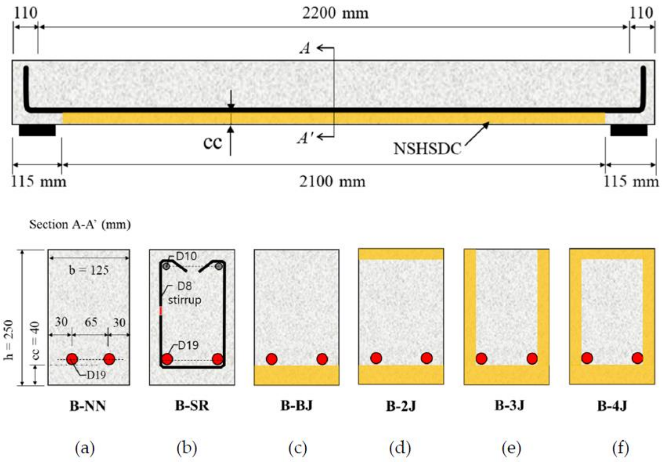

Figure 2- 12 Strengthening schemes of test beams (Yuan et al. (2020))

A summary of the aforementioned studies are provided in **Table 2 - 1**. Despite the previous valuable work, very few studies have focused on the shear-strengthening of higher-strength HSC beams ($f_c' \geq 60$ MPa). In addition, with the exception of ref. [15] which focused on NSHSDC, few studies have examined the ability of full-jacket (FJ) UHPFRC retrofits to increase shear capacity in shear-deficient RC beams.

References

[1] Ramachandra Murthy A, Karihaloo BL, Priya DS. Flexural behavior of RC beams retrofitted with ultra-high strength concrete. Construction and Building Materials. 2018;175:815-24.

[2] Paschalis SA, Lampropoulos AP, Tsioulou O. Experimental and numerical study of the performance of ultra high performance fiber reinforced concrete for the flexural strengthening of full scale reinforced concrete members. Construction and Building Materials. 2018;186:351-66.

[3] Tanarslan HM, Alver N, Jahangiri R, Yalçınkaya Ç, Yazıcı H. Flexural strengthening of RC beams using UHPFRC laminates: Bonding techniques and rebar addition. Construction and Building Materials. 2017;155:45-55.

[4] Al-Osta MA, Isa MN, Baluch MH, Rahman MK. Flexural behavior of reinforced concrete beams strengthened with ultra-high performance fiber reinforced concrete. Construction and Building Materials. 2017;134:279-96.

[5] Safdar M, Matsumoto T, Kakuma K. Flexural behavior of reinforced concrete beams repaired with ultra-high performance fiber reinforced concrete (UHPFRC). Composite Structures. 2016;157:448-60.

[6] Lampropoulos AP, Paschalis SA, Tsioulou OT, Dritsos SE. Strengthening of reinforced concrete beams using ultra high performance fibre reinforced concrete (UHPFRC). Engineering Structures. 2016;106:370-84.

[7] Moon J, Reda Taha MM, Kim JJ. Flexural Strengthening of RC Slabs Using a Hybrid FRP-UHPC System Including Shear Connector. Advances in Materials Science and Engineering. 2017:1-7.

[8] Shao Y, Billington SL. Predicting the two predominant flexural failure paths of longitudinally reinforced high-performance fiber-reinforced cementitious composite structural members. Engineering Structures. 2019;199.

[9] Pokhrel M, Bandelt MJ. Material properties and structural characteristics influencing deformation capacity and plasticity in reinforced ductile cement-based composite structural components. Composite Structures. 2019;224.

[10] Li Y, Aoude H. Ductility of Ultra-High Performance Concrete Beams Reinforced with Ordinary, High-Strength and Stainless Steel Bars. ACI Symposium Publication. 2022;351.

[11] Noshiravani T, Brühwiler E. Experimental Investigation on Reinforced Ultra-HighPerformance Fiber-Reinforced Concrete Composite Beams Subjected to Combined Bending and Shear. ACI Stuctural Journal. 2013;110:251-61.

[12] Hussein L, Amleh L. Structural behavior of ultra-high performance fiber reinforced concrete-normal strength concrete or high strength concrete composite members. Construction and Building Materials. 2015;93:1105-16.

[13] Sakr MA, Sleemah AA, Khalifa TM, Mansour WN, Beushausen H, Dehn F, Moyo P. Behavior of RC beams strengthened in shear with ultra-high performance fiber reinforced concrete (UHPFRC). MATEC Web of Conferences. 2018;199:09002.

[14] Yin H, Teo W, Shirai K. Experimental investigation on the behaviour of reinforced concrete slabs strengthened with ultra-high performance concrete. Construction and Building Materials. 2017;155:463-74.

[15] Yuan TF, Hong SH, Shin HO, Yoon YS. Bond Strength and Flexural Capacity of Normal Concrete Beams Strengthened with No-Slump High-Strength, High-Ductility Concrete. Materials. 2020;13.

Table 2 - 1 Previous studies on UHPFRC retrofitted slabs and beams under static loads

Authors	Load type	Element type	Flexural or shear strengthening ?	Dimensions (H ×W ×L)	Reference beam		UHPFRC retrofit details			
					f'_c (MPa)	Steel ratio ρ (%)	Type [a]	Thickness (mm) (overlay/retrofit) [b]	f'_c (MPa)	Fiber content (%)
Safdar et al (2016)	Static (4PT)	Beam	Flexure	250×400×3000	29.7	0.44	T-sided C-sided	20-40-60 (retrofit)	156	-
Lampropoulos et al. (2016)	Static (FEM)	Beam	Flexure	150×200×2200	39.5	0.71	T-sided C-sided UJ	50 (overlay)	164	3%
Tanarslan et al. (2017)	Static (4PT)	Beam	Flexure	150×250×3200	20.4	1.00	T-sided	30 (overlay)	200	3%
Al-Osta et al (2017)	Static (4PT)	Beam	Flexure	140×230×1600	54	0.73	T-sided 2-sided UJ	30 (overlay)	128	-
Moon et al. (2017)	Static (4PT)	Slab	Flexure	900×130×2440	49	-	C-sided	- (hybrid system)	79	-
Murthy et al. (2018)	Static (4PT)	Beam	Flexure	100×200×1500	35	1.26	T-sided	5-15 (overlay)	123	2%
Paschalis et al. (2018)	Static (4PT)	Beam	Flexure	150×200×2200	30.9	0.89	T-sided	50 (overlay)	137	3%
Yin (2017)	Static (3PT)	Slab	Shear	100×300×1600	23	2.50	T-sided	25-50 (retrofit or overlay)	156	3%
Noshiravani and Brühwiler (2013)	Static (Cantilever)	Beam	Shear	150×250×1600	42	1.02	T-sided	50 (retrofit)	160	3%
Sakr et al. (2018)	Static (4PT)	Beam	Shear	150×300×2000	30	1.32	1-sided 2-sided	30-60 (overlay)	135	2%
Yuan et al. (2020)	Static (3PT)	Beam	Shear	125×250×2420	45	2.26	T-sided C-sided UJ/ FJ	20-40 (retrofit)	120	1.5%
Hussein and Amleh (2015)	Static (4PT)	Beam	Shear	150×300×1284	51/70	8.81	T-sided	51 (hybrid system)	160	1-2%

[a] T-sided: applied on the tension side, C-sided: applied on the compression side, UJ: applied on three sides in the form of U-jacket, FJ: applied on 4 sides in the form of Full-jacket

[b] Retrofit: the UHPFRC is used to replace the existing concrete cover; Overlay: the UHPFRC is added an additional layer which increases the section dimensions

2.3 Previous research on UHPFRC retrofitted members under blast/impact

Table 2 - 2 provides an overview of previous dynamic studies. The table reports the loading type (impact or blast); element type (beam, slab or column); specimen dimensions, properties of the reference elements (concrete strength and steel ratio); and UHPFRC retrofit details (type, thickness, strength, fiber content).

Fan et al. (2018) [1] numerically studied the impact behavior of UHPFRC strengthened bridge columns under vehicle collisions (see **Figure 2- 13**), and carried out a parametric study on the influences of UHPFRC jacket thickness, UHPFRC strength, reinforcement ratios, and impact speed on the impact performance. The UHPFRC significantly reduced the impact-induced damage and displacements in the columns, while the parametric study showed that the UHPFRC jacket thickness played the most important role in affecting the impact resistance under relatively low impact speeds.

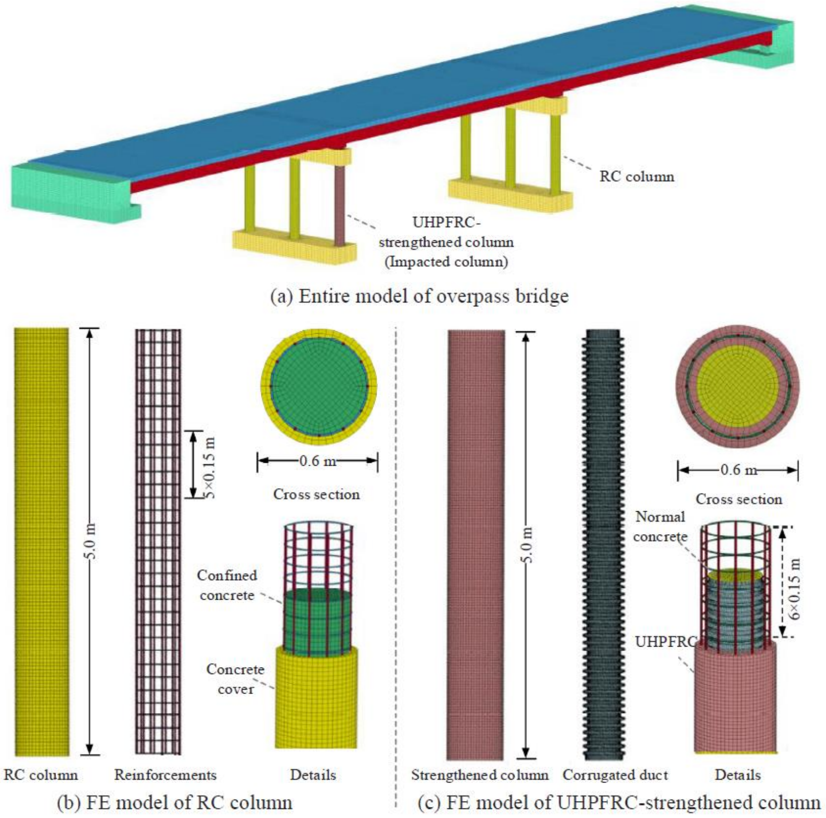

Figure 2- 13. High-resolution FE model of overpass bridge (Fan et al. (2018))

In a further study, **Fan et al. (2019)** [2] conducted low-velocity impact tests on columns (f_c' = 40 MPa) using three UHPFRC retrofit schemes (see **Figure 2- 14**), with the existence of axial load. The tests confirmed the superior crash-worthiness of the axially-loaded UHPFRC columns when compared to conventional RC columns. Placing the UHPFRC at the "two ends" outperformed the other retrofit schemes of "contact zone" or combination of "contact zone/two ends", while the latter tended to cause brittle shear failure.

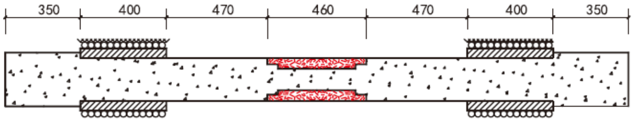

(a) L06S100M with a UHPFRC jacket in contact-impact zone

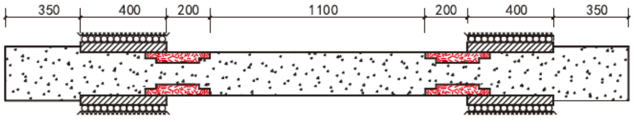

(b) L06S100E with two UHPFRC jackets distributed in two ends

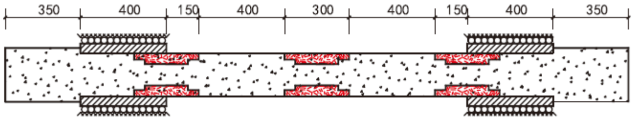

(c) L06S100T with three UHPFRC jackets

Figure 2- 14 Dimensions and retrofitting configurations (Fan et al. (2019))

Using the same data for validation, **Kadhim et al. (2022)** [3] numerically studied the effects of UHPFRC segment length shown in **Figure 2- 15**, pre-load level, impact location and slenderness ratio on the impact performance of hybrid UHPFRC-NSC columns. Using a UHPFRC segment greater than 600 mm (0.27 of the column length) resulted in great improvement in displacement control and impact resistance and changed the failure from the impact location to the end of the UHPFRC segment. Applying a higher axial pre-load was beneficial at low steel ratios, and the use of UHPFRC segments was also found beneficial in slender columns.

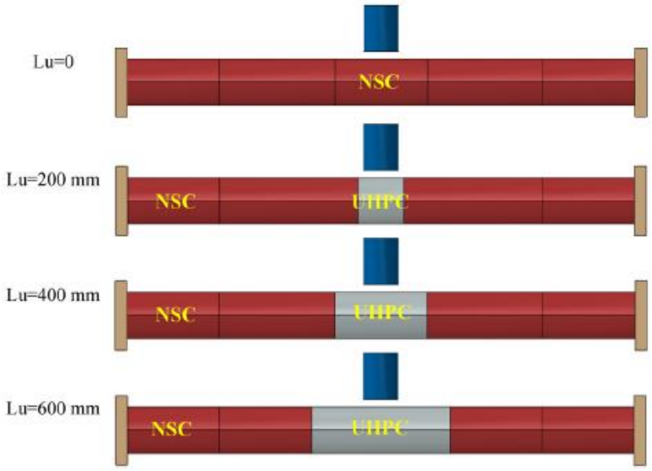

Figure 2- 15 Locations of UHPFRC segments (Kadhim et al. (2022))

Hanifehzadeh et al. (2021) [4] proposed a combined retrofitting configuration consisting of a 30 mm UHPFRC jacket and an exterior 5 mm steel shell to improve the blast resistance of normal-strength concrete columns ($f_c' = 42$ MPa) shown in **Figure 2- 16**. The experimental tests studied the behaviour of the columns under cyclic loading, while the blast behaviour was studied numerically. The proposed retrofitting was shown to increase the energy absorption and residual axial capacity of the columns under blast loading.

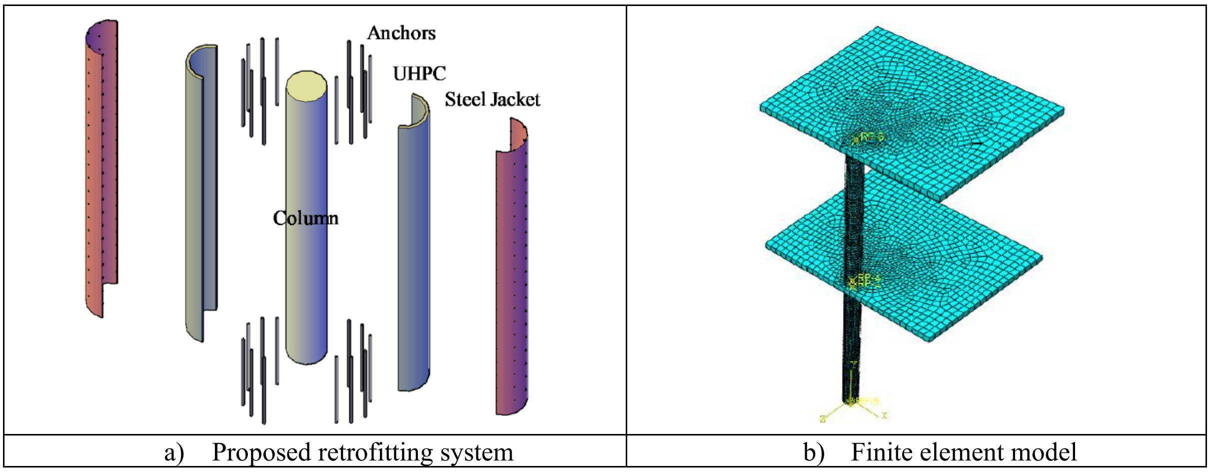

a) Proposed retrofitting system

b) Finite element model

Figure 2- 16 Retrofitting configuration and meshing (Hanifehzadeh et al. (2021))

Lee et al. (2020) [5] carried out a series of tests to study the effect of seismic detailing and UHPFRC jacketing on the behavior of normal-strength concrete columns ($f_c' = 22$ MPa) under both impact and shock-tube blast loading, and found that the combination of seismic detailing and UHPFRC jacketing significantly improved the blast and impact resistance of the columns, resulting in decreased displacements, better control of cracking/damage and increased capacity under both impact and blast loading.

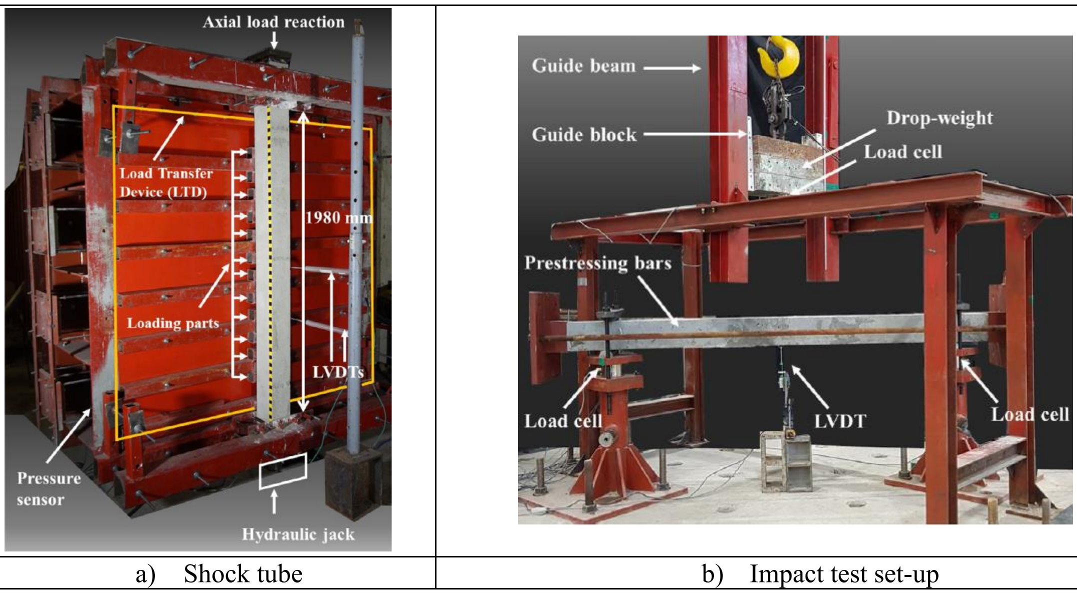

a) Shock tube

b) Impact test set-up

Figure 2- 17. Test setup (Lee et al. (2020))

A limited number of impact/blast studies have focused on beams. **Zanuy and Ulzurrun (2020)** [6] studied the low-velocity impact resistance of shear-critical reinforced concrete beams (f_c' = 30 MPa) strengthened by a layer of UHPFRC on the tension side (seen in **Figure 2- 18**), and found that the UHPFRC layer worked like a stress ribbon increasing the impact resistance and reducing the impact debris. Meanwhile, the interface between the old concrete and the UHPFRC placed at the level of the longitudinal reinforcement was susceptible to debonding.

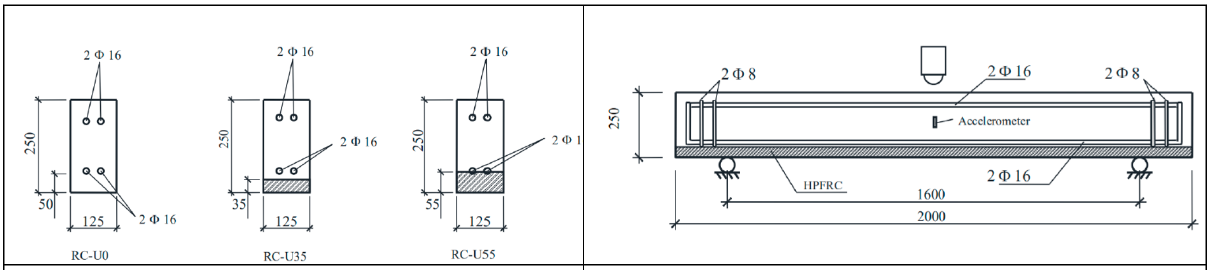

a) Specimen dimensions

b) Test set-up

Figure 2- 18 Dimensions and retrofitting configurations (Zanuy and Ulzurrun (2020))

Wei et al. (2021) [7] carried out a series of low-velocity drop hammer impact tests to investigate the dynamic behavior of UHPFRC-strengthened normal-strength RC beams (f_c' = 30 MPa) under single or repeated impacts. Three retrofit types were examined, including a UHPFRC layer placed on the tension side without a spacing gap, a UHPFRC layer placed on both the tension and compression sides without a spacing gap, and a UHPFRC layer placed on the tension side with a spacing gap of 5 mm. The results showed that the UHPFRC restrained shear cracking and increasing the energy dissipating capacity, while the spacing gap further improved the impact performance.

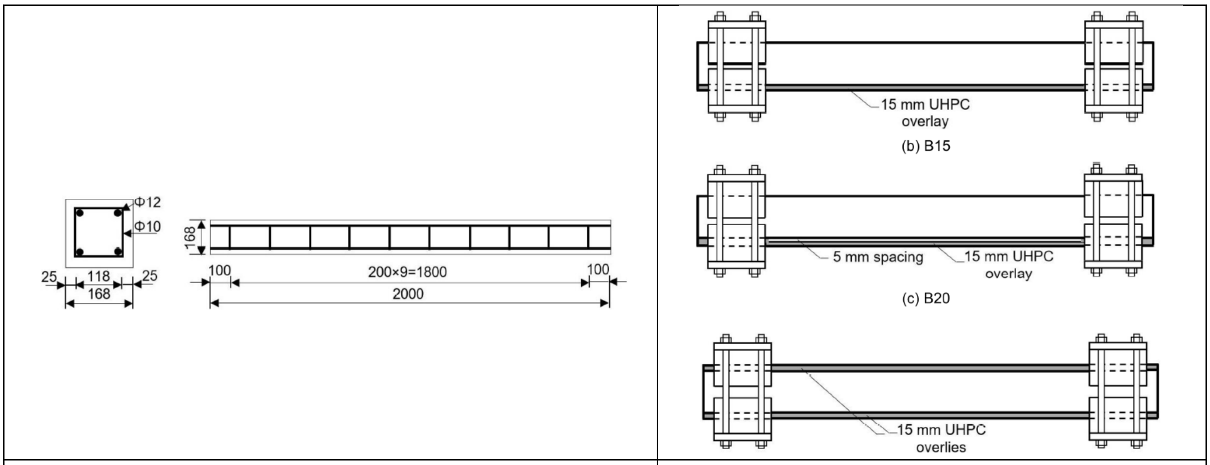

a) Specimen dimensions and reinforcement

b) Retrofitting types

Figure 2- 19 Dimensions and retrofitting configurations (Wei et al. (2021))

Habel and Gauvreau (2009) [8] studied the impact response of normal-strength concrete (f_c' = 33 MPa) slab strips with UHPFRC overlays under drop-weight impacts using a three-point bending or cantilever setup (see **Figure 2- 20**). The UHPFRC significantly improved the impact performance of the slabs by preventing crushing/spalling at the impact point, reduced deflections, and had a load distribution function. Adding reinforcement in the UHPFRC layer in tension increased the load capacity and resulted in better crack distribution due to tension-stiffening.

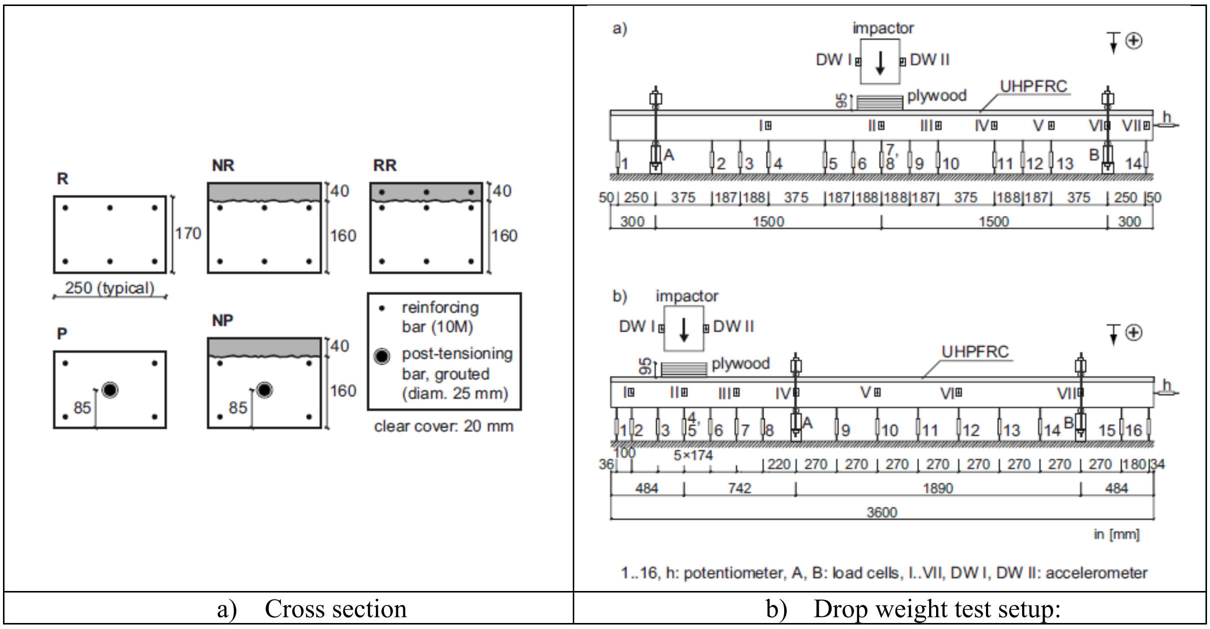

a) Cross section

b) Drop weight test setup:

Figure 2- 20 Cross section of specimens and test setup (Habel and Gauvreau (2009))

A summary of the aforementioned studies in the literature is provided in **Table 2 - 2**. It can be noted that no studies in the literature have examined the effect of UHPFRC jacketing on the blast behaviour of RC beams. In general, studies on the impact and blast performance of higher-strength concrete members retrofitted with UHPFRC are also limited.

References

[1] Fan W, Xu X, Zhang Z, Shao X. Performance and sensitivity analysis of UHPFRC-strengthened bridge columns subjected to vehicle collisions. Engineering Structures. 2018;173:251-68.

[2] Fan W, Shen D, Yang T, Shao X. Experimental and numerical study on low-velocity lateral impact behaviors of RC, UHPFRC and UHPFRC-strengthened columns. Engineering Structures. 2019;191:509-25.

[3] Kadhim MMA, Semendary AA, Hammed M, Cunningham LS. Numerical investigation of hybrid UHPC columns subject to lateral impact. Journal of Building Engineering. 2022;47.

[4] Hanifehzadeh M, Aryan H, Gencturk B, Akyniyazov D. Structural Response of Steel Jacket-UHPC Retrofitted Reinforced Concrete Columns under Blast Loading. Materials (Basel). 2021;14.

[5] Lee JY, Aoude H, Yoon YS, Mitchell D. Impact and blast behavior of seismically-detailed RC and UHPFRC-Strengthened columns. International Journal of Impact Engineering. 2020;143.

[6] Zanuy C, Ulzurrun GSD. Impact Resisting Mechanisms of Shear-Critical Reinforced Concrete Beams Strengthened with High-Performance FRC. Applied Sciences. 2020;10.

[7] Wei J, Li J, Wu C, Liu Z-x, Fang J. Impact resistance of ultra-high performance concrete strengthened reinforced concrete beams. International Journal of Impact Engineering. 2021;158.

[8] Habel K, Gauvreau P. Behavior of Reinforced and Posttensioned Concrete Members with a UHPFRC Overlay under Impact Loading. Journal of Structural Engineering. 2009;3:292-300.

Table 2 - 2 Previous studies on impact and blast behavior of UHPFRC retrofitted members

Authors	Load type	Element type	Flexural or shear strengthening ?	Dimensions (in mm)	Reference beam		UHPFRC retrofit details			
					f'_c (MPa)	Steel ratio ρ (%)	Type [a]	Thickness (mm) [b]	f'_c (MPa)	Fiber content (%)
Fan et al. (2018)	Impact (FEM)	Column	Flexure	Ø600×5000	30	1.3	Jacketing	100 (retrofit)	152.5	2%
Fan et al. (2019)	Impact (Drop-weight)	Column	Flexure	Ø200×2200	40	0.96/1.92	Jacketing: 2-Ends Middle Combination	50 (retrofit)	155	2.5%
Kadhim et al. (2022)	Impact (FEM)	Column	Flexure	Ø200×2200	40	0.96/1.92	Jacketing: Middle (0-600mm)	50 (retrofit)	155	2.5%
Lee et al. (2020)	Impact (Drop-weight) Blast (Shock-tube)	Column	Flexure	160 × 160 × 2468	20	2.78	Jacketing	15 (retrofit)	152	2% 3%
Hanifehzadeh et al. (2021)	Blast (FEM)	Column	Flexure	Ø400 × 1600	49	1.75	Steel-jacket with UHPC	20-80 (overlay)	146	2.5%
Habel and Gauvreau. (2009)	Impact (Drop-weight)	Slab	Flexure	170 × 250 × 3600	33	0.70	T-sided C-sided	40 (overlay)	128	5.5%
Zanuy and Ulzurrun (2020)	Impact (Drop-weight)	Beam	Flexure	125 × 250 × 2000	54	1.60	T-sided	35/55 (retrofit)	135	2%
Wei et al. (2021)	Impact (Drop-weight)	Beam	Flexure	168 × 168 × 2000	35	6.40	T-sided C-sided	15 (overlay)	147	2.5%

[a] T-sided: applied on the tension side, C-sided: applied on the compression side, Jacketing: applied on 4 sides or circumference

[b] Retrofit: the UHPFRC is used to replace the existing concrete cover; Overlay: the UHPFRC is added an additional layer which increases the section dimensions

Chapter 3: Experimental Program

3.1 Chapter Overview

This chapter presents a description of the experimental program in terms of specimen designs, material properties, specimen construction, test setups and testing procedures.

3.2 Specimen Specifications

As part of this study, a total twenty-one (21) beams were retrofitted with ultra-high-performance fiber reinforced concrete (UHPFRC) and tested under either static or blast loads. The following provides details on the specimen designs and test variables in the two series of tests.

3.2.1 Specimens in Series 1

Series 1 included nine (9) beams built with high-strength concrete (HSC) and strengthened with UHPFRC. Two beams were tested under static four-point (4PT) bending and seven beams were tested under repeated blast loads using the shock-tube. Consistent with the static tests, the blast tests were conducting using a 4PT bending setup. As shown in **Figure 3 - 1**, all beams had dimensions of 125 mm × 250 mm × 2440 mm (width × height × length) and were tested over a simply supported span of 2232 mm, with a constant moment region of 750mm, and shear spans of 741mm. The beams were singly reinforced with either 2-15M or 2-20M bars in tension (ρ=1.6% or 2.4%). To ensure sufficient development length, the 15M and 20M bars were bent with 90° and 180° hooks at their ends. The tests included beams built with and without stirrups to examine shear and flexural behaviour. In the specimens with stirrups, transverse reinforcement consisted of U-shaped stirrups made from 6.3 mm wire spaced at s = 100 mm (d/2) in the shear spans, which met the minimum shear reinforcement requirement in the CSA A23.3-19 standard.

All beams were cast using plain HSC first, and then retrofitted with UHPFRC by replacing the existing concrete cover. As shown in **Figure 3 - 2**, three retrofit types were considered: Full-Jacket, U-jacket and T-sided (tension). The substrate interface was roughened to the outer edge of the longitudinal steel bars, using preparation methods were considered (Bush hammer or Point chisel), resulting in a roughness of 6 mm/10 mm (Concrete Surface Profiles of CSP6-10 as specified by the International Concrete Repair Institute, ICRI) [1]. The UHPFRC thickness after retrofitting was 41 mm on the bottom face, and 20 mm on the other sides. The specimens details are summarized in **Table 3 - 1** and the nomenclature is explained in **Figure 3 - 3**. The results from the tests are compared to eight control HSC beams tested in references [2, 3].

The specimen designs can be organized in three groups:

The **15M Group** consists of three UHPFRC retrofitted beams built with 2-15M bars (ρ = 1.6%) and without stirrups. Two retrofit types (Full-Jacket and U-jacket) and interface preparation methods (bush hammer and chisel) were considered. *C100-15M-UJ-BH* was retrofitted by U-jacket, and the interface was prepared by bush hammer to a roughness of CSP6. *C100-15M-FJ-C* is retrofitted by Full-jacket, and roughened by point chisel to CSP10. Two beams were tested under repeated blast loads and the remaining one was tested under static loading. The results are compared to four control HSC beams (2 static and 2 dynamic) built with 2-15M bars, and either with or without stirrups in the shear spans (*C100-15M-S* and *C100-15M*).

The **20M Group** consists of six UHPFRC retrofitted beams with 2-20M bars (ρ = 2.4%). The first four beams were built without stirrups. Two retrofit types (Full-Jacket and U-jacket) and interface preparation methods (bush hammer and chisel) were considered. *C100-20M-UJ-BH* and *C100-20M-FJ-BH* were retrofitted with a U-Jacket and Full-jacket, and roughened by bush hammer to a roughness of CSP6. *C100-20M-FJ-C* was retrofitted by Full-jacket and roughened by point chisel to CSP10. Three beams were tested under repeated blasts and the remaining one was tested under static loads. The results are compared to four control HSC beams (2 static and 2 dynamic) built with 2-20M bars, and either with or without stirrups (*C100-20M-S* and *C100-20M*).

The remaining two beams were built with 2-20M bars (ρ = 2.4%), but with stirrups in the shear spans. Two retrofit types (Full-Jacket and T-side) and a single interface preparation method (bush hammer) were considered. Specimens *C100-20M-S-FJ-BH* and *C100-20M-S-T-BH* were roughened by bush hammer to a roughness of CSP6, and retrofitted by Full-jacket and T-sided UHPFRC, respectively. All specimens were tested under repeated blast loads. The results are compared to two control HSC beams (1 static and 1 dynamic) built with 2-20M bars and stirrups (*C100-20M-S*).

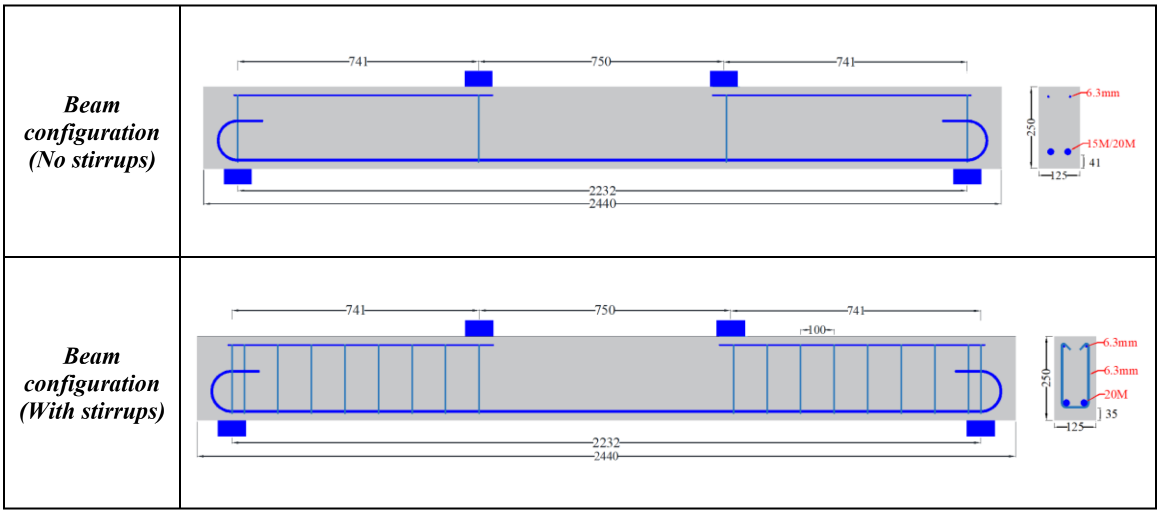

Figure 3 - 1 Specimen dimensions and reinforcement in Series 1

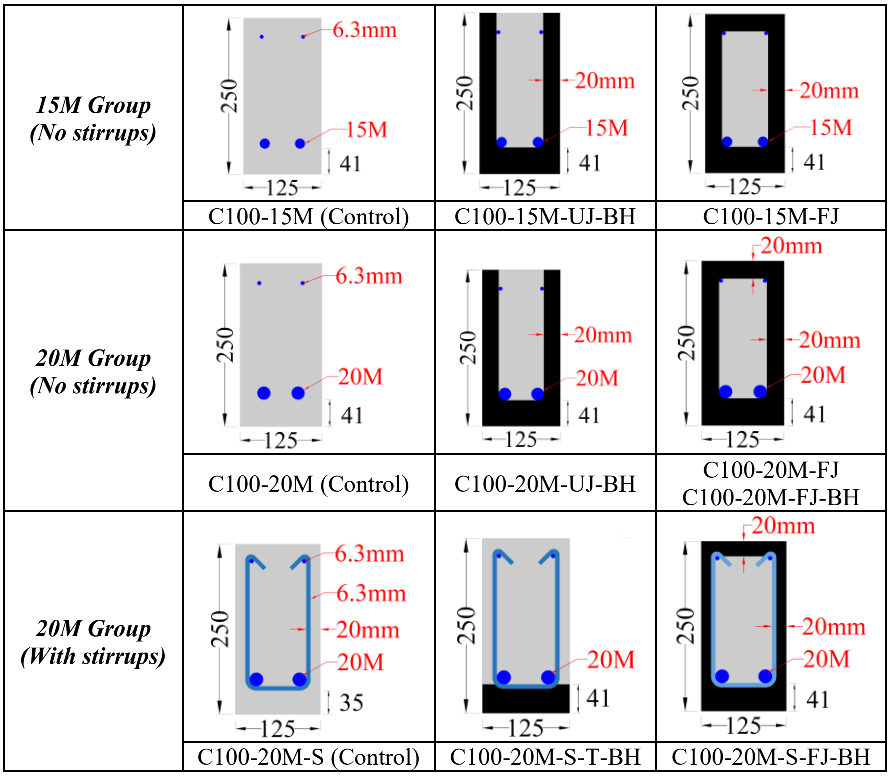

Figure 3 - 2 Retrofit types in Series 1

Table 3 - 1 Beams properties in series 1

Set	Specimen ID	f'_c (MPa)		Retrofitting type	Roughness method	Steel Reinforcement		Load type
		HSC	UHPFRC			Longitudinal	Transverse	
15M Group (No stirrups)	C100-15M-UJ-BH	100	164	U-Jacket	Bush-Hammer	2-15M	-	D
	C100-15M-FJ	100	164	Full-Jacket	Chisel	2-15M	-	S/D
20M Group (No stirrups)	C100-20M-UJ-BH	97	164	U-Jacket	Bush-Hammer	2-20M	-	D
	C100-20M-FJ-BH	97	164	Full-Jacket	Bush-Hammer	2-20M	-	D
	C100-20M-FJ	101	164	Full-Jacket	Chisel	2-20M	-	S/D
20M Group (With stirrups)	C100-20M-S-FJ-BH	100	164	Full-Jacket	Bush-Hammer	2-20M	s = 100 mm U stirrups	D
	C100-20M-S-T-BH	100	164	T-sided	Bush-Hammer	2-20M	s = 100 mm U stirrups	D
Control beams	C100-15M (control)	100	-	-	-	2-15M	-	S/D
	C100-15M-S (control)	100	-	-	-	2-15M	s = 100 mm U stirrups	S/D
	C100-20M (control)	100	-	-	-	2-20M	-	S/D
	C100-20M-S (control)	100	-	-	-	2-20M	s = 100 mm U stirrups	S/D

Note 1: S/D = specimens tested under static and dynamic loads, D = specimen tested under dynamic loads;
Note 2: Control beams have already been tested (from reference [2] [3]).

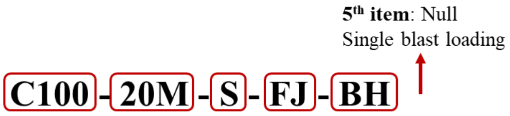

1st item: Substrate concrete types
C100-High strength concrete(100MPa)

2nd item: Long. Reinf size and types
Longitudinal bar size: 15M, 20M
Reinforced types: Singly reinforced

3rd item: Transverse steel spacing
S: Intermediate detailing (d/2=100mm)
Null: No transverse reinforcement

4th item: Retrofitting types
T, UJ, FJ:
Tension-sided, U-jacket, Full-jacket types
Null: Control specimen

5th item: Roughness method
BH: Roughened by bush hammer
Null: Roughened by point chisel

6th item: Loading types
S: Single blast loading
Null: Repeated blast loadings

Figure 3 - 3 Nomenclature in Series 1

3.2.2 Specimens in Series 2

Series 2 included a total of twelve (12) beams built with normal-strength concrete (NSC), including four control specimens and 8 specimens retrofitted with UHPFRC. Two beams were tested under static loads using a four-point bending setup, whereas the eight remaining beams were tested under uniformly distributed blast loads (UDL) using the shock-tube. As shown in **Figure 3 - 4**, all specimens had the same dimensions of 150 mm × 200 mm × 2440 mm, with a simply supported span of 2232mm. The specimens were doubly reinforced with 2-10M bars in tension and compression, resulting in reinforcement ratios of ρ= 0.8% and ρ'= 0.8%. The 10M bars were bent with 180° hooks at their ends to ensure sufficient development length. Transverse reinforcement consisted of closed ties which were made from the 6.3 mm steel wire and spaced at s = 75 mm through the span. The tie spacing was chosen to meet minimum shear reinforcement requirement for beams, and the requirements for moderate seismic detailing ($R_d = 2.5$) for columns in the CSA A23.3-19 standard.

All specimens were first constructed with the plain normal strength concrete (NSC), followed by roughening of the concrete surface, and retrofitting with UHPFRC. As shown in **Figure 3 - 5**, various retrofitting types/configurations were considered, including: Tension-sided, U-jacket, Full-jacket, Full-jacket (Hinge zone only) and the combination of Tension-sided and Full-jacket (Hinge zone). The surface of the retrofitted specimens was roughened by point chisel to a roughness of ~ 10 mm (CSP10 based on roughness grade), to the edge of the ties. Thereafter, the beams were retrofitted by UHPFRC, with a thickness of 20 mm on all faces.

The specimens in Series 2 are divided into three groups and the details of specimen properties are summarized in **Table 3 - 2** and **Figure 3 - 5**. The parameters investigated include the effect of retrofit type, repeated/single blast loadings, and axial load. The nomenclature is explained in **Figure 3 - 6**.

Group 1 consisted of six beams, including two control beams (*NSC-10M-75*) and four UHPFRC retrofitted specimens. Two beams were tested under quasi-static conditions with the remaining beams tested under repeated blast loads. Three retrofit types were considered, including: Tension-sided, U-jacket and Full-jacket (designated by *T*, *UJ*, *FJ* in the beam ID). The interface between the NSC and UHPFRC was roughened by hammering with a point chisel to a roughness of CSP 10. No axial load was applied on the specimens.

Group 2 is composed of four beams, including one control beam (*NSC-10M-75-S*) and three UHPFRC retrofitted specimens. All beams were tested under singly applied blast loads (indicated by *S* in the beam ID). Three retrofit types/configurations were considered: Full-jacket over the full span: *FJ*, Full-jacket over the middle 400 mm hinge zone: *FJ(Hinge)*, and a combination of tension-sided (full-span) and Full-jacket (hinge zone): *T&FJ(Hinge)*. The interface between the NSC and UHPFRC was roughened by hammering with a point chisel to a roughness of CSP 10. No axial load was applied on the specimens.

Group 3 is composed of two columns, including one control and one UHPFRC retrofitted specimen, which were tested under combined blast and axial loading. Within this set, *NSC-10M-75-AL* is the control specimen, while *NSC-10M-75-FJ-AL* is retrofitted by Full-jacket over the full span. The interface between the NSC and UHPFRC was roughened by hammering with a point chisel to a roughness of CSP 10. In this set, the specimens were preloaded with an axial load of 400kN, and then tested under repeated blast loadings.

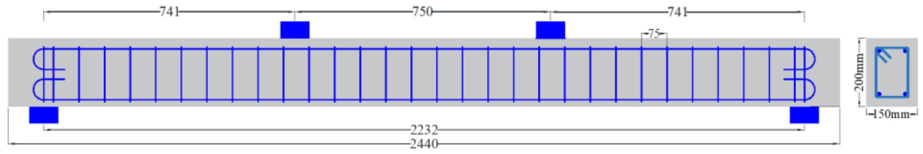

(a) Specimen dimensions and reinforcement details

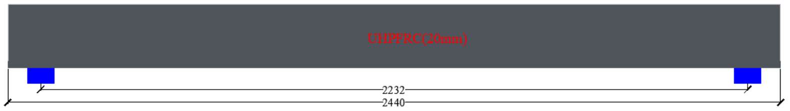

(b) FJ and UJ retrofits

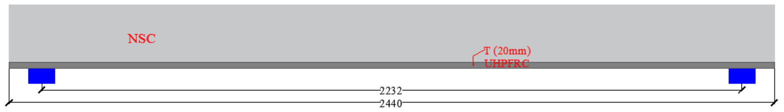

(c) T-sided retrofit

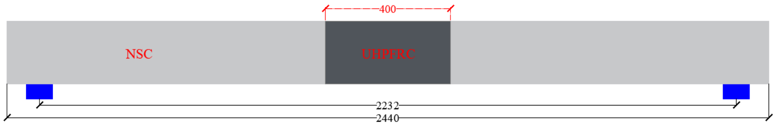

(d) Hinge retrofit

Figure 3 - 4 Specimen dimensions in Series 2

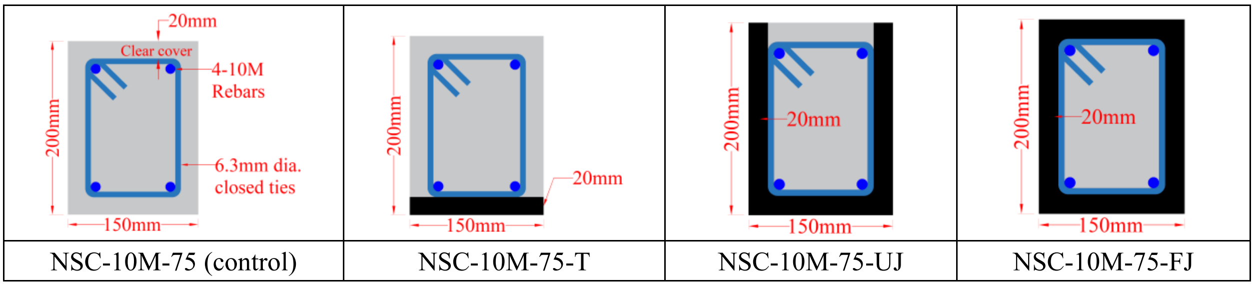

Figure 3 - 5 Cross section and retrofit schemes in Series 2

Table 3 - 2 Specimen properties in series 2

Set	Specimen ID	f'_c (MPa)		Retrofitting			Steel Reinforcement		Load type
		NSC	UHPC	Type	Roughness	Thickness (mm)	Longitudinal	Transverse	
Group 1: Static loads or Repeated Blasts	NSC-10M-75	58.4	-	-	-	-	4-10M	S = 75 mm Closed stirrup	S/D
	NSC-10M-75-T		174	T-sided	Chisel	20	4-10M	S = 75 mm Closed stirrup	D
	NSC-10M-75-UJ		180	U-Jacket	Chisel	20	4-10M	S = 75 mm Closed stirrup	D
	NSC-10M-75-FJ		174	Full-Jacket	Chisel	20	4-10M	S = 75 mm Closed stirrup	S/D
Group 2: Single Blast	NSC-10M-75-S		-	-	-	-	4-10M	S = 75 mm Closed stirrup	Dx1
	NSC-10M-75-FJ-S		180	Full-Jacket	Chisel	20	4-10M	S = 75 mm Closed stirrup	Dx1
	NSC-10M-75-FJ(Hinge)-S*		180	Full-Jacket	Chisel	20	4-10M	S = 75 mm Closed stirrup	Dx1
	NSC-10M-75-T&FJ(Hinge)-S		174	Full-Jacket	Chisel	20	4-10M	S = 75 mm Closed stirrup	Dx1
Group 3: Axial Load	NSC-10M-75-AL		-	-	-	-	4-10M	S = 75 mm Closed stirrup	D
	NSC-10M-75-FJ-AL		174	Full-Jacket	Chisel	20	4-10M	S = 75 mm Closed stirrup	D

Note: S/D = specimens tested under static and dynamic loads, D = specimen tested under dynamic loads, Dx1 = specimen tested under singly-applied blast loads (designated with –S in the specimen ID).

NSC-10M-75-FJ(Hinge)-S*: was named NSC-10M-75-FJ(Mid)-S in chapter 9 (paper 6).

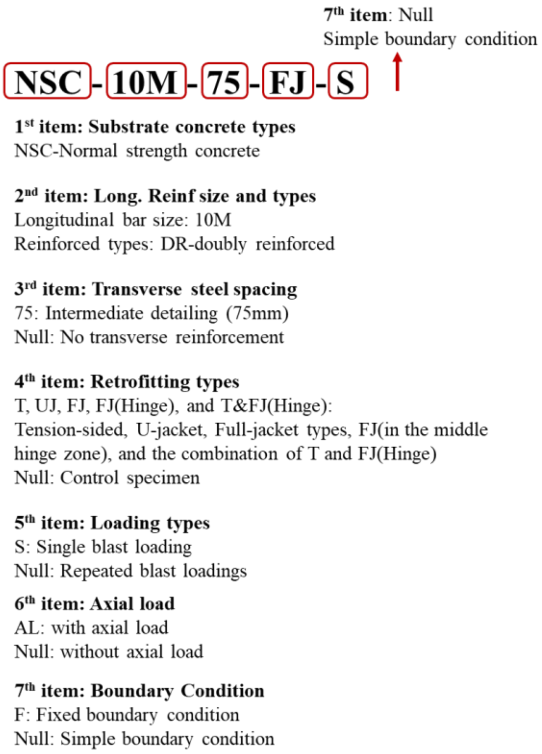

7th item: Null
Simple boundary condition

NSC-10M-75-FJ-S

1st item: Substrate concrete types
NSC-Normal strength concrete

2nd item: Long. Reinf size and types
Longitudinal bar size: 10M
Reinforced types: DR-doubly reinforced

3rd item: Transverse steel spacing
75: Intermediate detailing (75mm)
Null: No transverse reinforcement

4th item: Retrofitting types
T, UJ, FJ, FJ(Hinge), and T&FJ(Hinge):
Tension-sided, U-jacket, Full-jacket types, FJ(in the middle hinge zone), and the combination of T and FJ(Hinge)
Null: Control specimen

5th item: Loading types
S: Single blast loading
Null: Repeated blast loadings

6th item: Axial load
AL: with axial load
Null: without axial load

7th item: Boundary Condition
F: Fixed boundary condition
Null: Simple boundary condition

Figure 3 - 6 Nomenclature in Series 2

3.3 Materials

3.3.1 Concrete

The substrate used in the construction of the Series 1 and Series 2 beams consisted of high-strength concrete (HSC) and normal-strength concrete (NSC), respectively. Ultra-high performance fiber reinforced concrete (UHPFRC) with the same fiber type and fiber content was used as the retrofitting material in both series.

3.3.1.1 Concrete components

The HSC mix in Series 1 consisted of general use (GU) Portland cement, slag, silica fume, sand, two sizes of coarse aggregate (10 and 20 mm) and admixtures (a super-plasticizer and a set retarder), with the quantities shown in **Table 3 - 3**. This mix was prepared at the University of Ottawa using a large concrete pan mixer. The target compressive strength of the HSC mix at 28 days was 100MPa. The NSC in Series 2 was a ready-mixed concrete supplied by a local concrete supplier (see **Figure 3 - 8**(a)). The mix had the following specifications: compressive strength of 40MPa, max aggregate size of 10 mm, and a slump of 120 mm.

The ultra-high performance fiber reinforced concrete was supplied by *KING (a SIKA company*) and had a minimum compressive strength at 28 days of 120 MPa. The UHPFRC components consist of premix material, water, liquid admixtures (A, B and C) and straight steel fibers (with length of 13 mm, diameter of 0.2 mm and aspect ratio of 65, added at a ratio of 2.5% by volume (**Figure 3 - 7**). **Table 3 - 4** lists the proportions of the UHPFRC mix components. All UHPFRC concrete was mixed in a large pan-mixer at the University of Ottawa (**Figure 3 - 8**(b)).

Table 3 - 3 HSC mix proportions

Cement (kg/m^3)	Slag (kg/m^3)	Silica Fume (kg/m^3)	Sand (kg/m^3)	Coarse aggregate 1 10 mm (kg/m^3)	Coarse aggregate 2 20 mm (kg/m^3)	Water (kg/m^3)	SP (L/m^3)	Retarder (L/m^3)
373	164	48	738.9	560	560	157.2	13.3	2.8

Table 3 - 4 UHPFRC (UP-F2) mix proportions

Premix (kg/m^3)	Water (kg/m^3)	Admixture A (kg/m^3)	Admixture B (kg/m^3)	Admixture C (kg/m^3)	Steel Fibers (kg/m^3)
1928.81	195.98	14.61	25.55	27.59	195.00

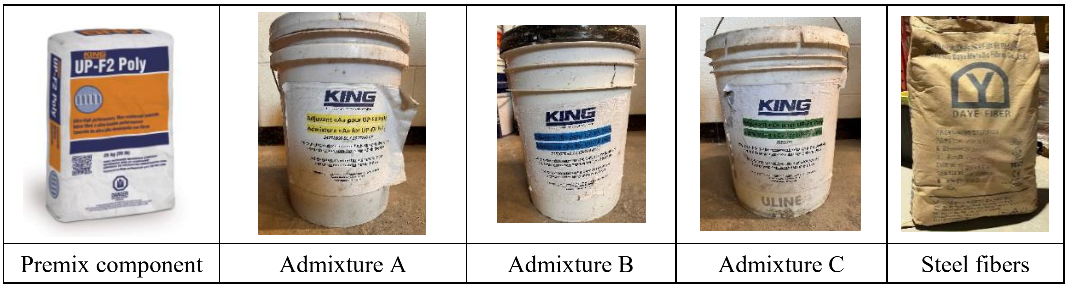

Premix component | Admixture A | Admixture B | Admixture C | Steel fibers

Figure 3 - 7 UHPFRC (UP-F2) components

a) Ready mix NSC for series 2 | **b)** Pan-mixer at the University of Ottawa

Figure 3 - 8 Pan-mixer and ready-mixed concrete casting

3.3.1.2 Compression tests

Standard tests were conducted to determine the compressive strengths of the NSC, HSC and UHPFRC concrete. The compression tests were carried out using a 1000 KN PILOT Control System cylinder testing machine, as shown in **Figure 3 - 9(a)**. In accordance with the CSA A23.1:19/CSA A23.2:19 standards, no less than six cylindrical specimens with dimensions (dia. × height) of 100 mm × 200 mm for NSC and HSC, or 75 mm × 150 mm for UHPFRC were fabricated for each batch to obtain the compressive properties. The rate of loading was within 0.15 MPa/s to 0.35 MPa/s for NSC/HSC and 0.9-1.1MPa/s for UHPFRC. **Table 3 - 5** summarizes the results of the compressive tests for all concrete types on the testing day. Additional compressive tests were conducted on a 2500 KN MTS testing machine (seen in **Figure 3 - 9(b)**) to obtain the stress-strain relationships of UHPFRC. Two LVDTs were used to measure the average vertical displacement and strain. The resulting stress-strain curves of the UHPFRC from both series are shown in **Figure 3 - 10**.

Table 3 - 5 Compressive test results

Sets ID	Specimen ID	Average compressive strength of Substrate concrete		Average compressive strength of UHPFRC		Loading types*
		Cylinder size (mm)	f'_c (MPa)	Cylinder size (mm)	f'_c (MPa)	
Series 1	C100-15M-UJ-BH	100 × 200	110	75 × 150	175	D
	C100-15M-FJ		110(D),99 (S)		145(D),182(S)	S/D
	C100-20M-UJ-BH		102		151	D
	C100-20M-FJ-BH		102		151	D
	C100-20M-FJ		112		145(D),182(S)	S/D
	C100-20M-d/2-FJ-BH		109		171	D
	C100-20M-d/2-T-BH		109		171	D
Series 2	NSC-10M-75	100 × 200	58.4	75 × 150	-	S/D
	NSC-10M-75-T				174	D
	NSC-10M-75-UJ				180	D
	NSC-10M-75-FJ				174(D),180(S)	S/D
	NSC-10M-75-S				-	Dx1
	NSC-10M-75-FJ-S				180	Dx1
	NSC-10M-75-FJ(Hinge)-S				180	Dx1
	NSC-10M-75-T&FJ(Hinge)-S				174	Dx1
	NSC-10M-75-AL				-	D
	NSC-10M-75-FJ-AL				174	D

*S = static test, D = dynamic test (repeated blasts), Dx1= dynamic test (singly-applied blast)

a) 1000 KN PILOT Control System cylinder testing machine

b) σ-ε curve testing machine (MTS) with LVDT setup

Figure 3 - 9 Compression test set-up

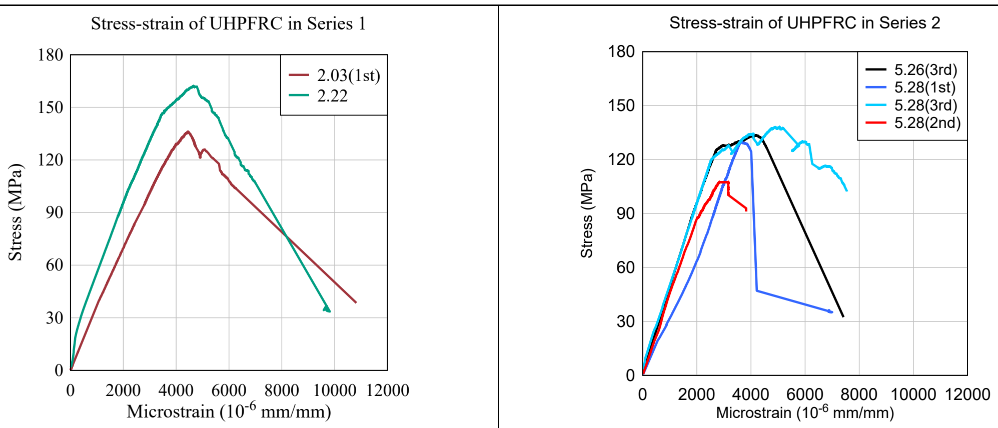

a) σ- ε curve of UHPRC in series 1

b) σ- ε curve of UHPRC in series 2

Figure 3 - 10 Stress-strain relationships of UHPFRC

3.3.1.3 Flexural prism tests

The flexural properties of the UHPFRC were determined by conducting flexural tests on standard prisms. Flexural tests were conducted using a GALDIBINI SUN 60 Universal Floor Standing Testing Machine, as shown in **Figure 3 - 11**. The machine load cell was used to record the load and two LVDTs were instrumented in the middle span to record the vertical deflection. The UHPFRC prisms had dimensions of 75 mm × 75 mm × 280 mm in accordance with the ASTM C1856 and C1609 standards. The resulting load-deflection relationships are shown in **Figure 3 - 12**, while **Table 3 - 6** provides a summary of the flexural stress and toughness data.

Table 3 - 6 Results from the ASTM C1609 toughness tests

Concrete: UHPFRC		P_P	δ_P	f_P	P_{600}^D	f_{600}^D	P_{150}^D	f_{150}^D	T_{150}^D
Series 1	Sample 1	48	0.3	23.5	45.5	22.3	30	14.7	60.4
	Sample 2	41.6	0.15	20.4	24.2	11.9	23.6	11.6	51.2
								Average:	55.8
Concrete: UHPRRC		P_P	δ_P	f_P	P_{600}^D	f_{600}^D	P_{150}^D	f_{150}^D	T_{150}^D
Series 2	Sample 1	51	0.59	24.8	46.6	22.7	33.7	16.4	65.2
	Sample 2	50	0.49	24.2	46.9	22.7	30	14.5	62.3
	Sample 3	47.5	0.47	23.4	46.4	22.9	29	14.3	56.9
	Sample 4	48.1	0.3	24.7	46.5	23.8	27.8	14.2	55.6
								Average:	60
L = Span Length (300 mm), (L/600 = 0.5, L/150 =2) P_1= First-Peak Load (kN) δ_1= Net Deflection at First-Peak Load (mm) P_p= Peak Load (kN) δ_p= Net Deflection at Peak Load (mm) f_1= First-Peak Strength (MPa) f_p= Peak Strength (MPa) P_{600}= Residual Load at net deflection of L/600 (kN) f_{600}= Residual Strength at net deflection of L/600 (MPa) P_{150}= Residual Load at net deflection of L/150 (kN) F_{150}= Residual Strength at net deflection of L/150 (MPa) T_{150}= Area under load vs. net deflection curve (0 to L/150), (kN*mm)					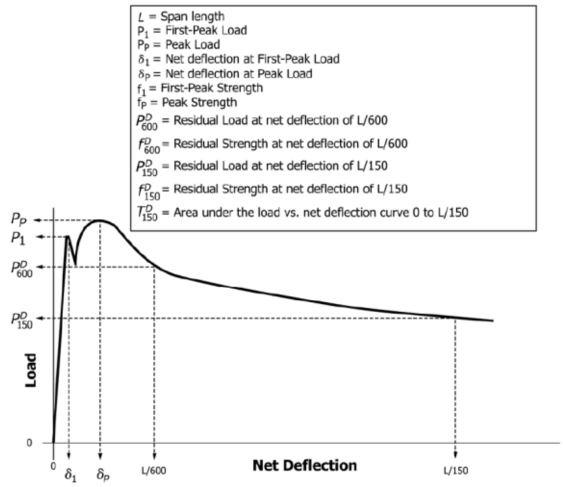				

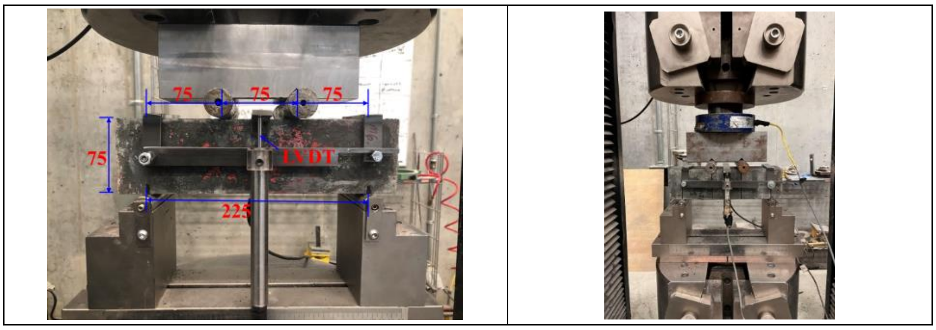

Figure 3 - 11 Flexural testing set-up

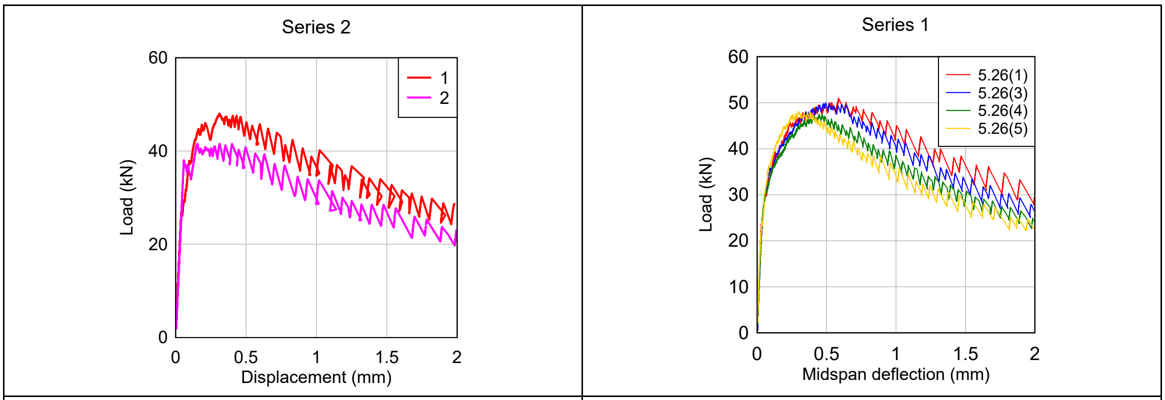

a) Load-deflection relationships in series 1	b) Load-deflection relationships in series 2

Figure 3 - 12 Load-deflection relationships

3.3.2 Steel reinforcement

Four types of steel reinforcement were used to fabricate the specimens, namely: non-deformed 6.3 mm steel wire, and Canadian 10M, 15M and 20M deformed bars. The 6.3mm steel wire with a diameter of 6.3 mm was used to build the stirrups and ties in series 1 and series 2, respectively. The 15M and 20M bars with diameters of 16 mm and 19.5 mm, respectively were used in series 1, while the 10M bars with a diameter of 11.3 mm were used in series 2. Three steel coupons taken from each bar size were tested using the GALDABINI SUN 60 Universal Floor Standing Testing Machine to determine the mechanical properties. The coupon tests were subjected to uniaxial tension loading at a rate of 5 mm/min and the vertical strain was recorded by an axial extensometer, as shown in **Figure 3 - 13**.

Table 3 - 7 summarized the mechanical properties of various size bars, in terms of steel ID, diameter, bar area, yield strain and stress, ultimate strain and stress, and rupture strain. From the table, it can be seen that the 6.3 mm steel wire had an average yield tensile strength of 413 MPa at strain of 0.0019 mm/mm, ultimate strength of 509 MPa at strain of 0.193 mm/mm, and rupture strain of 0.21 mm/mm. The 10M bars had an average yield strength of 484 MPa at strain of 0.0025 mm/mm, ultimate strength of 588 MPa at strain of 0.147 mm/mm, and rupture strain of

0.2 mm/mm. The 15M bars had an average yield strength of 458 MPa at strain of 0.0025 mm/mm, ultimate strength of 580 MPa at strain of 0.143 mm/mm, and rupture strain of 0.206 mm/mm. The 20M bars had an average yield strength of 472 MPa at strain of 0.0023 mm/mm, ultimate strength of 623 MPa at strain of 0.104 mm/mm, and rupture strain of 0.125 mm/mm. Sample stress-strain relationships for the various steel types are shown in **Figure 3 - 14**.

Figure 3 - 13 Steel coupon test setup

Table 3 - 7 Properties of steel reinforcement

ID	***Steel reinforcement***	***Bar diameter***	***Bar area***	***Yield***			***Ultimate***		***Rupture strain***
				f_y *(MPa)*	ε_y *(mm/mm)*	ε_{sh} *(mm/mm)*	f_u *(MPa)*	ε_u *(mm/mm)*	ε_r *(mm/mm)*
6.3NS	Non-deformed	6.44	32.6	413	0.0019	0.0302	509	0.193	0.21
10M	Regular	11.3	100	484	0.0025	0.0229	588	0.147	0.16
15M	Regular	16	200	458	0.0025	0.0207	580	0.143	0.206
20M	Regular	19.5	300	472	0.0023	0.0133	623	0.104	0.125

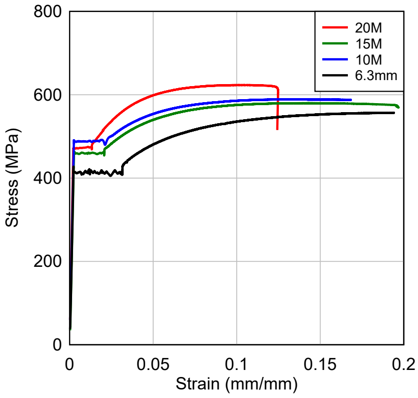

Figure 3 - 14 Stress-strain curves of steel reinforcement

3.3.3 Fibers

In this research, straight steel fibers were used with the UHPFRC as a reinforcement material, as shown in **Figure 3 - 15**. The mechanical properties of steel fibers are summarized in **Table 3 - 8**. In all cases the steel fibers were added at a ratio of 2.5% by volume (195 kg/m^3). From the table, it can be seen that these fibers have a length of 13 mm, and a diameter of 0.2 mm, resulting in the aspect ratio of 65 mm/mm, while the tensile strength is 2850 MPa.

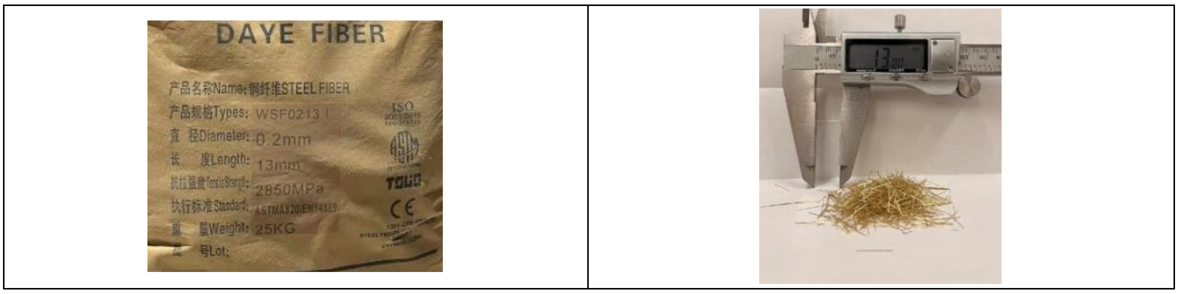

Figure 3 - 15 Sample of steel fibers

Table 3 - 8 Properties of steel fibers

Fiber Name	Length (mm)	Diameter (mm)	Aspect Ratio (mm/mm)	Tensile Strength (MPa)
Steel fiber	13	0.2	65	2850

3.4 Construction of Specimens

This section presents the procedure used in the construction of the specimens, in terms of the formwork, steel cage fabrication, strain gauge installation, casting and curing of the substrate concrete, roughening of the substrate surface, and the retrofitting with UHPFRC.

3.4.1 Preparation and casting

Steel formwork with the dimensions of 125 mm × 250 mm × 2440 mm were used in Series 1, as shown in **Figure 3 - 16(a)**. To improve the rigidity of the steel forms, four thread rods were used through the span. Before putting the steel cages in place, the interior sides of the forms were brushed with oil to ease demolding, and then plastic chairs as shown in **Figure 3 - 16(b)** were placed on the tension side to obtain a clear cover of 35 mm. A similar process was followed in Series 2; however, the specimens were cast in wood formwork as shown in **Figure 3 - 18**, with interior dimensions of 150 mm × 200 mm × 2440 mm, and clear cover of 20 mm.

In Series 1, a total of nine steel cages were built either with or without transverse reinforcement. No longitudinal reinforcement was installed on the compression side (at midspan), and the 6.3 mm steel wire was only used to ease the construction, as shown in **Figure 3 - 17**. Six out of nine steel cages were built with 2-20M bars on the tension side and the remaining cages were built with 2-15M bars. To ensure proper bar development the 15M and 20M bars were bent at both ends with 90° and 180° hooks, respectively. For the specimens with transverse reinforcement, U-shaped stirrups made of 6.3 mm steel wire spaced at 100 mm in the shear spans, while stirrups were provided only at the load points to ease construction for the specimens without stirrups. In Series 2, a total of twelve identical steel cages were built, consisting of 2-10M bars in tension and 2-10M bars compression, with closed ties made from 6.3 mm wire spaced at 75 mm throughout the whole span. All 10M bars were provided with 180° hooks at their ends.

After building the steel cages, strain gauges were installed at the mid-span of the longitudinal steel reinforcement, as shown in **Figure 3 - 19**. A handheld belt-grinder was used to smooth the steel at mid-span, and then the surface was cleaned by alcohol to remove the dust. Thereafter, 120-Ω strain gauges for the static tests, or 350-Ω strain gauges for the dynamic tests, were installed on the longitudinal reinforcement with adhesive. Finally, each strain gauge was protected using a plastic tape and its wires were extended using an electronic cable. The locations of the strain gages in both series are shown in **Figure 3 - 19(d)-(e)**.

HSC was used as the substrate concrete in series 1 and was mixed using a multi-flow pan mixer. The mixing procedure includes two steps: 1) premixing the fine aggregate, coarse aggregate, and sand with half quantity of water; and then 2) adding the cement and slag with the remaining water as well as the super-plasticizer and retarder. After uniformly mixing for 12 to 15 min, the fresh concrete was poured into the steel formworks and a vibrator was used to improve consolidation. NSC concrete was used as the substrate concrete in series 2. This concrete was supplied by a ready-mix truck and cast using a single batch. After the final set had started, the specimens in both series were cured using a humid burlap which was covering by an exterior plastic sheet. 24 hours later, the specimens were taken out the forms and then cured under moist conditions under ambient temperature.

a) Steel formworks

b) Plastic chair

Figure 3 - 16 Steel formworks used in Series 1

a) Sample steel cage with transverse shear reinforcement (20M)

b) Sample steel cage without transverse shear reinforcement (15M)

Figure 3 - 17 Samples of steel cage (Series 1)

Figure 3 - 18 Formworks and steel gauges in series 2

a) Sample of SG for dynamic test

b) Sample of installation SG

c) Adhesive for SG

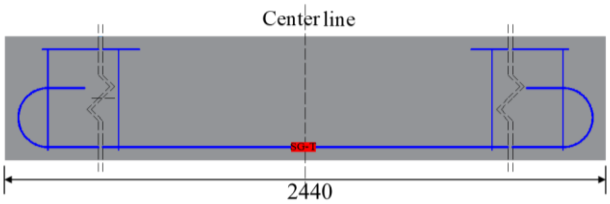

d) Location of strain gauge in series 1

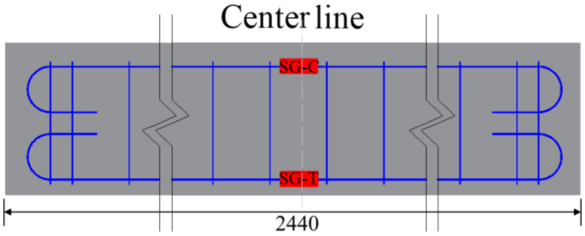

e) Location of strain gauge in series 2

Figure 3 - 19 Installation of strain gauge (SG)

3.4.2 Roughening and retrofitting

To ease the roughening process, the core of the RC beam with HSC was cast in steel molds with three 3/8 inch plywood boards in one side and two 5/8 inch plywood boards in the bottom, as shown in **Figure 3 - 21(a)**. Subsequently, a very thin layer of the substrate concrete was removed by a bush hammer or point chisel as shown in **Figure 3 - 21** when the specimens developed a compressive strength of around 50MPa. Then the surface was roughened to a roughness beyond CSP6 in accordance with the roughness grades of the International Concrete Repair Institute (ICRI), shown in **Figure 3 - 20(c)**. Then, the UHPFRC was mixed and applied onto the substrate concrete after the beams were moistened for 15-30min, as shown in **Figure 3 - 21(c)**. After the retrofitting, the beams were immediately covered by a hard plastic sheet. 24h later, the beams were demolded from the steel formworks and covered by wet burlap for curing until the time of testing. A similar process was followed for Series 2.

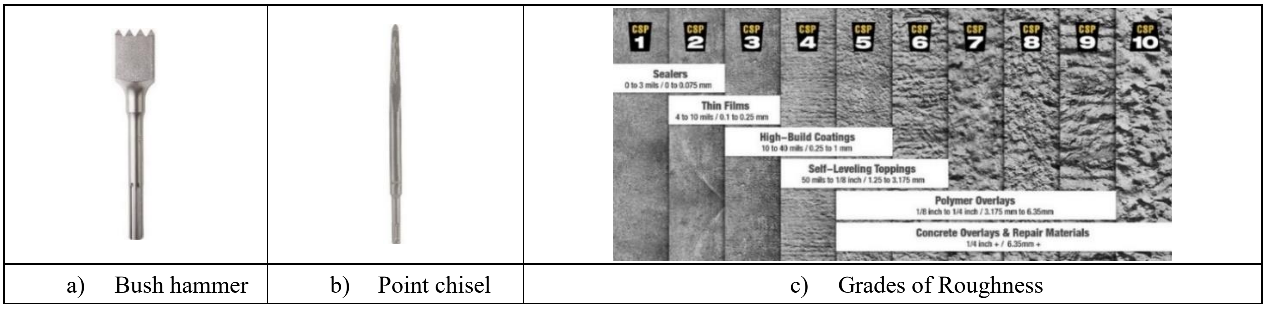

a) Bush hammer b) Point chisel c) Grades of Roughness

Figure 3 - 20 Roughening methods and grades

Series 1

a) Casting of substrate HSC b) Interfacial preparation c) Moistening

Series 2

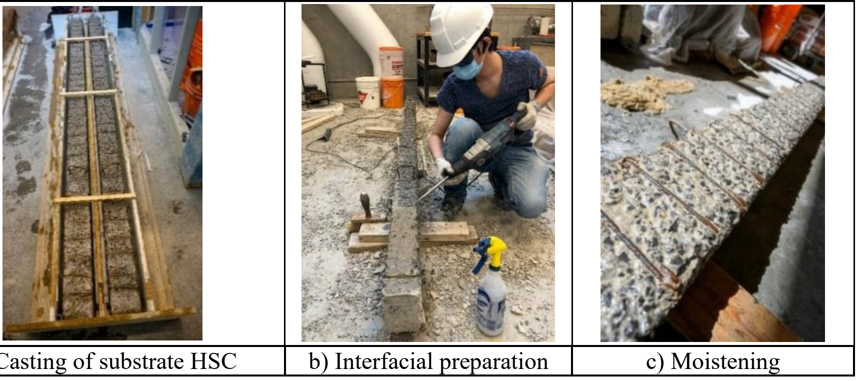

a) Casting of substrate HSC b) Interfacial preparation c) Moistening

Figure 3 - 21 Configuration of retrofitting, roughening, and moistening

3.5 Experimental Setup

In this study, companion beams were tested under quasi-static and blast conditions. Quasi-static tests were conducted using a 4PT bending setup. Series 1 blast tests were conducted using a 4PT setup consistent with the static tests. Series 2 blast tests were conducted under UDL blast loading, with some specimens tested under combined blast and axial loading.

3.5.1 Quasi-static tests

All static beam specimens were tested in flexure beyond the age of 28 days and subjected to a four-point bending configuration as shown in **Figure 3 - 22**. In all cases, the specimens were simply-supported and tested over a clear span of 2232mm, with a constant moment region between the loading points of 750mm, and two shear spans between the support and loading point of 741mm. A manually-operated hydraulic jack and transfer beam were used to apply the loading onto the beams. The load and displacement were recorded by a load cell and a cable displacement transducer placed at midspan. Strain gauges installed on the tension bars at midspan were used to record the strains in the longitudinal steel. All beams were first tested under load-control with an increment of 10kN until yielding. The loading was then switched to displacement-control and the specimens were continuously loaded until failure (crushing of concrete, rupture of tension steel or shear collapse).

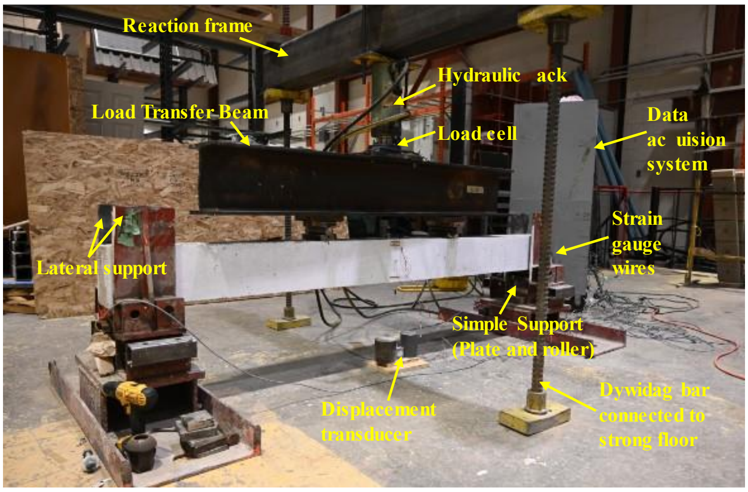

Figure 3 - 22 Quasi-static test setup

3.5.2 Blast tests (shock tube)

The blast tests were carried out using the shock tube testing facility at the University of Ottawa. As presented in **Figure 3 - 23**, the pneumatically driven shock tube consists of four main components, including 1) the variable length driver which generates the blast shockwave by compressed air, 2) the double-diaphragm spool section which triggers the shockwave, 3) the expansion section with a length of 7 m and (4) a rigid end test frame with a 2032 mm × 2032 mm square opening. The reflected pressure and the positive phase duration were controlled by the driver pressure and driver length, respectively. The driver length of 9 ft (2743 mm) was used in Series 1 while a driver length of 6ft was used in series 2.

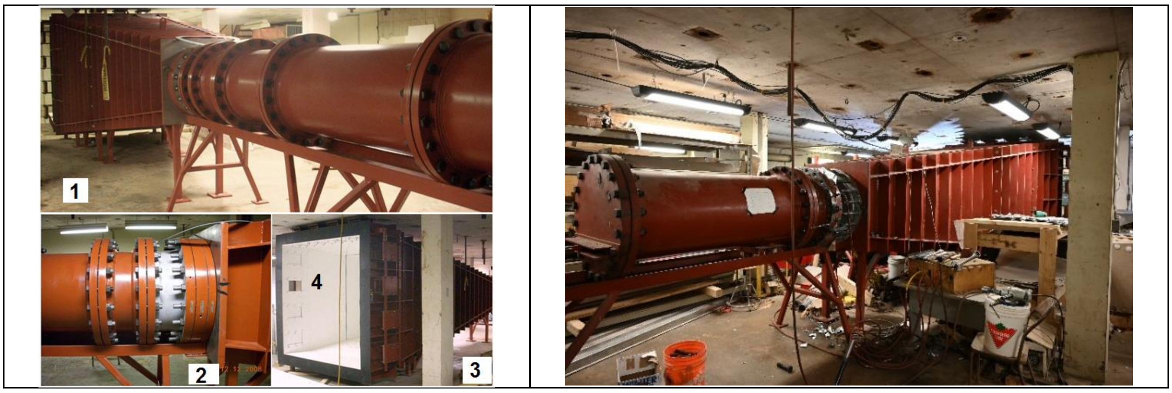

Figure 3 - 23 Shock tube components

A typical setup of a specimen in Series 1 is shown in **Figure 3 - 24(a)**. The setup includes a load transfer device (LTD), simple supports, a Linear Variable Displacement Transducer (LVDT), pressure gauges and high-speed cameras.

The LTD in Series 1 was used to redirect the blast shockwave onto the specimens under 4PT bending. The LTD consisted of two rigid steel panels with the dimensions of 2032 mm × 1000 mm and two I-type steel beams with dimensions of 160 mm × 165 mm × 1200 mm. The LTD components are connected by sliding hinges to allow for free movement in the bending configuration. The specimens were connected to shock-tube frame using simple supports, consisting of a rear support with a roller welded to a square HSS (51 mm × 51 mm × 500 mm) and a front support with an integrated load cell.

As seen in **Figure 3 - 24(b)**, the LTD in Series 2 was used to redirect the blast shockwave onto the specimens under UDL loading. The LTD consisted of a steel sheet and eight 76mm × 76mm × 6.35mm hollow steel sections (HSS) which were each secured to the steel sheet using four bolts. The specimens were connected to shock-tube frame using simple supports, consisting of two 51mm × 51mm × 610mm HSS sections with welded rollers and a set of four threaded rods at each support to allow rotation.

As shown in **Figure 3 - 24**, one LVDT with a gauge length of 300 mm was installed at the midspan of the specimens to record the horizontal displacement. Besides the LVDT, two *AOS Technology X-PRI* high-speed cameras were located at both sides, perpendicular to the specimens, to capture the deflections during the blast tests. The camera can provide a 1280 × 800 resolution video with a sampling-rate of 2000 frames per second (fps).

Two *PCB Piezotronics Model #112A22* piezoelectric pressure sensors, installed at the bottom and the side of the end rigid frame, were used to record the shock-wave pressure-time history during the tests. The reflected pressure time history data, midspan displacement from the LVDT, reactions from the load-cells, and strain readings from the strain gauges were recorded using a *Yokogawa SL1000* High Speed Data Acquisition Unit. All the above mentioned data was then read by *XViewer* software in the format of a .csv file.

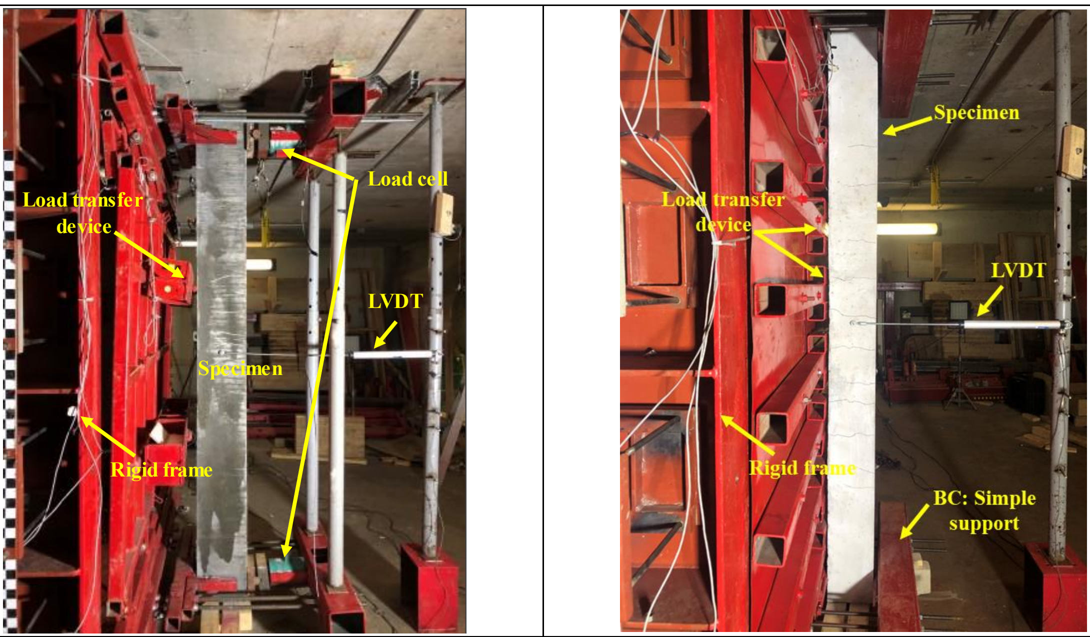

a) Dynamic test setup for series 1

b) Dynamic test setup for series 2

Figure 3 - 24 Dynamic test setup and LTD

All specimens in Series 1 were tested under repeated blast loadings until concrete crushing, significant crack opening/fiber pullout or bar rupture. The repeated blast loading sequence included five blast shots ranging from driver pressures of 17 psi to 90 psi (117 to 620 kPa), with a constant driver length of 9ft (2743 mm). **Table 3 - 9** presents a description of the various blasts in terms of driver length (L_d), driver pressure (P_d), average reflected impulse (I_r), average reflected pressure (P_r) and the average positive phase duration (t_d). **Figure 3 - 25(a)** showed sample reflected pressure time history curves for each blast.

The specimens in Series 2 were tested under either repeated blast loading (with/without axial load) or single blast loading, and the resulting failure modes included concrete crushing, bar-rupture or pullout of steel fibers. The tests used a constant driver length constant 6ft (1830mm). In the repeated tests, the loading sequence included three blast shots from 13psi to 50psi, while the 50psi blast was applied under single blast loading (Blasts 1-3 in Papers 3-4). An axial load of 400kN was applied on one set of control and FJ beams with blast loadings at 50psi to 70psi (Blasts 1-3 in Paper 5). The main parameters which define the various blasts are summarized in **Table 3 - 9**, and sample pressure time history curves are shown in **Figure 3 - 25(b)**.

Table 3 - 9 Repeated blast test sequence

Series		Test sequence	Driver Length mm (ft)	Driver Pressure kPa (psi)	Avg. Reflected Impulse (Ir) kPa-ms	Avg. Reflected Pressure (Pr) kPa	Avg. Positive Phase Duration (td) ms
Series 1	Paper 1-3	Blast 1	2743(9)	117(**17**)	221	24	18.4
		Blast 2	2743(9)	207(**30**)	339	41	16.6
		Blast 3	2743(9)	345(**50**)	520	63	16.4
		Blast 4	2743(9)	482(**70**)	702	83	17
		Blast 5	2743(9)	620(**90**)	883	98	18
Series 2	Paper 4-5	Blast 1	1829 (6)	90 (**13**)	129.3	19.4	13.3
		Blast 2	1829 (6)	207 (**30**)	255.4	39.1	13.06
		Blast 3	1829 (6)	345 (**50**)	403.8	58.3	13.86
	Paper 6	Blast 1	1829 (6)	345 (**50**)	403.8	58.3	13.86
		Blast 2	1829 (6)	413(**60**)	437.5	80.1	10.9
		Blast 3	1829 (6)	482(**70**)	474.2	81.2	11.7

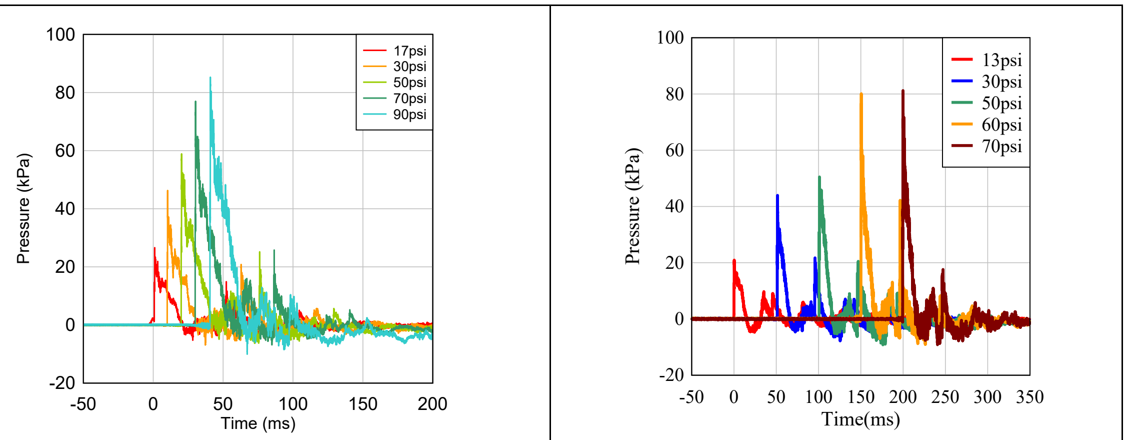

a) Sample pressure-time history curves in series 1

b) Sample pressure-time history curves in series 2

Figure 3 - 25 Sample reflected pressure time histories in series 1 and 2

References

[1] ICRI. ICRI Standard 310.2 Selecting and Specifying Concrete Surface Preparation for Sealers, Coatings, Polymer Overlays, and Concrete Repair with CSP Chips. 2013.

[2] Bastami R. Structural performance of high-strength reinforced concrete beams build with synthetic fibers: University of Ottawa; 2019.

[3] Algassem O. Parameters affecting the blast performance of high strength fibre reinforced concrete beams: University of Ottawa; 2016.

Chapter 4: Effect of UHPFRC Jacketing on the Shear and Flexural Behaviour of High-Strength Concrete Beams

Paper 1: extracted from static results in series 1 (published in journal- "Structures", vol. 51, pp. 1972-1996, 2023; DOI: 10.1016/j.istruc.2023.03.104*)*

Abstract

Ultra-high performance concrete fiber reinforced concrete (UHPFRC) is an advanced material which shows high compressive strength, tensile resistance, toughness and durability when compared to conventional concrete. One of the potential applications of UHPFRC is in the retrofit of ageing or deteriorated reinforced concrete structures. However, limited research exists on the use of UHPFRC to strengthen higher strength concrete members (with $f_c' \geq 60$ MPa). This paper examines the ability of UHPFRC to improve the shear and flexural performance of high-strength concrete (HSC) beams (with $f_c' = 100$ MPa). As part of the tests two shear-deficient HSC beams built without stirrups were retrofitted with a thin UHPFRC jacket and tested under four-point bending. The results are compared to a control set of HSC beams built with and without stirrups. The effect of steel ratio in the retrofitted beams was also investigated. The results show that the UHPFRC jacketing significantly increased the shear capacity of the shear-deficient HSC beams, allowing the beams to reach their full flexural resistance. The UHPFRC retrofit also allowed for improved flexural performance in terms of stiffness, strength and ductility when compared to the control beams built with stirrups. The failure mode and ductility in the UHPFRC retrofitted beams was affected by the longitudinal steel ratio, with the failure transitioning from bar fracture to concrete crushing as the steel ratio in the reference HSC beams was increased.

Keywords: UHPFRC, Retrofit, Beams, Shear, Flexure, Ductility, Bar fracture.

4.1 Introduction

Recently, there has been an increased need for solutions to strengthen ageing and deteriorated concrete structures. Indeed, nearly one in thirteen bridges in the United States is structurally-deficient, and 42% are more than 50 years old [1]. In Canada, the overall condition of bridge infrastructure also requires further improvement [2]. Likewise, parking garages and other concrete structures may be exposed to deterioration [3], or challenging loadings [4, 5], which may require repair or strengthening.

In addition to traditional retrofit measures, researchers have proposed advanced materials such as fiber reinforced polymer (FRP) or fabric-reinforced cementitious (FRCM) composites to strengthen existing concrete structures [6, 7]. However, these methods present some disadvantages such as debonding/delamination, installation difficulties, and reduced performance under elevated temperatures.

Recently, ultra-high performance fiber reinforced concrete (UHPFRC) has also been proposed to strengthen and rehabilitate existing concrete structures [8-10]. When compared to conventional concrete, UHPFRC shows many outstanding properties which include: high compressive strength (≥ 120-150 MPa), increased tensile resistance (≥ 8 MPa) and excellent durability [11, 12] due to careful selection of component materials, dense particle packing and the addition of fibers. The ability to cast UHPFRC in thin layers, combined with its high bond capacity, also make it an ideal retrofit material.

One promising application of UHPFRC is in the strengthening of existing concrete beams and slabs [13]. **Table 2 - 1** provides an overview of previous studies in this area [14-25] with an indication of retrofit type/configuration, concrete type in the reference beam/slab, and focus of the study (shear or flexure). In general, these studies confirm the ability of UHPFRC to improve flexural performance, with the results affected by UHPFRC retrofit type, overlay thickness, interface location and surface preparation method. However, most previous tests have focused on flexural-dominant beams, with limited tests on the use of UHPFRC for shear-strengthening. Previous studies have also primarily focused on T-sided (tension side) retrofits with limited tests on UHPFRC jacketing. In addition, very limited tests have studied the UHPFRC-strengthening of higher strength concrete (HSC) beams, with concrete compressive strengths, $f_c' \geq 60$ MPa.

Accordingly, this paper aims at examining the ability of UHPFRC jacketing to improve the performance of existing HSC beams, in both shear and flexure. The following sections provide a review of previous studies, and then present the experimental research program.

4.2 Research significance

Important research has investigated the UHPFRC strengthening of reinforced concrete beams and slabs. However, most previous tests have focused on T-sided retrofits to strengthen normal-strength concrete (NSC) beams/slabs in flexure, with limited tests on shear-strengthening, higher-strength concrete (HSC) members (with $f_c' \geq 60$ MPa), or the use of UHPFRC jacketing. Accordingly, this study aims to examine the ability of UHPFRC jacketing to improve the behavior of higher-strength HSC beams (with f_c' = 100 MPa), in both shear and flexure. The benefits of the UHPFRC to improve shear and flexural behaviour is examined by comparing the responses of the retrofit beams to companion HSC beams built without and with stirrups, respectively. The effect of longitudinal steel ratio, an important parameter which can affect the ductility and failure mode of UHPFRC beams, is also investigated.

4.3 Experimental program

4.3.1 Specimen designs

A total of six beams were included in this study, including four control beams and two retrofitted beams. **Table 4 - 1** provides a summary of the beam designs, while **Figure 4 - 1** presents the beam dimensions, reinforcement properties and retrofit details. All beams had the same dimensions of 125mm × 250mm × 2440mm and were tested under four-point bending, with a clear span of 2232mm. Longitudinal steel in tension consisted of either 2-15M (A_b=200 mm^2) or 2-20M bars (A_b=200 or 300 mm^2), resulting in steel ratios of ρ = 1.6% or 2.4%, respectively. The control specimens were built with plain high-strength concrete, and include two shear-deficient beams built without stirrups (C100-15M and C100-20M), and two flexural-dominant beams with stirrups made from 6.3 mm wire, spaced at 100 mm (d/2) in the shear spans (C100-15M-S and C100-20M-S). These beams were tested in a previous study at the University of Ottawa [26]. The retrofit beams (designated as C100-15M-FJ and C100-20M-FJ) were first cast with plain HSC, 2-15M or 2-20M bars, but without stirrups, followed by removal of the concrete cover and retrofitting with UHPFRC. As shown in **Figure 4 - 1**, full-jacketing was adopted as the retrofit type, and the thickness of the UHPFRC was 41mm on the tension face and 20mm on all other faces.

Table 4 - 1 Beam test matrix

Group	Beam I.D.	HSC f'c(MPa)	UHPFRC f'c(MPa)	Retrofit method [a] (surface prep.)	Steel fiber properties		Steel reinf. properties	
					Length/dia. (mm/mm)	Content V_f (%)	Flexural Steel (ρ)	Stirrups [b]
15M group	C100-15M	104	-	-	-	-	2- 15M (1.6%)	No
	C100-15M-S	95	-	-	-	-		Yes
	C100-15M-FJ	99	164	FJ (chiseling)	13/0.2	2		No
20M group	C100-20M	110	-	-	-	-	2- 20M (2.4%)	No
	C100-20M-S	106	-	-	-	-		Yes
	C100-20M-FJ	101	164	FJ (chiseling)	13/0.2	2		No

Note:

[a] FJ: UHPFRC applied on 4 sides in the form of Full-jacket

[b] U-shaped stirrups made from 6.3 mm wire applied at s = 100 mm in the shear spans

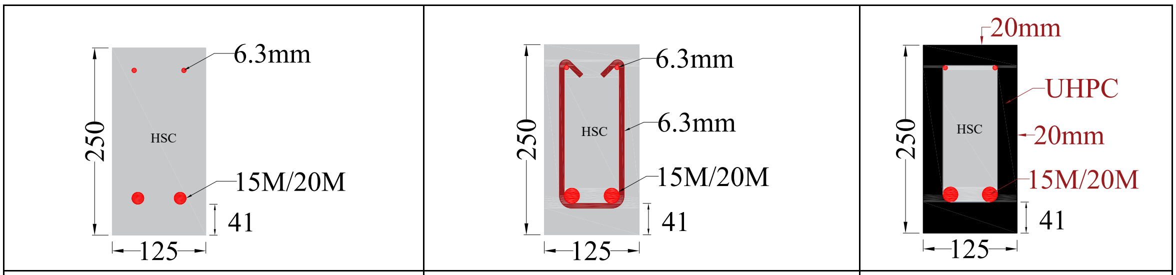

a) Control specimen (no stirrups) b) Control specimen (with stirrups) c) Full-jacket specimen

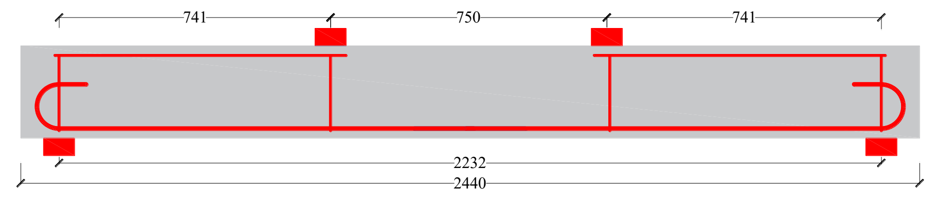

d) Specimen geometry (without stirrups)

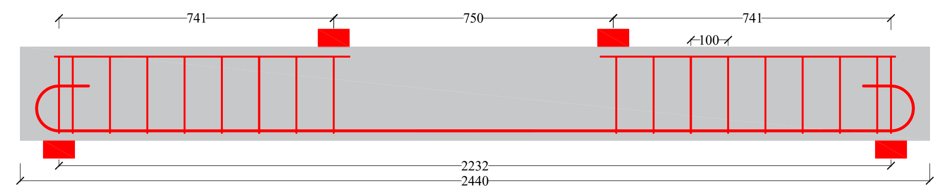

e) Specimen geometry (with stirrups)

Figure 4 - 1 Beam geometry and reinforcement detailing

4.3.2 Material Parameters

The HSC used in this study (designated as C100) was designed to have a compressive strength of 100 MPa at 28-days. The mix consisted of General Use (GU) Portland cement, slag, silica fume, two sizes of coarse aggregates (10 mm and 19 mm), sand, water as well as admixtures consisting of a set retarder and super-plasticizer. The UHPFRC consisted of proprietary mix (UP-FX Poly premix), steel fibers, and liquid admixtures which were added in quantities specified by the manufacturer. The steel fibers had a length of 13 mm, diameter of 0.2 mm, aspect ratio of 65, and tensile strength of 2850 MPa, and were added at a volumetric ratio of 2.5% (195 kg/m^3). **Table 4 - 1** reports the compressive strengths of the HSC and UHPFRC in each beam on the day of testing. The concrete strengths were determined by testing 100 mm × 200 mm or 75 mm × 150 mm cylinders in accordance with the ASTM C39 and C1856 standards for the HSC and UHPFRC, respectively. **Figure 4 - 2(a)** shows sample stress-strain curves for each concrete type. The flexural properties of the UHPFRC were determined by testing standard prisms, with dimensions of 75 mm × 75 mm × 285 mm, in accordance with the ASTM C1856 and C1609 standards. Sample load-displacement curves are shown in **Figure 4 - 2(b)**. Three sizes of steel reinforcement were used in this study, including: 15M/20M deformed bars and 6.3 mm steel wire, with corresponding yield strengths of 458 MPa, 472 MPa and 413 MPa. The steel properties were determined by testing a minimum of 3 coupons in tension according to ASTM A615. Sample stress-strain curves for each steel type are shown in **Figure 4 - 2(c)**.

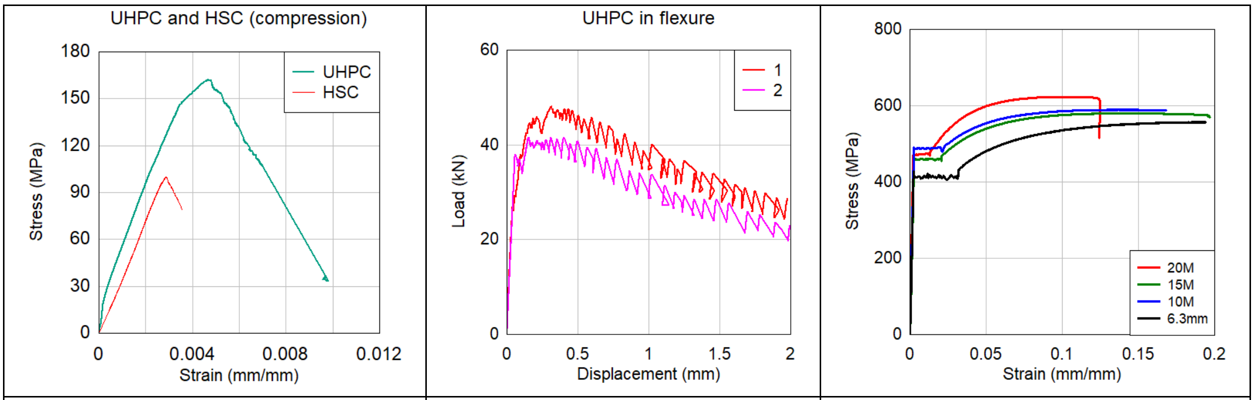

a) UHPFRC and HSC (compression)

b) UHPFRC (flexure)

c) Long. steel (tension)

Figure 4 - 2 Material test results

4.3.3 Specimen preparation

The preparation of the retrofit beam specimens included three stages. First, the steel cages were assembled, and the core HSC concrete was cast in steel molds. To simplify the cover removal process, 3 × 3/8-inch and 2 × 5/8-inch plywood boards were used to reduce the cover on the side and bottom faces, respectively (see **Figure 4 - 3(a)**). Next, the remaining thickness of the substrate cover concrete was removed using a point chisel when the HSC in beams C100-20M-FJ and C100-15M-FJ achieved compressive strengths of 51 MPa and 62 MPa respectively. The surface was chiseled to obtain a roughness in excess of CSP6 (where CSP is the concrete surface profile, as specified by the ICRI [27] (see **Figure 4 - 3(b)**). Finally, the UHPFRC was mixed and cast onto the substrate concrete after the beams were moistened for 15-30 minutes, as shown in **Figure 4 - 3(c)**. After casting (see **Figure 4 - 3(d)**), the beams were covered by a hard plastic sheet. One day (24h) later, the beams were lifted out from the steel molds and covered by wet burlap for curing until the aging of 28 days.

a) Casting of substrate HSC | b) Interface preparation | c) Moistening | d) UHPFRC casting

Figure 4 - 3 Casting and retrofit procedure

4.3.4 Test setup and instrumentation

All beam specimens were tested in flexure using the four-point bending configuration shown in **Figure 4 - 4**. The simply-supported beams had a clear span is 2232mm, with a constant moment region of 750mm and two equal shear spans of 741mm. A manually operated hydraulic jack was used to apply the load which was transferred onto the beams through a transfer beam and plates placed at the loading points. The load was captured using a load-cell, while the displacement at midspan was recorded using a cable displacement transducer. Strain gauges were placed on the tension bars at midspan to record the strains of longitudinal reinforcement. The beams were tested under load-control with an increment of 10 kN until yielding, and then switched to displacement-control with an increment of 5 mm until failure (crushing of concrete, rupture of tension steel or shear collapse).

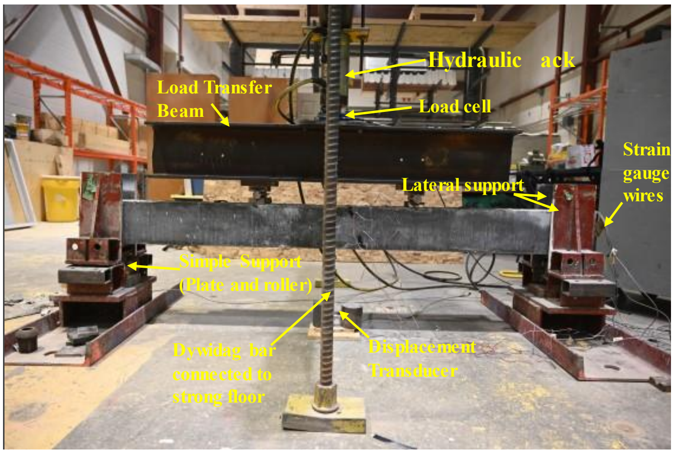

Figure 4 - 4 Setup of four-point bending test

4.4 Experimental results

4.4.1 Summary of results

The load-displacement curves of the retrofit beams are plotted in **Figure 4 - 6**, with an indication of key events. **Figure 4 - 7** compares the beam responses, while photos showing the progression of damage and failures are compared in **Figure 4 - 8** and **Figure 4 - 9**. **Table 4 - 2** presents key data from the load-deflection curves (see **Figure 4 - 5**), including: the secant stiffness (k_s), yield load (P_y) and yield displacement (D_y), peak load (P_{max}), displacement corresponding to 80% of peak load (D_{80}) and displacement at the end of testing (D_{max}). In addition, the table reports the ductility index (D_{80}/D_y), drift ratio (D_{80}/L_{shear}), and toughness (A_{80} and A_{max}), corresponding to the areas under the curves up to D_{80} and D_{max}. The toughness indices, I_{80} and

I_{max}, were determined by taking the ratios of the toughness at D_{80} and D_{max} and the area under the curves up to yielding (A_{80}/A_y and A_{max}/A_y).

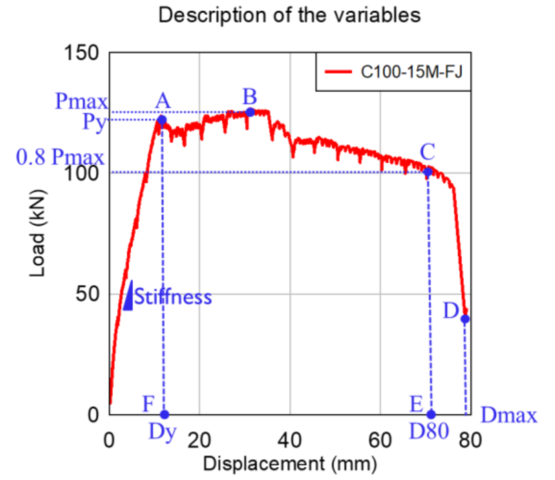

A: Yield load (P_y) corresponding to yielding of the longitudinal reinforcement;

B: Maximum load capacity (P_{max}) resisted by the specimen;

C: Load ($0.8P_{max}$) at 80% peak load;

D: Maximum displacement (D_{max}) at end of testing;

E: Displacement (D_{80}) corresponding to 80% of peak load;

F: Displacement (D_y) at yield;

A_{OAF}: Toughness A_y = area of OAF;

A_{OABCE}: Toughness A_{80} = area of OABCE;

A_{OABCD}: Toughness A_{max} = area of OABCD;

I_{80}: Toughness index at D_{80}, $I_{80} := \frac{A_{80}}{A_y}$

I_{max}: Toughness index at D_{max} , $I_{max} := \frac{A_{max}}{A_y}$

Figure 4 - 5 Description of load-deflection parameters

Table 4 - 2 Experimental results extracted from load-deflection curves

Beam I.D.	Load		Displacement			Stiffness k_s(N/mm)	Ductility D_{80}/D_y	Drift ratio D_{80}/L_{shear} (%)	Toughness J (kN-mm) [Toughness index]			Failure mode
	Yield P_y(kN)	Max. P_{max}(kN)	Yield D_y(mm)	Failure D_{80}(mm)	Max. D_{max}(mm)				A_y	A_{80} [I_{80}]	A_{max} [I_{max}]	
C100-15M	-	90	-	15.3	19.51	5882	-	2.06%	-	725	922	Shear
C100-15M-S	94.5	105	14.9	39.0	40.66	6342	2.62	5.26%	816	3205 [3.93]	3273 [4.01]	Concrete crushing
C100-15M-FJ	116.4	127	9.9	72	79.06	11758	7.27	9.72%	688	7807 [11.35]	8405 [12.22]	Bar fracture
C100-20M	-	84	-	10.67	10.67	7873	-	1.44%	-	470	470	Shear
C100-20M-S	118.2	138	15	30.51	31	7880	2.03	4.12%	935	2955 [3.16]	2999 [3.21]	Concrete crushing (sudden)
C100-20M-FJ	159	189	11.25	31.39	219	14133	2.79	4.24%	1014	4623 [4.56]	17046 [16.81]	Concrete crushing (ductile)

4.4.2 Responses of specimens

4.4.2.1 Response of Control Beams

The two reference HSC beams built without stirrups include C100-15M and C100-20M, with ρ = 1.6% and 2.4%. As expected, both beams failed in shear due to the absence of transverse reinforcement. The abrupt failures in beams C100-15M and C100-20M occurred at peak loads of 90kN and 84kN (see **Figure 4 - 7(a-b)**).

Provision of stirrups in C100-15M-S and C100-20M-S allowed the beams to fail in flexure (see **Figure 4 - 7(a-b)**). Yielding was captured at loads of 94.5kN and 118.2kN, respectively. Both beams show well-defined deflection plateaus, with maximum load capacities of 105kN and 138kN. Both beams failed due to the crushing of concrete in the midspan compression region with D_{80} displacements of 39mm and 30.5mm, resulting in ductility indices of 2.62 and 2.03, toughness (A_{80}) of 3205kN•mm and 2955kN•mm, and I_{80} indices of 3.93 and 3.16.

4.4.2.2 Response of Beam C100-15M-FJ

Beam C100-15M-FJ was built with plain HSC, 2-15M bars (ρ = 1.6%), no stirrups, and then retrofitted by UHPFRC. The beam response, damage progression and tension steel strain readings are shown in **Figure 4 - 6(a)**, **Figure 4 - 8** and **Figure 4 - 10(a)**. Provision of UHPFRC allowed the beam to fail in flexure despite the lack of stirrups. Yielding of the longitudinal steel was recorded at a load of 116.4kN, with a maximum capacity of 127kN. The beam initially shows an ascending load-deflection response after yielding, with crack localization at D = 20mm, and first signs of crushing at D = 35mm. Thereafter, the beam shows a stable but gradually descending load-deflection response, with failure occurring due to rupture of the tension steel bars at D = 76mm. Before failure, the beam showed a distinct cracking pattern with many closely spaced and fine cracks, with fiber pullout at a single crack (with crack widths of 0.2, 11 and 23 mm, at P_y, P_{max} and just before failure). Bar fracture occurred at the dominant crack, and is attributed to the high bond capacity of the UHPFRC and the build-up of strains in the longitudinal steel at this location. Despite the bar fracture, the beam response can be classified as ductile, with a ductility index of 7.27, drift capacity (D_{80}/L_{shear}) of 9.7%, toughness (A_{80}) of 7807kN.mm, and I_{80} index of 11.35.

4.4.2.3 Response of Beam C100-20M-FJ

Beam C100-20M-FJ was built with plain HSC, 2-20M bars (ρ = 2.4%), no stirrups, and then retrofitted by UHPFRC. The beam response, damage progression and tension steel strain readings are shown in **Figure 4 - 6(b), Figure 4 - 9** and **Figure 4 - 10(b)**. Despite the increase in shear demand and the lack of stirrups, the UHPFRC prevented shear failure and allowed the beam to reach its full flexural capacity. The load-deflection behavior shows a well-defined yield point at a load of 159kN, followed by increasing load until the initiation of concrete crushing. The maximum load resisted by the specimen was 189kN, with a corresponding deflection of 31.4mm. Crushing results in a more sudden drop in capacity (~ 25% of P_{max}) when compared to the previous specimen, followed by gradual but sustained reduction in capacity with increasing deflections up to the end of testing. Once again, the beam showed a distinct cracking pattern with many closely spaced and fine cracks, with fiber pullout at a single crack (with crack widths of 0.4, 6 and 12 mm at P_y, P_{max} and $80\%P_{max}$). Unlike the previous beam, the increase in tension steel ratio prevented bar fracture in this specimen. On the other hand, damage in the specimen was associated with more severe crushing, development of horizontal cracks at the top cover interface, and outward bulging of the UHPFRC jacket (on the top and side faces) at the end of testing. The beam recorded a ductility index of 2.79, drift capacity ($\mathrm{D}_{80}/\mathrm{L}_{shear}$) of 4.2%, toughness ($A_{80}$) of 4623kN•mm, and I_{80} index of 4.56, which are reduced when compared to the previous specimen.

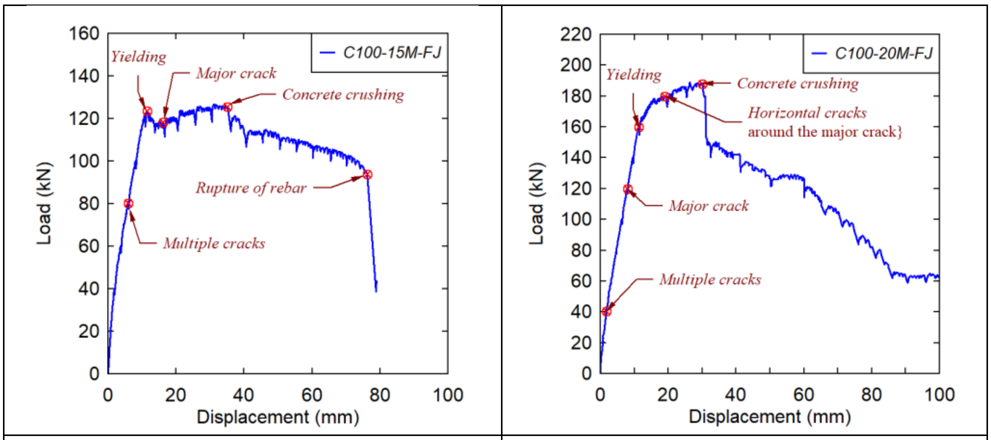

(a) Beam C100-15M-FJ

(b) Beam C100-20M-FJ

Figure 4 - 6 Load-deflection diagrams: stages in response

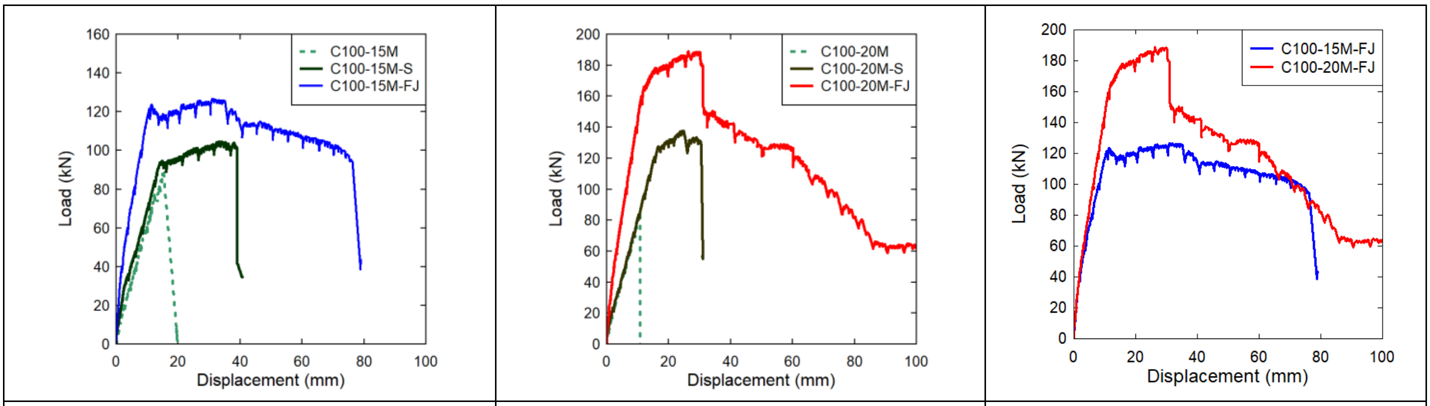

a) Effect of UHPFRC in 15M series

b) Effect of UHPFRC in 20M series

c) Effect of tension steel ratio

Figure 4 - 7 Load-deflection diagrams: effect of parameters

Beam I.D.	Displacement stage	Photo
C100-15M	End of test (Δ=15.3 mm)	
C100-15M-S	End of test (Δ=40.7 mm)	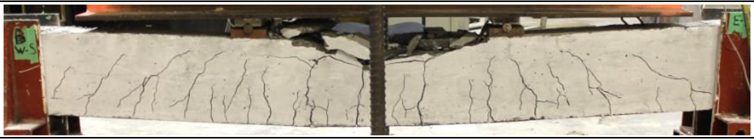
C100-15M-FJ	Δ= 5.94 mm (0.6y)	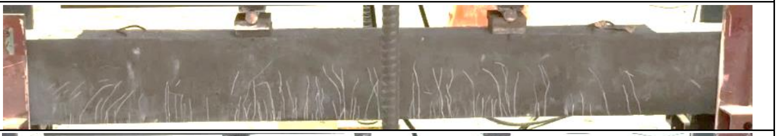
	Δ= 9.9 mm (y)	
	Δ= 19.8 mm (2y)	
	Δ= 29.7 mm (3y)	
	Δ= 49.5 mm (5y)	
	End of test (Δ=79.1 mm)	
	Close-up damage (bar-rupture)	

Figure 4 - 8 Progression of damage and failure in 15M group beams

Beam I.D.	Displacement stage	Photo
C100-20M	End of test (D=10.7 mm)	
C100-20M-S	End of test (D=31 mm)	
C100-20M-FJ	Δ= 6.75 mm (0.6Dy)	
	Δ= 11.25 mm (Dy)	
	Δ= 22.5 mm (2Dy)	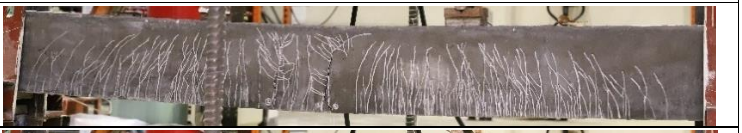
	Δ= 33.75 mm (3Dy)	
	Δ= 56.25 mm (5Dy)	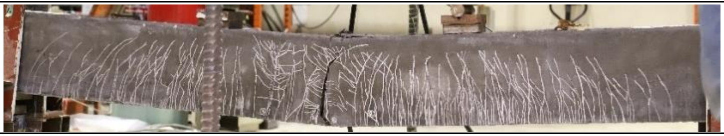
	End of test (Δ=146.3 mm)	
	Close-up damage (concrete crushing)	

Figure 4 - 9 Progression of damage and failure in 20M group beams

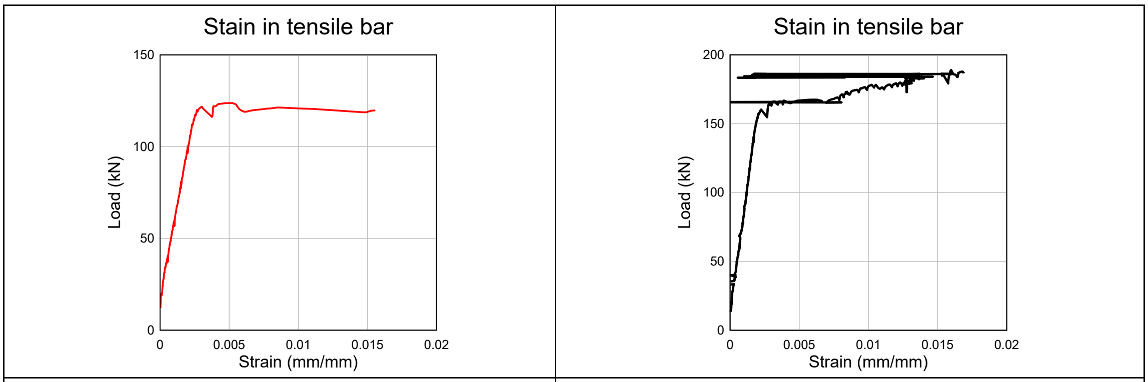

(a) Tension steel (C100-15M-FJ) (b) Tension steel (C100-20M-FJ)

Figure 4 - 10 Strain gage readings for tension steel in UHPFRC retrofit beams

4.4.3 Effect of UHPFRC in beams with 15M bars

The effect of UHPFRC in the 15M group (ρ = 1.6%) is first examined by comparing the responses of beams C100-15M-FJ (with retrofit) and C100-15M (plain HSC, no stirrups). As shown in **Figure 4 - 7(a)**, the lack of transverse reinforcement in beam C100-15M resulted in a brittle shear failure, with an abrupt loss in capacity. In contrast, the provision of UHPFRC resulted in a considerable increase in shear capacity and changed the failure mode from brittle to ductile. Indeed, beam C100-15M-FJ shows an increase of 41% in peak capacity, with a well-defined yield plateau prior to failure in flexure. The UHPFRC retrofit also results in an increase of 100% in stiffness, with a 10-fold increase in toughness (A_{max}).

Next, the ability of UHPFRC to improve flexural response is examined by comparing beams C100-15M-FJ and C100-15M-S (plain HSC and stirrups). As shown in **Figure 4 - 7(a)**, provision of UHPC improved all aspects of structural response, with increases of 85% and 21% in stiffness and peak capacity, and remarkable increases of 177%, 85% and 144% in ductility, drift capacity and overall toughness. Indeed, beam C100-15M-FJ records a ductility ($\mathrm{D_{80}/D_y}$) of 7.27, maximum drift ratio ($\mathrm{D_{80}/L_{shear}}$) of 9.7%, and toughness index (I_{80}) of 11.35, which are significantly increased when compared to beam C100-15M-S (2.62, 5.3% and 3.93).

The addition of UHPFRC also affected the cracking patterns and failure mode (see **Figure 4 - 8**). Failure in beam C100-15M-S was characterized by relatively sudden concrete crushing in the mid-span compression zone. In comparison, crushing remained well controlled in the UHPFRC specimen, with a distinct cracking pattern consisting of many fine and closely-spaced cracks, and the formation of a single dominant crack which eventually led to bar fracture. The bar fracture failure is attributed to the high bond capacity of UHPFRC and crack localization which leads to a build-up of strains over a small gage length of longitudinal steel at the dominant crack location.

Indeed, as noted by Khaksefidi et al. [28], UHPFRC shows a nearly five-fold increase in bond capacity when compared to conventional concrete. Hung et al. [29] also noted that the presence of fibers in UHPFRC results in crack localization, and increased strains in the embedded rebar, which can become detrimental in flexural members with small bar sizes or steel ratios. Likewise, Pokhrel and Bandelt [30] noted that the very high bond capacity of UHPFRC prevents the formation of multiple dominant cracks, resulting in strain concentration over a small gage length of longitudinal reinforcement, which can lead to fracture of the steel bars. The results from the current tests indicate that such bar fracture failures can also occur in UHPFRC-retrofitted beams having low or moderate steel ratios, even when the UHPFRC is applied just below the main tension steel reinforcement.

In the case of conventional concrete overlays, it is generally recommended that the "concrete removal continue past the steel reinforcement to allow the new concrete to fully surround the reinforcing bars" [31]. However, due to UHPFRC's high bond capacity, and the possibility of bar fracture, further research is recommended to study the influence of interface location (i.e. below the reinforcing bars, coinciding with the reinforcing bars, or above the reinforcing bars) on the failure mode in UHPFRC-retrofitted beams.

4.4.4 Effect of UHPFRC in beams with 20M bars

The ability of the UHPFRC to improve shear resistance in the 20M group (ρ = 2.4%) is studied in **Figure 4 - 7(b)** which compares the responses of beams C100-20M-FJ (with retrofit) and C100-20M (plain HSC, no stirrups). As expected, C100-20M showed a brittle shear failure due to the lack of stirrups. Once again, provision of UHPFRC led to a considerable increase in shear resistance, and allowed beam C100-20M-FJ to reach its full flexural capacity, with increases of 80% in stiffness, 125% in peak resistance, and a nine-fold increase in toughness (A_{max}). It is noted that the net increase in capacity is larger in the 20M versus 15M sets (125% vs 41%) due to the increased shear demand as the steel ratio ρ goes from 1.6% to 2.4%. The results indicate that UHPFRC jacketing can increase shear resistance and promote ductile flexural failure in HSC beams with varied shear demands.

Next, beams C100-20M-FJ and C100-20M-S (plain HSC, with stirrups) are compared to examine the ability of UHPFRC to improve flexural behaviour. As shown in **Figure 4 - 7(b)**, both beams failed in flexure, however the UHPFRC-retrofitted beam shows substantial improvements of 79% and 37% in stiffness and peak capacity. These enhancements can be explained by the increased modulus of the UHPFRC, its enhanced tension stiffening behaviour, and the ability of the UHPFRC in tension to contribute to moment capacity. The addition of UHPFRC further allowed for increases of 37%, 60% and 44% in ductility ($\mathrm{D_{80}/D_y}$), toughness (A_{80}), and toughness index (I_{80}) (2.79 vs. 2.03; 4623 vs. 2955 kN-mm; and 4.56 vs. 3.16), with an even more remarkable increase of 477% in overall toughness (A_{max} = 17046 vs. 2955 kN-mm).

Examining the failure mode, crushing in both beams initiates at a similar displacement of D ≈ 30 mm; however, the severe crushing in beam C100-20M-S results in a complete loss of load-carrying capacity (see **Figure 4 - 7(b)**). In contrast, beam C100-20M-FJ shows a more controlled drop of 25% in capacity, and continues to carry loads until the end of testing. However, when compared to the 15M set, the increased steel ratio in the beam with 20M bars leads to high strain demands on the midspan compression zone, which leads to more extensive crushing in the UHPFRC and HSC core, which in turn leads to a gradual reduction in capacity with increased deflections. Similar to the previous set, the UHPFRC jacket resulted in a distinct cracking pattern, with many fine and closely-spaced cracks, and the formation of one dominant crack in the mid-span zone (see **Figure 4 - 9**). However, the increased steel ratio prevented bar fracture, as further discussed in the next section.

4.4.5 Effect of tension steel ratio in UHPFRC retrofitted beams

The effect of tension steel ratio in the UHPFRC retrofitted beams is examined by comparing the responses of beams C100-15M-FJ and C100-20M-FJ (ρ = 1.6% and 2.4%). As shown in **Figure 4 - 7(c)**, increasing the steel ratio did not affect stiffness but resulted in a 48% increase in peak capacity. The beam with increased steel ratio shows a larger overall toughness (i.e. A_{max}), but reduced ductility (2.79 vs. 7.27), drift ratio (4.2% vs. 9.7%), and toughness/toughness index when calculated up to D_{80} (A_{80} = 4623 vs. 7807 kN-mm, and I_{80} = 4.56 vs. 11.35). Both beams show similar cracking patterns, with multiple fine cracks, and the formation of a dominant crack which results in fiber pullout; however, as the steel ratio increases from ρ = 1.6% to 2.4%, the failure mode transitions from bar fracture in beam C100-15M-FJ, to UHPFRC crushing in beam C100-20M-FJ.

The results are similar to those reported in previous UHPFRC beam tests. For example, Shao and Billington [32] found a change in failure mode, from crack localization leading to steel fracture, to one of UHPFRC crushing prior to steel fracture in conventional UHPFRC beams, by increasing ρ from 0.96% to 2.1%, and noted that a "*higher reinforcing ratio spread steel reinforcement plasticity across a longer length which delays steel fracture*". Likewise, Hasgul et al. [33] reported that increasing the steel ratio from 0.8% to 4.3% coincided with a change in failure mode from bar fracture to concrete crushing, with a net reduction in overall ductility, which matches the observation in the current tests. In case of retrofitted beams, Safdar et al. [15] reported bar fracture failure when applying tension side UHPFRC retrofits at or above the level of the tension steel in beams with a low steel ratio of ρ = 0.4%. Al-Osta et al. [19] also noted that increasing the steel ratio can reduce the ductility of UHPFRC-retrofitted members, which also matches the observation in the current tests.

On the other hand, several studies indicate that when bar fracture dominates, increasing the steel ratio in conventional UHPFRC beams leads to an increase in ductility. For example, Yoo et al. [34] observed an increase in ductility in UHPFRC beams as ρ increased from 0.53% to 1.71%, with all the beams failing by bar fracture. Pokhrel and Bandelt [30] also reported an increase in deformation capacity as ρ increased from 0.7% to 1.9% and noted that the increase in steel ratio delayed bar fracture. Therefore, further tests on UHPFRC retrofitted beams with a wider range of steel ratios are recommended. Since UHPFRC bond capacity and tensile resistance are also affected by fiber content [32], further tests on the influence of these parameters on the ductility and failure mode of UHPFRC-retrofitted beams is also recommended.

In the current tests increasing the tension steel ratio resulted in a relative reduction in ductility due to increased strain demands on the midspan compression zone. Specifically, the top UHPFRC overlay thickness was insufficient to continue to resist the load once crushing initiated, which resulted in crushing of the HSC core concrete, resulting in a reduction in ductility. This indicates the thickness/depth of UHPFRC in the compression zone should also be considered as the tension steel ratio is increased; further research is recommended.

4.5 Sectional analysis

4.5.1 Shear prediction

To better understand the ability of the UHPFRC jacketing to increase shear resistance, the shear capacity of beam C100-20M-FJ is predicted using a method which combines the concrete contribution from the shear design method in the CSA A23.3 standard [35], and the UHPFRC contribution from a model proposed by Yang et al. [36]. According to CSA A23.3 approach, the shear capacity of a conventional reinforced concrete beam without stirrups is given by:

$$V_c = \beta\sqrt{f_c'}b_w d_v \tag{1}$$

where: β = aggregate interlock factor, f_c' = concrete compressive strength, b_w = web width, d_v = shear depth, f_y = stirrup yield strength, s = stirrup spacing; θ = shear crack inclination). Using this equation, the shear capacity of the control C100-20M beam is estimated as 39 kN, which matches reasonably well with the tested shear capacity of 42 kN. In the case of the UHPFRC retrofitted beams the same approach is used, but with the core concrete dimensions of b_{wcore} = 85 mm, and h_{core} = 189 mm (with d_{core} = 179 mm), resulting in V_c = 27.3 kN for the core concrete contribution in beam C100-20M-FJ.

The Yang et al. [36] model predicts the shear resistance in a UHPFRC beam to be equal to:

$$V_{UHPFRC} = \Psi\left(\frac{1.4}{\lambda} + 0.45\right)K\sqrt{f_c'}b_w d \tag{2}$$

where Ψ depends on the shear-span-to depth ratio (λ), taken as 0.6 for $\lambda > 3$; and where the parameter K accounts for the effects of the fibers, $K = [v_f \times (\frac{l_f}{d_f})]^{0.2}$, where v_f, l_f and d_f are the fiber content, fiber length and fiber diameter (2.5%, 13 mm and 0.2 mm in the current study). Using the UHPFRC jacket dimensions, the equation predicts V_{UHPFRC} = 162.6 kN, which results in a total shear capacity $V_{c+UHPFRC} = V_c + V_{UHPFRC}$ = 189.9 kN, and a shear-to-flexure load ratio (P_v/P_{fl}) of 2 when using the actual (tested) ultimate capacity of beam C100-20M-FJ (where P_{fl} = P_{max} and P_v = 2 × $V_{c+UHPFRC}$). Using a similar approach, beam C100-15M-FJ is predicted to have a shear-to-flexure load ratio of 2.97. The results confirm that the UHPFRC jacket provided sufficient shear capacity to prevent shear failure in both retrofit specimens.

4.5.2 Moment prediction

The moment capacity of the UHPFRC retrofitted beams is further predicted by adapting a sectional analysis procedure proposed by Bae et al. [37]. As shown in **Figure 4 - 11,** Bae et al. [37] proposed a set of nine models, with varied assumptions for the compression and tension stress blocks, to predict the moment capacity of conventional UHPFRC beams. In this paper the **Type 9** model, which uses a modified rectangular stress block for UHPFRC in compression and a uniform stress block for UHPFRC in tension, is selected due to its simplified and conservative assumptions. According to this model, the neutral axis depth (c) and moment capacity (M_{UHPFRC}) of a conventional UHPFRC beam are predicted using the following equations based on equilibrium:

$$c = \frac{A_s f_y + \gamma f_t b h}{\alpha f'_{cUHPC} \beta b + \gamma \eta f_t b} \tag{3}$$

$$M_{UHPFRC} = (\alpha f'_{cUHPFRC} \beta b c)\frac{c}{2} + [\gamma f_t (h - e)](e - c + \frac{h-e}{2}) + A_s f_y (d - c) \tag{4}$$

where, $f'_{cUHPFRC}$ = UHPFRC compressive strength; f_y = steel yield strength; d, h, b = beam height, width and effective depth; $\alpha,\ \beta$ = rectangular stress block/depth parameters for UHPFRC (0.85 and 0.65); f_t = ultimate tensile strength of UHPFRC; γf_t = residual tensile stress of UHPFRC; γ = ratio between the post-cracking and ultimate tensile strength of UHPFRC; $e = \eta c$, where $\eta = 1 + \frac{\varepsilon_f}{\varepsilon_{cu}}$, and ε_f = strain at f_t and ε_{cu} = ultimate strain of UHPFRC in compression. In this paper, f_t is taken as 10.4 MPa using the following equation which is adapted from Wile et al. [38]: $f_t = 6.5 + \alpha\tau \frac{v_f l_f}{d_f}$ (where $\alpha\tau = 0.03$ and accounts for the group effect for the case of straight fibers), while the parameters γ and η are taken as 0.7 and 1.4 as recommended in Madanat et al. [39].

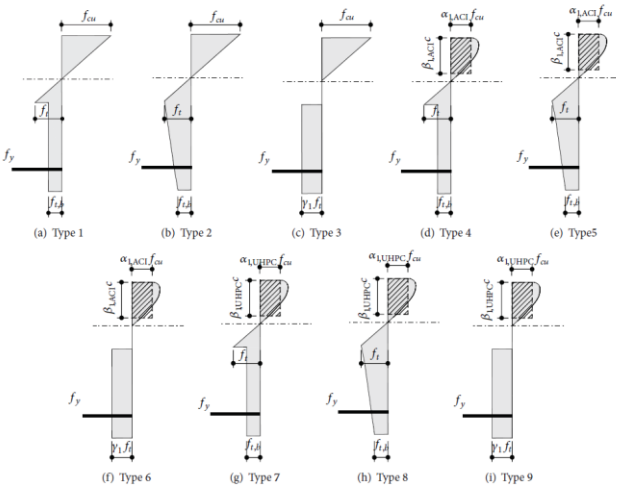

(a) Type 1 (b) Type 2 (c) Type 3 (d) Type 4 (e) Type5

(f) Type 6 (g) Type 7 (h) Type 8 (i) Type 9

Figure 4 - 11 Stress block models proposed by Bae et al. (2016) for UHPFRC beams

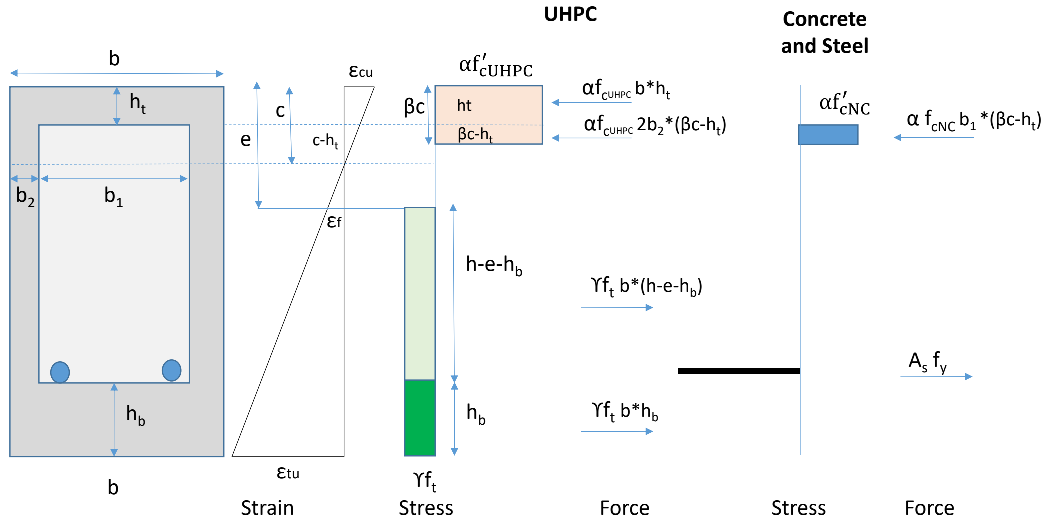

Figure 4 - 12 Strain and stress distribution for singly reinforced UHPFRC retrofitted beam

The equations in the Type 9 Bae model can be adapted for the case of a UHPFRC retrofitted beam using the strain and stress distributions shown in **Figure 4 - 12**. Accordingly, the neutral axis depth (c) and moment capacity (M_{UHPFRC}) can be determined as follows:

For the case of $c \leq h_t$:

$$c = \frac{A_s f_y + \gamma f_t b h_b + \gamma f_t(2b_2)(h-h_b)}{\alpha f'_{cUHPFRC} b\beta + \gamma f_t(2b_2)\eta} \tag{5}$$

$$M_{UHPFRC} = (\alpha f'_{cUHPFRC} bc) \times \left(\frac{c}{2}\right) + A_s f_y \times (d-c) + \gamma f_t(b)(h_b) \times (h - e - \frac{h_b}{2} + e - c) + \gamma f_t(2b_2)(h-e-h_b) \times (\frac{h-e-h_b}{2} + e - c) \tag{6}$$

For the case of $c > h_t$:

$$c = \frac{A_s f_y + \gamma f_t b h_b + \gamma f_t(2b_2)(h-h_b) - \alpha f'_{cUHPFRC} b h_t + \alpha f'_{cUHPFRC}(2b_2)h_t + \alpha f'_{cNC} b_1 h_t}{\alpha f'_{cUHPFRC}(2b_2)\beta + \gamma f_t(2b_2)\eta + \alpha f'_{cNC} b_1 \beta} \tag{7}$$

$$M_{UHPFRC} = \begin{array}{c} (\alpha f'_{cUHPFRC} b h_t) \times \left(c - \frac{h_t}{2}\right) + \alpha f'_{cUHPFRC}(2b_2)(\beta c - h_t) \times \left(c - h_t - \frac{\beta c - h_t}{2}\right) + \alpha f'_{cNC} b_1(\beta c - h_t) \times \left(c - h_t - \frac{\beta c - h_t}{2}\right) \\ + A_s f_y \times (d-c) + \gamma f_t(b)(h_b) \times (h - e - \frac{h_b}{2} + e - c) + \gamma f_t(2b_2)(h-e-h_b) \times (\frac{h-e-h_b}{2} + e - c) \end{array} \tag{8}$$

Using the above equations the predicted moment capacities (M_{UHPFRC}) for beams C100-20M-FJ and C100-15-FJ are found to be 58 and 45 kN-m, with corresponding load capacities ($P_{UHPFRC} = 2 \cdot M_{UHPFRC}/a$, where a = shear span length) of 156 and 120 kN. The results agree well with the tested load capacities at yielding of P_y = 159 and 116 kN, with prediction ratios of P_y/P_{UHPFRC} = 1.01 and 0.97. The analysis results indicate that the simplified sectional approach which modifies the Bae et al. equations can be used to predict the flexural capacities of UHPFRC retrofitted beams with reasonable accuracy.

4.6 Conclusions

This paper presented the results of an experimental study which examined the effect of UHPFRC jacketing on the shear and flexural behavior of high-strength concrete beams tested under four-point bending. The following conclusions and observations can be drawn from this study:

(1) Overall, the results showed that UHPFRC jacketing can significantly improve the shear and flexural resistance of higher-strength concrete beams. The application of UHPFRC not only improved shear capacity, but also switched the failure mode from brittle shear failure to ductile flexure failure, effectively substituting for transverse reinforcement in shear-deficient HSC beams built without stirrups;

(2) Provision of UHPFRC jacketing also increased the stiffness, load capacity, ductility ratio and energy absorption capacity (toughness) when compared to control HSC beams built with stirrups;

(3) No premature debonding occurred in all beams retrofitted by UHPFRC jacketing, indicating the surface preparation with a roughness beyond CSP6 was sufficient to achieve a desirable bond between the HSC substrate and the UHPFRC;

(4) The failure mode of the UHPFRC beams was affected by the tension steel ratio. In the 15M group ($\rho = 1.6\%$), bar-fracture occurred due to the high bond capacity of the UHPFRC and crack localization, which resulted in strain concentration over a small gage length of the longitudinal reinforcement. Further research on the effects of varied steel ratios, UHPFRC fiber content, and location of UHPFRC overlay interface with respect to the longitudinal steel reinforcement is recommended;

(5) Increasing the steel ratio to 2.4% in the 20M group prevented bar facture, with the failure transitioning to UHPFRC crushing. On the other hand, increasing the steel ratio resulted in a reduction in ductility due to increased strain demands on the midspan compression zone. Specifically, the top UHPFRC overlay thickness was insufficient to continue to resist the load once crushing initiated, which resulted in crushing of the HSC core concrete, resulting in a reduction in ductility. This indicates the thickness/depth of UHPFRC in the compression zone should be adjusted/increased as the tension steel ratio is increased; further research is recommended.

(6) The shear capacity of the UHPFRC retrofitted beams was estimated by combining the concrete contribution of the core section using the CSA A23.3 shear design method and the UHPFRC jacket contribution using an equation proposed by Yang et al. The analysis showed that the UHPFRC retrofitted beams had shear-to-flexure ratios of 2 and 2.97 for the beams with 20M and 15M bars respectively. The moment capacity of the beams was also predicted by adapting a sectional analysis procedure based on a model proposed by Bae et al. The analysis resulted in load prediction ratios P_y/P_{UHPFRC} of 1.01 and 0.97.

References

[1] ASCE. A comprehensive assessment of America's infrastructure. ASCE; 2021.

[2] McNally C, Bill Ferreira, and David LA Gordon. "The Canadian infrastructure report card." Canada: The State of the Federation 2015. Canadian Federalism and Infrastructure; 2018. p. 27.

[3] Litvan GG. Deterioration of Parking Structures. ACI Symposium Publication. 1991;126.

[4] Zhang C, Gholipour G, Mousavi AA. State-of-the-Art Review on Responses of RC Structures Subjected to Lateral Impact Loads. Archives of Computational Methods in Engineering. 2020;28:2477-507.

[5] Zhang C, Gholipour G, Mousavi AA. Blast loads induced responses of RC structural members: State-of-the-art review. Composites Part B: Engineering. 2020;195.

[6] Siddika A, Mamun MAA, Ferdous W, Alyousef R. Performances, challenges and opportunities in strengthening reinforced concrete structures by using FRPs – A state-of-the-art review. Engineering Failure Analysis. 2020;111.

[7] Koutas LN, Tetta Z, Bournas DA, Triantafillou TC. Strengthening of Concrete Structures with Textile Reinforced Mortars: State-of-the-Art Review. Journal Of Composites for Construction. 2019;23.

[8] Brühwiler E. UHPFRC is Ready to Revolutionize Existing and New Structures. IABSE Symposium Prague 2022: IABSE; 2022. p. 67-79.

[9] Hung C-C, El-Tawil S, Chao S-H. A Review of Developments and Challenges for UHPC in Structural Engineering: Behavior, Analysis, and Design. Journal of Structural Engineering. 2021;147.

[10] Brühwiler E, Denarié E. Rehabilitation and Strengthening of Concrete Structures Using Ultra-High Performance Fibre Reinforced Concrete. Structural Engineering International. 2018;23:450-7.

[11] Ullah R, Qiang Y, Ahmad J, Vatin NI, El-Shorbagy MA. Ultra-High-Performance Concrete (UHPC): A State-of-the-Art Review. Materials (Basel). 2022;15.

[12] Yoo D-Y, Banthia N. Mechanical properties of ultra-high-performance fiber-reinforced concrete: A review. Cement and Concrete Composites. 2016;73:267-80.

[13] Zhu Y, Zhang Y, Hussein HH, Chen G. Flexural strengthening of reinforced concrete beams or slabs using ultra-high performance concrete (UHPC): A state of the art review. Engineering Structures. 2020;205.

[14] Hussein L, Amleh L. Structural behavior of ultra-high performance fiber reinforced concrete-normal strength concrete or high strength concrete composite members. Construction and Building Materials. 2015;93:1105-16.

[15] Safdar M, Matsumoto T, Kakuma K. Flexural behavior of reinforced concrete beams repaired with ultra-high performance fiber reinforced concrete (UHPFRC). Composite Structures. 2016;157:448-60.

[16] Lampropoulos AP, Paschalis SA, Tsioulou OT, Dritsos SE. Strengthening of reinforced concrete beams using ultra high performance fibre reinforced concrete (UHPFRC). Engineering Structures. 2016;106:370-84.

[17] Ramachandra Murthy A, Karihaloo BL, Priya DS. Flexural behavior of RC beams retrofitted with ultra-high strength concrete. Construction and Building Materials. 2018;175:815-24.

[18] Tanarslan HM, Alver N, Jahangiri R, Yalçınkaya Ç, Yazıcı H. Flexural strengthening of RC beams using UHPFRC laminates: Bonding techniques and rebar addition. Construction and Building Materials. 2017;155:45-55.

[19] Al-Osta MA, Isa MN, Baluch MH, Rahman MK. Flexural behavior of reinforced concrete beams strengthened with ultra-high performance fiber reinforced concrete. Construction and Building Materials. 2017;134:279-96.

[20] Paschalis SA, Lampropoulos AP, Tsioulou O. Experimental and numerical study of the performance of ultra high performance fiber reinforced concrete for the flexural strengthening of full scale reinforced concrete members. Construction and Building Materials. 2018;186:351-66.

[21] Moon J, Reda Taha MM, Kim JJ. Flexural Strengthening of RC Slabs Using a Hybrid FRP-UHPC System Including Shear Connector. Advances in Materials Science and Engineering. 2017:1-7.

[22] Yin H, Teo W, Shirai K. Experimental investigation on the behaviour of reinforced concrete slabs strengthened with ultra-high performance concrete. Construction and Building Materials. 2017;155:463-74.

[23] Noshiravani T, Brühwiler E. Experimental Investigation on Reinforced Ultra-HighPerformance Fiber-Reinforced Concrete Composite Beams Subjected to Combined Bending and Shear. ACI Stuctural Journal. 2013;110:251-61.

[24] Sakr MA, Sleemah AA, Khalifa TM, Mansour WN, Beushausen H, Dehn F, Moyo P. Behavior of RC

beams strengthened in shear with ultra-high performance fiber reinforced concrete (UHPFRC). MATEC Web of Conferences. 2018;199:09002.

[25] Yuan TF, Hong SH, Shin HO, Yoon YS. Bond Strength and Flexural Capacity of Normal Concrete Beams Strengthened with No-Slump High-Strength, High-Ductility Concrete. Materials. 2020;13.

[26] Algassem O. Parameters affecting the blast performance of high strength fibre reinforced concrete beams: University of Ottawa; 2016.

[27] ICRI. ICRI Standard 310.2 Selecting and Specifying Concrete Surface Preparation for Sealers, Coatings, Polymer Overlays, and Concrete Repair with CSP Chips. 2013.

[28] Khaksefidi S, Ghalehnovi M, de Brito J. Bond behaviour of high-strength steel rebars in normal (NSC) and ultra-high performance concrete (UHPC). Journal of Building Engineering. 2021;33:101592.

[29] Hung C-C, Lee H-S, Chan SN. Tension-stiffening effect in steel-reinforced UHPC composites: Constitutive model and effects of steel fibers, loading patterns, and rebar sizes. Composites Part B: Engineering. 2019;158:269-78.

[30] Pokhrel M, Bandelt MJ. Material properties and structural characteristics influencing deformation capacity and plasticity in reinforced ductile cement-based composite structural components. Composite Structures. 2019;224:111013.

[31] Silfwerbrand J. Bonded Concrete Overlays. Concrete International. 2017;39:31-6.

[32] Shao Y, Billington SL. Impact of cyclic loading on longitudinally-reinforced UHPC flexural members with different fiber volumes and reinforcing ratios. Engineering Structures. 2021;241.

[33] Hasgul U, Turker K, Birol T, Yavas A. Flexural behavior of ultra-high-performance fiber reinforced concrete beams with low and high reinforcement ratios. Structural Concrete. 2018;19:1577-90.

[34] Yoo D-Y, Banthia N, Yoon Y-S. Experimental and numerical study on flexural behavior of ultra-high-performance fiber-reinforced concrete beams with low reinforcement ratios. Canadian Journal of Civil Engineering. 2016;44:18-28.

[35] CSA. Design of concrete structures. CSA A233:19. Toronto, Ontario: Canadian Standards Association; 2019.

[36] Yang J, Doh J-H, Yan K, Zhang X. Experimental investigation and prediction of shear capacity for UHPC beams. Case Studies in Construction Materials. 2022;16.

[37] Bae BI, Choi HK, Choi CS. Flexural strength evaluation of reinforced concrete members with ultra high performance concrete. Advances in Materials Science and Engineering. 2016.

[38] Wille K, El-Tawil S, Naaman AE. Properties of strain hardening ultra high performance fiber reinforced concrete (UHP-FRC) under direct tensile loading. Cement and Concrete Composites. 2014;48:53-66.

[39] Madanat J, Othman H, H M. Investigation on the Flexural Capacity of Ultra-high Performance Fibre Reinforced Concrete Beams. CSCE Annual Conference 2019.

Chapter 5: Blast Retrofit of Shear-deficient high-strength concrete beams with Ultra-High Performance Fiber Reinforced Concrete

Paper 2: extracted from static and dynamic results in series 1 (submitted to journal- "Engineering Structures")

Abstract

This research has investigated the ability of ultra-high performance fiber reinforced concrete (UHPFRC) to improve the blast performance of high-strength concrete (HSC) beams. As part of the study shear-deficient HSC beams built without stirrups were retrofitted with a UHPFRC jacket and tested under simulated blast loads using a shock-tube. A companion set of beams was also tested under quasi-static four-point bending. The results from the blast and static tests are compared to a control set of HSC beams built without and with stirrups to examine the ability of UHPFRC to increase shear and flexural resistance, respectively. The effect of steel ratio, an important parameter which affects the behaviour of HSC and UHPFRC beams, is also investigated. Under static loading, the results show that the UHPFRC jacket was able to prevent shear failure, and improve flexural performance by increasing strength, stiffness and overall toughness. Under blast loading, the UHPFRC increased shear capacity and improved blast performance by reducing displacements, increasing overall blast capacity and improving damage tolerance. The steel ratio was found to play an important role on the failure mode of the retrofitted beams under static loading. As part of the numerical study, the blast response of the UHPFRC retrofitted beams was predicted using 3D finite element (FE) modelling. The FE models were able to predict the failure modes and maximum displacements of the control and UHPFRC retrofitted beams, with good accuracy.

Keywords: Blast, Retrofit, HSC, UHPFRC, Beams, Jacketing, Shear, Shock-tube.

5.1 Introduction

In recent years, the vulnerability of structures to accidental explosions or blast threats from terrorist attacks has increased. While rare, events such as the Oklahoma City Bombing, Toronto Sunrise Explosion and Lac-Mégantic Disaster, demonstrate the significant damage that can be caused by blast loads on structures. As a result, there is a need to increase the blast resistance of critical and vulnerable structures such as government and corporate offices, strategic transportation links, and industrial facilities such as gas, petroleum and nuclear installations.

Recently, ultra-high performance fiber reinforced concrete (UHPFRC) has been proposed to strengthen or retrofit existing reinforced concrete (RC) structures [1-3]. UHPFRC is a novel cement-based composite which shows superior properties when compared to conventional concrete, including: improved tensile resistance, high compressive strength and impressive durability, which make it an ideal solution to retrofit or strengthen existing structures [4, 5]. The provision of fibers in UHPFRC also allows for remarkable toughness and fragmentation resistance, which make it an attractive material for the protection of structures against impact and blast loads.

While a few experimental studies have investigated the ability of UHPFRC to increase the shear and flexural capacity of existing RC beams and slabs under static loading [6], limited research has been conducted on the blast resistance of UHPFRC strengthened RC structures (refer to the literature review in Chapter 2, and Table 2-2). Accordingly, this paper presents the results of a research study which examines the ability of UHPFRC jacketing to improve the performance of high-strength concrete (HSC) beams under both static and blast loading.

5.2 Research significance

Important research has investigated the UHPFRC strengthening of reinforced concrete beams and slabs. However, most previous tests have focused on NSC beams/slabs tested under either static or impact, with limited tests on higher-strength concrete (HSC) members, or under blast. Accordingly, this study examines the ability of UHPFRC jacketing to improve the behavior of higher-strength HSC beams (with $f_c' = 100$ MPa) under static and blast loading. The ability of UHPFRC to improve shear and flexural behaviour is studied by comparing the results to those of companion HSC beams built with and without shear reinforcement.

5.3 Experimental Program

5.3.1 Specimen designs

As part of this study four UHPFRC strengthened HSC beams were tested under blast loads or quasi-static conditions. **Table 5 - 1** provides an overview of the test matrix, while **Figure 5 - 1** presents the beam dimensions and retrofit details. All specimens had constant dimensions of 125mm × 250mm × 2440mm (b × h × L), with an effective depth (d) of ~ 200 mm. Longitudinal reinforcement consisted of 2-15M or 2-20M bars in tension, resulting in steel ratios of $\rho = 1.6\%$ or 2.4%. The retrofit specimens were built without stirrups in the shear spans and first cast with plain high-strength concrete. Thereafter the concrete cover was removed and replaced with a UHPFRC jacket. The thickness of the UHPFRC was 41mm on the bottom face and 20mm on the top and side faces. To examine the ability of the UHPFRC to improve shear and flexural behaviour, the results are compared to a control set of plain HSC beams with the same dimensions and longitudinal reinforcement details (either 2-15M or 2-20M bars), and built either without or with stirrups spaced at 100 mm in the shear spans [7] (see **Table 5 - 1** and **Figure 5 - 1**). This control set included 4 beams tested under blast loads, and 4 beams tested under quasi-static conditions.

The beam nomenclature in **Table 5 - 1** reflects the concrete type in the control/reference beams, longitudinal steel bar size, and whether the beam contains stirrups or was retrofitted with UHPFRC: C100-15M and C100-20M are the control beams built without stirrups, C100-15M-S and C100-20M-S are the control beams built with stirrups, and C100-15M-FJ and C100-20M-FJ are the beams built without stirrups and retrofitted with a UHPFRC full-jacket (FJ).

Table 5 - 1 Beam test matrix

Group	Beam I.D.	HSC beam properties			UHPFRC f'_c(MPa)	Retrofit	Steel fiber properties		Number beams	Test type
		f'_c(MPa)	Longitudinal reinforcement	Transverse reinforcement			Length/dia. (mm/mm)	Content V_f (%)		
Retrofit beams	C100-15M-FJ	99	2- 15M	None	164	UHPFRC jacket	13/0.2	2.5	2	Static/Blast
	C100-20M-FJ	101	2- 20M		164	UHPFRC jacket	13/0.2	2.5	2	Static/Blast
Control Group 1	C100-15M	104	2- 15M	None	-	-	-	-	2	Static/Blast
	C100-20M	110	2- 20M		-	-	-	-	2	Static/Blast
Control Group 2	C100-15M-S	95	2- 15M	Stirrups at s = 100 mm	-	-	-	-	2	Static/Blast
	C100-20M-S	106	2- 20M		-	-	-	-	2	Static/Blast

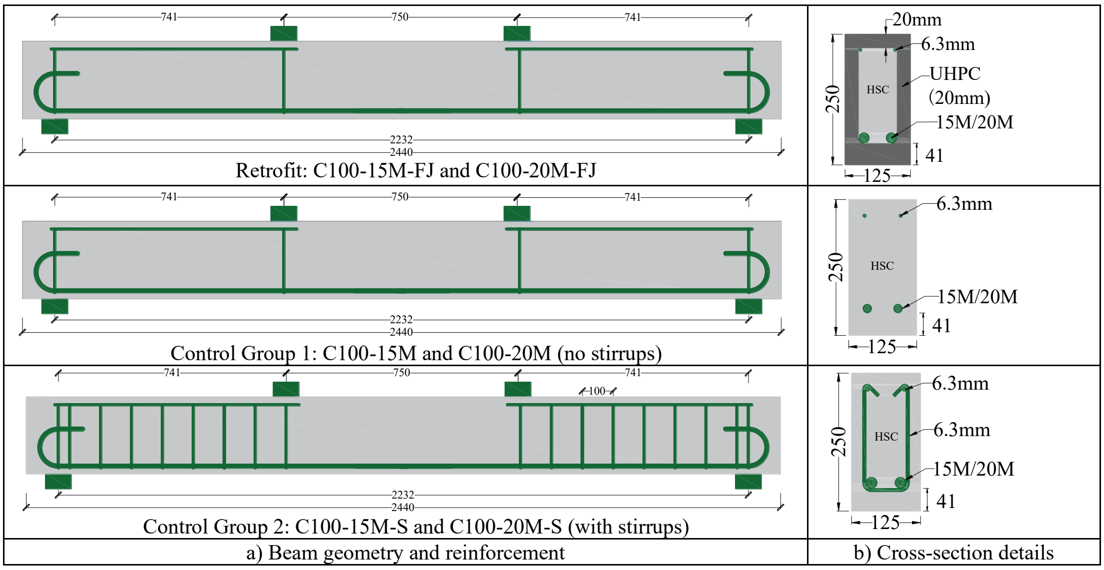

a) Beam geometry and reinforcement

b) Cross-section details

Figure 5 - 1 Beam geometry and reinforcement detailing

5.3.2 Material Parameters

The high-strength concrete used in the control and retrofit beams had a target compressive strength of 100 MPa and was mixed using cement, slag, silica fume, 19 and 10 mm coarse aggregates, sand, a super-plasticizer and set retarder. The proprietary UHPFRC used in this study consisted of a dry premix, steel fibers, and three types of liquid admixtures which were added according to the manufacturer’s specifications. The fibers had an aspect ratio of 65, with a length and diameter of 13 mm/0.2 mm, and tensile strength of 2850 MPa. The mix used a fiber content of 2.5% by volume of the UHPFRC (195 kg/m^3). The UHPFRC properties in compression and flexure were determined by testing standard cylinders (diameter × length: 75 × 150 mm) and prisms (base × height × length: 75 × 75 × 285 mm) according to the ASTM C1856 specifications. The HSC properties in compression were determined by testing standard cylinders (100 × 200 mm) according to ASTM C39. Sample results from the material tests and average properties of the UHPFRC/HSC in compression are reported in **Figure 5 - 2 (a-b)** and **Table 5 - 1**, respectively. The steel properties were determined by testing standard steel coupons in tension in accordance with the ASTM A615 specifications and sample stress-strain curves are shown in **Figure 5 - 2(c)**.

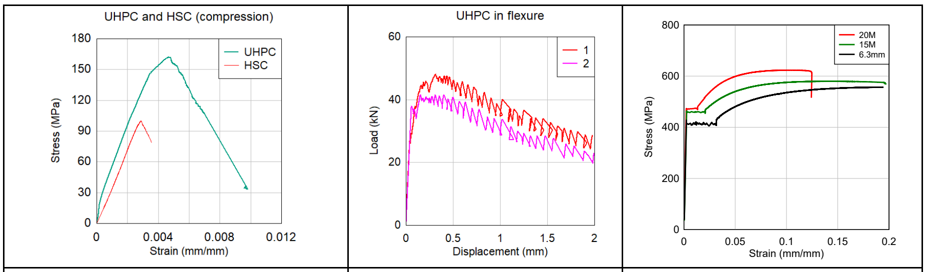

a) UHPFRC and HSC (compression) b) UHPFRC (flexure) c) Steel reinforcement (tension)

Figure 5 - 2 Material properties

5.3.3 Specimen preparation

The construction of the test beams included several stages: building the reinforcement cages, casting the HSC beams, preparing the substrate surface using a concrete chisel, moistening the surface and then casting the UHPFRC jacket. As shown in **Figure 5 - 3(a)** the cover removal process was simplified by reducing the cover section dimensions using 5/8-inch or 3/8-inch plywood sheets on the bottom and side faces respectively. Once the HSC concrete strength reached at least 50 MPa, the remaining substrate thickness was removed using a concrete chisel to ensure a concrete surface profile of at least CSP6 [8] (see **Figure 5 - 3(b)**). Thereafter the substrate surface was moistened for at least 15 minutes, followed by casting of the UHPFRC jacket and moist curing with wet burlap and plastic sheets for at least 7 days (see **Figure 5 - 3(c-d)**). The beams were then cured under laboratory conditions until the day of testing.


a) Casting of HSC concrete | b) Interface preparation | c) Moistening | d) UHPFRC casting

Figure 5 - 3 Casting and retrofit procedure

5.3.4 Test setup and instrumentation

The static specimens were tested using the four-point bending setup shown in **Figure 5 - 4(a)**. In all cases the beams were simply-supported over a span of 2232 mm, with two equal shear spans of 741 mm and a constant moment region of 750 mm. Loading was applied using a hydraulic jack and monitored using a load-cell with the loading transferred as two points using a load-transfer beam. The mid-span displacement was captured using a displacement transducer, while the strains in the longitudinal steel were captured using strain gages placed on the tension bars at midspan. Testing was conducted under load-control until yielding, and switched to displacement control until the failure of the beam specimens.

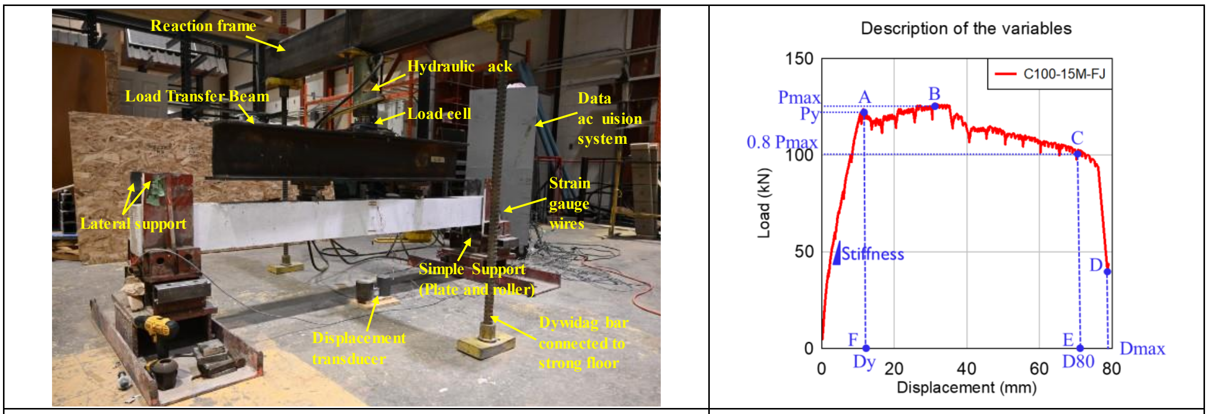

a) Static test setup | b) Load-deflection parameters

Figure 5 - 4 Setup for static and definition of load-deflection parameters

The blast tests were conducted using the University of Ottawa shock-tube and four-point bending setup shown in **Figure 5 - 5(a)** and **Figure 5 - 6(a)**. The pressure-driven shock-tube consists of four main parts [9]: (1) a driver section which produces the blast pressure, (2) a spool section with a double-diaphragm system which triggers the shockwave, (3) an expansion section which ensures the formation of a uniform shock front, and (4) a rigid end frame with a 2 m × 2 m opening. A load-transfer device (LTD), consisting of a set of steel panels with sliding hinges, was used to collect and transfer the blast loads onto the specimens. Consistent with the static tests, the beams were tested under four-point bending, with a clear span of 2232 mm, two equal shear spans and a constant moment region of ~ 744 mm. The beams were connected to the end-frame using the support assemblies which resulted in simple (pin-pin) boundary conditions [10]. During the tests, pressure and displacement time histories were recorded using two pressure sensors which were placed near the end-frame, and a midspan linear variable displacement transducer (LVDT) with a 300 mm gage length. The displaced shape during each test was also captured using two high-speed cameras at 2000 frames per second. Dynamic reactions were captured using load-cells which were attached to the support assemblies.

To allow for comparison with the control specimens, the beams were tested under repeated blast loads until failure. Blasts 1, 2 and 3/4/5 were intended to test the beams under elastic, yield and ultimate conditions, respectively. All blasts used a constant shock-tube driver length of 2743 mm (9ft) and gradually increasing driver pressures (P_d) which varied between 117 and 620 kPa (17 and 90 psi). The average parameters which define each blast are reported in **Table 5 - 2** including: maximum reflected pressure (P_r) and reflected impulse over the positive phase (I_r). In the control set, C100-15M and C100-20M failed in shear at Blast 2, while C100-15M-S and C100-20M-S failed by concrete crushing at Blasts 3 and 4, respectively.

The retrofit beams with 15M and 20M survived up to the end of Blasts 4 and 5, respectively, and were subsequently tested under static loads to assess their residual capacity.

Table 5 - 2 Blast test sequence (average properties)

Test sequence	Driver Length mm (ft)	Driver Pressure kPa (psi)	Avg. Reflected Impulse (I_r) kPa-ms	Avg. Reflected Pressure (P_r) kPa	Avg. Positive Phase Duration (t_p) ms
Blast 1	2743 (9)	117 (17)	213	26.5	16.1
Blast 2	2743 (9)	207 (30)	328	45.7	14.4
Blast 3	2743 (9)	345 (50)	514	59.3	17.4
Blast 4	2743 (9)	482 (70)	686	80.7	17.1
Blast 5	2743 (9)	620 (90)	821	85.3	19.2

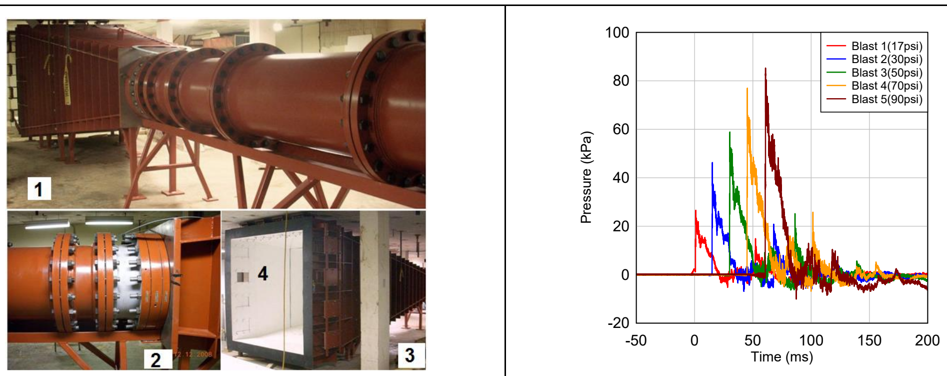

(a) Shock-tube components (b) Blast testing sequence

Figure 5 - 5 Shock-tube description and Blast testing sequence

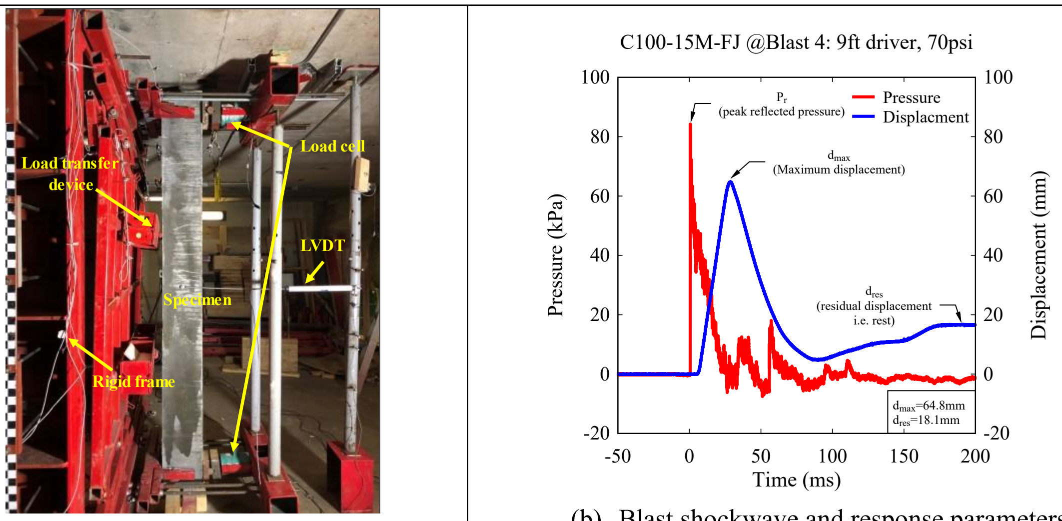

(a) Blast test setup (b) Blast shockwave and response parameters

Figure 5 - 6 Blast setup and blast test parameters

5.4 Experimental Results

5.4.1 Summary of results from the static tests

A summary of the results from the static tests is provided in **Table 5 - 3** which presents key data from the load-deflection responses, including: secant stiffness (k_s), maximum load (P_{max}), and displacements at yield, 80%P_{max} and at the end of the testing (D_y, D_{80} and D_{max}). The table also reports the ductility (D_{80}/D_y), drift ratio (D_{80}/L_{shear}), and toughness, defined as the area under the load deflection curves up to D_{80} and D_{max} (A_{80} and A_{max}) , as well as the corresponding toughness indices I_{80} and I_{max} (see **Figure 5 - 4(b)**).

Table 5 - 3 Static test results

Group	Beam I.D.	Max. Load P_{max}(kN)	Displacement			Stiffness k_s(N/mm)	Ductility D_{80}/D_y	Drift ratio D_{80}/L_{shear} (%)	Toughness (kN-mm) [Toughness index]		Failure mode
			Yield D_y(mm)	Failure D_{80}(mm)	Max. D_{max}(mm)				A_{80} [I_{80}]	A_{max} [I_{max}]	
Retrofit beams	C100-15M-FJ	127	9.9	72	79.06	11758	7.27	9.72%	7807 [11.35]	8405 [12.22]	Bar fracture
	C100-20M-FJ	189	11.25	31.39	219	14133	2.79	4.24%	4623 [4.56]	17046 [16.81]	UHPC crushing
Control Group 1	C100-15M	90	-	15.3	19.51	5882	-	2.06%	725	922	Shear
	C100-20M	84	-	10.67	10.67	7873	-	1.44%	470	470	Shear
Control Group 2	C100-15M-S	105	14.9	39.0	40.66	6342	2.62	5.26%	3205 [3.93]	3273 [4.01]	Concrete crushing
	C100-20M-S	138	15	30.51	31	7880	2.03	4.12%	2955 [3.16]	2999 [3.21]	Concrete crushing

5.4.2 Summary of results from the blast tests

A summary of the results from the blast tests is provided in **Table 5 - 4** which presents key data from the pressure and displacement time histories, including: peak reflected pressure (P_r), positive phase duration (t_d), reflected impulse over the positive phase (I_r), maximum displacement (d_{max}), residual displacement (d_{res}) and the maximum support rotation (θ_{max}). Sample pressure and displacement time histories for one of the beams, with an overview of the key parameters, are shown in **Figure 5 - 5(b) and Figure 5 - 6(b)**. **Table 5 - 5** also reports the maximum dynamic loads (P^D_{max}), which correspond to the sum of the dynamic reactions recorded during the blast tests, as well as a comparison of load and toughness from the blast and static tests.

The UHPFRC strengthened beams survived the blast tests and were subsequently tested under static loading to assess their post-blast residual capacity. **Table 5 - 6** reports key parameters from the residual static tests, including the maximum residual load (P^R_{max}), residual secant stiffness (k_s^R), residual resistance index (RRI, defined as P_{max}^R/P_{max}) and residual stiffness index (RSI, defined as k_s^R/k_s). The table also reports the “damage index” ($D = 1 - RRI$) and “total energy index” (TEI), as defined by Adhikary et al. [11] and Zanuy and Ulzurrun [12].

Table 5 - 4 Blast test results

Group	Specimen ID [a]	Blast ID	Blast Loading (9ft)	P_r (kPa)	t_d (ms)	I_r (kPa·ms)	D_{max} (mm)	D_{res} (mm)	θ_{max} (°)	CSA S850 Damage [b]	Failure mode
Retrofit beams	C100-15M-FJ	1	17psi	26.4	15.9	209.9	3.9	0	0.2	Superficial	Ductile (fiber pullout)
		2	30psi	45.1	14.0	315.2	13.5	2.8	0.7	Superficial	
		3	50psi	59.6	17	506.8	29.2	12.1	1.5	Moderate	
		4	70psi	84.3	16.2	681.0	64.8	18.1	3.3	Heavy	
	C100-20M-FJ	1	17psi	26.6	16.3	216.4	3.9	2.1	0.2	Superficial	Ductile (fiber pullout)
		2	30psi	46.3	14.8	341.6	11.2	2.3	0.6	Superficial	
		3	50psi	58.9	17.7	521.3	20	0	1.0	Moderate	
		4	70psi	77	18	691.7	41.8	8.4	2.1	Heavy	
		5	90psi	85.3	19.2	820.7	116.3	76.7	5.9	Hazardous	
Control Group 1	C100-15M (Control)	2	30psi	35.9	19.4	323.6	16.08	5.49	0.8	(shear)	Brittle (shear)
	C100-20M (Control)	1	17psi	23.93	20.02	239.53	12.55	3.37	0.6	Superficial	Brittle (shear)
		2	30psi	38.7	19.16	370.8	19.31	9.21	1.0	(shear)	
Control Group 2	C100-15M-S (Control)	1	17psi	23.89	18.67	223	11.5	2.66	0.6	Superficial	Ductile (crushing)
		2	30psi	42.88	15.89	340.7	21.4	4.71	1.1	Moderate	
		3	50psi	58.64	17.6	516	79.6	33	4	Heavy	
	C100-20M-S (Control)	1	17psi	23.58	20.72	244.28	10.44	1.98	0.5	Superficial	Ductile (crushing)
		2	30psi	39.22	18.36	360	15.12	0.15	0.8	Superficial	
		3	50psi	57.4	18.75	538.18	32.91	12.43	1.7	Moderate	
		4	70psi	68.83	20.42	702.59	118.06	71.69	6.0	Hazardous	

Note: P_r= Reflected pressure; I_r = Reflected impulse; t_d = positive phase duration; D_{max}= maximum displacement; D_{res}= residual displacement; θ_{max}= maximum support rotation.

[a] Control beams tested by Algassem [13] and Bastami [7].

[b] CSA S850 response limits: In the case of singly-reinforced beams, *B1*, *B2*, *B3* and *B4* correspond to ductility ratio of $\mu_{max} = 1$, and support rotations of $\theta_{max} = 2°$, $\theta_{max} = 5°$, and $\theta_{max} = 10°$, respectively, which define component damage levels: *“Blowout”* (greater than *B4*), *“Hazardous failure”* (between *B4* and *B3*); *“Heavy”* (between *B3* and *B2*); *“Moderate”* (between *B2* and *B1*) and *“Superficial”* (less than *B1*).

Table 5 - 5 Results from dynamic reaction load-displacement curves

Group	Beam I.D.	Dynamic results					
		Peak load & ratio			Toughness (kN-mm)		
		P_{max}^s(kN)	P_{max}^D(kN)	P_{max}^D/P_{max}^s	A_{max}^s	A_{max}^D	A_{max}^D/A_{max}^s
Retrofit beams	C100-15M-FJ	127	183	1.44	8405	7738	0.92
	C100-20M-FJ	189	272	1.44	17046	20878	1.22
Control Group 1	C100-20M	84	142	1.7	470	1395	2.97
Control Group 2	C100-15M-S	105	139	1.32	3273	4461	1.36
	C100-20M-S	138	142	1.49	2999	6954	2.32

Note: P_{max}^s= maximum static load; P_{max}^D = maximum dynamic load; A_{max}^s = static toughness; A_{max}^D = dynamic toughness.

Note: P_{max}^D and A_{max}^D are obtained using the envelope of the dynamic load-displacement curves considering all blasts.

Table 5 - 6 Post-blast test results

Beam ID	Load			Stiffness		Energy absorption capacity		
	P_{max}^R (kN)	*RRI*	*D*	k_s^R (N/mm)	*RSI*	*IEI*	*REI*	*TEI*
C100-15M-FJ	129.8	1.02	0	9546	0.81	0.28	0.66	0.94
C100-20M-FJ	42.8	0.23	0.77	3168	0.22	0.76	0.14	0.90

Note: P_{max}^R= Peak residual load; k_s^R= Residual stiffness; D = Damage index; $RRI = \frac{P_{max}^R}{P_{max}}$ = Residual resistance index: $RSI = \frac{k_s^R}{k_s}$ = Residual stiffness index; *IEI* = Impact energy index; REI= Residual energy index, TEI = Total energy index.

5.4.3 Effect of UHPFRC on shear response

The ability of UHPFRC to improve shear behaviour under static and blast loads is examined by comparing the responses of the control HSC beams (C100-15M and C100-20M) and the companion beams built with UHPFRC jacketing (C100-15M-FJ and C100-20M-FJ). It is noted that the use of 15M and 20M bars resulted in varied shear demands in the specimens due to the increase in flexural capacity as the steel ratio is increased.

Figure 5 - 7(a-b) compare the beam responses under static loading. Photos comparing the failure modes are shown in **Figure 5 - 8**. As expected, both control beams failed abruptly in shear due to the lack of transverse reinforcement, with maximum capacities of 90 kN and 84 kN for C100-15M and C100-20M. The UHPFRC jacketing resulted in considerable increases in shear strength and stiffness. Beams C100-15M-FJ and C100-20M-FJ show peak capacities of 127 kN and 189 kN, representing increases of 41% and 125% when compared to C100-15M and C100-20M. Likewise, both beams show important increases of 100% and 80% in stiffness. Importantly, provision of UHPFRC prevents shear failure and allows both beams to reach their full flexural capacities, with ductility ratios $(\mathrm{D}_{80}/\mathrm{D}_{\mathrm{y}})$ of 7.27 and 2.79, and drift ratios (D_{80}/L_{shear}) of 9.7% and 4.2%. During the static tests, failure in beams C100-15M-FJ and C100-20M-FJ occurred due to bar fracture and UHPFRC/concrete crushing, respectively. Both beams show considerable increases in toughness, with toughness indices (I_{80}) of 11.35 and 4.56.

Similar trends are observed under blast loading. As shown in **Figure 5 - 11**, failure in beams C100-15M and C100-20M occurred abruptly at Blast 2 (I_r = 324 and 371 kPa-ms) with the formation of diagonal shear crack in the beam shear spans. Provision of UHPFRC jacketing prevented the shear failure at Blast 2, and allowed beams C100-15M-FJ and C100-20M-FJ to survive up to Blasts 4 and 5 (I_r = 681 and 821 kPa-ms), respectively. Both specimens showed flexural-dominant cracking patterns, characterized by the formation of many closely-spaced fine cracks, and fiber pullout at the dominant crack locations. Comparing the displacements at the common Blast 1 loading, C100-20M-FJ shows reductions of 69% and 38% in maximum and residual displacements when compared to C100-20M due to the increase in stiffness (see **Figure 5 - 9**). At Blast 2, C100-20M-FJ and C100-15M-FJ show low support rotations of 0.6-0.7°, and superficial damage, compared to the larger displacements/rotations and shear failures in C100-20M and C100-15M (see **Figure 5 - 11** and **Table 5 - 4**).

Overall, the results demonstrate that the UHPFRC jacketing allowed for considerable increases in capacity in the shear-deficient HSC beams under both static and blast loads. Provision of UHPFRC also changed the failure mode from shear to flexure, despite the lack of stirrups and varied shear demands. The improvements can be explained by the increased diagonal tension capacity of the UHPFRC and the ability of the fibers in the UHPFRC to control and arrest shear cracking. The next section studies the ability of the UHPFRC to improve flexural response.

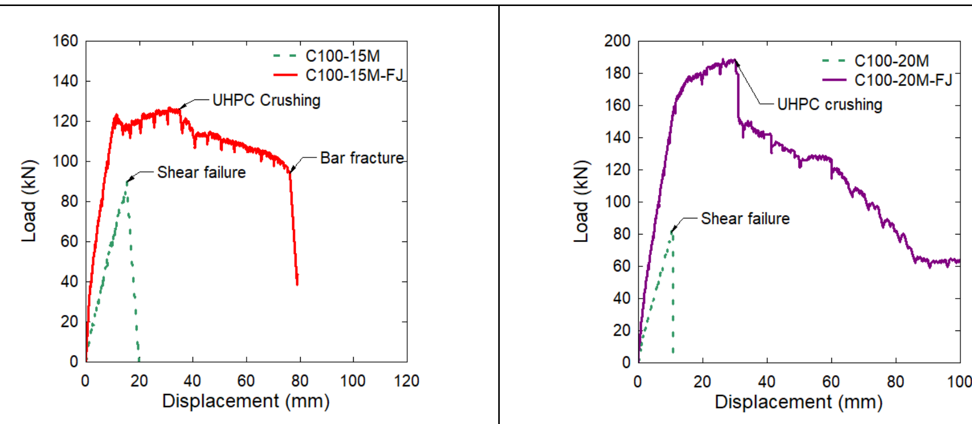

a) Effect of UHPFRC on shear response (15M)

b) Effect of UHPFRC on shear response (20M)

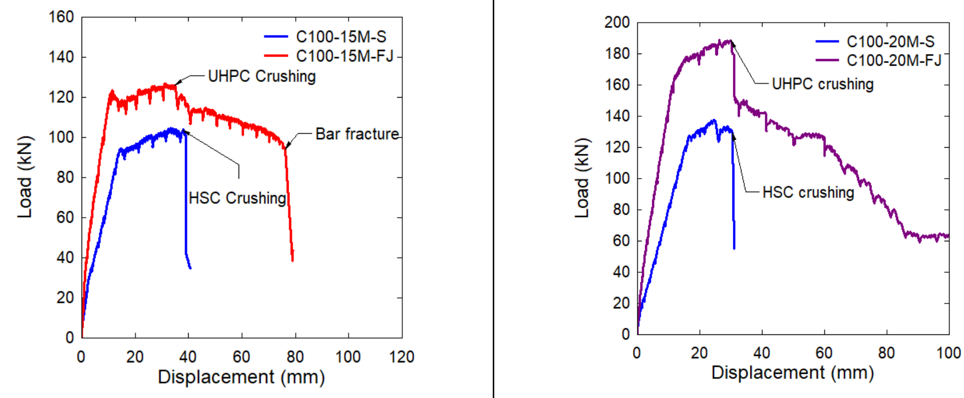

c) Effect of UHPFRC on flexural response (15M)

d) Effect of UHPFRC on flexural response (20M)

Figure 5 - 7 Static test results: effect of UHPFRC on shear and flexural response

15M beams (ρ =1.6%)	
C100-15M Δ=15.3 mm Failure: shear	
C100-15M-S Δ=40.7 mm Failure: Flexure (Concrete crushing)	
C100-15M-FJ Δ=79.1 mm Failure: Flexure (Bar fracture)	
20M beams (ρ =2.4%)	
C100-20M Δ=10.7 mm Failure: shear	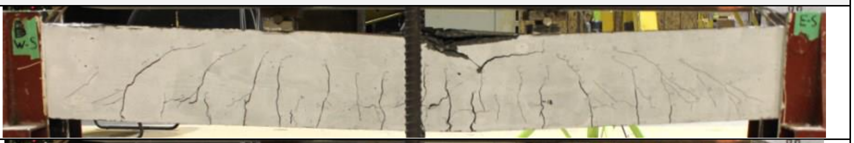
C100-20M-S Δ=31.0 mm Failure: Flexure (Concrete crushing)	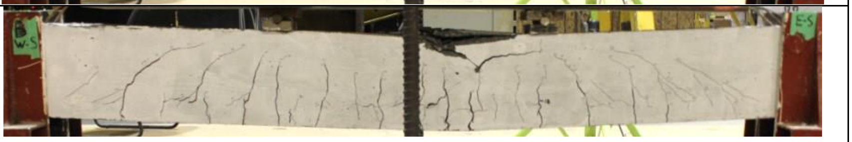
C100-20M-FJ Δ=146.3 mm Failure: Flexure (UHPC crushing)	

Figure 5 - 8 Failure modes in control and UHPFRC retrofit beams under static loading

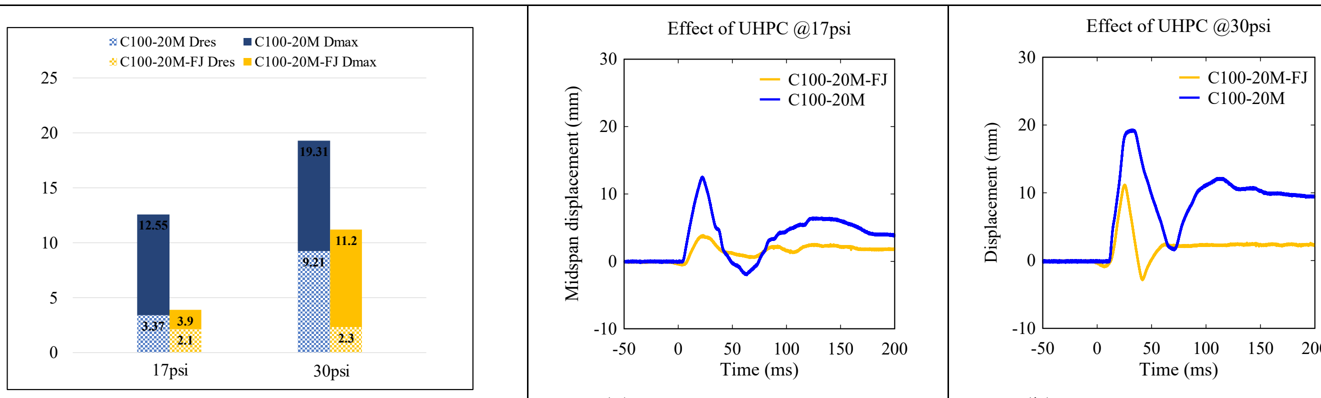

Maximum and residual displacements (all blasts)

(a) Blast 1 displacement-history

(b) Blast 2 displacement history

Figure 5 - 9 Effect of UHPFRC on displacements under blast loading (Shear)

5.4.4 Effect of UHPFRC on flexural response

The ability of UHPFRC to improve flexural response is examined by comparing the responses of control beams C100-15M-S and C100-20M-S, with longitudinal steel ratios of 1.6% and 2.4%, and companion beams C100-15M-FJ and C100-20M-FJ, which were strengthened with UHPFRC. To promote flexural failure, the control beams were built with stirrups in the shear spans.

As shown in **Figure 5 - 7(c-d)** and **Figure 5 - 8**, provision of stirrups in C100-15M-S and C100-20M-S allowed the beams to fail in flexure under static loading, with yield loads of 94.5kN and 118.2kN, maximum capacities of 105kN and 138kN, and ductility ratios of 2.62 and 2.03. Failure in the beams occurred due to concrete crushing in the midspan region.

In comparison, beams C100-15M-FJ and C100-20M-FJ recorded increased yield loads of 116kN and 159kN, maximum capacities of 127kN and 189kN, and ductility ratios of 7.27 and 2.79. Both beams failed in flexure but with distinct cracking patterns, consisting of many closely-spaced fine cracks and the formation one dominant crack prior to failure which occured due to bar fracture in C100-15M-FJ, and UHPFRC crushing in C100-20M-FJ.

Comparing the data, provision of UHPFRC in C100-15M-FJ resulted in increases of 85% in stiffness, 21% in peak capacity, and important increases of 177% and 85% in ductility and drift ratio. Likewise, C100-20M-FJ shows improvements of 79%, 37% and 37% in stiffness, peak capacity and ductility when compared to C100-20M-S. Examining the area under the curves, beams C100-15M-FJ and C100-20M-FJ show increases of 144% and 56% in toughness (A_{80}), with increased toughness indices (I_{80}) of 11.35 and 4.56.

The ability of UHPFRC to improve flexural response under blast loading is first studied by comparing the displacements in the companion beams at equivalent blasts in **Figure 5 - 10**. In the 15M set, the use of UHPFRC in C100-15M-FJ resulted in significant reductions of 66%, 37% and 76% in maximum displacements at Blasts 1, 2 and 3, respectively. The UHPFRC retrofitted specimen shows an obvious reduction of 67% in the rebound displacement at Blast 2, with a more pronounced reduction of 63% in the residual displacement at Blast 3.

Similar trends are observed in the 20M set, where C100-20M-FJ shows substantial reductions of 63%, 26% 39% and 65% in maximum displacements when compared to the control beam at Blasts 1, 2, 3 and 4, respectively. The UHPFRC strengthened beam also shows reductions of 100% and 88% in the residual displacements at Blasts 3 and 4.

Failure in the control beams C100-15M-S and C100-20M-S occurred at Blasts 3 and 4 (I_r = 516 and 703 kPa-ms) and was associated with maximum support rotations of 6.3° and 6.0°, which correspond to "Hazardous" damage according to the response limits in the CSA S850 Blast standard. Indeed, both beams failed by severe concrete crushing in the midspan region, with the development of significant blast fragments at failure (see **Figure 5 - 11**). In comparison, beams C100-15M-FJ and C100-20M-FJ resisted the corresponding blasts with low support rotations of 1.5° and 2.1°, limited damage and no blast fragments.

C100-15M-FJ survived up to Blast 4 (I_r = 681 kPa-ms), with a support rotation of 3.3°. The CSA S850 predicts "Heavy" damage, however the actual damage is limited to fiber pullout at the dominant crack location, and minor crushing of UHPFRC at midspan. Indeed, the beam further showed significant post-blast residual static capacity (P^R_{max}) of 130 kN, with residual resistance and stiffness indices (RRI and RSI) of 1.0 and 0.8 (see **Section 5.4.7**).

C100-20M-FJ resisted Blast 4 (I_r = 692 kPa-ms) with a support rotation of 2.1°, but experienced a considerable support rotation of 5.9° at Blast 5 (I_r = 821 kPa-ms). The CSA S850 standard predicts a "Hazardous" failure, however the beam was still standing after this test. Nonetheless the beam showed large widening of the dominant crack at midspan, with complete fiber pullout, and crushing of the UHPFRC cover in the compression zone. Indeed, the intense and repeated blasts nearly exhausted the beam's capacity, and the beam showed limited residual strength and stiffness during the post-blast static test, with RRI and RSI indices of 0.23 and 0.22 (see **Section 5.4.7**).

In summary, the results demonstrate that the UHPFRC jacketing allowed for important improvements in flexural response under both static and blast loading. Under quasi-static conditions the UHPFRC increased strength, stiffness, ductility and overall toughness. Under blast conditions, the UHPFRC allowed for better control of displacements at equivalent blasts, with significant enhancements in overall blast capacity. The high toughness of the UHPFRC also reduced damage and eliminated blast fragments, even under more intense blast loading.

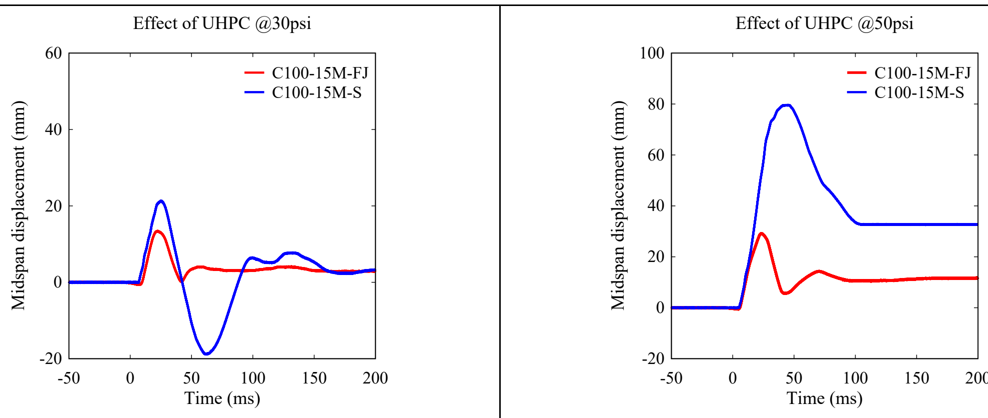

(a) Blast 2 (15M beams) (b) Blast 3 (15M beams)

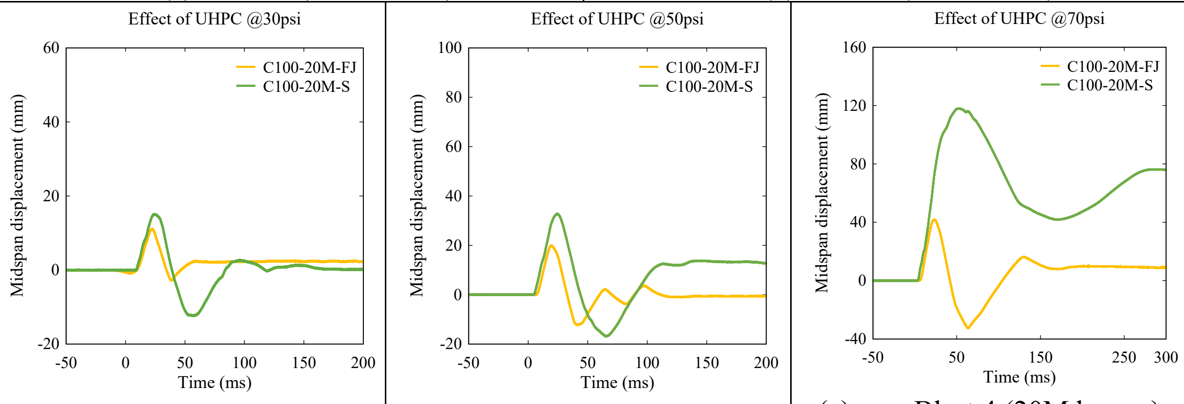

(c) Blast 2 (20M beams) (d) Blast 3 (20M beams) (e) Blast 4 (20M beams)

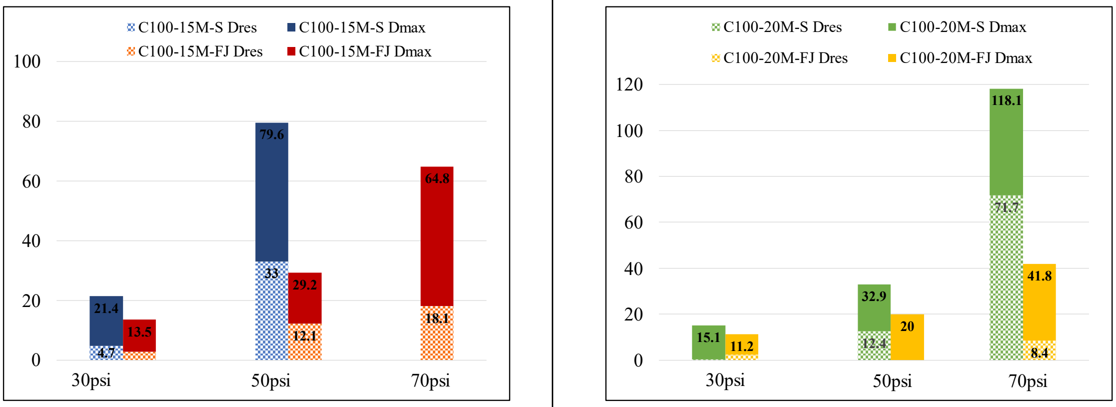

Maximum and residual displacements (15M beams – all blasts) Maximum and residual displacements (20M beams – all blasts)

Figure 5 - 10 Effect of UHPFRC on displacements under blast loading (Flexure)

C100-15M	C100-15M-S	C100-15M-FJ			
Blast 2 (30psi)	Blast 3 (50psi)	Blast 2 (30psi)	Blast 3 (50psi)	Blast 4 (70psi)	Close in view
					
C100-20M	C100-20M-S	C100-20M-FJ			
Blast 2 (30psi)	Blast 4 (70psi)	Blast 3 (50psi)	Blast 4 (70psi)	Blast 5 (90psi)	Close in view
		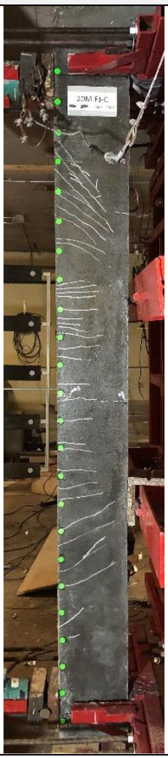			

Figure 5 - 11 Damage propagation and failure modes under blast loading

5.4.5 Effect of UHPFRC on damage tolerance and failure mode

As noted above, the use of UHPFRC jacketing and the provision of fibers had an important influence on damage tolerance under blast loading. **Figure 5 - 12** compares high speed video stills for the companion control and UHPFRC strengthened beams during the final blast tests. The photos show significant concrete crushing and spalling in the control beams at failure (C100-15M-S and C100-20M-S). The high speed stills further show the development of significant blast fragments as crushing and spalling occur in the HSC concrete. In comparison, the UHPFRC strengthened beams show limited damage in the compression zone, with tension damage limited to the formation of a dominant crack at midspan. Secondary blast fragments and flying debris can be a danger to building occupants during a blast event. The results show that the UHPFRC jacketing shows a remarkable ability to eliminate or reduce blast fragments, which can protect building occupants in the case of blast incident.

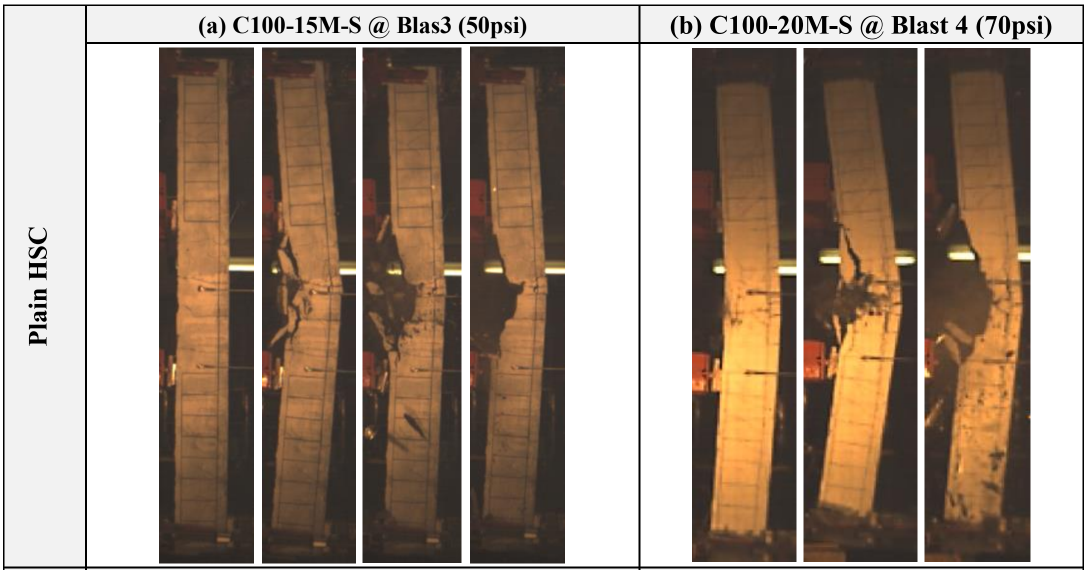

(a) C100-15M-S @ Blas3 (50psi) **(b) C100-20M-S @ Blast 4 (70psi)**

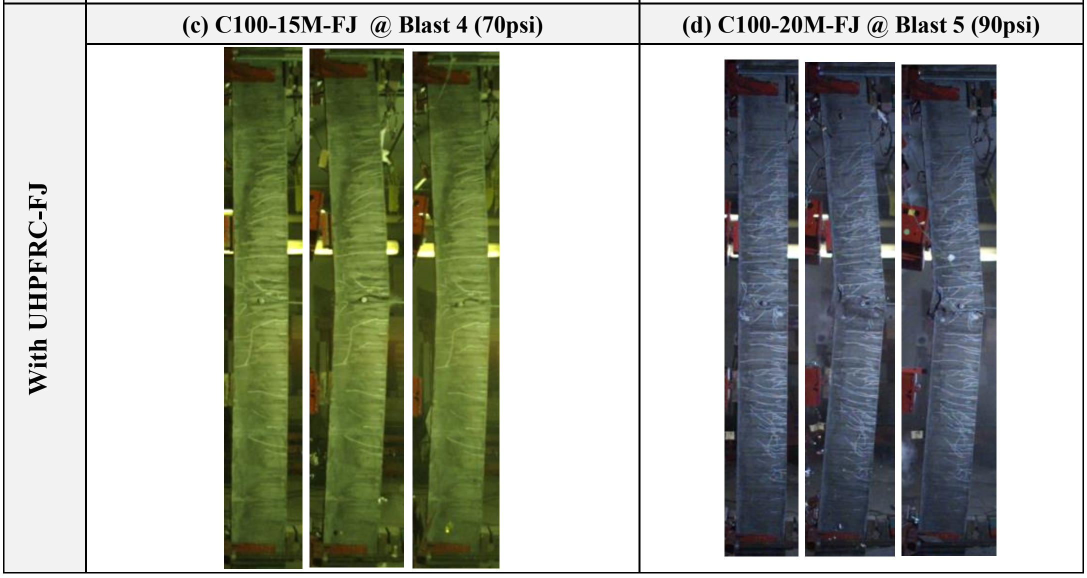

(c) C100-15M-FJ @ Blast 4 (70psi) **(d) C100-20M-FJ @ Blast 5 (90psi)**

Figure 5 - 12 High-speed stills showing the failure propagation in beams

5.4.6 Effect of tension steel ratio

The effect of longitudinal tension steel ratio (ρ) in the UHPFRC retrofit beams is studied by comparing the responses of beams C100-15M-FJ and C100-20M-FJ (ρ = 1.6% and 2.4%) under static and blast loading.

As shown in **Figure 5 - 13**, the tension steel ratio affected the load capacity, ductility and failure mode under static loading. As expected, increasing ρ from 1.6% to 2.4% resulted in a 49% increase in peak load capacity. The beam with increased steel ratio also shows a larger overall toughness A_{max}, when considering the entire area under the load-deflection curves, but reduced ductility (2.79 vs. 7.27), drift ratio (4.2% vs. 9.7%), and toughness index (I_{80} = 4.56 vs. 11.35). Both beams show similar cracking patterns, with multiple fine cracks, and the formation of a dominant crack which results in fiber pullout; however, the beam with reduced steel ratio fails by fracture of the tension steel reinforcement. As the steel ratio increases from 1.6% to 2.4%, the failure mode transitions from bar fracture in C100-15M-FJ, to UHPFRC crushing in C100-20M-FJ.

Under blast loading, increasing the tension steel ratio resulted in better control of displacements at equivalent blasts (see **Figure 5 - 14**). Both beams show similar responses under Blast 1 which tested the beams under elastic conditions, however C100-20M-FJ shows reductions of 17%, 32% and 35% in maximum displacements when compared to C100-15M-FJ at Blasts 2, 3 and 4. Likewise, increasing the tension steel ratio resulted in reduced residual displacements by margins of 18%, 100% and 54% at these same blasts. Testing of C100-15M-FJ ended at Blast 4 with the beam showing crack localization but limited damage in the compression zone (see **Figure 5 - 11**). The beam showed significant residual capacity during the post-blast static test, with an RRI index ≥ 1.0. Testing of C100-20M-FJ continued to Blast 5, which resulted in a maximum displacement of 116 mm, residual displacement of 77 mm, and a significant support rotation of 5.9°, with the beam retaining less than 25% of its initial capacity during the post-blast test (RRI = 0.23) (see **Section 5.4.7**).

No previous studies have examined the effects of steel ratio in UHPFRC strengthened beams or slabs. However, several studies indicate that bar fracture is a common failure mode in conventional UHPFRC beams, and is sensitive to the tension steel ratio. For example, Yoo et al. [14] tested a series of UHPFRC beams with ρ = 0.53% to 1.71%, with all the beams failing by bar fracture. Pokhrel and Bandelt [15] also reported bar fracture failures in beams having ρ = 0.7% to 1.9%, but noted that the increase in steel ratio delayed bar fracture. Shao and Billington [16] indicated that increasing the steel ratio from 0.96% to 2.1% led to a change in failure mode, from crack localization leading to steel fracture, to one of UHPFRC crushing prior to steel fracture, with the authors noting that a "*higher reinforcing ratio spread steel reinforcement plasticity across a longer length which delays steel fracture*". In the case of retrofitted beams, Safdar et al. [17] reported bar fracture failure, and a reduction in ductility, when applying tension side UHPFRC retrofits at or above the level of the tension steel in beams with ρ = 0.4%. The limited results from the current tests indicate that bar fracture may also occur when using UHPFRC jacketing, due to UHPFRC's high bond capacity, and the crack localization phenomenon. Further research is recommended.

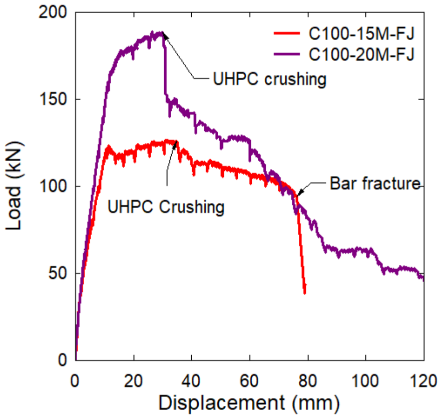

Figure 5 - 13 Static test results: effect of steel ratio in Retrofit beams

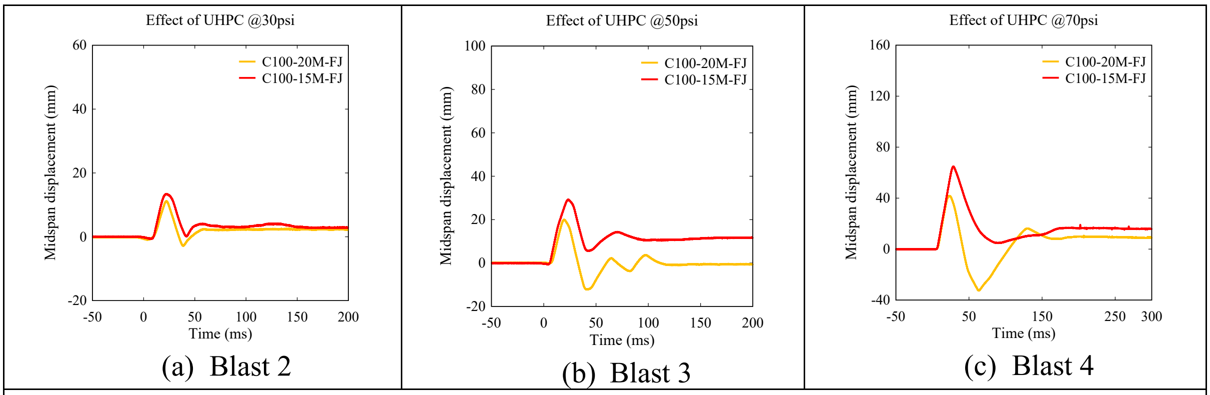

(a) Blast 2

(b) Blast 3

(c) Blast 4

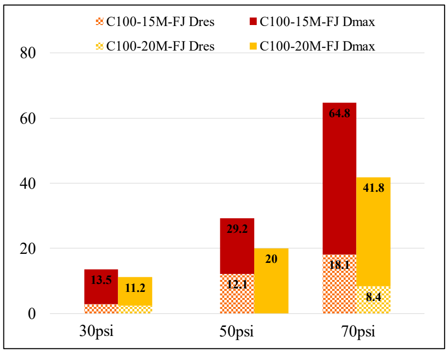

Maximum and residual displacements (all blasts)

Figure 5 - 14 Effect of steel ratio on displacements under blast loading

5.4.7 Results from post-blast residual static tests

The UHPFRC strengthened beams survived the blast tests and were tested under static loads to assess their post-blast residual capacity. A comparison of the undamaged and damaged beam responses under static four-point bending is presented in **Figure 5 - 15**. **Table 5 - 6** reports key parameters from the residual tests, including: P_{max}^{R} (peak residual resistance), k_s^R (residual stiffness), and several indices: RRI (residual resistance index), RSI (residual stiffness index) and TEI (total energy index).

Adhikary et al. [11] proposed the RRI and a damage index ($D = 1 - RRI$) to assess the residual capacity of impact-damaged beams and noted that the degree of damage caused by dynamic loading can be considered "low", "medium", "high" or "severe" if D < 0.2, D = 0.2-0.5, D = 0.5-0.8 or D = 0.8-1.0, respectively. Beam C100-15M-FJ which was tested to Blast 4, shows an RRI index > 1.0 and damage index of 0, which confirms the low damage in the UHPFRC strengthened beam, even after the repeated blast tests. The beam also shows an RSI of 0.81, which indicates the beam had high residual stiffness after blast testing. On the other hand, beam C100-20M-FJ which was tested to more intense loading up to Blast 5 had an RRI of 0.23, with a damage index of 0.77, which confirms the "high" damage sustained during the blast tests. The beam also shows very low residual stiffness with an RSI of 0.22.

Zanuy and Ulzurrun [12] proposed a "Total Energy Index" (TEI) to assess the failure mode and residual static performance of conventional RC beams after impact testing. As shown in **Figure 5 - 15**, $TEI = IEI + REI$, where IEI is calculated using the undamaged beam response (using the area ratio: $\frac{A}{A+B}$), and REI considers the energy absorbed during the residual test, and is calculated using the area ratio $\frac{C}{A+B}$. According to this study, a TEI of approximately 1.0 indicates the same ductility and failure mode for undamaged and damaged specimens, whereas a TEI < 0.85 indicates a change in failure mode in undamaged versus damaged beams. Examining the results, the blast-damaged C100-15M-FJ beam shows a TEI of ~ 1.0 which confirms that the beam showed similar energy-absorption capacity and ductility when compared to its undamaged companion. Conversely, C100-20M-FJ shows a TEI above 0.9 but low REI , which confirms the beam had low residual capacity but similar failure mode when compared to the undamaged test. The results confirm that the RRI, RSI and TEI are useful parameters that can be used to assess the residual capacity, stiffness and failure mode of blast-damaged beams strengthened with UHPFRC.

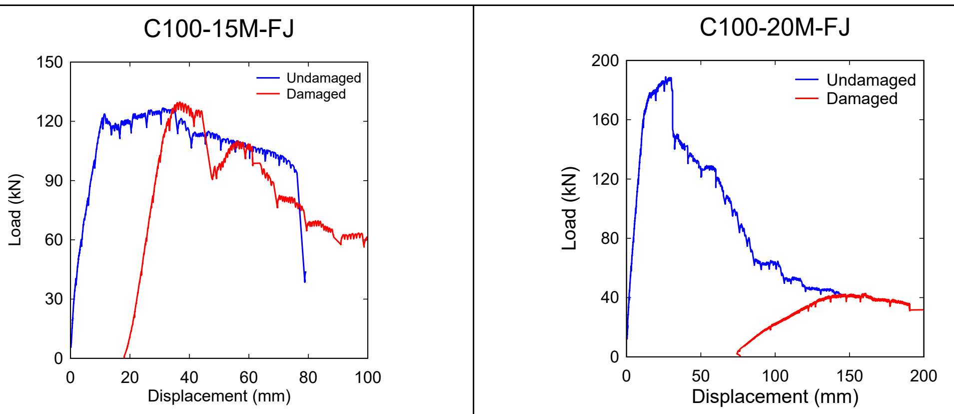

a) C100-15M-FJ **b) C100-20M-FJ**

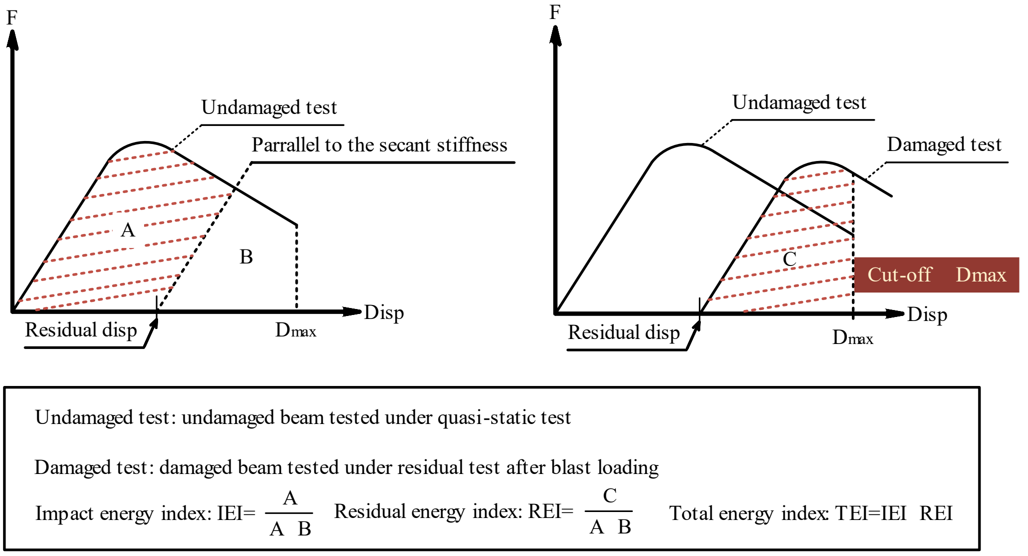

Undamaged test: undamaged beam tested under quasi-static test

Damaged test: damaged beam tested under residual test after blast loading

Impact energy index: IEI= $\frac{A}{A\quad B}$ Residual energy index: REI= $\frac{C}{A\quad B}$ Total energy index: TEI=IEI REI

c) Calculation of energy indices (IEI, REI and TEI)

Figure 5 - 15 Residual capacity and energy absorption resistance

5.4.8 Dynamic vs. static resistance

In this study, companion beams with identical properties were tested under static and blast loads using the same four-point bending configuration. In the blast tests, dynamic reactions were captured using two load cells at the supports, while the LVDT installed at the midspan captured the displacements. **Figure 5 - 16(a-b)** show the dynamic load displacement-histories for the retrofit beams, where the dynamic load corresponds to the sum of the load-cell readings after each blast.

Examining the results at the individual blasts, it can be observed that Blasts 1-2 tested both beams under elastic conditions, while the largest peak dynamic loads (P_{max}^{D}) were reached under Blast 4. The largest P_{max}^{D} value for beam C100-20M-FJ was found at Blast 4 prior to the final shot (Blast 5). The reduced dynamic strength at Blast 5 can be attributed to the significant damage in the beam which occurred at Blast 4, prior to the application of the final blast.

Figure 5 - 16(c-d) compares the static and dynamic load-displacement curves of beams C100-15M-FJ and C100-20M-FJ, where the dynamic curve is computed from the envelope of the results from all blasts. **Table 5 - 5** also reports the maximum dynamic loads (P_{max}^{D}), and toughness values (A_{max}^{D}) obtained from the envelope of the dynamic load-displacement curves which considers all blasts. Comparing to the static results, both specimens show higher maximum loads under dynamic loading when compared to static loading, with dynamic-to-static strength ratios (P_{max}^{D}/P_{max}^{s}) of ~ 1.44. Considering the control and retrofit beams, the dynamic strength ratios vary between 1.32-1.7 (see **Table 5 - 5**), which falls within the range of 1.04-1.8 previously reported by Magnusson et al. [18] for ultra-high strength concrete beams tested under impact loading. The increase in load capacity can be explained by the effects of increased strain-rates which increase the strengths of the concrete and steel reinforcement under blast loading [19], and due to the effect of dynamic loading which results in dynamic load factor (DLF).

The effects of the test parameters on the dynamic load-displacement curves are further studied in **Figure 5 - 16(e-f-g)**. Consistent with the static tests, the UHPFRC retrofitted beams in the 20M and 15M sets (C100-20M-FJ and C100-15M-FJ) show increased maximum loads (P_{max}^{D}) under dynamic loading when compared to the companion C100-20M-S and C100-15M-S beams (**Figure 5 - 16(e-f)**). The UHPFRC specimens further show enhancements in dynamic toughness (A_{max}^{D}), with increases of 200% and 73% for C100-20M-FJ and C100-15M-FJ when compared to C100-20M-S and C100-15M-S, which further confirms the ability of the

UHPFRC to enhance energy absorption under blast loading. Examining the effects of steel ratio (**Figure 5 - 16(g)**), the UHPFRC beam with 20M bars shows increased dynamic strength and toughness when compared to the companion with 15M bars, which also matches the observation in the static tests.

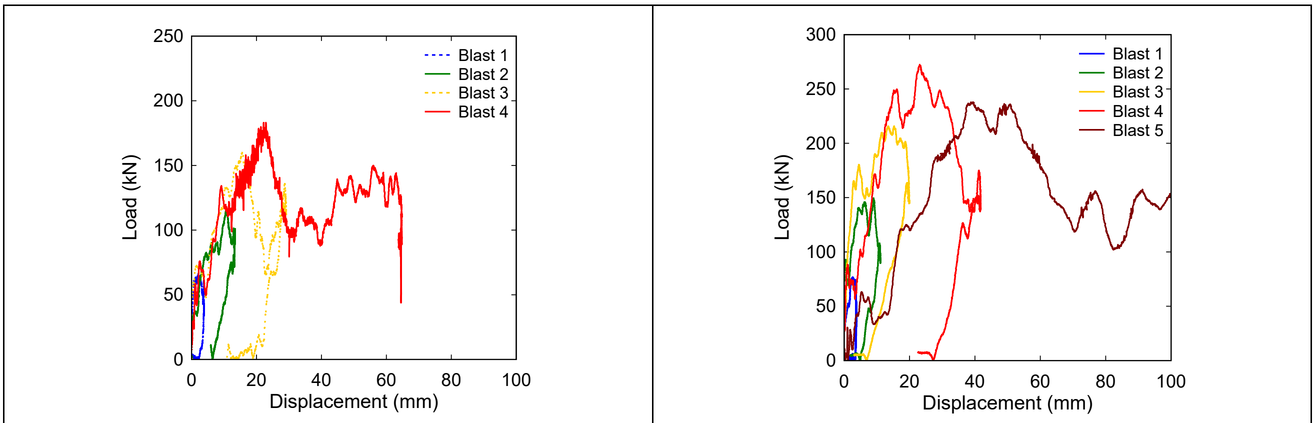

(a) Dynamic load-displacement: C100-15M-FJ (all blasts)

(b) Dynamic load-displacement: C100-20M-FJ (all blasts)

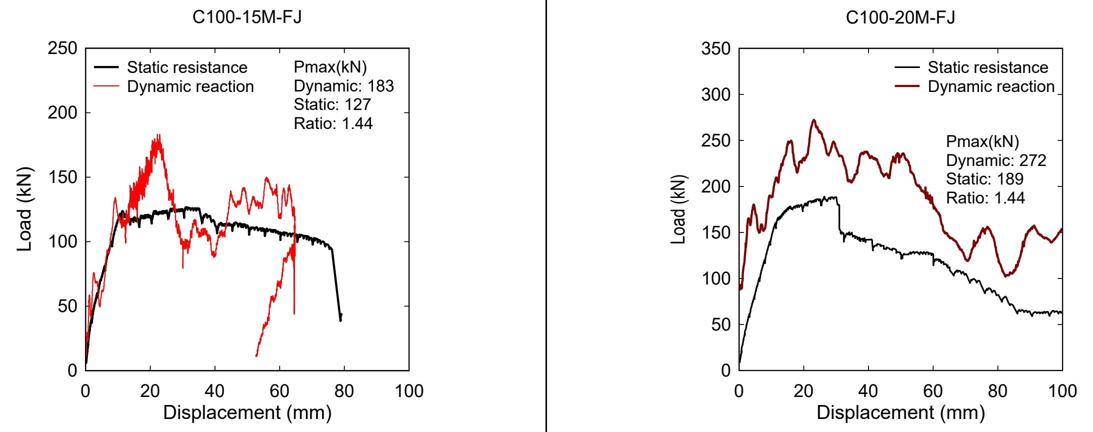

(c) Dynamic vs. Static resistance: C100-15M-FJ

(d) Dynamic vs. Static resistance: C100-20M-FJ

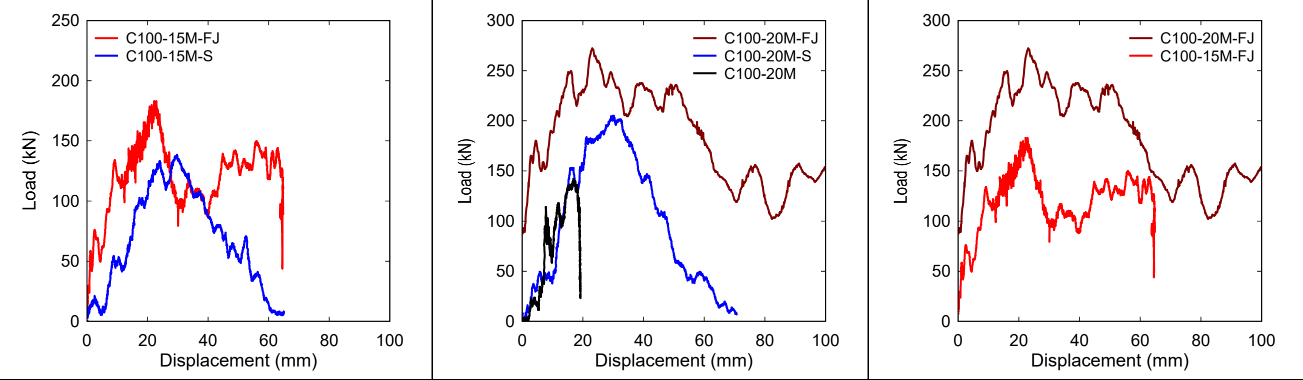

(e) Effect of UHPC (15M)

(f) Effect of UHPC (20M)

(g) Effect of steel ratio (retrofit beams)

Figure 5 - 16 Dynamic load-displacement curves (from dynamic reactions).

5.5 FE analysis

Finite element (FE) analysis was conducted to reproduce the blast response of the beams using LS-DYNA, a simulation software which is suitable for non-linear and transient dynamic analysis. The 3D model used in the FE simulations is shown in **Figure 5 - 17,** consisting of a beam, specimen, shock-tube load transfer device and support boundary conditions. Eight node solid hexahedron cube elements (**SECTION_SOLID*), with a mesh size of 10 × 10 × 10 mm were used to model the concrete elements, while two node Hughes-Liu beam elements (**SECTION_BEAM*), with size of 10 mm, were used to simulate the longitudinal and transverse reinforcement in the beams. Perfect bond and strain compatibility between the steel and concrete were assumed by keyword **CONSTRAINED_LAGRANGE_IN_SOLID* in LS-DYNA [20], and this coupling method provides the convenience of concrete meshing without considering the location of the embedded steel rebar. Perfect bond between the core HSC concrete and UHPFRC was assumed by sharing common nodes. **Figure 5 - 17(a)** shows a sample mesh for a typical UHPFRC retrofitted beam. The resulting mesh consisted of 80069 solid concrete elements, and 992 beam elements for the steel reinforcement. The load transfer device (LTD) was simulated by using shell elements (**SECTION_SHELL*) as shown in **Figure 5 - 17(b)**. To allow for free rotation, the side plates and middle portion of the LTD were connected by using keyword **CONSTRAINED_JOINT_SPHERICAL* [20]. In this study, the beams were simply supported, and hence, two steel plates (**SECTION_SOLID*) were built to support the specimen and allow the specimen to freely rotate while preventing translation (**BOUNDARY_SPC_SET*) as shown in **Figure 5 - 17(b)**). In addition, the **CONTACT_AUTOMATIC_SURFACE_TO_SURFACE* algorithm was utilized to simulate the contact between the concrete and load transfer device and that between the concrete and steel supports.

LS-DYNA features an extensive material model library [21], and the corresponding material models used in this investigation are listed in **Table 5 - 7**. The nonlinear behavior of high strength concrete (HSC) was modelled by using the continuous surface cap model (CSCM) which is designated as **MAT_CSCM_CONCRETE (159)* in LS-DYNA. The ability of this model to simulate concrete damage under blast or impact has been verified in several previous studies [22-24]. Rate effect formulations are implemented in the CSCM model and applied to the plasticity surface, damage surface and fracture energy [25]. For the case of concrete in direct tension and compression the rate effects were considered using the equations shown in

Table 5 - 7 [25, 26]. Due to its unique mechanical properties (e.g., superior compressive/tensile strength and toughness), UHPFRC cannot be directly modelled using the default parameters in the **MAT_CSCM (159)* model. Guo et. at [26] calibrated the parameters in the CSCM model for UHPFRC exposed to impact loading with consideration of strain rate effects. In the calibrated model, the TXC (Triaxial compression), TXE (Triaxial extension) and TOR (Torsion) failure surface functions were calibrated based on test data for UHPFRC, while the strain-rate parameters were modified based on experimental data in Fujikake et al. [27, 28]. Subsequently, this modified model was confirmed to provide sufficient accuracy for impact and blast simulations of UHPFRC structures [29-31] or UHPFRC strengthened members [32]. Therefore, the verified CSCM model was used in this study to capture the blast response of the UHPFRC retrofitted beams. As shown in **Figure 5 - 17(c)**, the model was well able to simulate the behaviour of the UHPFRC in compression when compared to the results from the experimental cylinder tests. Model **MAT_PLASTIC_KINEMATIC (003)* is well suited for steel reinforcement [33] and was employed to model the behavior of the longitudinal reinforcement in the beams. The model input parameters were determined using the stress-strain properties of the reinforcement obtained from the steel coupon tests (see **Figure 5 - 17(d)**), with rate effects assigned using the Cowper and Symonds model [34]. Blast loading on the beams, ranging from Blast 1 to 5 (17psi to 90psi), was applied on the load transfer device with the **LOAD_SEGMENT_SET* keycard in LS-DYNA. The blasts were approximated using idealized triangular pressure time histories generated from the positive phase of each shock wave. In this study, the effects of accumulated damage were considered by applying repeated blast loadings with a sufficient time gap between each loading [35] (see **Figure 5 - 17(e)**).

Table 5 - 7 Constitutive material models used in LS-DYNA

FE models	
High-strength Concrete: *MAT_CSCM_CONCRETE (159) (MAT_159) Default model parameters generated with f_c' based on cylinder tests	Ultra-high performance fiber reinforced concrete (UHPFRC): *MAT_CSCM (159) (MAT_159) Material properties determined by 45 input parameters using the calibrated values presented in Guo et al. [26]
DIF formulations for concrete in tension and compression: $DIF_t = f_{t,d}'/f_t' = 1 + E\dot{\varepsilon}\,\eta_{0t}/(f_t'\dot{\varepsilon}^{N_t})$ $DIF_c = f_{c,d}'/f_c' = 1 + E\dot{\varepsilon}\,\eta_{0t}/(f_c'\dot{\varepsilon}^{N_c})$	Rate effect parameters $\eta_{ot}, \eta_{oc}, N_t, N_c$ were updated based on the following expressions in Guo et al. [26] $\eta_{0t} = 0.7912\, f_t'/E,\ N_t = 0.7087$ $\eta_{0c} = 0.311\, f_c'/E,\ N_c = 0.7817$
Longitudinal steel: *MAT-PLASTIC_KINEMATIC (MAT_003) Mass density: 7800 kg/m^3 Poisson's ratio: 0.3 Young's modulus: 200 GPa Yield stress: varies – based on coupons Failure strain: varies – based on coupons DIF: Cowper & Symonds strain rate model which scales the yield stress with the factor $1 + (\frac{\dot{\varepsilon}}{C})^{\frac{1}{p}}$	

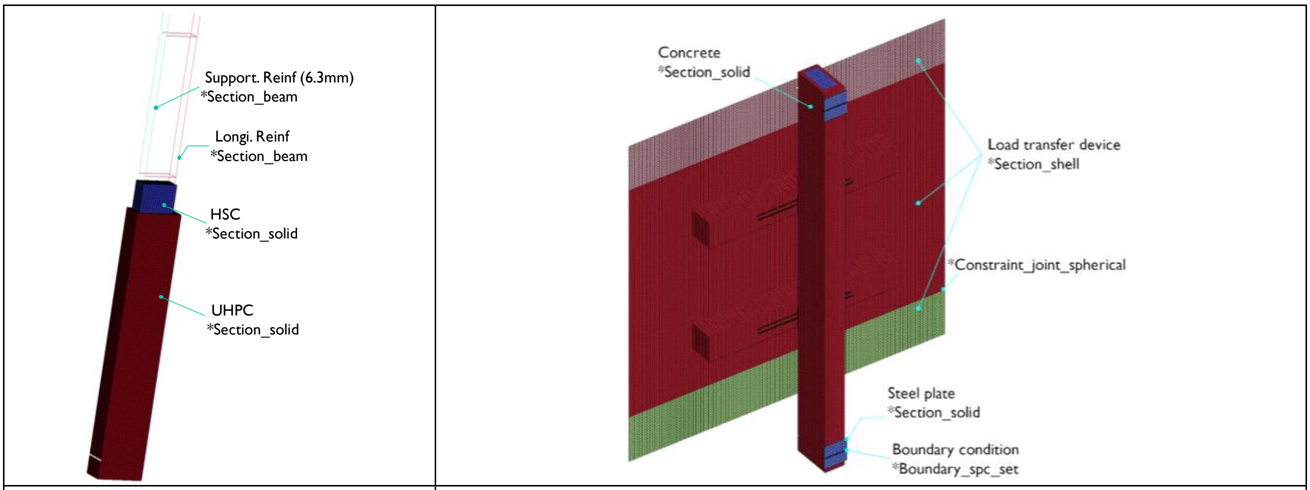

a) Concrete and steel meshing

b) 3D numerical models

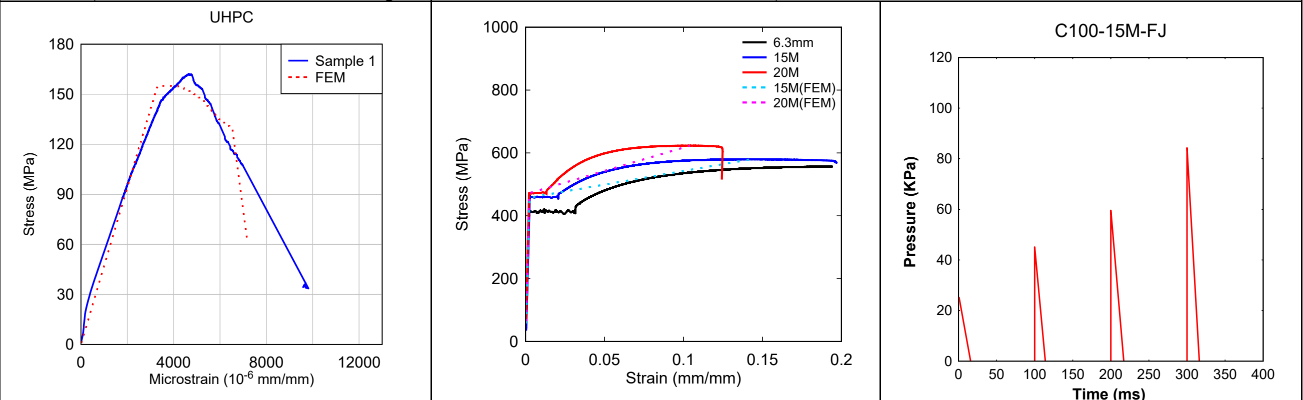

c) UHPFRC response under compression: FEM and experimental results

d) Steel stress-strain response: FEM and experimental results

e) Sequential blast pressures

Figure 5 - 17 FE modelling: 3D model, blast approximations and material models

5.5.1 Analysis results

The results from the numerical blast analyses are presented in **Table 5 - 8** and **Figure 5 - 18 & Figure 5 - 19**. **Table 5 - 8** compares the maximum displacements from the FE predictions (d_{num}) and experiments (d_{exp}) along with their ratio (d_{num}/d_{exp}). A comparison of the displacements is also represented in **Figure 5 - 18**, which also presents sample displacement time-histories. Considering all beams and all blast tests, the numerical predictions showed an average d_{num}/d_{exp} ratio of 0.88, with an average absolute error of 21%, and coefficient of variation of 29.6%. Considering the individual blasts, the average d_{num}/d_{exp} ratios were 1.04, 0.89, 0.83 and 0.92 for Blasts 1, 2, 3 and 4, respectively. In general, the numerical predictions for the maximum displacements show reasonable agreement with the experimental results. **Figure 5 - 19** presents a comparison of damage patterns and failure modes for the control and retrofit beams in the 15M and 20M groups. The FE simulations correctly predict shear failure in the two control beams (C100-15M and C100-20M) with failure patterns which closely matches the experimental results. The FE simulation of beam C100-15M-FJ shows that shear failure was avoided at Blast 2, with similar flexural damage patterns at Blasts 3-4 when compared to the experiments. Concrete crushing is well controlled, and crack localization at midspan is detected, which coincides with the experimental result. Likewise, the ability of UHPFRC to prevent shear failure and promote flexural response is also well predicted in beam C100-20M-FJ. Overall, reasonably good agreement was obtained between the FE simulations and experimental tests in terms of displacement response, damage patterns and failure modes.

Table 5 - 8 Blast analysis results

Beam ID	Shot #	Blast ID	Idealized Shockwave Properties [1]			Midspan Displacements [2]			
			P_r	I_r	t_d	d_{exp}	d_{num}	d_{num}/d_{exp}	Error%
			(kPa)	(kPa·msec)	(msec)	(mm)	(mm)		
C100-15M	1	Blast 2[3]	35.9	324	19.4	16.1	18.9	1.17	17%
C100-20M	1	Blast 1	23.9	240	20.0	12.5	8.0	0.64	36%
	2	Blast 2	38.7	371	19.2	19.3	17.0	0.88	12%
C100-15M-FJ	1	Blast 1	26.4	210	15.9	3.9	4.7	1.21	20%
	2	Blast 2	45.1	315	14.0	13.5	9.0	0.67	33%
	3	Blast 3	59.6	507	17.0	29.2	21.0	0.72	28%
	4	Blast 4	84.3	681	16.2	64.8	45.0	0.69	30%
C100-20M-FJ	1	Blast 1	26.6	216	16.3	3.9	4.4	1.13	13%
	2	Blast 2	46.3	342	14.8	11.2	10.9	0.97	3%
	3	Blast 3	58.9	521	17.7	20.0	18.6	0.93	7%
	4	Blast 4	77	692	18.0	41.8	44.6	1.07	7%
	5	Blast 5	85.3	821	19.2	116.3	60.0	0.52	48%
Statistical analysis			**d_{num}/d_{exp}**		**Overall**	**Blast 1**	**Blast 2**	**Blast 3**	**Blast 4**
FE analysis			**Mean**		0.88	1.04	0.89	0.83	0.92
			Standard deviation		0.26	0.23	0.19	0.11	0.19
			Coefficient of variation		29.6%	22.29%	21.05%	12.73%	21.11%

[1] P_r = Reflected pressure; I_r = Reflected impulse; t_d = Idealized positive phase duration = $2\times I_r / P_r$;

[2] d_{max} = experimental mid-span displacement; d_{num}= numerical mid-span displacement.

[3] No Blast 1 applied to this specimen

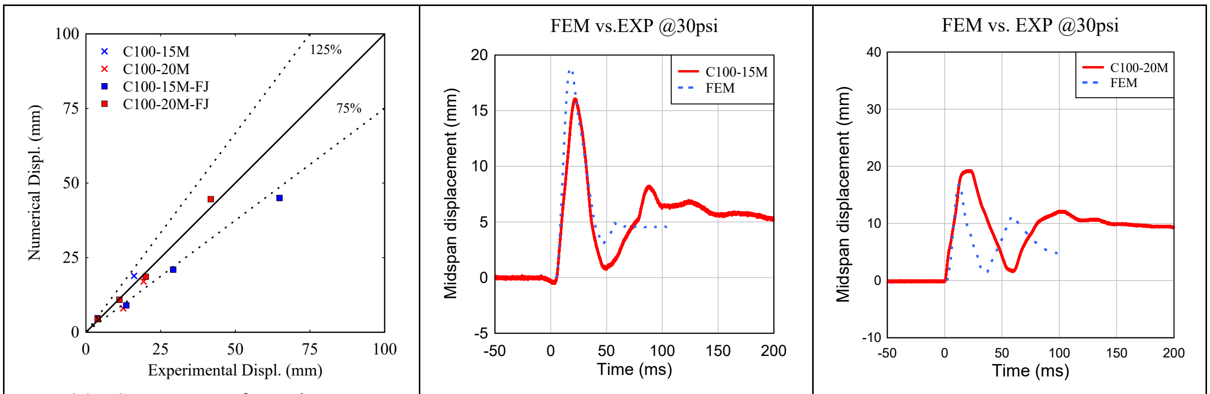

(a) Summary of results (b) C100-15M at Blast 2 (c) C100-20M at Blast 2

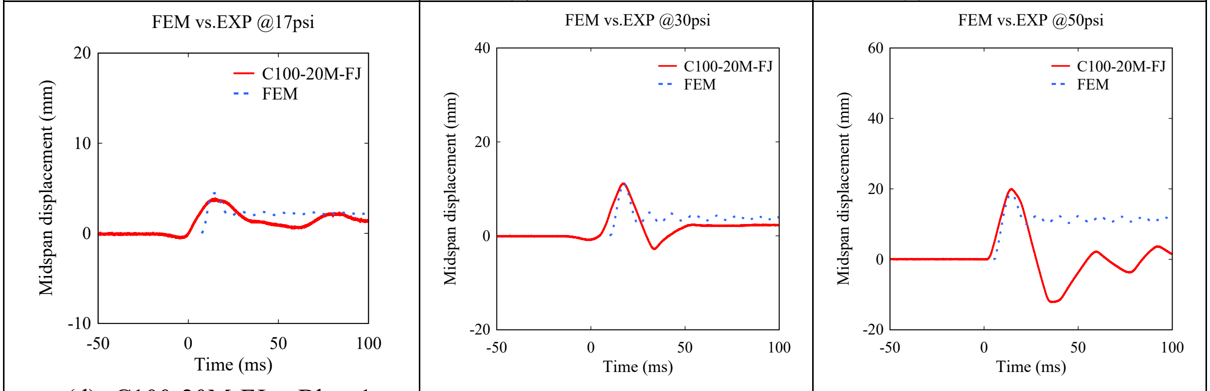

(d) C100-20M-FJ at Blast 1 (e) C100-20M-FJ at Blast 2 (f) C100-20M-FJ at Blast 3

Figure 5 - 18 Comparison of numerical and experimental displacements under blast loading

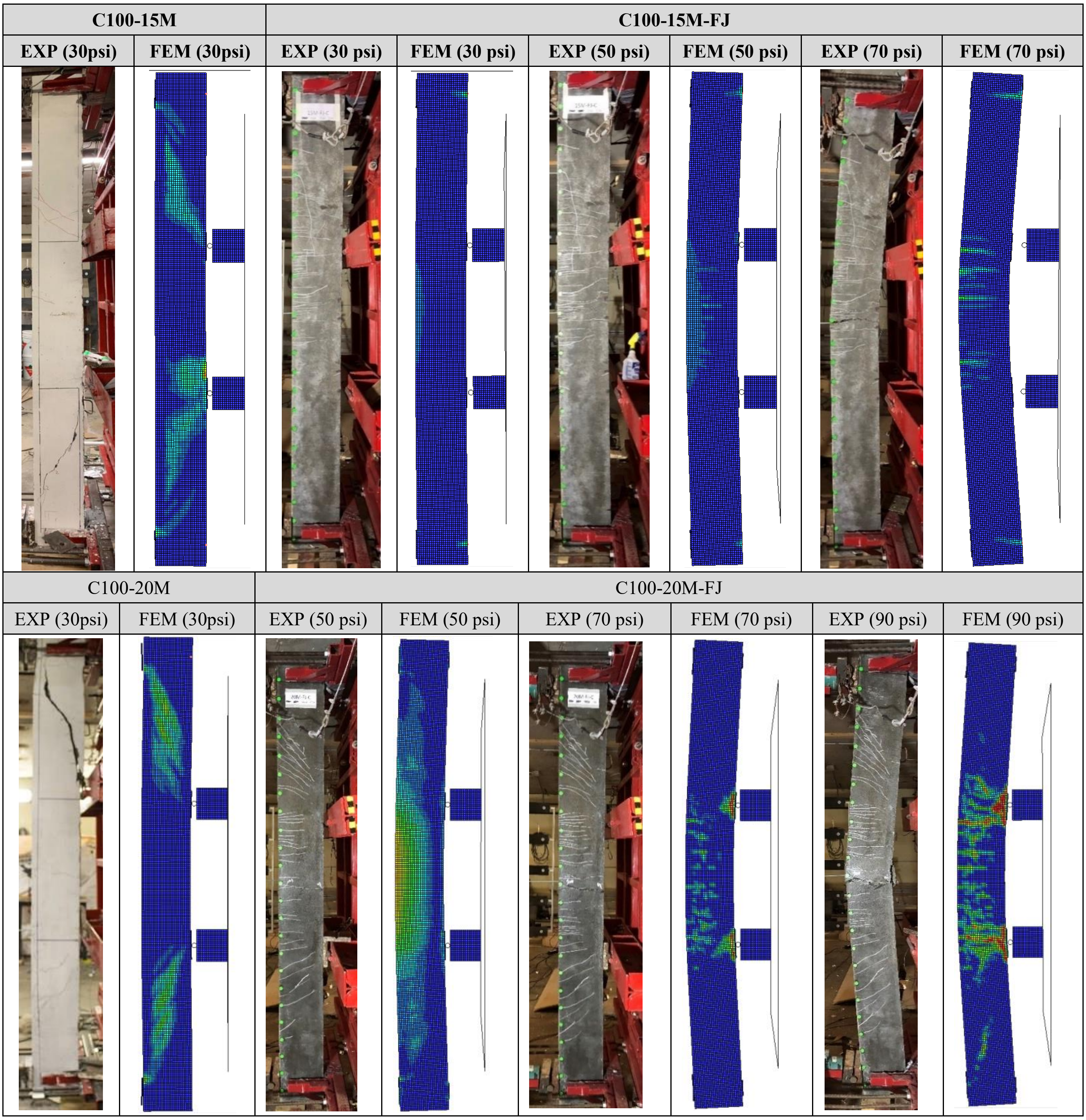

Figure 5 - 19 Comparison of experimental and numerical damage under blast loading

5.6 Conclusions

This paper studied the ability of UHPFRC jacketing to improve the shear and flexural response of shear-deficient high-strength concrete beams under static four-point bending and shock-tube blast loading. The following conclusions can be drawn from this study:

(1) The use of UHPFRC jacketing improved the shear behaviour of the high-strength concrete beams under both static and blast conditions. The application of UHPFRC not only improved shear capacity, but also allowed the beams to fail in flexure and avoid brittle shear failure under both static and blast loads;

(2) The use of UHPFRC jacketing also improved flexural behaviour under static loading by increasing the stiffness, load capacity, ductility ratio and energy absorption capacity when compared to companion HSC beams built with stirrups;

(3) Under blast loading, the use of UHPFRC jacketing resulted in improved control of displacements at equivalent blasts, and an increase in overall blast capacity when compared to the companion HSC beams built with stirrups. The use of UHPFRC further resulted in improved control of damage (crushing and spalling) and reduced the amount of secondary blast fragments even under intense blast loading;

(4) Under static loading, the failure mode of the UHPFRC retrofitted beams was affected by the tension steel ratio, with the failure transitioning from bar-fracture to UHPFRC crushing in the beams with 15M and 20M bars respectively. While bar fracture was not observed in the blast tests, this failure mode should be considered when applying UHPFRC jacketing, especially in beams with smaller steel bar sizes or steel ratios due to the crack localization phenomenon and the high bond capacity of the UHPFRC;

(5) Comparison of the dynamic and static load-displacement curves showed an increased in peak load in the retrofit beams under dynamic loading due to the effects of increased strain-rates. The retrofit beams also showed larger dynamic reactions when compared to the companion control HSC beams;

(6) FE analysis was conducted to reproduce the blast response of test beams using LS-DYNA. The numerical simulations showed a reasonable ability to predict the maximum displacements of the control and retrofit beams with an average d_{num}/d_{exp} ratio of 0.88 when considering all blasts. Importantly the FE modelling was able to capture the failure modes and damage patterns in the control and UHPFRC retrofitted specimens.

References

[1] Brühwiler E. UHPFRC is Ready to Revolutionize Existing and New Structures. IABSE Symposium Prague 2022: IABSE; 2022. p. 67-79.

[2] Hung C-C, El-Tawil S, Chao S-H. A Review of Developments and Challenges for UHPC in Structural Engineering: Behavior, Analysis, and Design. Journal of Structural Engineering. 2021;147.

[3] Brühwiler E, Denarié E. Rehabilitation and Strengthening of Concrete Structures Using Ultra-High Performance Fibre Reinforced Concrete. Structural Engineering International. 2018;23:450-7.

[4] Ullah R, Qiang Y, Ahmad J, Vatin NI, El-Shorbagy MA. Ultra-High-Performance Concrete (UHPC): A State-of-the-Art Review. Materials (Basel). 2022;15.

[5] Yoo D-Y, Banthia N. Mechanical properties of ultra-high-performance fiber-reinforced concrete: A review. Cement and Concrete Composites. 2016;73:267-80.

[6] Zhu Y, Zhang Y, Hussein HH, Chen G. Flexural strengthening of reinforced concrete beams or slabs using ultra-high performance concrete (UHPC): A state of the art review. Engineering Structures. 2020;205.

[7] Algassem O. Parameters affecting the blast performance of high strength fibre reinforced concrete beams: University of Ottawa; 2016.

[8] ICRI. ICRI Standard 310.2 Selecting and Specifying Concrete Surface Preparation for Sealers, Coatings, Polymer Overlays, and Concrete Repair with CSP Chips. 2013.

[9] Lloyd A, Jacques E, M S, Palermo D, Nistor I, Tikka T. Capabilities of a Shock Tube to Simulate Blast Loading on Structures. ACI SP-281: Behaviour of concrete structures subjected to blast and impact loadings. 2011:1-20.

[10] Jacques E. Characteristics of Reinforced Concrete Bond at High Strain Rates: University of Ottawa; 2016.

[11] Adhikary SD, Li B, Fujikake K. Residual resistance of impact-damaged reinforced concrete beams. Magazine of Concrete Research. 2015;67:364-78.

[12] Zanuy C, Ulzurrun GSD. Residual behavior of reinforced steel fiber-reinforced concrete beams damaged by impact. Structural Concrete. 2018;20:597-613.

[13] Bastami R. Structural performance of high-strength reinforced concrete beams build with synthetic fibers: University of Ottawa; 2019.

[14] Yoo D-Y, Banthia N, Yoon Y-S. Experimental and numerical study on flexural behavior of ultra-high-performance fiber-reinforced concrete beams with low reinforcement ratios. Canadian Journal of Civil Engineering. 2016;44:18-28.

[15] Pokhrel M, Bandelt MJ. Material properties and structural characteristics influencing deformation capacity and plasticity in reinforced ductile cement-based composite structural components. Composite Structures. 2019;224:111013.

[16] Shao Y, Billington SL. Impact of cyclic loading on longitudinally-reinforced UHPC flexural members with different fiber volumes and reinforcing ratios. Engineering Structures. 2021;241:112454.

[17] Safdar M, Matsumoto T, Kakuma K. Flexural behavior of reinforced concrete beams repaired with ultra-high performance fiber reinforced concrete (UHPFRC). Composite Structures. 2016;157:448-60.

[18] Magnusson J, Hallgren M, Ansell A. Air-blast-loaded, high-strength concrete beams. Part I: Experimental investigation. Magazine of Concrete Research. 2010;62:127-36.

[19] Zhang L, S. M. Dynamic compressive toughness of high strength fiber reinforced concrete. ACI Spec Publ. 2011;281:1–21.

[20] LSTC. LS-DYNA Keyword User's Manual. California: Livermore Software Technology Corporation (LSTC); 2018.

[21] Hallquist JO. LS-DYNA theory manual. 2006.

[22] Gholipour G, Zhang C, Mousavi AA. Loading rate effects on the responses of simply supported RC beams subjected to the combination of impact and blast loads. Engineering Structures. 2019;201:109837.

[23] Li RW, Zhou DY, Wu H. Experimental and numerical study on impact resistance of RC bridge piers under lateral impact loading. Engineering Failure Analysis. 2019:104319.

[24] Zhang C, Gholipour G, Mousavi AA. Nonlinear dynamic behavior of simply-supported RC beams subjected to combined impact-blast loading. Engineering Structures. 2019;181:124-42.

[25] Murray YD. Users Manual for LS-DYNA Concrete Material Model 159. Cambridge, MA: Federal Highway Administration; 2007.

[26] Guo W, Fan W, Shao XD, Shen DJ, Chen BS. Constitutive model of ultra-high-performance fiber-reinforced concrete for low-velocity impact simulations. Composite Structures. 2018;185:307-26.
[27] Fujikake K, Uebayashi K, Ohno T, Shimoyama Y, M K. Dynamic properties of steel fiber reinforced mortar under high-rates of loadings and triaxial stress states. Structures Under Shock and Impact VII. 2002:437-46.
[28] Fujikake K, Senga T, Ueda N, Ohno T, M. K. Effects of strain rate on tensile behavior of reactive powder concrete. Journal of Advanced Concrete Technology. 2006;4:79-84.
[29] Fan W, Guo W, Sun Y, Chen BS, Shao XD. Experimental and numerical investigations of a novel steel-UHPFRC composite fender for bridge protection in vessel collisions. Ocean Engineering. 2018;165:1-21.
[30] Fan W, Shen D, Zhang Z, Huang X, Shao X. A novel UHPFRC-based protective structure for bridge columns against vehicle collisions: Experiment, simulation, and optimization. Engineering Structures. 2020;207:110247.
[31] Wang W, Wu C, Li J, Liu Z, Lv Y. Behavior of ultra-high performance fiber-reinforced concrete (UHPFRC) filled steel tubular members under lateral impact loading. International Journal of Impact Engineering. 2019:103314.
[32] Gholipour G, Muntasir Billah AHM. Nonlinear Analysis of Shear-Deficient Beams Strengthened Using UHPFRC under Combined Impact and Blast Loads. Journal of Structural Engineering. 2022;148.
[33] Li J, Wu CQ. Damage evaluation of ultra-high performance concrete columns after blast loads. International Journal of Protective Structures. 2018;9:44-64.
[34] Cowper G, Symonds P. Strain-hardening and strain-rate effects in the impact loading of cantilever beams. Brown Univ. Applied Mathematics Report; 1957. p. 28.
[35] Hammoud A. Blast Behavior of Columns Built with High-Strength Concrete and Grade 690 MPa High-Strength Reinforcement 2019.

Chapter 6: Effect of Retrofit Type on the Blast Performance and Failure mode of HSC beams Retrofitted with UHPFRC

Paper 3: extracted from dynamic results in series 1 (submitted to journal- "Engineering Failure Analysis")

Abstract

This primary objective of this paper was to investigate the effects of various ultra-high performance fiber reinforced concrete (UHPFRC) retrofits on the blast performance of beams built with high-strength concrete (HSC). As part of the tests, seven singly-reinforced HSC beams were tested under blast loads using a shock-tube. Three UHPFRC retrofit types were considered in the tests; a Tension-sided layer, U-jackets and full-jackets (T, UJ and FJ). The UJ and FJ retrofits were considered in five shear-deficient beams which did not contain stirrups, and which had 15M or 20M bars (steel ratios of 1.6% and 2.4%). T-sided and FJ retrofitting were applied in flexural-dominant beams built with stirrups and 20M bars. In addition to the effect of retrofit type, the influence of roughening (substrate preparation) method was also studied. In general, the use of UJ and FJ jacketing was shown to prevent shear failure in the beams which did not contain stirrups, while the increase in member strength and stiffness led to reduced displacements and an increase in blast resistance to comparable control (unstrengthened) HSC beams built with stirrups. Both retrofits showed similar performance, however, optimal performance was obtained when using full-jacketing. In the beams with stirrups, both the T-sided and FJ retrofits reduced blast-induced displacements, however the use of full-jacketing was better able to control damage and increase blast capacity. The roughening was found to play a limited role on blast behaviour of the retrofitted beams.

Keywords: Blast, UHPFRC, Beams, Retrofit type, Roughening method, Shock-tube.

6.1 Introduction

Recently ultra-high performance fiber-reinforced concrete (UHPFRC) has been proposed as a novel material to rehabilitate and strengthen existing concrete structures. Indeed, the technique of shear and flexural strengthening of reinforced concrete (RC) beams with UHPFRC is well established in several experimental studies [1-12]. A review reveals three common forms of strengthening, including: tension-sided bonded layer (T), U-jackets (UJ) or full-jackets (FJ). In these tests, UHPFRC was shown to increase shear capacity and flexural resistance in both shear-deficient [1-5] and flexural-dominant beams [6-12], with the performance affected by retrofit type/configuration, overlay/jacket thickness, roughening/bonding/casting method.

Among these tests, Lampropoulos et al. [6] studied the effects of T-sided and UJ overlays and noted that the three-sided UJ scheme resulted in the greatest increase in moment capacity and overall structural performance. Al-Osta et al. [7] presented a series of experiments on beams strengthened using three UHPFRC overlay schemes (T-sided, two-sided and UJ); all techniques were found to increase stiffness and load capacity, however the UJ scheme showed the highest strength enhancement, but with an unfavorable reduction in ductility. Yuan et al. [1] presented further tests on RC beams with various "no-slump high-strength high-ductility concrete" retrofit schemes (T-sided, UJ and FJ) and noted superior performance for the UJ and FJ retrofits in terms of stiffness, strength, ductility and ability to change the failure from shear to flexure in the as-built beams.

The remarkable properties of UHPFRC, also make it an ideal material to enhance the impact and blast resistance of existing concrete structures [13-17]. Indeed, a few studies confirm the ability of UHPFRC strengthening to improve the behaviour of RC columns [13, 14], beams [15, 16] and slabs [17] under impact loading. Among them, Fan et al. [13] demonstrated the superior crash-worthiness of axially-loaded UHPFRC-jacketed columns under low-velocity impact loads using three retrofit schemes ("middle", "two-ends" and their combination), with the "two-end" scheme proving to be most effective. Lee et al. [14] further verified the ability of UHPFRC jacketing to enhance the resistance, damage tolerance and displacement control of axially-loaded RC columns with seismic detailing under both drop-weight impact and shock-tube blast loads. A few other studies [15-17] also confirm the ability of T-sided UHPFRC bonded overlays to improve shear resistance of beams and slabs, also under impact loading.

However, data on the blast behaviour of UHPFRC-retrofitted RC beams is scarce. Moreover, no previous studies have characterized and compared the effects of retrofit type (T, UJ and FJ) on blast resistance. The ability of such retrofits to improve both shear and flexural resistance of higher-strength concrete has also not been investigated. Finally, the effect of substrate roughening method on blast performance also requires further study.

Accordingly, this paper presents specifically studies the influence of UHPFRC retrofit type and roughening method on the blast resistance of both shear-deficient and flexural-dominant RC beams retrofitted with UHPFRC. Various retrofit schemes (T, UJ and FJ) are considered in beams with different steel ratios, and with and without shear reinforcement. The results are compared to companion unstrengthened beams built which are also built with and without shear reinforcement. The effect of the substrate concrete surface profile (CSP) is considered by using two roughening methods. The results are compared in terms of displacement response, damage, blast capacity and post-blast resistance.

6.2 Experimental Program

6.2.1 Specimen designs

This chapter presents the results from seven UHPFRC-strengthened HSC beams. **Table 6 - 1** and **Figure 6 - 1** present the specimen designs, beam dimensions and retrofit details. All beams had dimensions of 125 × 250 × 2440 mm. The bottom tension reinforcement consisted of either 2-15M or 2-20M bars, corresponding to steel ratios (ρ) of 1.6% or 2.4%. Except for two beams, the specimens were built with stirrups. When present, the transverse reinforcement consisted of stirrups made from 6.3mm wire, spaced at s = 100mm in the shear spans.

All beams were first cast with plain high-strength concrete (HSC), and then strengthened by replacing the existing concrete cover with UHPFRC. Three retrofit types were considered: a bonded overlay applied on the tension-side (T), and jacketing applied in the form of U- or full-jacketing (UJ and FJ). The substrate concrete was prepared using a pneumatic bush-hammer (BH) or point-chisel (PC). After strengthening, the UHPFRC was 41 mm thick on the bottom face, and 20 mm thick on the top and side faces when present.

The seven beams can be divided into two groups. The **15M group** included two beams without stirrups, strengthened with UJ or FJ retrofits. Both roughening methods were used (BH and PC for the UJ and FJ beams, respectively). The **20M group** included five beams. The first three beams did not contain stirrups and were strengthened with UJ or FJ retrofits. Both roughening types were considered in the FJ specimens, while the bush-hammer was used in the

UJ beam. The remaining two beams contained stirrups and were strengthened with T-sided or FJ retrofits. The substrate concrete in both beams was roughened using a bush-hammer.

To study the ability of UHPFRC to improve flexural and shear response, the results are compared to blast tests from four unstrengthened HSC beams [18]. This **control group** included HSC beams with 15M or 20M bars, and included specimens with or without stirrups.

The beam nomenclature in **Table 6 - 1** reflects the substrate concrete type (C100 to designate 100MPa HSC), longitudinal bar size (15M or 20M), UHPFRC retrofit type (UJ, FJ or T), roughening method (BH: bush hammer, null: point-chisel), and whether the beam contains stirrups (S: for the beams with stirrups). For example, C100-20M-FJ-BH had 20M bars, no stirrups, and was strengthened with full-jacketing, applied after BH-roughening. C100-20M-S-FJ-BH had the same characteristics but contained stirrups. C100-15M and C100-20M are the controls without stirrups, while C100-15M-S and C100-20M-S are the controls with stirrups.

Table 6 - 1 Beam test matrix

Group	Beam I.D.	HSC beam properties			UHPFRC f'_c(MPa)	Retrofit	Test type
		f'_c(MPa)	Longitudinal reinforcement	Transverse reinforcement			
Retrofits 15M Group	**C100-15M-UJ-BH**	110	2- 15M	None	164	UJ	Blast
	C100-15M-FJ	99	2- 15M	None	164	FJ	Blast
Retrofits 20M Group	**C100-20M-UJ-BH**	102	2- 20M	None	164	UJ	Blast
	C100-20M-FJ-BH	102	2- 20M	None	164	FJ	Blast
	C100-20M-FJ	101	2- 20M	None	164	FJ	Blast
	C100-20M-S-T-BH	109	2- 20M	Stirrups at s = 100 mm	164	T-sided	Blast
	C100-20M-S-FJ-BH	109	2- 20M		164	FJ	Blast
Control 15M Group	C100-15M	104	2- 15M	None	-	-	Blast
	C100-15M-S	95	2- 15M	Stirrups at s = 100 mm	-	-	Blast
Control 20M Group	C100-20M	110	2- 20M	None	-	-	Blast
	C100-20M-S	106	2- 20M	Stirrups at s = 100 mm	-	-	Blast

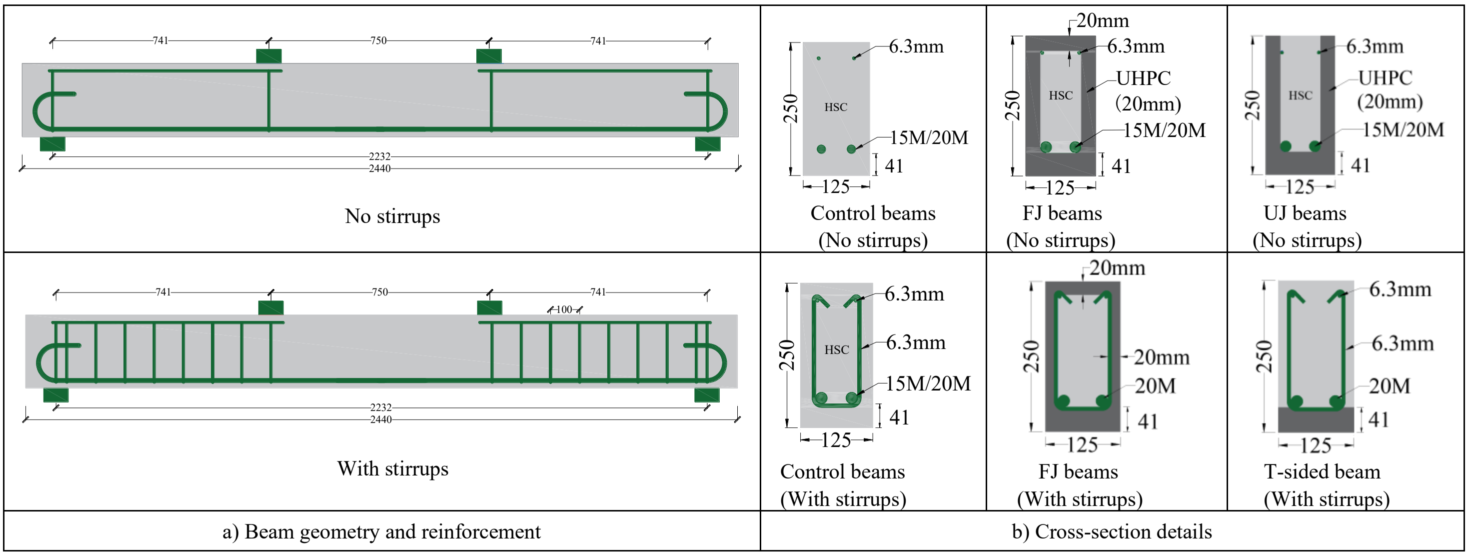

a) Beam geometry and reinforcement

b) Cross-section details

Figure 6 - 1 Beam geometry and reinforcement detailing

6.2.2 Material Parameters

As noted above, all retrofitted beams were first cast with plain high-strength concrete. The same mix was also used in the control specimens. The components for this concrete included cement, slag, silica fume, sand, two sizes of coarse aggregate (10 and 19 mm), a super-plasticizer and set retarder. The proprietary UHPFRC components included a dry premix, steel fibers, and three types of liquid admixtures. The straight steel fibers had a length of 13 mm, diameter of 0.2 mm, tensile strength of 2850 MPa, and were added a volumetric ratio of 2.5% (195 kg/m^3). Both concrete types were mixed using a pan-mixer at the University of Ottawa.

The properties of the UHPFRC in compression and flexure were determined by testing standard cylinders (75×150mm) and prisms (75×75×285mm) according to ASTM C1856. The properties of the HSC in compression were determined from standard cylinders (100 × 200 mm) tested according to ASTM C39. Sample results from these material tests are presented in **Figure 6 - 2(a-b)**, while the average strength of the UHPFRC/HSC at the time of the blast tests is reported in **Table 6 - 1**. The steel properties were determined by testing standard steel coupons in tension according to ASTM A615 and sample results from these tests are shown in **Figure 6 - 2(c)**.

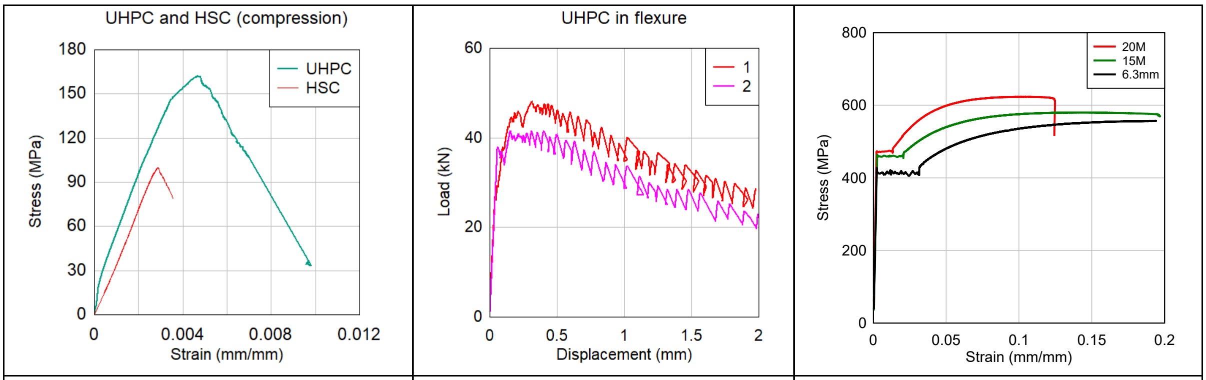

a) UHPFRC and HSC (compression) b) UHPFRC (flexure) c) steel reinforcement (tension)

Figure 6 - 2 Material properties

6.2.3 Specimen preparation

The construction of the test beams included several stages which are illustrated in **Figure 6 - 3**. The first stage consisted of building the steel cages and casting the beams with HSC concrete. After the concrete reached a minimum strength of 50 MPa, the cover in the retrofit zone was removed using a pneumatic bush-hammer or point-chisel to produce concrete surface profiles of approximately CSP6 and CSP10, respectively [19]. Then, the roughened substrate surface was moistened, followed by UHPFRC strengthening. After construction the beams were moist-cured for 7 days, followed by curing under ambient lab conditions until the day of testing.

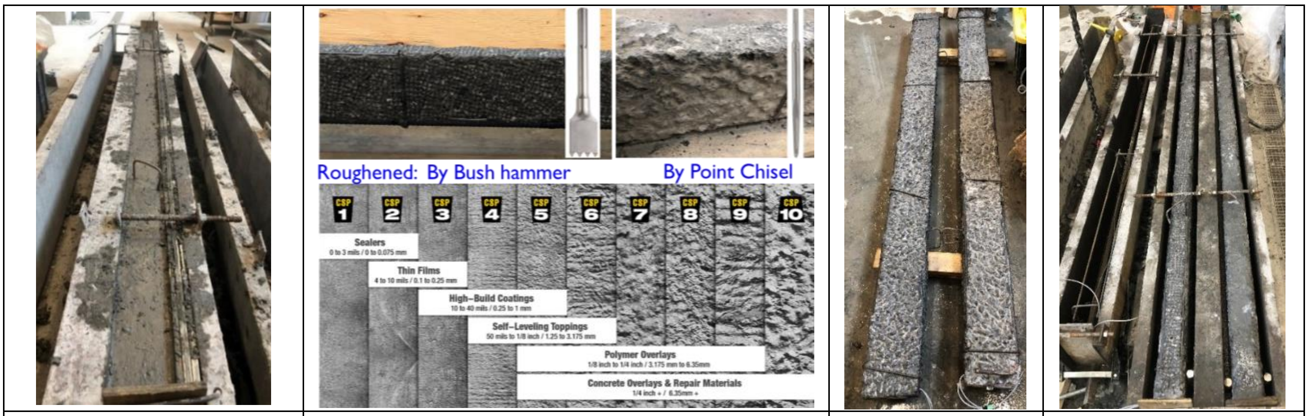

a) Casting of HSC concrete b) Interface preparation c) Moistening d) UHPFRC casting

Figure 6 - 3 Casting and retrofit procedure

6.2.4 Test setup and instrumentation

The blast tests were conducted using the University of Ottawa shock-tube and four-point bending setup shown in **Figure 6 - 4**. The pressure-driven shock-tube includes four main components [20]: (1) a variable-length driver section which produce the blast energy, (2) a spool section which triggers the shockwave, (3) an expansion section which ensures the formation of a uniform shock front, and (4) a rigid end frame with a 2 m × 2 m opening where specimens are attached (see **Figure 6 - 4(a)**). A load-transfer device (LTD), consisting of a set of steel panels with sliding hinges and a loading beam, was used to transfer the blast pressure onto the specimens in a four-point bending configuration (see **Figure 6 - 4(b)**). The beams were tested over a clear span of 2232 mm and were connected to the shock-tube using support assemblies which resulted in simple boundary conditions [21]. Data recorded during the tests included reflected pressure and displacement-time histories, captured using two piezoelectric pressure sensors and a midspan LVDT, respectively. The displaced shape during each test was also captured using two high-speed cameras at 2000 frames/second. In addition, dynamic reactions were recorded using load-cells which were attached to the support assemblies.

To allow for comparison with the control specimens, the beams were tested under repeated blast loads. Blasts 1, 2 and 3/4/5 were intended to test the beams under elastic, yield and ultimate conditions, respectively. All blasts used a constant shock-tube driver length of 2743 mm (9ft) and gradually increasing driver pressures (P_d) which varied between 117 and 620 kPa (17 and 90 psi). The average parameters which define each blast are reported in **Table 6 - 2**, while sample pressure-time histories for each test are shown in **Figure 6 - 4(c)**.

In the control set, C100-15M and C100-20M failed in shear at Blast 2, while C100-15M-S and C100-20M-S failed in flexure due to concrete crushing at Blasts 3 and 4, respectively. The retrofit beams with 15M and 20M survived up to the end of Blasts 4 and 5, respectively, and were subsequently tested under static four-point bending using the setup shown in **Figure 6 - 5** to assess their residual capacity.

Table 6 - 2 Blast test sequence (average properties)

Test sequence	Driver Length mm (ft)	Driver Pressure kPa (psi)	Avg. Reflected Impulse (I_r) kPa-ms	Avg. Reflected Pressure (P_r) kPa	Avg. Positive Phase Duration (t_p) ms
Blast 1	2743 (9)	117 (17)	213	26.5	16.1
Blast 2	2743 (9)	207 (30)	328	45.7	14.4
Blast 3	2743 (9)	345 (50)	514	59.3	17.4
Blast 4	2743 (9)	482 (70)	686	80.7	17.1
Blast 5	2743 (9)	620 (90)	821	85.3	19.2

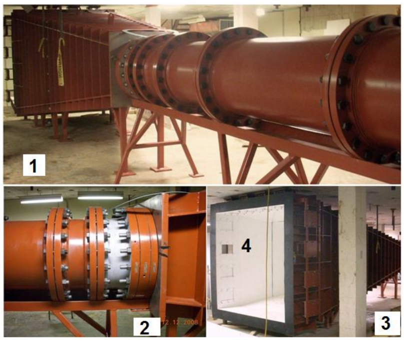

(a) Shock-tube components

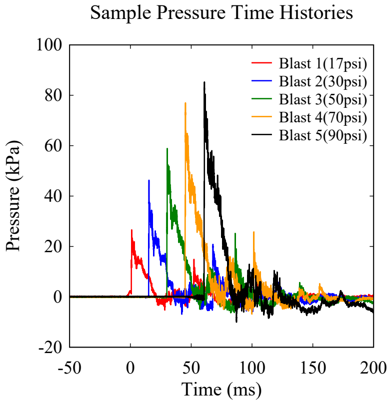

(c) Blast testing sequence

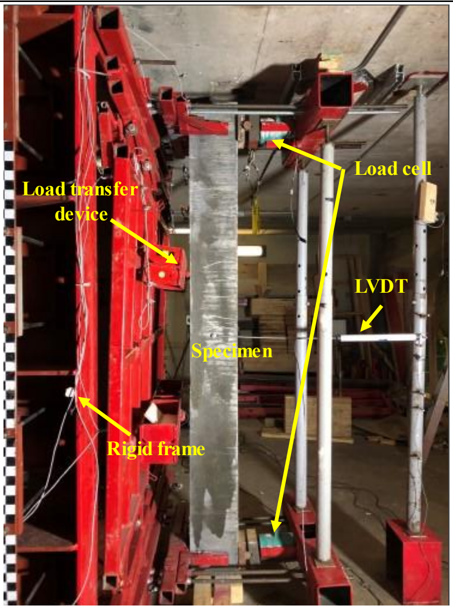

(b) Blast test setup

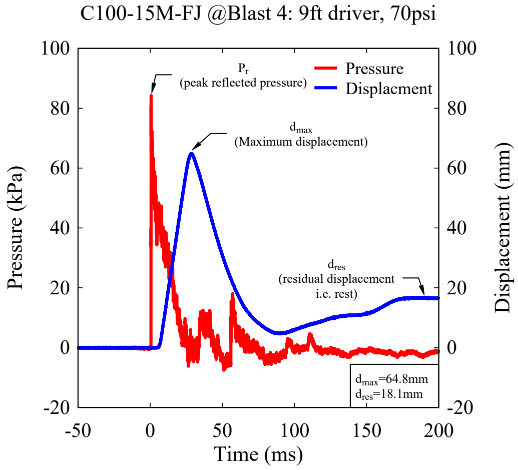

(d) Blast shockwave and response parameters

Figure 6 - 4 Details of the dynamic test setup and blast testing parameters

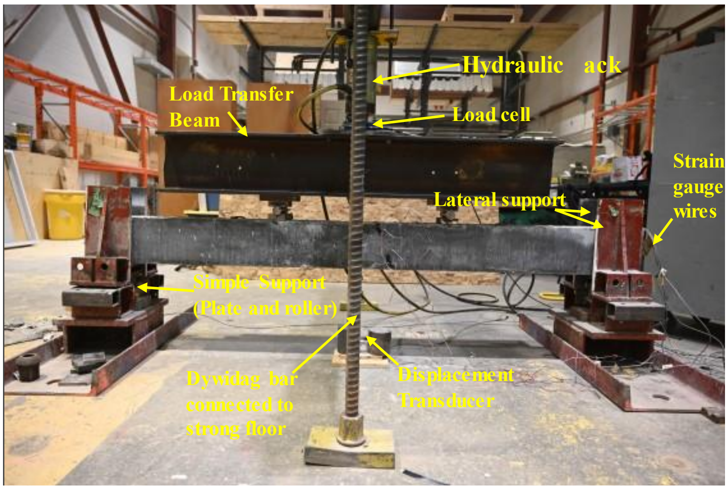

Figure 6 - 5 Four point bending static test setup (Post blast tests)

6.3 Experimental Results

6.3.1 Summary of results from the blast tests

Table 6 - 3 presents detailed data from the blast tests, including: the peak reflected pressure (P_r), positive phase duration (t_d), reflected impulse over the positive phase (I_r), maximum displacement (d_{max}), residual displacement (d_{res}) and the maximum support rotation (θ_{max}) after each test. A sample pressure and displacement time history for one test is shown in **Figure 6 - 4(d)**. The following sections discuss the results from the blast tests.

Table 6 - 3 Blast test results

Specimen ID [a]	Blast ID	Blast Loading (9ft)	P_r (kPa)	t_d (ms)	I_r (kPa·ms)	d_{max} (mm)	d_{res} (mm)	θ_{max} (°)	CSA S850 Damage [b]	Failure mode
C100-15M (Control)	2	30psi	35.9	19.4	323.6	16.1	5.5	0.8	(shear)	Brittle (shear)
C100-20M (Control)	1	17psi	23.9	20.0	239.5	12.6	3.4	0.6	Superficial	Brittle (shear)
	2	30psi	38.7	19.2	370.8	19.3	9.2	1.0	(shear)	
C100-15M-S (Control)	1	17psi	23. 9	18. 7	223	11.5	2.7	0.6	Superficial	Ductile (crushing)
	2	30psi	42.9	15. 9	340.7	21.4	4.7	1.1	Moderate	
	3	50psi	58.6	17.6	516	79.6	33	4	Heavy	
C100-20M-S (Control)	1	17psi	23.6	20.7	244.3	10.4	2.0	0.5	Superficial	Ductile (crushing)
	2	30psi	39.2	18.4	360	15.1	0.2	0.8	Superficial	
	3	50psi	57.4	18.8	538.2	32.9	12.4	1.7	Moderate	
	4	70psi	68.8	20.4	702.6	118.1	71.7	6.0	Hazardous	
C100-15M-UJ-BH	1	17psi	25.6	16.6	212.7	7.4	2.4	0.4	Superficial	Ductile (fiber pullout)
	2	30psi	44.1	15	330.1	13.7	2.0	0.7	Superficial	
	3	50psi	56.3	18.4	519.1	25.5	3.5	1.3	Moderate	
	4	70psi	65.2	21.6	703.1	75.1	46.3	3.8	Heavy	
C100-15M-FJ	1	17psi	26.4	15.9	209.9	3.9	0	0.2	Superficial	Ductile (fiber pullout)
	2	30psi	45.1	14.0	315.2	13.5	2.8	0.7	Superficial	
	3	50psi	59.6	17	506.8	29.2	12.1	1.5	Moderate	
	4	70psi	84.3	16.2	681.0	64.8	18.1	3.3	Heavy	
C100-20M-FJ	1	17psi	26.6	16.3	216.4	3.9	2.1	0.2	Superficial	Ductile (fiber pullout)
	2	30psi	46.3	14.8	341.6	11.2	2.3	0.6	Superficial	
	3	50psi	58.9	17.7	521.3	20	0	1.0	Moderate	
	4	70psi	77	18	691.7	41.8	8.4	2.1	Heavy	
	5	90psi	85.3	19.2	820.7	116.3	76.7	5.9	Hazardous	
C100-20M-UJ-BH	1	17psi	28.8	14.7	211	7.9	0.4	0.4	Superficial	Ductile (crushing)
	2	30psi	48	13.3	319.6	12.6	2.8	0.6	Superficial	
	3	50psi	64.8	15.6	504.1	18	3.3	0.9	Superficial	
	4	70psi	77.8	17.7	688.9	27.7	0	1.4	Moderate	
	5	90psi	106	16.3	864.9	105	60.4	5.4	Hazardous	
C100-20M-FJ-BH	1	17psi	28.2	15	211.5	5.7	1.8	0.3	Superficial	Ductile (mild crushing)
	2	30psi	48.4	13.8	334.1	13.9	2.3	0.7	Superficial	
	3	50psi	61.7	16.6	513.5	19.6	4.2	1.0	Moderate	
	4	70psi	78.1	17.9	699.9	25.5	5.1	1.3	Moderate	
	5	90psi	89.9	19.9	896.4	44.9	12.9	2.3	Heavy	
C100-20M-S-T-BH	1	17psi	25.1	17	213.6	6.8	1.9	0.3	Superficial	Fragmentation
	2	30psi	41.1	16.1	330.5	13.7	3.6	0.7	Superficial	
	3	50psi	61.8	16.6	512.2	20.8	2.6	1.1	Moderate	
	4	70psi	68.1	19.5	665.1	53.2	17.0	2.7	Heavy	
C100-20M-S-FJ-BH	1	17psi	31.1	13.9	215.9	5.8	1.1	0.3	Superficial	Ductile (crushing)
	2	30psi	43	15.5	332.2	12.2	3.5	0.6	Superficial	
	3	50psi	59	17.6	520.6	17.2	2.0	0.9	Superficial	
	4	70psi	70.8	18.3	649.4	25.9	0	1.3	Moderate	
	5	90psi	85.4	20	853	74.9	37.7	3.8	Heavy	

Note: P_r= Reflected pressure; I_r = Reflected impulse; t_d = positive phase duration; d_{max}= maximum displacement; d_{res}= residual displacement; θ_{max}= maximum support rotation.

[a] Control beams tested by Bastami [22] and Algassem [18].

[b] CSA S850 response limits: In the case of singly-reinforced beams, *B1*, *B2*, *B3* and *B4* correspond to ductility ratio of $\mu_{max} = 1$, and support rotations of $\theta_{max} = 2°$, $\theta_{max} = 5°$, and $\theta_{max} = 10°$, respectively, which define component damage levels: *"Blowout"* (greater than *B4*), *"Hazardous failure"* (between *B4* and *B3*); *"Heavy"* (between *B3* and *B2*); *"Moderate"* (between *B2* and *B1*) and *"Superficial"* (less than *B1*).

6.3.2 Effect of UHPFRC in the 15M group (no stirrups)

The ability of UHPFRC to improve shear behaviour under blast loads is first examined in the 15M group by comparing the results of the UHPFRC-strengthened beams with UJ and FJ jacketing (C100-15M-UJ-BH and C100-15M-FJ) and the companion control beams with and without shear reinforcement (C100-15M-S and C100-15M). In this comparison, stirrups were only provided in the C100-15M-S beam. BH and PC roughening were used in the UJ and FJ beams, respectively. The displacement and damage results are compared in **Figure 6 - 6** and **Figure 6 - 7**.

As expected, the control C100-15M beam failed abruptly in shear at Blast 2 (I_r = 336 kPa-ms) due to the lack of transverse reinforcement, while the provision of stirrups in C100-15M-S delayed failure in flexure to Blast 3 (I_r = 517 kPa-ms). Both retrofit beams (C100-15M-UJ-BH and C100-15M-FJ) survived to the end of Blast 4 (I_r = 685 kPa-ms), demonstrating the ability of the UHPFRC jacketing to prevent shear failure and increase blast resistance.

In addition to promoting flexural response, the UHPFRC retrofits reduced displacements due to the increase in member stiffness. Comparing to the control with stirrups (C100-15M-S), the beam with the UJ retrofit (C100-15M-UJ-BH) shows reductions of 36%, 36% and 68% in maximum displacements (d_{max}) at Blasts 1, 2 and 3. Likewise, the retrofitted beam shows declines of 11%, 57% and 89% in residual displacements (d_{res}) when compared to the same control during these tests. In a similar way, the beam with FJ jacketing (C100-15M-FJ) shows important reductions of 66%-37%-63% and 100%-40%-63% in d_{max} and d_{res} displacements at these same blasts.

Failure in the control C100-15M-S beam was associated with a support rotation (θ_{max}) of 4.1° at Blast 3, which coincides with "Heavy" component damage in the CSA S850 Blast standard [23]. Indeed, the beam failed by severe concrete crushing in the midspan zone, with the development of significant blast fragments at failure (see **Figure 6 - 7**). In comparison, beams C100-15M-UJ-BH and C100-15M-FJ resisted this blast with support rotations of 1.3° and 1.5°, and limited damage consisting of multiple fine cracks and the formation of single dominant cracks at midspan (with widths of 3mm and 5mm, respectively). Under further Blast 4 loading these beams showed rotations of 3.8° and 3.3°. Even after this fourth blast, damage remained well-controlled and was primarily characterized by widening of the dominant cracks at midspan, though fiber pullout and more obvious crushing occurred in the UJ beam.

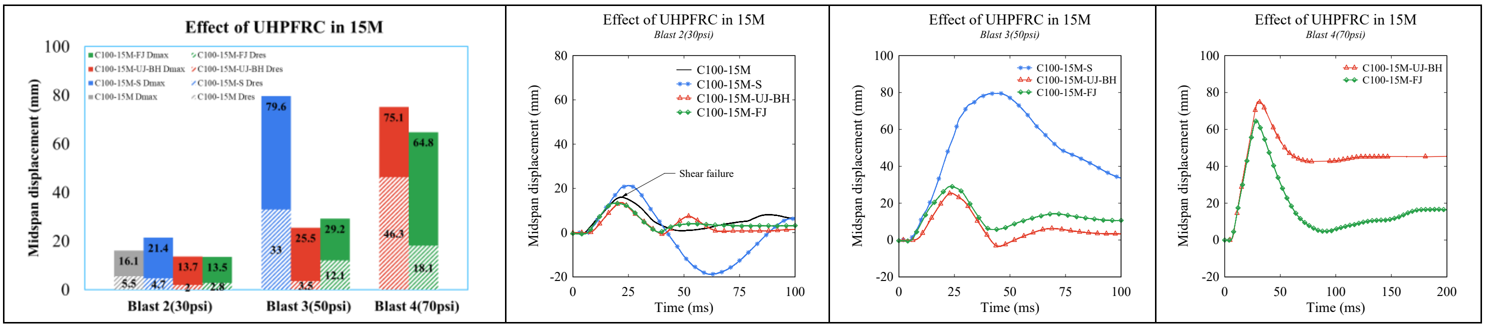

Figure 6 - 6 Effect of UHPFRC in the 15M group (no stirrups)

Figure 6 - 7 Damage profiles of specimens with 15M

6.3.3 Effect of UHPFRC in the 20M group (no stirrups)

The ability of UHPFRC jacketing to enhance shear and flexural behaviour is further studied in the 20M group by comparing the results of the UJ and FJ beams which did not contain stirrups (C100-20M-UJ-BH and C100-20M-FJ-BH), and the counterpart control beams built with and without shear reinforcement (C100-20M-S and C100-20M). In this comparison, stirrups were only provided in the C100-20M-S beam. BH roughening was used in both retrofit beams. The displacements and damage results are compared in **Figure 6 - 8** and **Figure 6 - 9**.

Continuing the previous trend, both UHPFRC retrofits showed a remarkable ability to enhance shear resistance, promote flexural failure and increase blast capacity. Due to the absence of stirrups, the control C100-20M beam failed in shear at Blast 2 (I_r = 336 kPa-ms), while failure in the control beam with stirrups (C100-20M-S) was delayed to Blast 4 (I_r = 685 kPa-ms). In comparison, the C100-20M-UJ-BH and C100-20M-FJ-BH beams survived up to Blast 5 (I_r = 859 kPa-ms), with improved performance when compared to both controls.

Under common blasting, both retrofits also enhanced the control of displacements due to the increase in member stiffness. At Blasts 1-2-3-4, the beam with UJ jacketing (C100-20M-UJ-BH) shows reductions of 24%-17%-45%-77% in maximum displacements when compared to the control C100-20M-S beam. Likewise, the beam with FJ jacketing (C100-20M-FJ-BH) shows decreases of 45%-8%-40%-78% in d_{max} displacements when compared to the control at these same blasts. Both retrofits further enhance the control of permanent displacements at Blast 3-4, with declines of 73%-100% and 66%-93% for the UJ and FJ specimens, respectively.

At Blast 4, the C100-20M-S beam underwent a support rotation (θ_{max}) of 6.0°, which coincides with "Hazardous" damage in the CSA S850 standard. Indeed, as shown in **Figure 6 - 9**, the beam showed severe crushing, wide cracks, and initiation of concrete spalling after this test. Both retrofits survived this blast with θ_{max} rotations that do not exceed 1.5°; damage after this test was limited to multiple fine cracks, and the formation of one or two dominant cracks in the midspan zone (with widths ≤ 0.8mm). Compression damage was also well-controlled, however the rebound (and lack of top UHPFRC or compression bars) in the UJ specimen caused the extension of the primary crack up to the top beam surface. Under Blast 5, the UJ beam showed a rotation of 5.4°; though damage remained well controlled, the beam showed obvious core concrete crushing, and buckling of the side UHPFRC jacket after this test. The rotation for the FJ beam was only 2.3° after this same test, with a remarkable ability to control damage even after the repeated and intense blasts. Indeed, damage was limited to opening of the two primary cracks near the loading points (with widths of 4-6mm, indicating the fibers were near pullout).

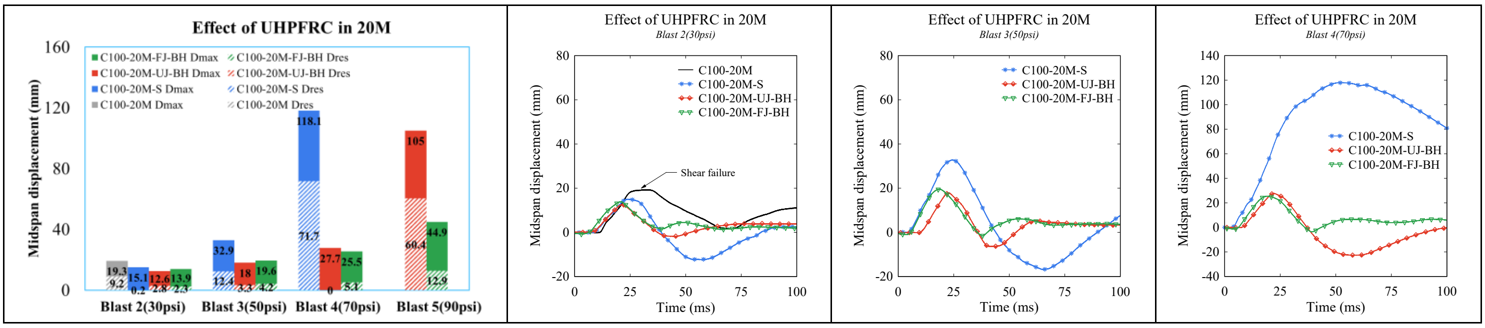

Figure 6 - 8 Effect of UHPFRC in the 20M group (no stirrups)

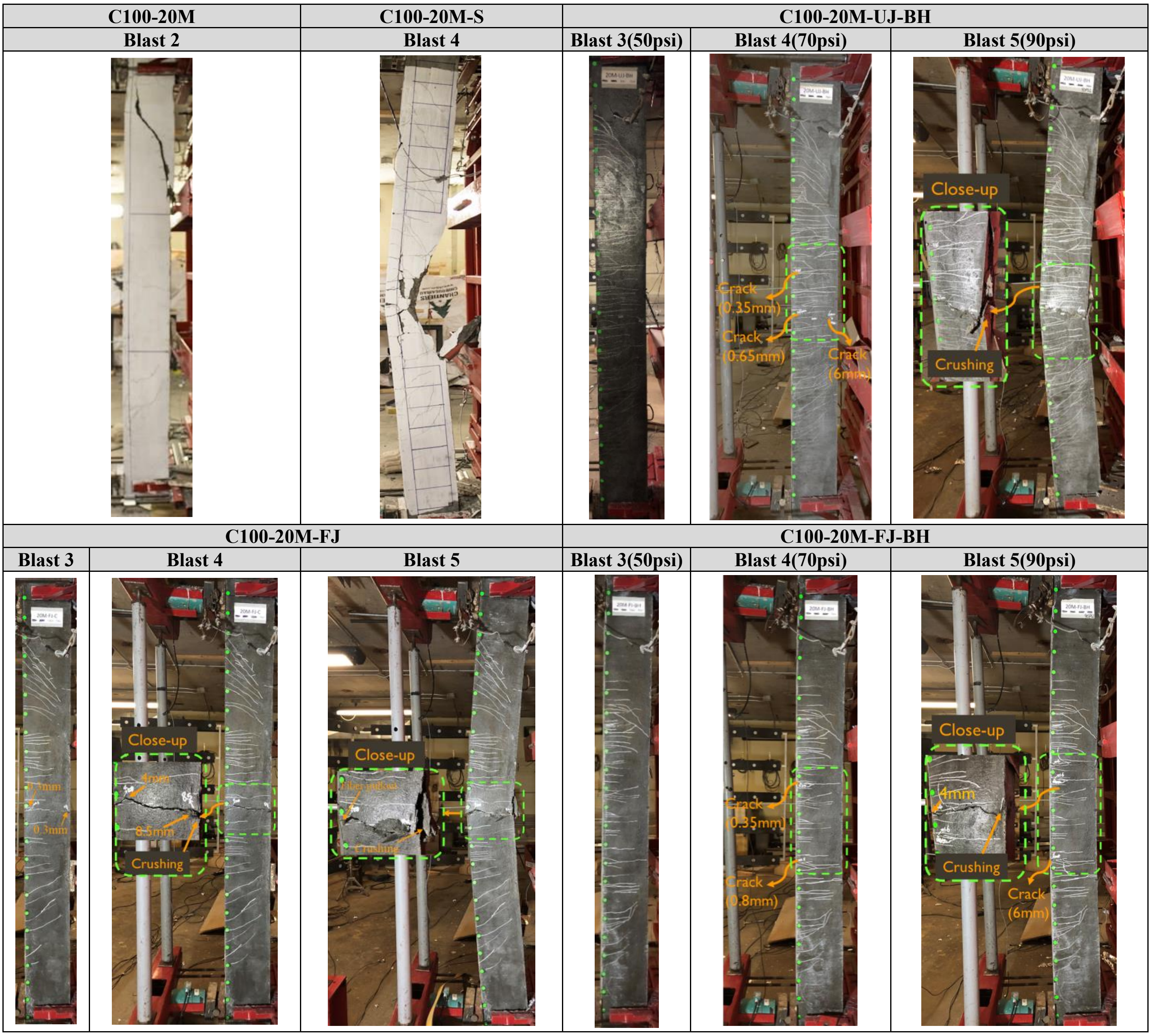

Figure 6 - 9 Damage profiles of specimens with 20M (no stirrups)

6.3.4 Effect of UHPFRC in the 20M group (with stirrups)

The ability of UHPFRC to improve flexural response in the 20M group is further studied by comparing the results of comparable control and UHPFRC beams with shear reinforcement, namely: C100-20M-S (control) vs. C100-20M-S-FJ-BH and C100-20M-S-T-BH, which had FJ and T-sided strengthening, respectively. All beams in this comparison set had stirrups in the shear spans. BH roughening was used in the retrofit specimens.

As shown in **Figure 6 - 10** and **Figure 6 - 11**, all beams in this comparison failed in flexure, however provision of UHPFRC improved the control of displacements at equivalent blasts, and delayed failure in the case of FJ beam. Comparing to the control, the T-sided specimen shows reductions of 35%-9%-37%-55% in peak displacements at Blasts 1-2-3-4, while the FJ beam shows reductions of 44%-19%-48%-78% at these same blasts. Residual displacements at Blast 3-4 are reduced by 79%-76% and 84%-100% for the beams with T-sided and FJ retrofits, respectively.

Failure of the as-built C100-20M-S beam occurred at Blast 4 (I_r = 685 kPa-ms) with a support rotation of 6° ("Hazardous") and was associated with severe concrete crushing and damage. The T-sided beam also failed at this blast, but with a much smaller support rotation of 2.7° ("Heavy" in CSA S850). Due to the lack of top bars or compression-sided UHPFRC, this beam showed extensive concrete damage after this blast. Indeed, the beam initially showed a full-depth crack just below the loading point at Blast 3, which then resulted in fracture of the top HSC concrete during the subsequent rebound at Blast 4 (see video stills in **Figure 6 - 12**).

Comparatively, the beam with FJ-jacking only showed multiple cracking and one dominant crack (with width of 0.3mm) after Blast 3. Under Blast 4 this crack extended across the full-depth of the beam, with widths of 1.5mm and 6mm on the "tension" and "compression" faces respectively, due to the rebound effect. However, the beam survived this blast with a support rotation of only 1.3° ("Moderate" in CSA S850). Further Blast 5 loading (I_r = 859 kPa-ms) resulted in widening of the main crack, with fiber pullout and controlled crushing of the UHPFRC. The maximum support rotation during this final test was 3.8° ("Heavy").

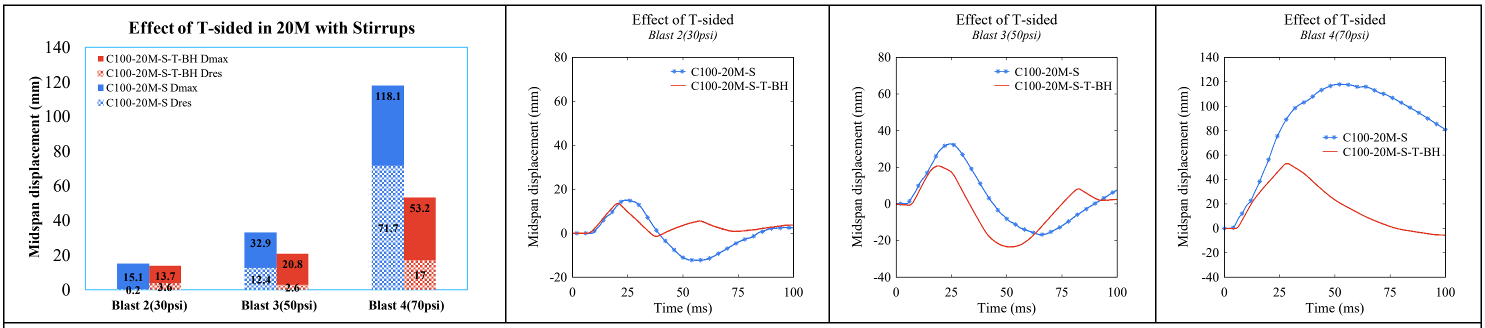

a) Effect of T-sided in 20M with stirrups

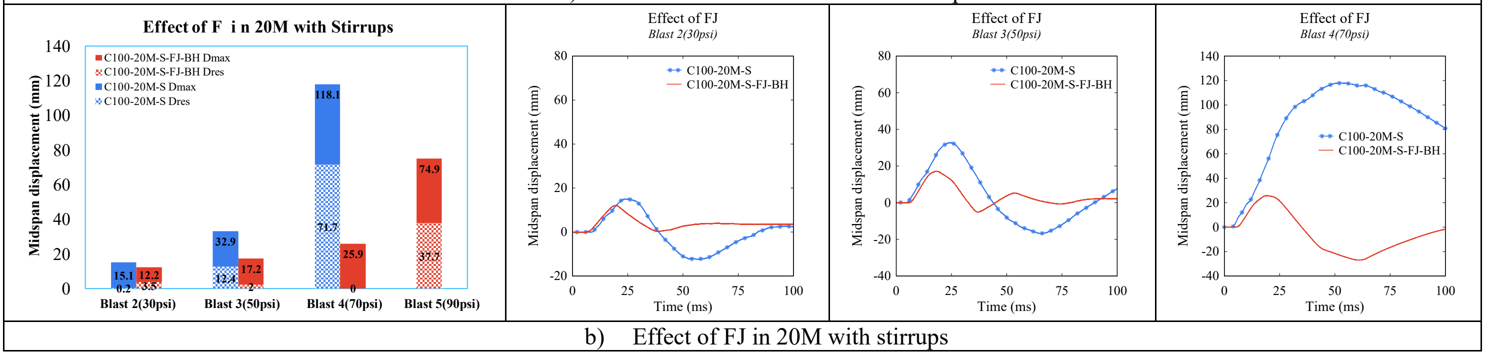

b) Effect of FJ in 20M with stirrups

Figure 6 - 10 Effect of UHPFRC in 20M with stirrups

Figure 6 - 11 Damage profiles of specimens with 20M and stirrups

Figure 6 - 12 High-speed stills showing the failure propagation in beam C100-20M-S-T-BH

6.3.5 Effect of UHPFRC type

The effect of UHPFRC retrofit type is studied in comparable beams with different strengthening configurations and constant steel detailing.

First, the effect of jacket type is examined in beams C100-15M-UJ-BH and C100-15M-FJ. Both beams had 15M bars, no stirrups, but had UJ and FJ jackets, respectively. BH and PC roughening were used in the UJ and FJ beams, respectively. Both retrofits survived up to Blast 4, with excellent control of displacements and increased blast resistance when compared to the controls. As shown in **Figure 6 - 13(a)**, both retrofits showed similar displacement responses under the first three blasts, however the FJ beam shows notable decreases of 14% and 61% in peak and permanent displacements at Blast 4. The cracking patterns were also initially similar, however the UJ beam showed more obvious fiber pullout and crushing damage after Blast 4 (see **Figure 6 - 7**). Indeed, Crushing was negated in the FJ beam, though the primary crack extended to the top beam surface due to the rebound effect and increase in member stiffness.

The effect of jacket type is further studied in beams C100-20M-UJ-BH and C100-20M-FJ-BH. Both beams had 20M bars, no stirrups, but had UJ and FJ jackets, respectively. BH roughening was used in both beams. Comparing the results in **Figure 6 - 13(b)**, the peak displacements were reduced by 28% in the FJ beam at Blast 1, but remained otherwise similar at Blasts 2-3-4. Under Blast 5, the d_{max} displacement was more obviously reduced by 57% in the FJ beam when compared to the UJ counterpart. Likewise, the residual displacement was clearly reduced by 80% under this same test. The support rotation also reduced from 5.4° to 2.3° ("Hazardous" to "Heavy") when comparing the two specimens. Both beams showed similar cracking patterns, and similar dominant cracks after Blast 4 (widths < 1mm). The primary crack widened to 6mm and extended to the full beam depth in the FJ beam at Blast 5. In comparison, the UJ beam showed more extensive damage, with crushing of core concrete and outward buckling of the side UHPFRC which is attributed to the instability of the jacket after crushing (**Figure 6 - 9**).

The effect of retrofit type, is further studied in beams C100-20M-S-T-BH and C100-20M-S-FJ-BH. Both beams contained stirrups and 20M bars but had T-sided and FJ retrofits, respectively. BH roughening was used in both specimens. As seen in **Figure 6 - 13(c)**, the FJ retrofit led to a greater increase in member stiffness, which reduced the peak displacements by 15%-11%-17% when compared to the T-sided counterpart at Blast 1-2-3. Permanent displacements were also obviously reduced by 42%-3%-23% at these same blasts. More significant reductions of 51% and 100% in peak and permanent deformations are further observed at Blast 4. Indeed, this blast caused complete failure of the T-sided beam, while the FJ beam survived the blast, and halved the support rotation from 2.7° ("Heavy") to 1.3° ("Moderate"). Failure in the T-sided specimen was associated with severe fracture of the HSC concrete in the midspan zone which was induced by the rebound at Blast 4. In comparison, the FJ beam only showed a single (but full-depth) dominant crack after this test, and continued to show controlled damage (limited to crack opening and controlled crushing) after Blast 5.

In general, the results confirm the increased effectiveness of full-jacketing when compared to the other retrofit types. In the case of singly-reinforced beams the UJ and FJ jacketing show similar performance except when the beam approaches failure, and especially as the flexural demand on the compression zone becomes greater (as in the 20M beams). In beams with T-sided retrofitting the benefit of the retrofit is limited by the beam's crushing capacity in compression.

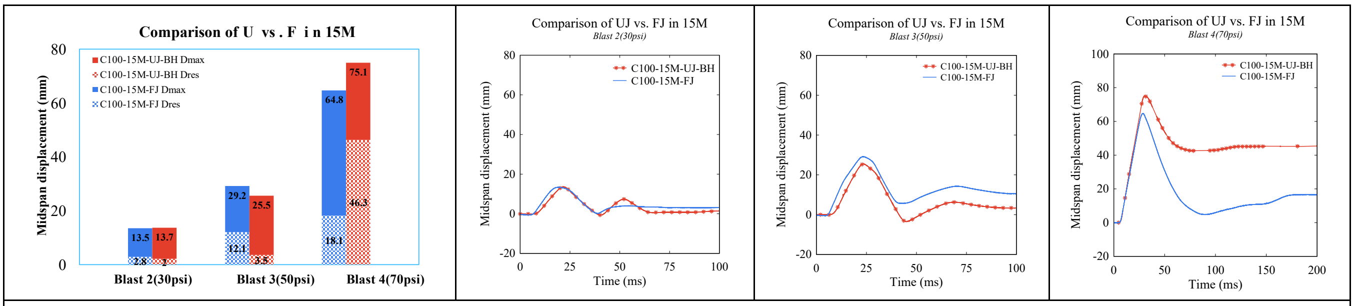

(a) Comparison of UJ vs. FJ in 15M

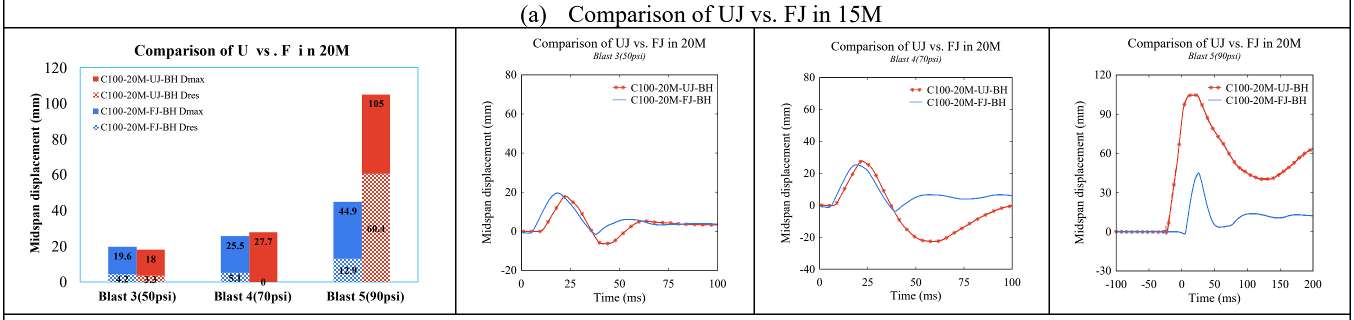

(b) Comparison of UJ vs. FJ in 20M

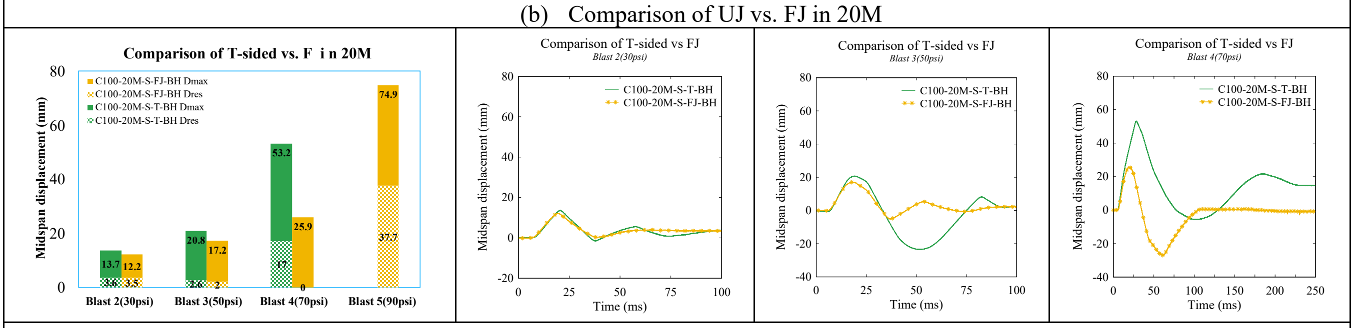

(c) Comparison of T vs. FJ in 20M with stirrups

Figure 6 - 13 Comparison of retrofitting types

6.3.6 Effect of roughening method

Two types of roughening were considered in the tests, with the substrate surface prepared using a pneumatic bush-hammer (BH) or point-chisel (PC), and corresponding concrete surface profiles of CSP6 and CSP10, respectively. In general, roughening with the BH resulted in a more uniform roughening pattern, while greater (deeper) but less uniform roughness was obtained when using the point-chisel (see **Figure 6 - 3**). In addition, the PC roughening resulted in relatively more noticeable concrete damage in the substrate concrete.

The effect of roughening method can be studied in beams C100-20M-FJ-BH and C100-20M-FJ, which had the same reinforcement details and retrofit type, but had BH and PC roughening, respectively. First, it is important to note that both beams showed an ability to prevent shear failure, increase blast resistance, and improve control of displacements when compared to the as-built RC beams with 20M bars (see **Figure 6 - 9** and **Figure 6 - 14**). Moreover, no delamination of UHPFRC occurred in either specimen even after intense and repeated blasting.

Comparing their displacements (see **Figure 6 - 14**), both beams showed similar responses during testing, though some differences can be noted. Under Blast 1-2 loads (low intensity), the specimen with PC roughening showed slightly lower peak displacements when compared to the BH counterpart, though the permanent displacements are nearly equal. At Blast 3 (medium intensity), both beams record nearly equal displacements. Under Blast 4 (high intensity) both retrofits show important reductions of 65-80% in peak displacements when compared to the control C100-20M-S beam, however the decrease is greater in the BH beam. The trend is yet more obvious at Blast 5, with the beams with BH and PC roughening showing support rotations of 2.3° and 5.9°, respectively; indeed, the BH beam shows decreases of 61% and 83% in d_{max} and d_{res} displacements when compared to the PC counterpart at this blast.

Progression of damage was similar in both beams up to Blast 3, however a full-depth major crack formed in the PC beam at Blast 4, with widths of 4 and 8 mm on the tension and compression-sides. In comparison, the width of the dominant crack does not exceed 0.8mm and is restricted to the tension zone in the BH specimen. The difference in cracking behaviour is possibly linked to the greater rebound effect caused by the slight increase in UHPFRC jacket thickness along the deeper roughening pattern in the beam with PC roughening. The UHFRC damage at Blast 5 is clearly greater in this specimen, with core crushing and buckling of the side UHPFRC in the midspan zone. At Blast 5, the BH beam developed full-depth cracking with maximum crack widths of 4-6mm, but no crushing.

Based on the limited tests, uniform roughening (with a CSP of ~ 6) is suggested for the interface preparation in UHPFRC-retrofitted beams with FJ jacketing; however, further studies are needed to quantify the effects of roughening type (roughening method and CSP grade) on blast performance.

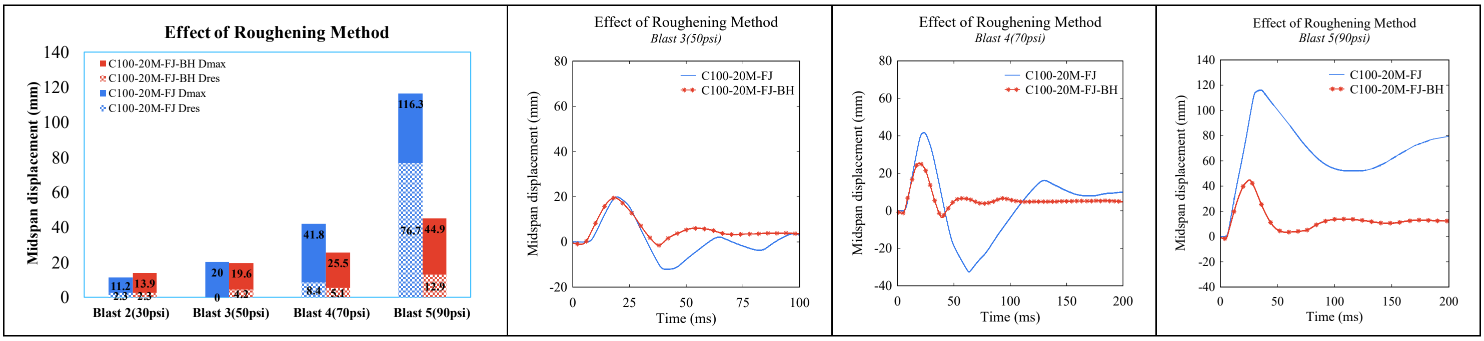

Figure 6 - 14 Effect of roughening method (BH vs. C)

6.3.7 Effect of steel ratio and stirrups in the UHPFRC retrofitted beams

The test program included comparable UHPFRC-retrofitted beams with different longitudinal steel ratios, as well as specimens with and without stirrups.

The effect of steel detailing is first studied in beams C100-15M-UJ-BH and C100-20M-UJ-BH which were retrofitted with UJ jacketing and had steel ratios of 1.6% and 2.4%, respectively. Both beams did not contain stirrups and had BH roughening. **Figure 6 - 15(a)** confirms the beneficial effect of the increased steel ratio on displacements, where the beam with 20M bars shows reductions 8-29-63% in d_{max} displacements at Blasts 2-3-4. Increasing the steel ratio also led to reductions in support rotations and damage. For example, under Blasts 3-4, the support rotations were reduced from 1.3°-3.8°, to 0.9°-1.4° as the bar size increased from 15M to 20M. Reduced damage can also be observed in **Figure 6 - 16**. Under Blast 3 the 15M beam developed a dominant crack (width of 3mm), with fiber pullout and crushing damage at Blast 4. In comparison, damage remained limited in the 20M beam after these same two blasts.

The benefit of increased steel ratio can also be observed when comparing beams C100-15M-FJ and C100-20M-FJ, which had full-jacket retrofits and the same PC roughening. Once again the beam with increased steel ratio (ρ = 2.4%) shows reductions in d_{max} displacements of 17%-32%-35% under Blasts 2-3-4 (**Figure 6 - 15(b)**). Improved damage control is also observed as the steel area is increased as shown in **Figure 6 - 16**.

Finally, the effect of stirrups can be studied in beams C100-20M-FJ-BH and C100-20M-S-FJ-BH. The beams had the same design properties (20M bars, FJ retrofitting and BH roughening), except for the use of stirrups in C100-20M-S-FJ-BH. Since both beams failed in flexure, the beams show nearly the same displacement responses under Blast 1-4 (**Figure 6 - 15(c)**). However, the beam which contains stirrups shows a more obvious rebound displacement at Blast 4 (**Figure 6 - 17**), resulting in a major crack of 6mm width on the compression side. This damage caused a larger peak displacement in this beam at Blast 5, with an increase of 40% in d_{max}, and more obvious damage (fiber pullout and crushing), when compared to the counterpart without stirrups. However, given that the stirrups were only placed in the shear spans (away from the damage area), the difference in results is likely related to experimental scatter, rather than the influence of the shear reinforcement; further research is recommended.

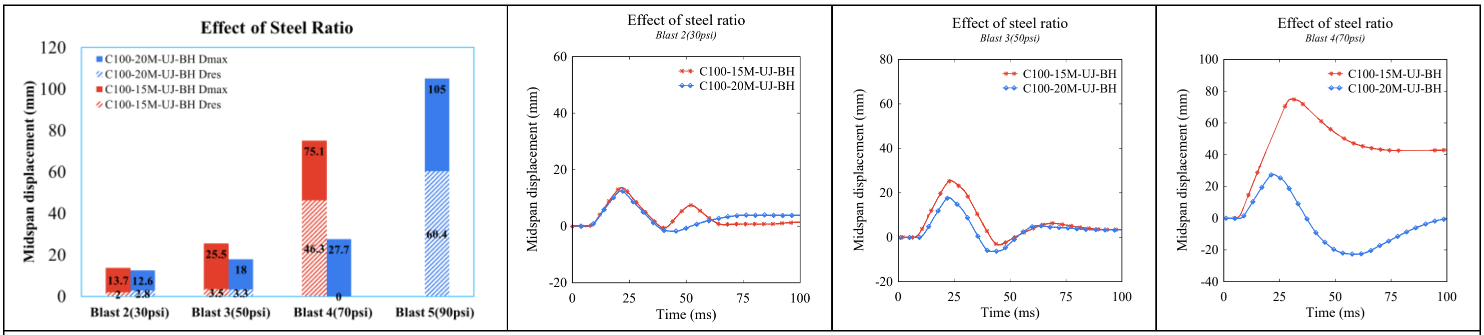

(a) Effect of steel ratio (UJ)

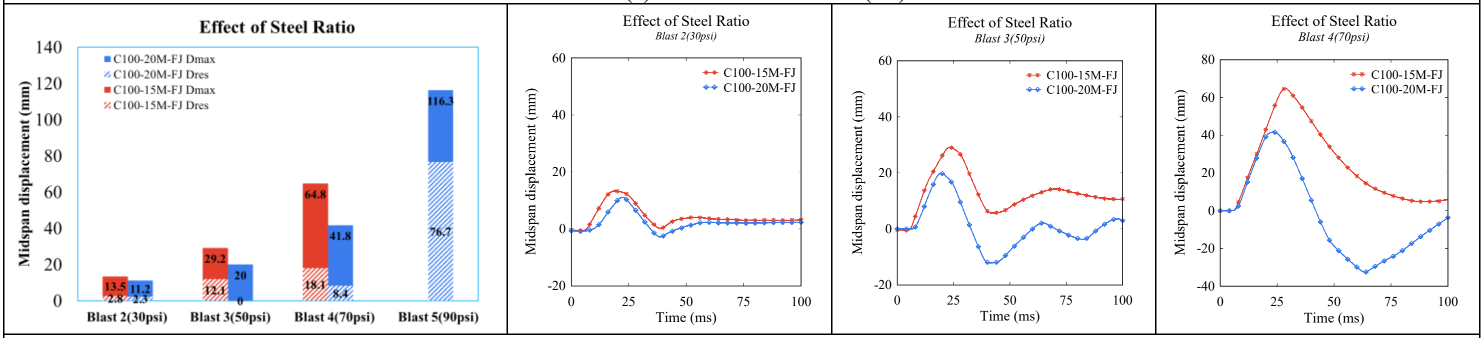

(b) Effect of steel ratio (FJ)

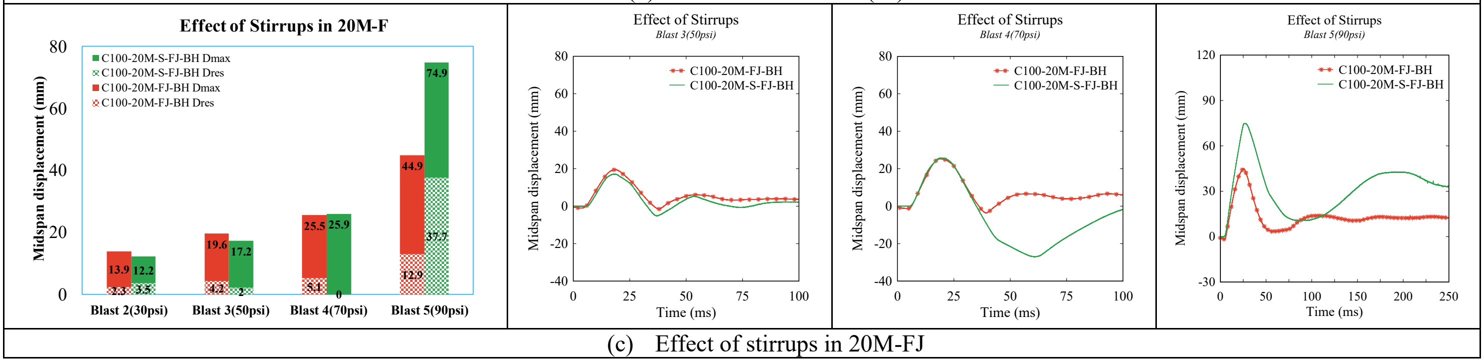

(c) Effect of stirrups in 20M-FJ

Figure 6 - 15 Effect of steel ratio and stirrups

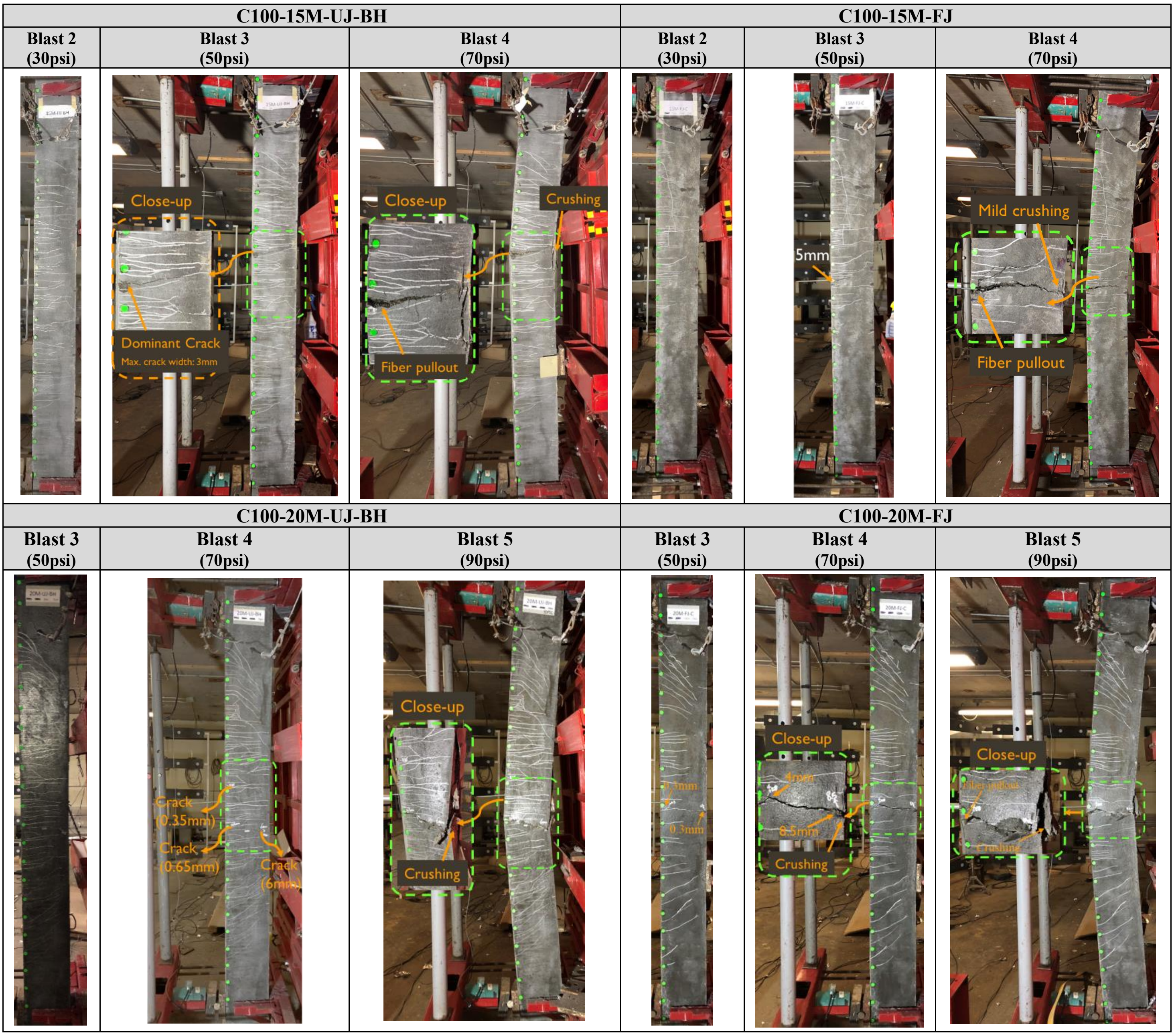

Figure 6 - 16 Damage profiles of specimens with varied steel ratios

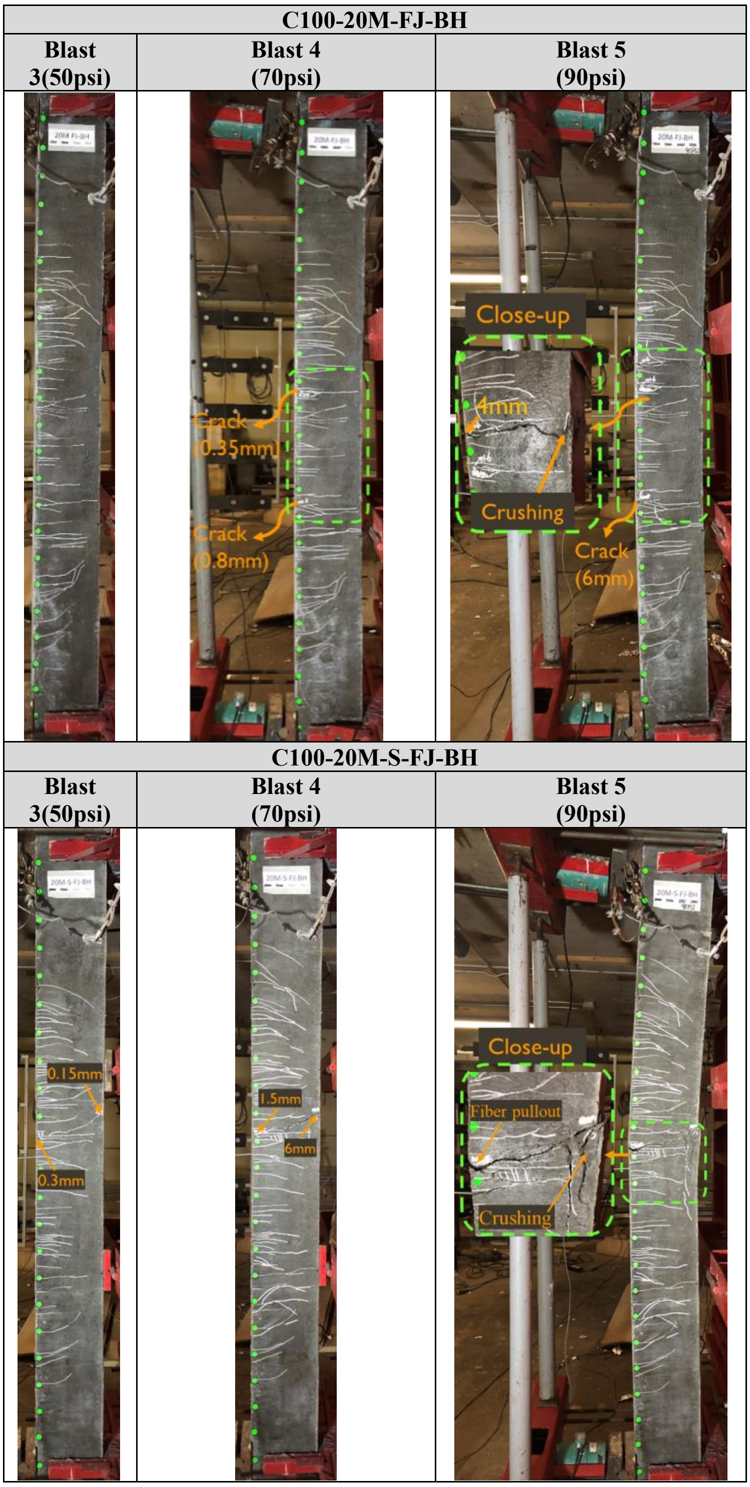

Figure 6 - 17 Damage profiles of specimens with or without stirrups

6.3.8 Results from post-blast residual static tests

With the exception of beam C100-20M-S-T-BH, all UHPFRC-strengthened beams survived the blast tests and were tested under static loads to assess their post-blast capacity. The four-point-bending setup used in the static tests (see **Figure 6 - 5**) matched the loading configuration used in the blast tests. The results from these tests are shown in **Figure 6 - 18**, along with the results from companion "undamaged" beams previously tested by the authors. **Table 6 - 4** reports key data from these tests, including the maximum residual load (P_{max}^{R}), residual secant stiffness (k_s^R) and maximum residual displacement at the end of the tests (Δ_{max}^{R}).

The post-blast behavior of the FJ beam with 15M bars (C100-15M-FJ) is first compared to the response of the comparable "undamaged" beam tested by the authors (C100-15M-FJ-undamaged). As shown in **Figure 6 - 18**, despite the intense blast testing (with θ_{max} =3.3° after Blast 4), the blast-damaged C100-15M-FJ beam retained a substantial post-blast resistance of P_{max}^{R} = 130 kN, with nearly the same capacity in the undamaged test. The stiffness also remains considerable, though the blast-damage reduces the stiffness by 19%. In comparison, the C100-15M-UJ-BH beam (with UJ-jacketing), which suffered a rotation of nearly 4° (θ_{max} = 3.8°) and greater blast-damage after Blast 4, shows a much lower post-blast capacity of 64 kN, with decreases of 51% and 79% in P_{max}^{R} and k_s^R when compared to the beam with full-jacketing (C100-15M-FJ).

The beams in the 20M group were tested to more intense loads corresponding to Blast 5. Beam C100-20M-FJ suffered a large support rotation (θ_{max}) of ~ 6° after Blast 5 and therefore shows a post-blast capacity (P_{max}^{R}) of 43 kN, representing just 23% of the "undamaged" capacity in the C100-20M-FJ-undamaged test. In contrast, beam C100-20M-FJ-BH which experienced a less severe rotation (θ_{max} =2.3°) after Blast 5, shows substantial post-blast capacity of 171 kN, while also retaining significant residual stiffness when compared to the undamaged test. A lower capacity and stiffness is recorded for the C100-20M-S-FJ-BH specimen which had a θ_{max} of ~ 4° at Blast 5. Continuing the trend, beam C100-20M-UJ-BH which suffered a rotation of θ_{max} = 5.4° and significant damage after Blast 5 shows a severely diminished resistance (P_{max}^{R}) of just 26 kN. Thus, limiting the blast rotation in the beams to ~ 3° ensured adequate residual capacity after blast loading, while rotations exceeding 4° were detrimental to post-blast performance.

Table 6 - 4 Post-blast test results

Beam ID	Load	Stiffness	Maximum displacement	Failure mode
	P^R_{max} (kN)	k^R_s (kN/mm)	Δ^R_{max} (mm)	
C100-15M-UJ-BH	63.9	2.020	100	Concrete crushing
C100-15M-FJ	129.8	9.546	141	Concrete crushing
C100-20M-UJ-BH	25.9	0.735	101	Concrete crushing
C100-20M-FJ-BH	170.7	7.697	100	Concrete crushing
C100-20M-FJ	42.8	3.168	127	Concrete crushing
C100-20M-S-FJ-BH	116.2	4.482	102	Concrete crushing

Note: P^R_{max}= Peak residual load; k^R_s= Residual stiffness;
C100-15M-FJ(Undamaged): $P_{max} = 127\ kN$; $k_s = 11.8\ kN/mm$
C100-20M-FJ(Undamaged): $P_{max} = 189\ kN$; $k_s = 14.1\ kN/mm$

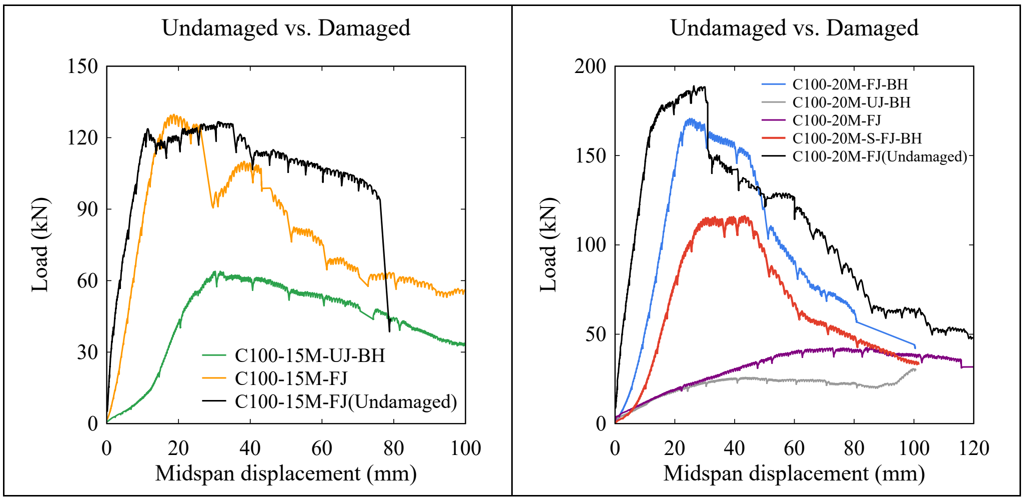

Figure 6 - 18 Load deflection curves of damage retrofit beams

6.4 Conclusions

This paper examined the effect of UHPFRC retrofit type method on the blast high-strength concrete beams under gradually increasing blast loadings applied using a shock-tube. Other parameters investigated in this study include the effects of roughening method and steel detailing. The following conclusions can be drawn from this study:

(1) Regardless of retrofit type (UJ or FJ), and in both the 15M and 20M groups, the use of UHPFRC jacketing not only improved shear resistance in the shear-deficient beams, but also allowed the beams to fail in flexure. Likewise, both UHPFRC retrofits allowed for obvious improvements in flexural behavior, in terms of displacement and damage control, and allowed for an increase in blast capacity when compared to companion unstrengthened RC beams with stirrups. Both retrofits presented multiple fine cracks, followed by the

development of one or two dominant cracks and crushing of concrete, which was more obvious in the UJ beams as the steel ratio increased.

(2) In the beams without stirrups, the UJ and FJ retrofits showed nearly the same displacements under Blasts 1-2-3 in the 15M group, and under Blast 1-2-3-4 in the 20M group. The benefit of full-jacketing only became evident as the 15M and 20M beams approached failure at Blasts 4 and 5, respectively. This benefit was yet more obvious as the flexural demand was increased (i.e. in the 20M set). Indeed, eventual failure in the UJ beam with 20M bars was associated with outward buckling of the side UHPFRC jacket due to core concrete crushing, whereas such damage was negated in the beam with full-jacketing;

(3) Two retrofit types (T-sided and FJ) were considered in the 20M beams with stirrups. Both retrofits showed improved displacement and damage control when compared to the as-built control beam. Similar displacements were observed under the low intensity blasts, while the benefit of FJ jacketing became more obvious at Blasts 3-4. Failure in the T-sided beam occurred at Blast 4 due to severe fracture of the HSC concrete in the midspan zone, while the FJ beam safely survived this blast, and further Blast 5 loading with limited damage;

(4) Two roughening methods were considered in the tests (bush-hammer: BH and point-chisel: PC, with CSPs of 6 and 10, respectively). Regardless of roughening method, no premature debonding was found in the blast tests, indicating the effectiveness of both roughening types. Comparing the companion FJ beams with PC and BH roughening, no obvious differences in performance were observed up to Blast 3. Under Blast 4-5 the PC beam showed greater displacements and more severe damage which was attributed to the less uniform roughness and greater substrate damage caused by the point-chisel roughening.

(5) Increasing the steel ratio from 1.6 to 2.4% (15M to 20M bars) improved member stiffness which in turn led to reductions in midspan displacements and damage in the UJ and FJ retrofit beams. The existence of stirrups didn’t show obvious effects on the blast responses of the FJ-retrofitted beams since the specimens failed in flexure.

(6) Most beams survived the blast tests and were tested under quasi-static four-point bending to assess their residual capacity. In general, damaged FJ beams showed substantially higher load capacities close to that of undamaged beams when compared to damaged UJ beams. Examining all tests, limiting the blast rotation in the retrofitted beams to ~ 3° ensured adequate residual capacity after blast loading, while rotations exceeding 4° were detrimental to post-blast performance.

References

[1] Yuan TF, Hong SH, Shin HO, Yoon YS. Bond Strength and Flexural Capacity of Normal Concrete Beams Strengthened with No-Slump High-Strength, High-Ductility Concrete. Materials. 2020;13.

[2] Yin H, Teo W, Shirai K. Experimental investigation on the behaviour of reinforced concrete slabs strengthened with ultra-high performance concrete. Construction and Building Materials. 2017;155:463-74.

[3] Sakr MA, Sleemah AA, Khalifa TM, Mansour WN, Beushausen H, Dehn F, Moyo P. Behavior of RC beams strengthened in shear with ultra-high performance fiber reinforced concrete (UHPFRC). MATEC Web of Conferences. 2018;199:09002.

[4] Noshiravani T, Brühwiler E. Experimental Investigation on Reinforced Ultra-HighPerformance Fiber-Reinforced Concrete Composite Beams Subjected to Combined Bending and Shear. ACI Stuctural Journal. 2013;110:251-61.

[5] Hussein L, Amleh L. Structural behavior of ultra-high performance fiber reinforced concrete-normal strength concrete or high strength concrete composite members. Construction and Building Materials. 2015;93:1105-16.

[6] Lampropoulos AP, Paschalis SA, Tsioulou OT, Dritsos SE. Strengthening of reinforced concrete beams using ultra high performance fibre reinforced concrete (UHPFRC). Engineering Structures. 2016;106:370-84.

[7] Al-Osta MA, Isa MN, Baluch MH, Rahman MK. Flexural behavior of reinforced concrete beams strengthened with ultra-high performance fiber reinforced concrete. Construction and Building Materials. 2017;134:279-96.

[8] Tanarslan HM, Alver N, Jahangiri R, Yalçınkaya Ç, Yazıcı H. Flexural strengthening of RC beams using UHPFRC laminates: Bonding techniques and rebar addition. Construction and Building Materials. 2017;155:45-55.

[9] Safdar M, Matsumoto T, Kakuma K. Flexural behavior of reinforced concrete beams repaired with ultra-high performance fiber reinforced concrete (UHPFRC). Composite Structures. 2016;157:448-60.

[10] Ramachandra Murthy A, Karihaloo BL, Priya DS. Flexural behavior of RC beams retrofitted with ultra-high strength concrete. Construction and Building Materials. 2018;175:815-24.

[11] Paschalis SA, Lampropoulos AP, Tsioulou O. Experimental and numerical study of the performance of ultra high performance fiber reinforced concrete for the flexural strengthening of full scale reinforced concrete members. Construction and Building Materials. 2018;186:351-66.

[12] Moon J, Reda Taha MM, Kim JJ. Flexural Strengthening of RC Slabs Using a Hybrid FRP-UHPC System Including Shear Connector. Advances in Materials Science and Engineering. 2017:1-7.

[13] Fan W, Shen D, Yang T, Shao X. Experimental and numerical study on low-velocity lateral impact behaviors of RC, UHPFRC and UHPFRC-strengthened columns. Engineering Structures. 2019;191:509-25.

[14] Lee JY, Aoude H, Yoon YS, Mitchell D. Impact and blast behavior of seismically-detailed RC and UHPFRC-Strengthened columns. International Journal of Impact Engineering. 2020;143.

[15] Wei J, Li J, Wu C, Liu Z-x, Fang J. Impact resistance of ultra-high performance concrete strengthened reinforced concrete beams. International Journal of Impact Engineering. 2021;158.

[16] Zanuy C, Ulzurrun GSD. Impact Resisting Mechanisms of Shear-Critical Reinforced Concrete Beams Strengthened with High-Performance FRC. Applied Sciences. 2020;10.

[17] Habel K, Gauvreau P. Behavior of Reinforced and Posttensioned Concrete Members with a UHPFRC Overlay under Impact Loading. Journal of Structural Engineering. 2009;3:292-300.

[18] Algassem O. Parameters affecting the blast performance of high strength fibre reinforced concrete beams: University of Ottawa; 2016.

[19] ICRI. ICRI Standard 310.2 Selecting and Specifying Concrete Surface Preparation for Sealers, Coatings, Polymer Overlays, and Concrete Repair with CSP Chips. 2013.

[20] Lloyd A, Jacques E, M S, Palermo D, Nistor I, Tikka T. Capabilities of a Shock Tube to Simulate Blast Loading on Structures. ACI SP-281: Behaviour of concrete structures subjected to blast and impact loadings. 2011:1-20.

[21] Jacques E. Characteristics of Reinforced Concrete Bond at High Strain Rates: University of Ottawa; 2016.

[22] Bastami R. Structural performance of high-strength reinforced concrete beams build with synthetic fibers: University of Ottawa; 2019.

[23] CSA. Design and assessment of buildings subjected to blast loads. CSA S850-12. Mississauga, ON: Canadian Standards Association; 2012.

Chapter 7: Influence of UHPFRC jacketing on the static, blast and post-blast behaviour of doubly-reinforced concrete beams

Paper 4: extracted from static and dynamic results in series 2 (submitted to journal- "International Journal of Impact Engineering")

Abstract

This paper investigates the effects of ultra-high performance fiber-reinforced concrete (UHPFRC) jacketing on the static and blast behaviour of reinforced beams. The test program included a total of six beams with dimensions of 150mm × 200mm × 2440mm, including three replicate control beams, and three replicate beams retrofitted with a 20 mm UHPFRC jacket. The beams were doubly-reinforced, with provision of compression bars and ties spaced at 75 mm throughout the beam span. Each beam type included specimens tested under quasi-static four-point bending, and repeated or singly-applied blast loads applied using a shock-tube. Under static loading the UHPFRC is shown to increase beam stiffness and capacity, however the high bond capacity of the UHPFRC, crack localization effect, and relatively low steel ratio resulted in bar rupture, thereby reducing ductility. Under repeated blast loading the UHPFRC effectively reduced maximum and residual displacements at equivalent blasts, but the crack localization which initiated at the earlier blasts eventually led to bar rupture. Under the singly-applied blast, the UHPFRC was found to reduce displacements, and better control damage when compared to the companion RC beam, without bar rupture. As part of the numerical study, finite element (FE) modelling was used to predict the blast response and damage in the test beams. A parametric study is also used to examine the effects of steel ratio, jacket thickness and jacket interface location on blast behaviour.

Keywords: UHPFRC, Jacketing, Blast, Retrofit, Beams, Detailing

7.1 Introduction

Recent worldwide events have highlighted the vulnerability of concrete structures against the effects of blast loads caused by accidental or intentional explosions. While rare, events such as the Beirut explosion, Lac-Mégantic disaster and Oklahoma City bombing demonstrate the significant loss of life and damage that can be caused by blast loads on structures. Conversely, many existing concrete structures have not been specifically designed to resist blast loads, and may also face increased vulnerability due to ageing and deterioration. Thus, there is a need to explore novel strengthening methods that can improve the blast capacity of vulnerable structures such as government offices, corporate buildings and critical infrastructure.

As a novel and specifically tailored fiber-reinforced cementitious material [1], UHPFRC (ultra-high performance fiber-reinforced concrete) presents superior properties when compared to conventional concrete, including improved compressive strength, tensile resistance, energy absorption capacity and durability [2, 3]. In addition, UHPFRC shows substantially improved mechanical properties under dynamic loading [3-5], leading to high toughness and damage tolerance under high strain rates. The abovementioned properties make UHPFRC an ideal material for the blast-strengthening of existing concrete structures.

Brühwiler [6] first proposed UHPFRC for the rehabilitation and retrofit of existing structures, in which the material's advanced properties could be exploited in bending, combined bending/shear, and under fatigue loading, with the concept applied in numerous field applications in viaducts, bridges, building slabs and tunnel linings. A number of research studies have also examined the behaviour of UHPFRC strengthened beams and slabs under static loading [7], with the UHPFRC either applied as a retrofit (to replace part of the existing substrate concrete) [8-13], or as an overlay (as an additional layer) [9, 10, 12, 14-19], and in various configurations (Tension or Compression-sided, or as U or full-jackets). Among these studies most demonstrate the ability of tension-sided (T-sided) UHPFRC overlays to improve flexural or shear capacity, while studies on UHPFRC jacketing retrofits are limited.

As shown in **Table 2 - 2**, only a few studies have examined UHPFRC strengthening under impact or blast loads. Among these studies, the majority have focused on impact behaviour. Fan et al. [20, 21] demonstrated the superior crash-worthiness of UHPFRC jacketed columns under low-velocity drop-weight impact loads, with a "two-end" scheme proving to be most effective. UHPFRC-jacketing was further applied numerically in a three-span bridge with multi-column bents, and was shown to significantly reduce column displacements under vehicle collisions, with the results especially sensitive to the jacket thickness. Habel and Gauvreau [1] studied the impact response of UHPFRC-strengthened concrete slabs, applied as an overlay in tension, using a drop-weight setup; the overlay was effective in reducing crushing and spalling at the impact point, and reduced deflections. Wei et al. [22] presented a further impact study on the use of UHPFRC overlays in beams under combined shear and flexure; the overlay was effective in restraining the development of "Type I" shear cracks, while increasing the thickness further improved impact resistance. Zanuy and Ulzurrun [23] presented a further study examining the ability of T-sided UHPFRC to increase the impact resistance of shear-critical concrete beams under impact loading; the retrofit was found to be effective in increasing impact resistance due to a "stress ribbon" effect, which also reduced the impact debris. Lee et al. [24] examined the ability of UHPFRC jacketing combined with "moderate" seismic detailing to improve the impact and blast behavior of reinforced concrete columns. The UHPFRC retrofit was found effective in decreasing displacements and controlling damage under both drop-weight impact and shock-tube induced blast loads.

Based on the above review, research on UHPFRC-retrofitted members under blast loads is extremely scarce. The limited previous impact tests have also primarily focused on tension-sided overlays, with limited tests on UHPFRC jacketing. Accordingly, this paper examines the influence of UHPFRC jacketing on the behavior of reinforced concrete flexural members subjected to quasi-static and blast loading. The effects of the retrofit are studied in replicates tested under static, repeated blast or singly-applied blast loads using a shock-tube. In addition, finite element modelling of the test beams is conducted using software LS-DYNA. The validated numerical models are then further used to conduct parametric studies on the effects of the longitudinal steel ratio and UHPFRC jacket thickness and interface location on blast resistance.

7.2 Experimental Program

7.2.1 Description of test specimens

A total of six beams were tested in this study, including three control specimens and three retrofit beams. Each beam type includes a replicate tested under static, repeated blast, or singly-applied blast loads. **Table 7 - 1** presents the test matrix, while **Figure 7 - 1** shows the beam properties and retrofit details. All specimens had constant dimensions of 150mm × 200mm × 2440mm, with a clear test span of 2232mm. All beams were doubly-reinforced, with provision of compression bars and moderately-spaced ties. Equal amounts of longitudinal reinforcement were provided on the tension and compression sides, consisting of 2-10M bars on each side, resulting in steel ratios of ρ = 0.8% and ρ' = 0.8% in tension and compression. Transverse reinforcement consisted of closed ties made from 6mm steel wire spaced at 75mm throughout the beam span, with a clear cover of 20mm of all faces. It is noted that with the exception of the tie spacing, the detailing meets the requirements for beams in the Canadian CSA S850 blast standard [25]. Both the control and retrofit specimens were first cast with the same ready-mix normal-strength concrete (NSC) with specified strength of 50MPa. Thereafter, the retrofit specimens were strengthened by removing the existing concrete cover and replacing it with UHPFRC applied in the form of a jacket, with a constant thickness of 20mm on all faces.

The specimen ID in **Table 7 - 1** indicates the concrete type in the reference beams (NSC for normal-strength concrete), steel bar size (10M), tie spacing (75 mm) and retrofit type ("FJ" to indicate the UHPFRC was applied as a full-jacket), where NSC-10M-75 and NSC-10M-75-FJ are the control and retrofit beams, with replicates of each type tested under static and repeated blast loads. The "-S" in NSC-10M-75-S and NSC-10M-75-FJ-S indicates the beams were tested under singly-applied blast loading.

Table 7 - 1 Beam test matrix

Beam ID	Specimen	Concrete and beam properties			UHPFRC Retrofit properties			Test type
		f'_c(MPa)	Longitudinal reinforcement	Transverse reinforcement	f'_c(MPa)	Retrofit type	UHPFRC thickness	
NSC-10M-75	Control Replicate 1	58.4	2-10M (T) 2-10M (C)	6mm ties s = 75 mm	-	-	-	Static
NSC-10M-75	Control Replicate 2	58.4						Blast 1-2-3
NSC-10M-75-S	Control Replicate 3	58.4						Blast 3
NSC-10M-75-FJ	Retrofit Replicate 1	58.4	2-10M (T) 2-10M (C)	6mm ties s = 75 mm	180	FJ jacket	20 mm (full-jacket)	Static
NSC-10M-75-FJ	Retrofit Replicate 2	58.4			174			Blast 1-2-3
NSC-10M-75-FJ-S	Retrofit Replicate 3	58.4			174			Blast 3

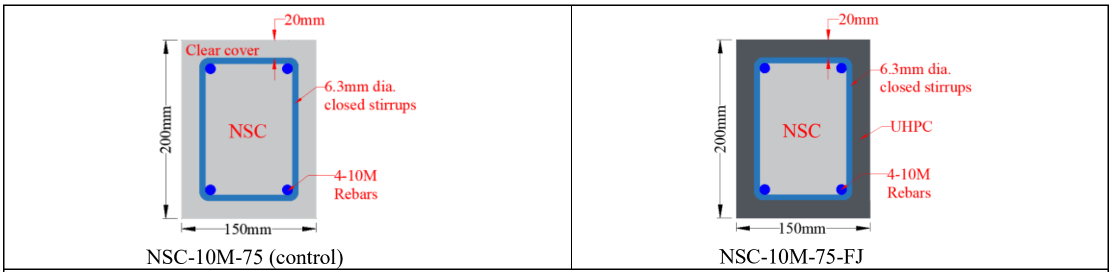

NSC-10M-75 (control)

NSC-10M-75-FJ

a) Cross-section details

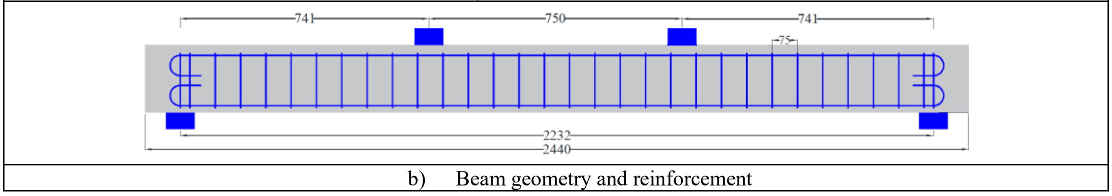

b) Beam geometry and reinforcement

Figure 7 - 1 Beam geometry and reinforcement detailing

7.2.2 Material properties

The ready-mix concrete used in the construction of the control and retrofit specimens had a specified strength of 50MPa, with a maximum aggregate size of 10 mm and slump of 120 mm. The actual compressive strength was determined by testing standard cylinders (100 × 200 mm) according to ASTM C39, and the average properties are reported in **Table 7 - 1**. The proprietary UHPFRC consisted of a dry premix, steel fibers, and three types of liquid admixtures which were mixed according to the manufacturer's specifications. The fibers had a length (l_f) of 13 mm, diameter (d_f) of 0.2 mm, aspect ratio (l_f/d_f) of 65 and a tensile strength of 2850 MPa, and were added at a constant fiber dosage of 2.5% by volume (195 kg/m^3). The UHPFRC properties in compression and flexure were determined by testing standard cylinders (diameter × length: 75 × 150 mm) and prisms (base × height × length: 75 × 75 × 285 mm) according to the ASTM C1856 specifications, and sample results are presented in **Figure 7 - 2(a-b)**. The slump flow of the UHPFRC was also determined according to the same ASTM standard as shown in **Figure 7 - 2(d),** resulting in an average flow of 225mm. The steel properties were determined by testing standard steel coupons in tension according to ASTM A615, and sample stress-strain results are shown in **Figure 7 - 2(c)**.

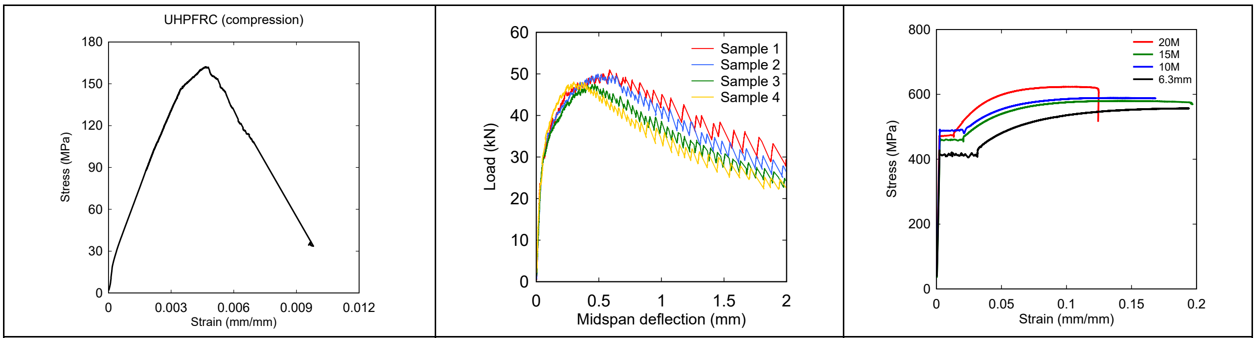

a) UHPFRC (compression) b) UHPFRC (flexure) c) Steel reinforcement

d) Slump flow test

Figure 7 - 2 Material properties

7.2.3 Specimen preparation

The construction of the retrofit beams followed several stages, including: building the reinforcement cages, casting of the normal-strength concrete, preparing the substrate surface using a concrete chisel, moistening the surface and casting the UHPFRC jacket (see **Figure 7 - 3**). Once the NSC concrete strength reached 30 MPa, the remaining substrate cover surface was roughened using a concrete chisel to ensure a concrete surface profile (CSP) of at least CSP6 as defined by the International Concrete Repair Institute [26]. Thereafter, the substrate surface was moistened, followed by casting of the UHPFRC jacket and moist curing for at least 7 days. The beams were then cured under laboratory ambient conditions until the day of testing.

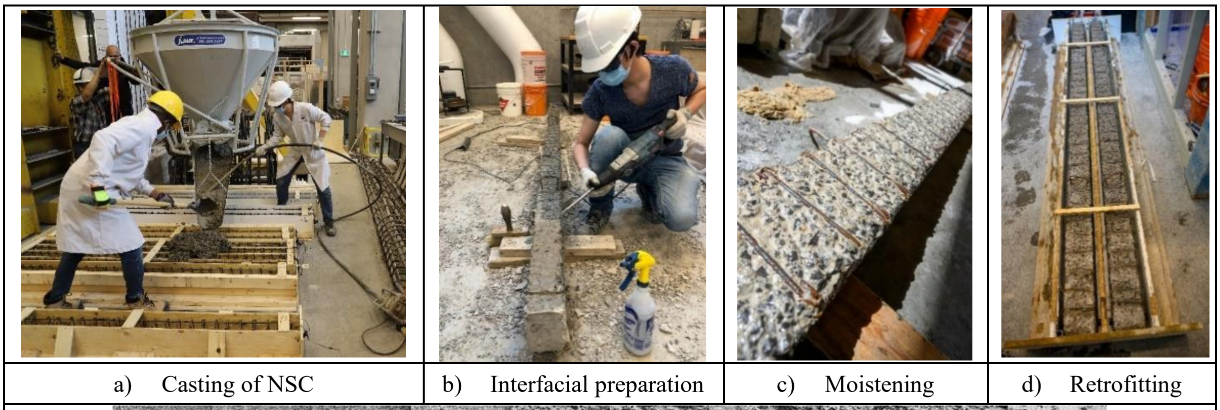

a) Casting of NSC b) Interfacial preparation c) Moistening d) Retrofitting

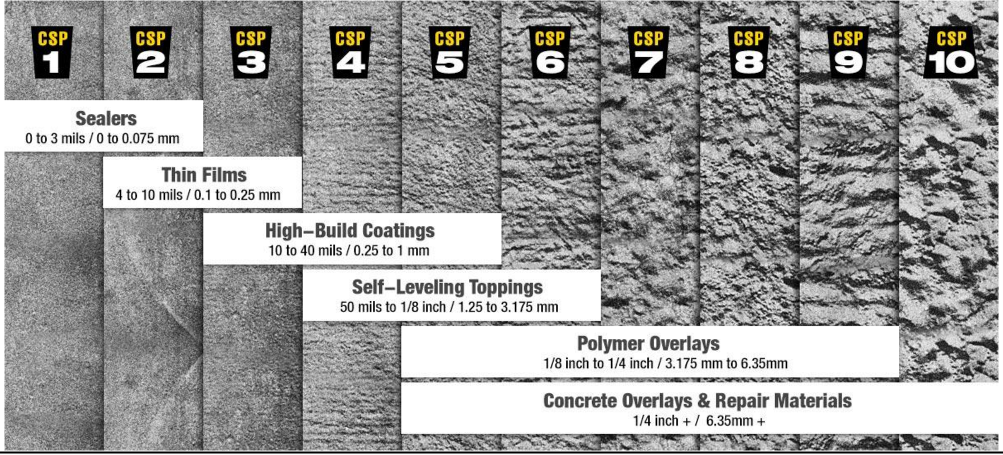

e) Concrete surface profiles (CSP) (source: ICRI)

Figure 7 - 3 Casting and retrofit procedure

7.2.4 Test setup and procedure

The flexural response of the static beams was examined using the four-point bending setup shown in **Figure 7 - 4(a)**. In all cases the beams were simply-supported over a span of 2232 mm, with two equal shear spans of 741 mm and a constant moment region of 750 mm. Loading was generated by a manually operated hydraulic jack and applied onto the specimen as two point loads. The load and displacement data were recorded using a load-cell and displacement transducer placed at midspan. Strain gauges were also used to monitor the strains in the longitudinal steel reinforcement. The tests were conducted under load-control until yielding, and continued under displacement control until failure of the specimens. The same setup was also used to the assess the residual capacity of those beams that survived the blast tests.

Blast testing was conducted using the University of Ottawa shock-tube [27]. As shown in **Figure 7 - 5(a),** the shock tube consists of four main components, including: (1) a driver section which produces the blast pressure, (2) a spool section with a double-diaphragm system which triggers the blast load, (3) an expansion section which ensures the formation of a uniform shock front, and (4) a rigid end frame with a 2 m × 2 m opening where the specimens are attached. A load-transfer device (LTD) was used to collect and transfer the blast load at the shock-tube opening onto the specimens as shown in **Figure 7 - 5(b)**. This LTD consisted of a thin metal sheet and a series of steel HSS beams which simulated a uniformly distributed blast load pattern. The specimens were connected to the shock-tube end-frame using simple support assemblies which allowed rotation but prevented translation. The pressure time histories and displacements were captured using two pressure sensors placed near the end-frame, and a linear variable displacement transducer (LVDT) installed at midspan. Strains in the longitudinal steel were monitored using strain gages installed on the tension and compression bars at midspan. The displaced shape during each test was captured using two high-speed cameras which recorded the beam response at 2000 frames per second. All data was captured using a data acquisition system with a sampling rate of 100kHz.

In the blast testing phase, the beams were tested under either repeated blast loads corresponding to Blasts 1-2-3, or a singly applied blast corresponding to Blast 3. **Figure 7 - 5(c)** shows sample pressure-time histories for each of these blasts. Blast 1, 2 and 3 were generated by fixing the shock-tube driver length at 6ft (1830mm), and gradually increasing the driver pressure from 13psi to 50psi (89 to 344 kPa). **Table 7 - 2** presents the actual shockwave parameters for each blast, including average maximum reflected pressure (P_r), reflected impulse (I_r), and positive phase duration (t_d) as defined in **Figure 7 - 5(d)**. For those beams that survived the blasts, the specimens were further tested under static loading to assess their residual capacity.

Table 7 - 2 Driver and shockwave properties for Blast 1-2-3

Blast ID	Driver Pressure kPa (psi)	Driver Length mm (ft)	Avg. Reflected Pressure P_r(kPa)	Avg. Reflected Impulse I_r(kPa·msec)	Avg. Positive Phase Duration, t_d(ms)
Blast 1	90 (13)	1829 (6)	18.9	140	14.8
Blast 2	207 (30)		40.7	256	12.6
Blast 3	345 (50)		50.1	376	15.0

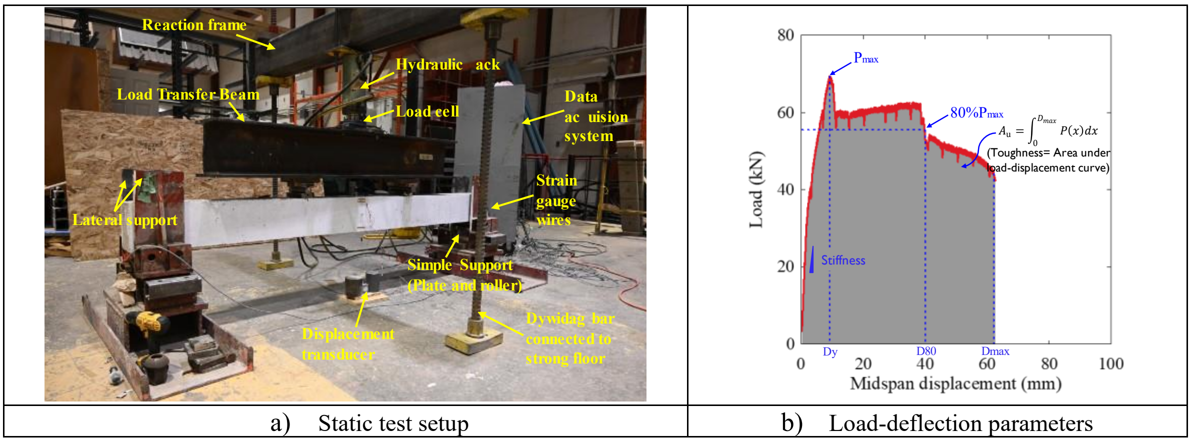

a) Static test setup b) Load-deflection parameters

Figure 7 - 4 Static test setup and definition of load-deflection parameters

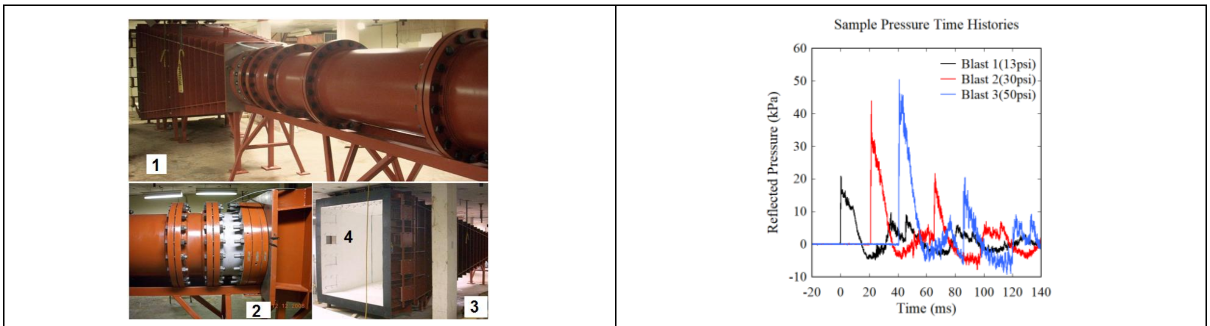

(a) Shock-tube components (c) Blast testing sequence

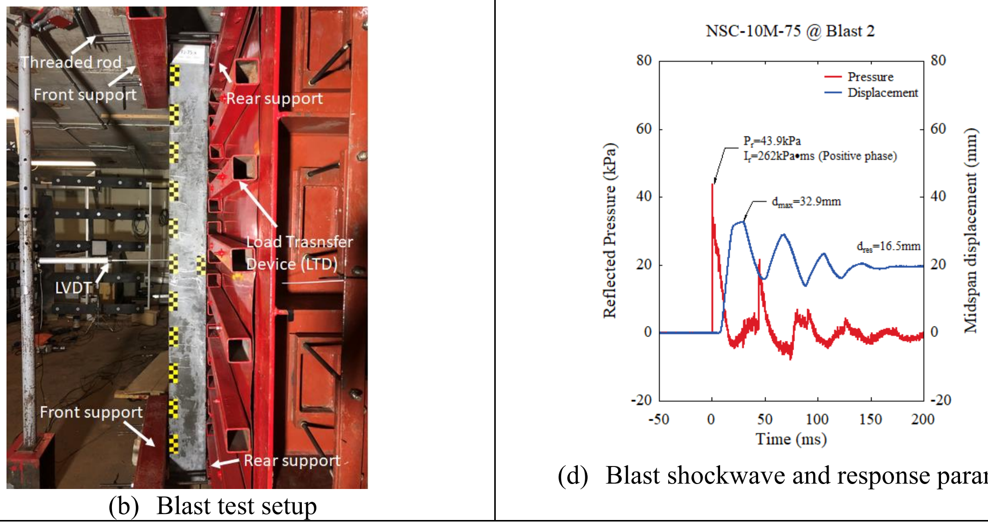

(b) Blast test setup (d) Blast shockwave and response parameters

Figure 7 - 5 Details of the dynamic test setup and blast testing parameters

7.3 Experimental Results

7.3.1 Results from static tests

The effect of the UHPFRC retrofit is first studied under static loading. **Figure 7 - 6** compares the beam responses, while key parameters extracted from the load-displacement curves are defined in **Figure 7 - 4(b)** and reported in **Table 7 - 3**, including: the yield load (P_y), maximum load (P_{max}), stiffness (k_s), displacements at yielding, 80% of P_{max} and end of the testing (D_y, D_{80} and D_{max}). The table also reports the ductility (D_{80}/D_y), drift ratio (D_{80}/L_{shear}), toughness (A_{80} and A_{max}, representing the area under the curves up to D_{80} and D_{max}), and corresponding toughness indices (I_{80} and I_{max} as defined in **Figure 7 - 4(b)**). The progression of damage and photos illustrating the failure modes are shown in **Figure 7 - 6** and **Figure 7 - 7**.

Table 7 - 3 Summary of static test results

Beam I.D.	Load (kN)		Displacement (mm)			Stiffness k_s(N/mm)	Ductility D_{80}/D_y	Drift ratio D_{80}/L_{shear} (%)	Toughness (kN-mm) [Toughness index]		Failure modes
	Yield P_y	Max. P_{max}	Yield D_y	Failure D_{80}	Max. D_{max}				A_{80} [I_{80}]	A_{max} [I_{max}]	
NSC-10M-75	42.4	49	11.2	75.9	160.5	3786	6.8	10.2	3217 [11.2]	6591 [23]	Concrete crushing
NSC-10M-75-FJ	69.4	69.4	9.1	39.7	62.7	7626	4.4	5.4	2278 [5.5]	3422 [8.2]	Bar-rupture

Beginning with the control specimen (NSC-10M-75), it can be observed that the use of moderate reinforcement detailing consisting of top compression bars and closely-spaced ties allowed beam NSC-10M-75 to show excellent ductility, with an ability to sustain significant loads up to the end of testing at D_{max} = 160mm. The beam shows a yield load P_y of 42.4kN, maximum load P_{max} of 49kN, with limited damage until crushing of the top concrete cover occurs at D_{80} = 76mm. Overall the beam shows a ductility D_{80}/D_y of 6.8, drift ratio of 10.2% and toughness indices of I_{80} = 11.2 and I_{max} = 23. The final damage pattern consists of relatively widely-spaced flexural cracks and crushing of the top cover concrete in the midspan region. In general, the results confirm the benefits of implementing moderate reinforcement detailing, similar to that what is required by modern blast standards, even under static loading.

When compared to the control specimen, the UHPFRC retrofit beam (NSC-10M-75-FJ) shows obvious increases in capacity (P_y = P_{max} of 69.4kN) and stiffness (k_s = 7.6 vs. 3.8 kN/mm), representing increases of 64%, 42% and 100% in P_y, P_{max} and k_s. In the initial stage (up to peak), the UHPFRC-retrofitted beam shows a stiffer response with the formation of multiple fine cracks. Upon reaching its maximum capacity the beam shows a decrease in strength due to the formation of a major localized crack. This is followed by a gradual reduction in capacity due to the increase in crack opening, and gradual crushing of the top UHPFRC cover, before the beam fails due to bar rupture in tension. As shown in **Figure 7 - 7**, the beam shows a distinct crack pattern, with many fine cracks, and one dominant crack which shows rapid opening. This crack localization and UHPFRC's high bond capacity result in the build-up of strains over a small length of steel reinforcement, leading to bar rupture. Overall, the beam shows a ductility of 4.4, drift ratio of 5.4% and toughness indices of I_{80} = 5.5 and I_{max} = 8.2, which are reduced when compared to the control specimen.

In general, the results confirm that UHPFRC jacketing results in enhancements in strength and stiffness, however the material's high bond capacity can result in early bar fracture. Khaksefidi et al. [28] previously noted that UHPFRC shows a nearly five-fold increase in bond capacity when compared to conventional concrete. Hung et al. [29] have also noted that the fibers in UHPFRC transform the failure in reinforced UHPFRC members in tension from multiple to single localized cracks leading to bar fracture, especially in members with small bar sizes. Indeed, several studies also report that bar rupture is a common failure mode in conventional UHPFRC beams, especially at low or moderate steel ratios. For instance, Yoo et al. [30] reported bar rupture failures in beams with ρ = 0.53% to 1.71%, which also matches the observations in Pokhrel and Bandelt [31] (ρ = 0.7% to 1.9%) and Shao and Billington [32] (ρ = 0.96% to 2.1%). These studies also report a consistent trend of a delay in bar fracture as ρ is increased, due to the spread of plasticity over a longer length of reinforcement [32]. Safdar et al. [11] reported bar-fracture failure, and a compromise in ductility in UHPFRC-retrofitted beams with low steel ratio (ρ = 0.4%), which matches the observation in the current tests (ρ =0.8%). Therefore, the steel ratio is a key parameter which may affect the failure mode and ductility of UHPFRC-retrofitted beams.

It is noted that bar rupture in reference [11] occurred when the UHPFRC was applied at or above the level of the tension bars, while the UHPFRC was applied just below the bars in the current tests. In the case of conventional concrete retrofits, it is generally advised that the "concrete removal continue past the steel reinforcement to allow the new concrete to fully surround the reinforcing bars" [33]. However, based on the above results, the interface location (i.e. below the reinforcing bars, coinciding with the reinforcing bars, or above the reinforcing bars) may be an important driver which may affect the ductility and failure mode in UHPFRC retrofitted members due to the possibility of bar fracture; further research is recommended.

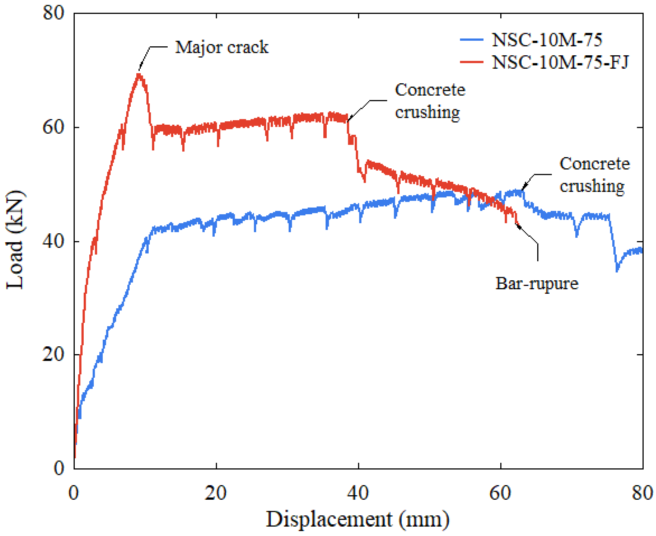

Figure 7 - 6 Static load-deflection results

NSC-10M-75 (control beam)

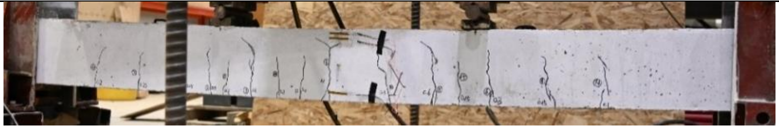

(a) Yielding

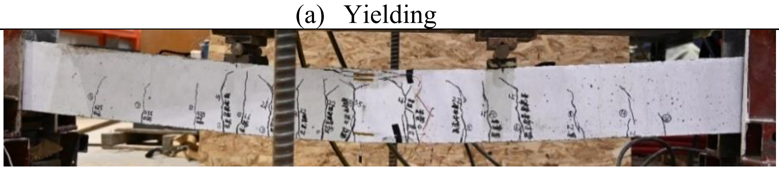

(b) Crushing

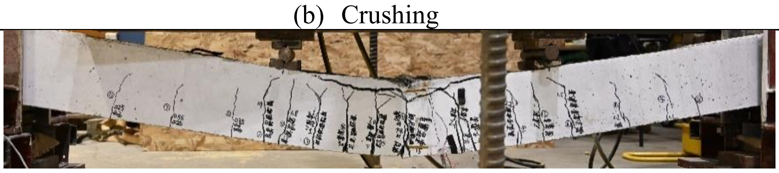

(c) End of test

NSC-10M-75-FJ (retrofit beam)

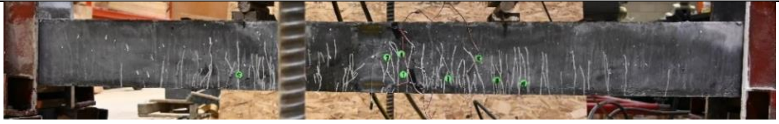

(d) Yielding

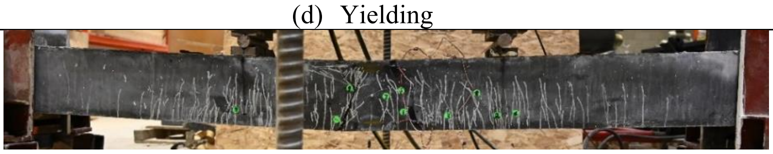

(e) UHPFRC crushing

(f) End of test

Figure 7 - 7 Beam test photos

7.3.2 Results from repeated blast tests

The results from the repeated blast tests for the control and retrofit beams are presented in **Figure 7 - 8a** and **Figure 7 - 9** which show a comparison of displacements (including maximum and residual displacements: d_{max} and d_{res}) and damage photos. Key data from the blast tests are reported in **Table 7 - 4**, including the peak reflected pressure (P_r), positive phase duration (t_d), reflected impulse over the positive phase (I_r) and response data in terms of maximum/residual displacements and maximum support rotations (θ_{max}) after each test. The expected damage states based on the response limits in the CSA S850 standard are also reported [25].

Table 7 - 4 Summary of dynamic test results

Beam ID	Blast ID	Shockwave Properties[1]			Specimen Response[2]				CSA S850 Response limits and Component damage Failure mode[3]	
		P_r (kPa)	t_d (ms)	I_r (kPa·ms)	d_{max} (mm)	d_{res} (mm)	θ_{max} (°)	Observed damage	Response limit	Expected Damage level
NSC-10M-75 (repeated blasts)	1	20.9	13.9	145	14.8	4.2	0.8	1st hairline cracks	<B1	Superficial
	2	43.9	11.9	262	39.8	23.2	2.0	Further crack opening	B2-B1	Moderate
	3	50.5	14.3	362	85.5	65	4.4	Concrete crushing	B3-B2	Heavy
NSC-10M-75-FJ (repeated blasts)	1	16.9	16.0	135	10.5	3.8	0.5	1st hairline cracks	<B1	Superficial
	2	37.5	13.3	250	27.2	15.2	1.4	Crack localization	B2-B1	Moderate
	3	49.1	15.5	380	Rupture	-	-	Bar-rupture	-	-
NSC-10M-75-S (single blast)	3	53.0	14.1	375	84.1	70	4.3	Concrete crushing & fragmentation	B3-B2	Heavy
NSC-10M-75-FJ-S (single blast)	3	47.8	16.2	388	50.6	40.2	2.6	Concrete crushing & crack localization & fiber pull-out	B2-B1	Moderate

Note:
[1]: P_r = Reflected pressure; I_r = Reflected impulse; t_d = positive phase duration;
[2]: D_{max} = maximum mid-span displacement; D_{res}= residual mid-span displacement; θ_{max} = max support rotation;
[3]: Double-reinforced concrete beams: Superficial: $\theta < 1°$, Moderate: $1° \leq \theta < 4°$, Heavy: $4° \leq \theta < 6°$, Hazardous: $6° \leq \theta < 10°$, Blowout: $\theta \geq 10°$.

Beams NSC-10M-75 and NSC-10M-75-FJ were tested under *Blasts 1-2-3* to examine their response under yield, post-yield and ultimate conditions. After *Blast 1* (I_r = 140 kPa-ms), the control beam shows a maximum displacement d_{max} of 14.8 mm, residual displacement d_{res} of 4.2 mm, and support rotation θ_{max} of 0.8° (Response limit < B1, “superficial damage”). The actual damage consists of the formation of hairline flexural cracks at midspan. In comparison, NSC-10M-75-FJ shows displacements d_{max} of 10.5 mm and d_{res} of 3.8 mm, which are reduced by 29% and 10%, with a support rotation of θ_{max} of 0.5° (< B1, “superficial”), Damage is indeed superficial in the UHPFRC-retrofitted beam, however as the beam has passed yielding, crack localization is already evident.

Blast 2, with an average impulse I_r of 256 kPa-ms, brought both specimens well into the post-yield range as evidenced by the increased residual displacements and damage. The control beam shows displacements d_{max} and d_{res} of 39.8 mm and 23.2 mm, with a support rotation θ_{max} of 2.0° (Response limit B2-B1, "moderate" damage). The actual damage consists of the formation of full-depth flexural cracks at midspan, and initiation of concrete crushing on the compression face. Beam NSC-10M-75-FJ shows a reduced support rotation of 1.4°, and displacements d_{max} of 27.2 mm, and d_{res} of 15.2 mm, which are reduced by 32% and 34%. Damage in the beam is still well-controlled with the formation of multiple and closely-spaced fine cracks, however the primary crack at midspan is now clearly dominant with a measured crack width of 8 mm > $l_f/2$ (where l_f is the fiber length), indicating the loss of fiber bridging at this location.

Blast 3, with an average impulse I_r of 376 kPa-ms, caused significant damage in both specimens, but with different damage modes. Beam NSC-10M-75 shows a support rotation θ_{max} of 4.4° (Response limit: B3-B2, "heavy" damage), with significant displacements d_{max} and d_{res} of 85.5 mm and 65 mm. Indeed, the failure results in wide opening of the flexural cracks, the onset of concrete crushing and the development of significant blast debris/fragments as shown in **Figure 7 - 9** (see also high-speed stills in **Figure 7 - 10**). In comparison the UHPFRC-retrofitted specimen fails due to bar rupture, which causes the beam to split into two segments. The finite element modelling and high-speed video indicate that the bar rupture initiated a maximum displacement of approximately 65 mm, which is similar to the failure displacement of 63 mm observed in the static tests. The bar fracture occurred at the previously formed localized crack, and is attributed to the repeated blast tests, the high bond capacity of the UHPFRC, and the relatively low steel ratio which results in the build-up of strains across a small gage length of reinforcement. Despite the brittle failure the UHPFRC prevents the formation of secondary blast fragments, with the debris limited to a fine powder at failure (see **Figure 7 - 10**).

The results indicate that the application of UHPFRC jacketing results in improved control of damage and displacements at low or moderate blasts, but may cause bar fracture failure, especially after crack localization. The results match those reported in previous blast tests on conventional UHPFRC columns. Aoude et al. [34] reported improved control of displacements and reduced damage, but observed crack localization and bar fracture in UHPFRC columns with steel ratios of $\rho = 0.86\%$ (in tension) under repeated blasts. The next section examines the performance of the control and retrofit beams under singly-applied blast loads.

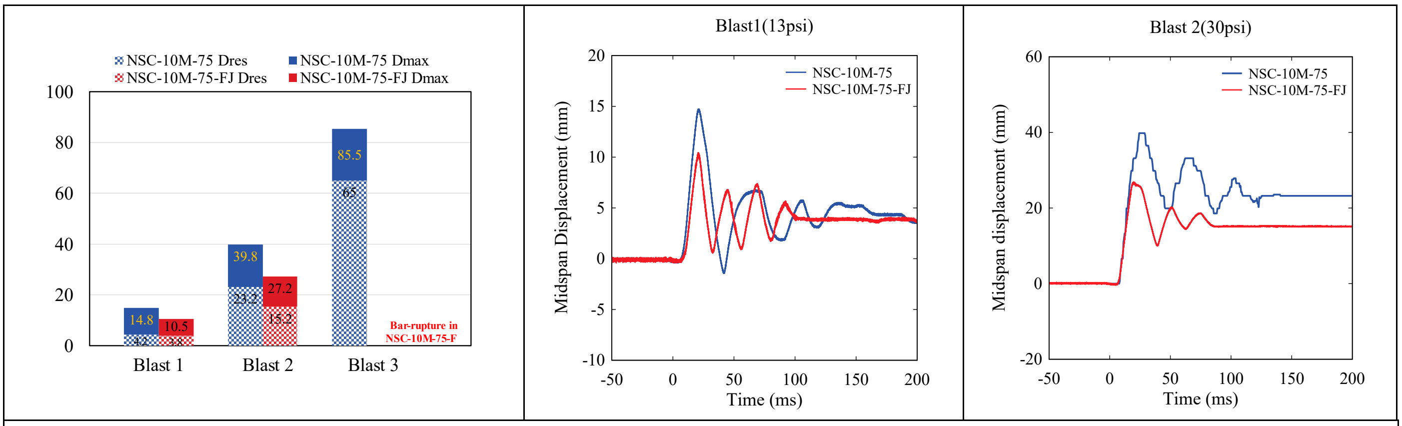

a) Effect of UHPFRC under repeated Blast 1-2-3 loading

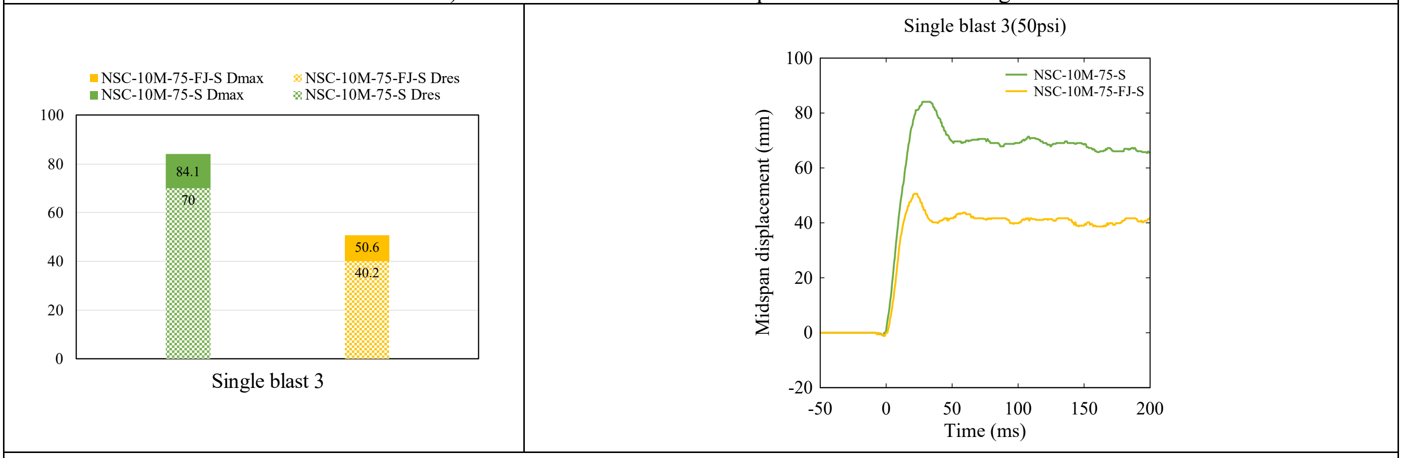

b) Effect of UHPFRC under single Blast 3 loading

Figure 7 - 8 Effect of UHPFRC jacketing under single and repeated blast loadings

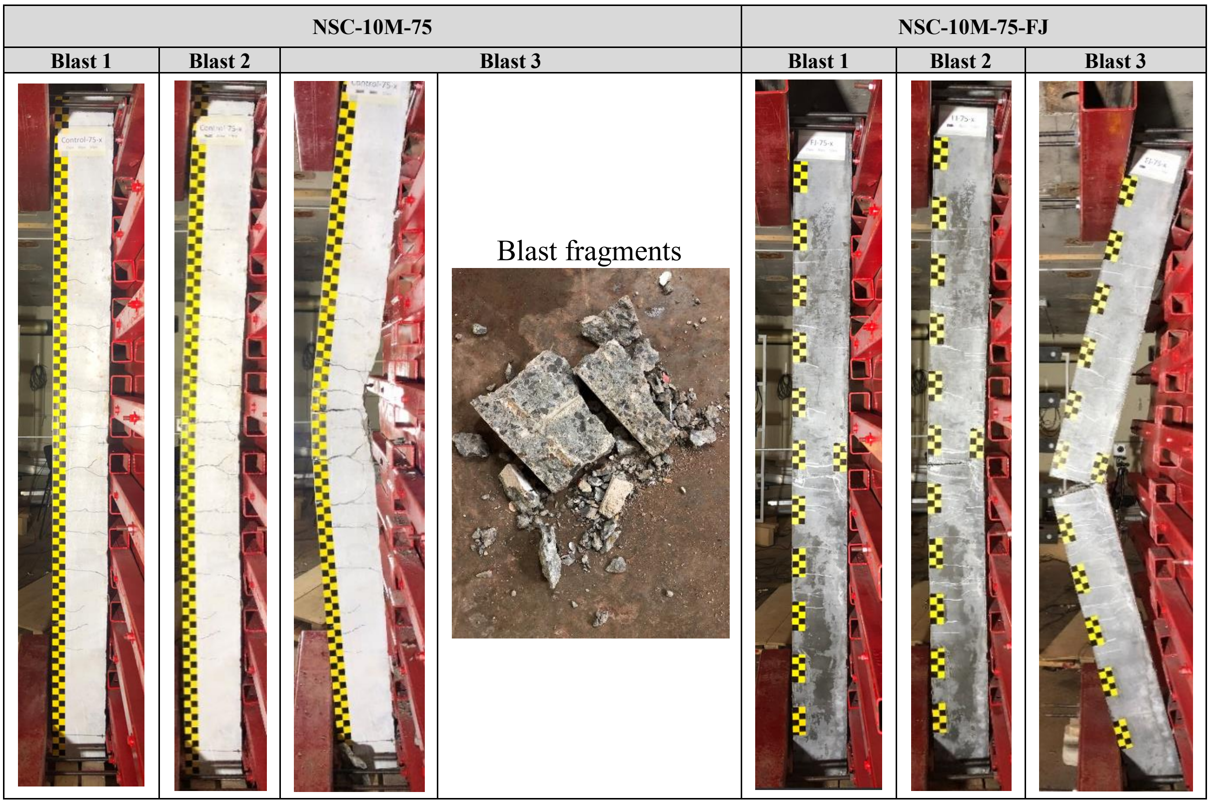

Figure 7 - 9 Progression of damage in beams under repeated blast loading (Blast 1-2-3)

Repeated blasts

(a) NSC-10M-75 @ Blast 3

(b) NSC-10M-75-FJ @ Blast 3

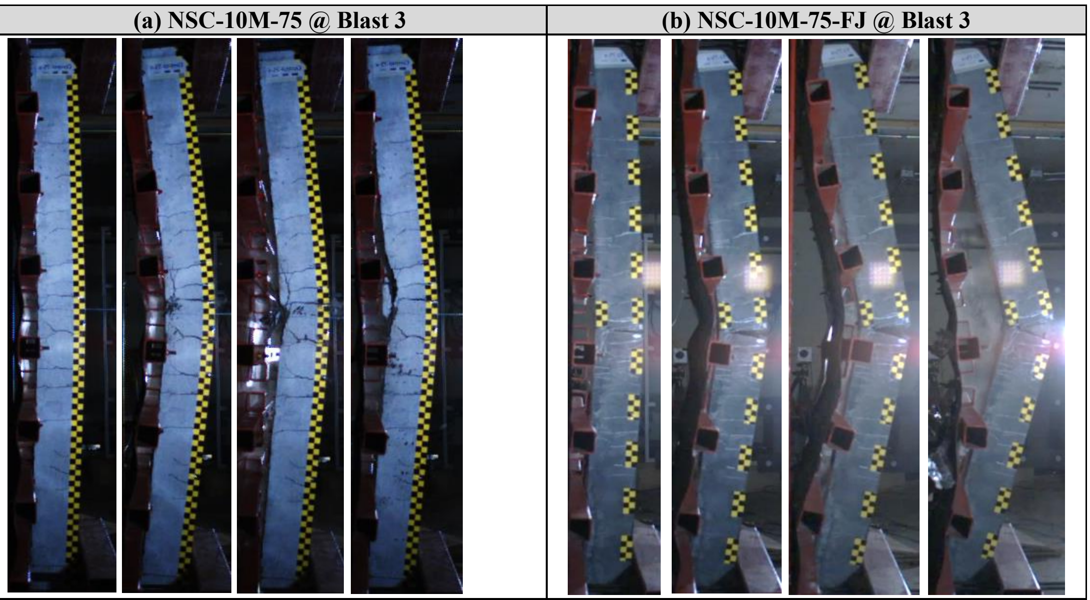

Single blast

(c) NSC-10M-75-S @ single @ Blast 3

(d) NSC-10M-75-FJ-S @ single @ Blast 3

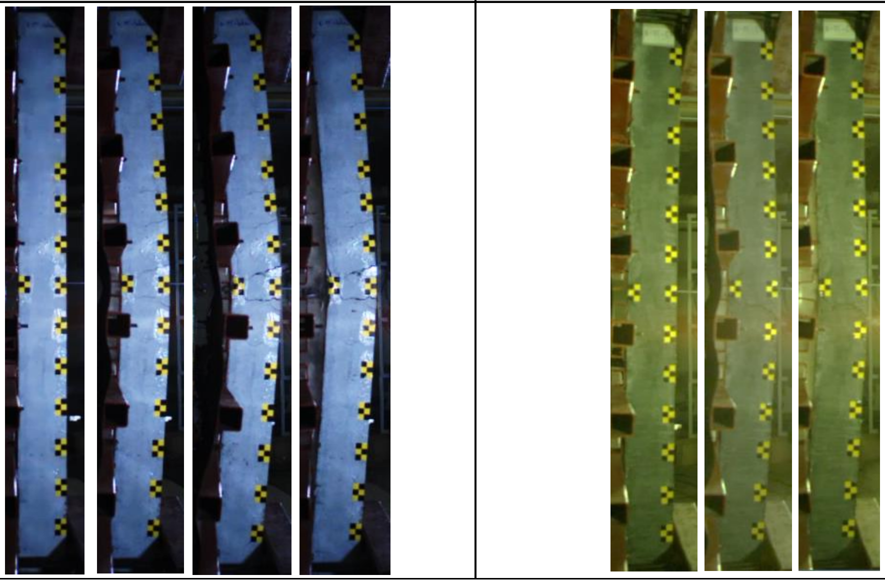

Figure 7 - 10 High-speed stills showing the failure propagation in beams

7.3.3 Results from singly-applied blast tests

The results from the singly-applied blast tests for the control and retrofit beams (NSC-10M-75-S and NSC-10M-75-FJ-S) are presented in **Figure 7 - 8(b)** and **Figure 7 - 11** which show a comparison of displacement histories, displacement data (d_{max} and d_{res}) and photos after application of *Blast 3*. Complete blast data from this test is reported in **Table 7 - 4**.

Single Blast 3, with an average impulse of I_r = 381 kPa-ms, resulted in a support rotation of θ_{max} of 4.3° in the control specimen ("heavy" damage), with significant displacements d_{max} and d_{res} of 84.1 mm and 70 mm. It is noted that the displacements and rotations closely match those of the companion beam tested under repeated *Blast 1-2-3* loading (as also shown in **Figure 7 - 12(a)**). The single blast results in full-depth and wide flexural cracks (with a maximum crack width of 7.5 mm at midspan), with concrete crushing on the compression face. However, as shown in **Figure 7 - 12(b)**, the damage is less significant when compared to the companion control beam tested under repeated blasts. The results coincide with those reported in Li and Aoude [35] where high-strength reinforced concrete beams tested under single blasts showed similar displacements, but less significant concrete damage, when compared to replicates tested under repeated blasts.

Unlike the companion retrofit beam tested under repeated blasts, beam NSC-10M-75-FJ-S survives the singly-applied *Blast 3* load without bar fracture. The result indicates that the repeated testing, and the pre-existing localized crack (from *Blast 2*) was a key driver of the bar rupture observed in the beam tested under repeated blast loading. Under the single *Blast 3* load the NSC-10M-75-FJ-S specimen shows a support rotation of θ_{max} of 2.6° (which qualifies as "moderate" damage according to the CSA S850 standard), with reduced displacements d_{max} = 50.6 mm and d_{res} = 40.2 mm, representing decreases of 40% and 43% when compared to the control reinforced concrete specimen. Actual damage is associated with many closely-spaced and fine cracks, and the formation of a dominant crack, with a width of 14 mm indicating complete fiber pullout. Although the maximum crack width is greater when compared to the control beam (14 vs 7.5 mm), crushing and damage is clearly better controlled in the retrofit specimen. The next section examines the residual capacity of the beams which survived the blast tests.

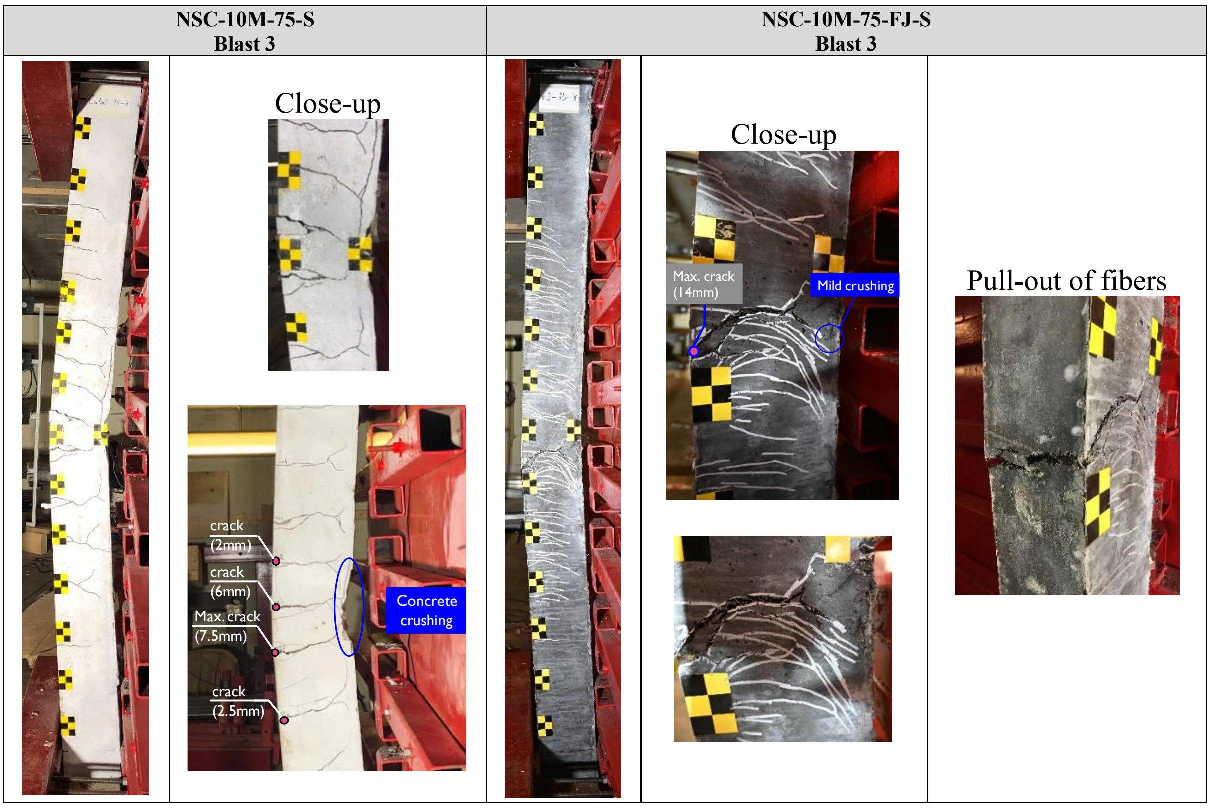

Figure 7 - 11 Progression of damage in beams under single blast loading (Blast 3)

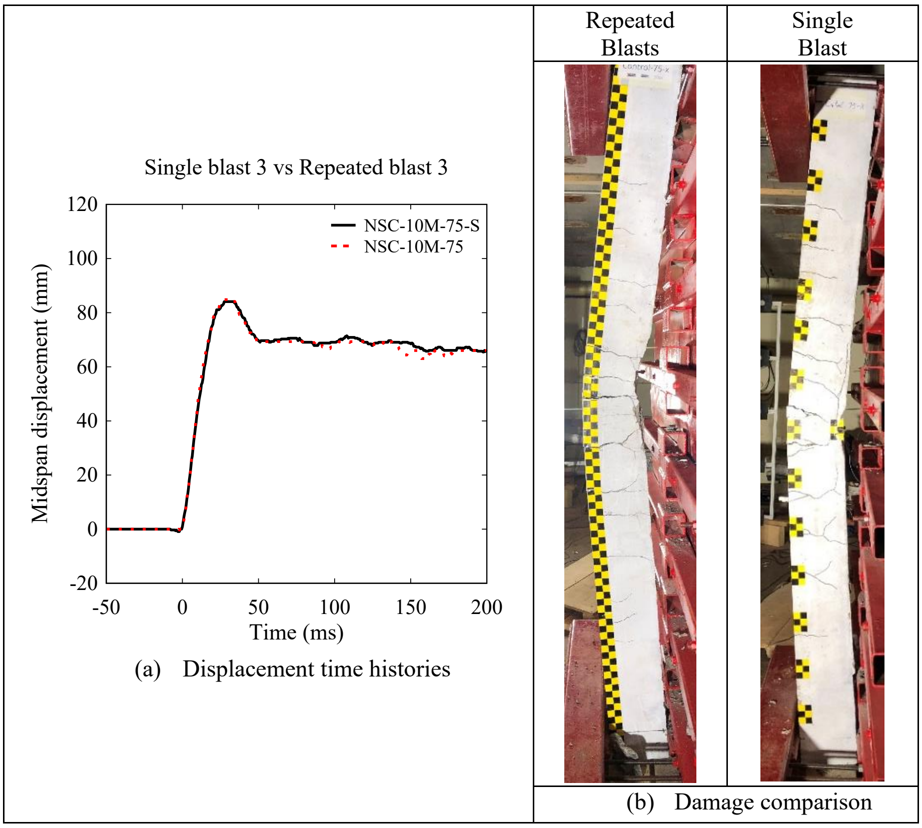

(a) Displacement time histories

(b) Damage comparison

Figure 7 - 12 Effect of repeated blast loads in control beams

7.3.4 Post-blast residual static flexural capacity

The beams which survived the blast tests were subsequently tested under static loading to assess their post-blast residual flexural capacity. The residual load-displacement curves of the beams are plotted in **Figure 7 - 13**. Photos at end of testing are shown in **Figure 7 - 14**. The parameters extracted from the residual tests include the maximum residual load (P^R_{max}) and residual stiffness (k^R_s). To compare to the results from the undamaged beam tests, **Table 7 - 5** also reports the residual resistance index, defined as $RRI = P^R_{max}/P_{max}$, the damage index, defined as $D = 1 - RRI$, and the residual stiffness index, defined as $RSI = k^R_s/k_s$. According to Adhikary et al. [36] the damage index can assess the degree of damage after impact testing, with $D < 0.2$, $D = 0.2 - 0.5$, $D = 0.5 - 0.8$ and $D > 0.8$, qualifying as “low”, medium”, “high” and “severe” damage, and the same criteria is adopted for the current blast tests.

Table 7 - 5 Summary of post-blast residual static test results

Beam ID	Blast load type	Residual Load			Residual Stiffness		Energy absorption capacity		
		P^R_{max} (kN)	RRI	D	k^R_s (N/mm)	RSI	IEI	REI	TEI
NSC-10M-75	Repeated blasts	42.9	0.88	0.12	2692	0.71	0.62	0.37	0.99
NSC-10M-75-S	Single blast	42.2	0.86	0.14	3232	0.85	0.48	0.51	0.99
NSC-10M-75-FJ-S	Single blast	52.6	0.76	0.24	7351	0.96	0.73	0.29	1.02

Note: P^R_{max}= Peak residual load; k^R_s= Residual stiffness; D = Damage index; $RRI = \frac{P^R_{max}}{P_{max}}$ = Residual resistance index: $RSI = \frac{k^R_s}{k_s}$ = Residual stiffness index; *IEI* = Impact energy index; *REI*= Residual energy index, *TEI* = Total energy index.

The first replicate control beam (NSC-10M-75) was tested under repeated blasts corresponding to *Blasts 1-2-3*, with a cumulative maximum displacement of d^c_{max} = 113 mm and cumulative residual displacement of d^c_{res} = 93 mm. The beam damage after the blast tests consisted of the loss of top concrete cover and the formation of wide cracks in the midspan region. Despite this, as shown in **Figure 7 - 13(b)** the beam retained significant post-blast residual capacity, with a maximum load of $\mathrm{P^R_{max}}$ = 42.9kN, representing an RRI of 0.88 and damage index of 0.12, which qualifies as “low damage”. The beam also shows reasonably high residual stiffness, with an RSI of 0.71. After shifting by $\mathrm{d^c_{res}}$ it can be seen that the damaged beam response matches well with the response in the “undamaged” static test (**Figure 7 - 13(e)**). The beam ultimately failed due to rupture of the tension steel at a total cumulative displacement of 181mm. The results clearly demonstrate the beneficial effects of “moderate” reinforcement detailing on the blast and post-blast resilience of conventional reinforced concrete beams.

The second replicate control beam (NSC-10M-75-S) was tested under a single blast corresponding to *Blast 3*, with displacements of d_{max} = 84 mm and d_{res} = 70 mm recorded during the blast test. While crushing had initiated, the top cover was still attached to the beam after the blast test. The response of the beam during the residual test is shown in **Figure 7 - 13(c)**. Once again, the result shows that the beam retained significant capacity of P_{max}^{R} = 42.2kN, with an RRI of 0.86 and damage index of 0.14 ("low" damage). The beam also retained significant residual stiffness with an RSI of 0.85, which is higher when compared to the beam tested under repeated blasts. After shifting the displacement by d_{res} the damaged beam response matches well with the "undamaged" static test result, with the beam surviving up to a total cumulative displacement of 195 mm (**Figure 7 - 13(f)**). Comparing the responses of the two replicates, the beam tested under repeated blast loads shows a similar residual capacity, but lower residual stiffness, and suffered bar rupture due to the effects of accumulated damage and larger cumulative displacement (**Figure 7 - 13(a)**).

Beam NSC-10M-75-FJ was tested under single *Blast 3* loading, with displacements of d_{max} = 51 mm and d_{res} = 40 mm recorded during the blast test. At the end of the blast the beam showed crack localization with pullout of fibers at the dominant crack. The beam also showed signs of UHPFRC crushing at midspan. As shown in **Figure 7 - 13(d)**, the beam showed a residual capacity of P_{max}^{R} = 52.6kN, with an RRI of 0.76, damage index of 0.24 ("medium" damage) during the residual test. The beam also retained nearly perfect residual stiffness with an RSI of 0.96. After shifting the displacement by d_{res} the damaged beam response of NSC-10M-75-FJ matches well with the "undamaged" static test response. It is noted that bar rupture was delayed during the residual test, with the beam surviving up to a total cumulative displacement of 82 mm (**Figure 7 - 13(g)**). Consistent with the undamaged static tests, the retrofit beam shows higher residual capacity and residual stiffness, but lower residual ductility, when compared to the control blast-damaged beam (**Figure 7 - 13(a)**).

In general, the results indicate that both the control and retrofit beams retained important residual capacity, stiffness and energy absorption capacity when compared to the undamaged beam tests. Zanuy and Ulzurrun [37] proposed the "Total Energy Index" to compare the energy absorption and failure modes of undamaged and impact-damaged beams under static loading. As shown in **Figure 7 - 15**, this index is defined as $TEI = IEI + REI$, where IEI and REI are impact and residual energy indices, calculated as $IEI = \frac{A}{A+B}$ and $REI = \frac{C}{A+B}$, where $A + B$ is the total energy absorbed in the undamaged specimen under static loading, and C is the residual energy absorbed in the damaged beam during the residual static test. According to Zanuy and Ulzurrun [37], a TEI ≤ 0.85 indicates a change in failure mode from "ductile" to "brittle" for undamaged versus damaged specimens, and a TEI of approximately 1.0 indicates the same failure mode for undamaged and damaged beams. As shown in **Table 7 - 5**, both NSC-10M-75 replicates and the NSC-10M-75-FJ beam tested under single blast loading show TEI indices of 0.99, 0.99 and 1.02 which confirms that the specimens showed similar failure modes and energy absorption capacities when compared to the undamaged beam tests.

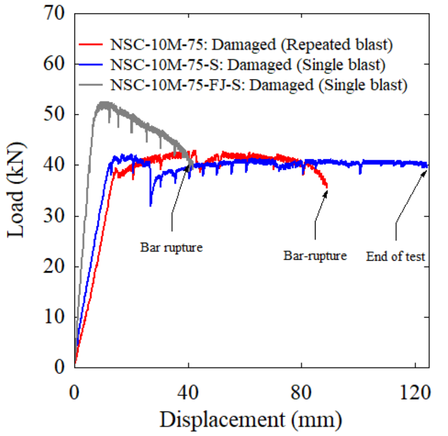

a) Residual static test results (all beams)

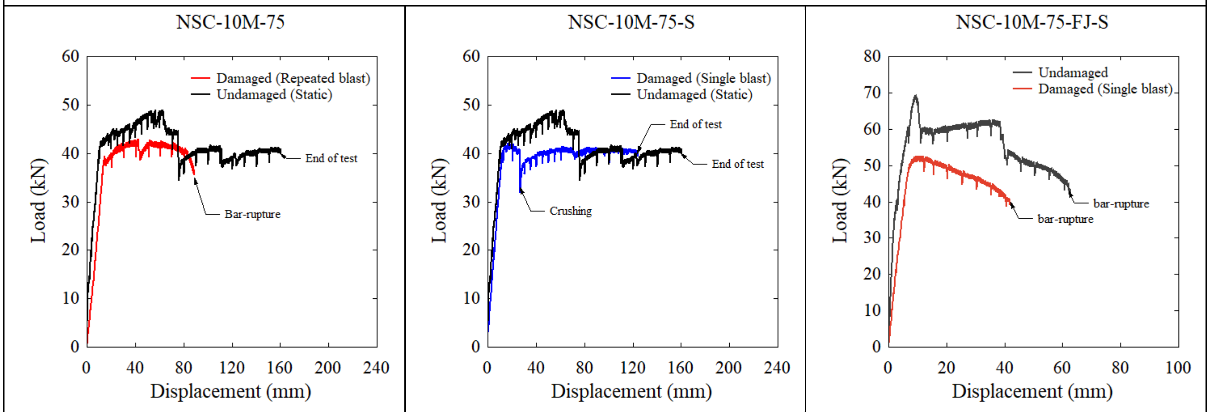

b) NSC-10M-75 – repeated blasts

c) NSC-10M-75-S – single blast

d) NSC-10M-75-FJ-S – single blast

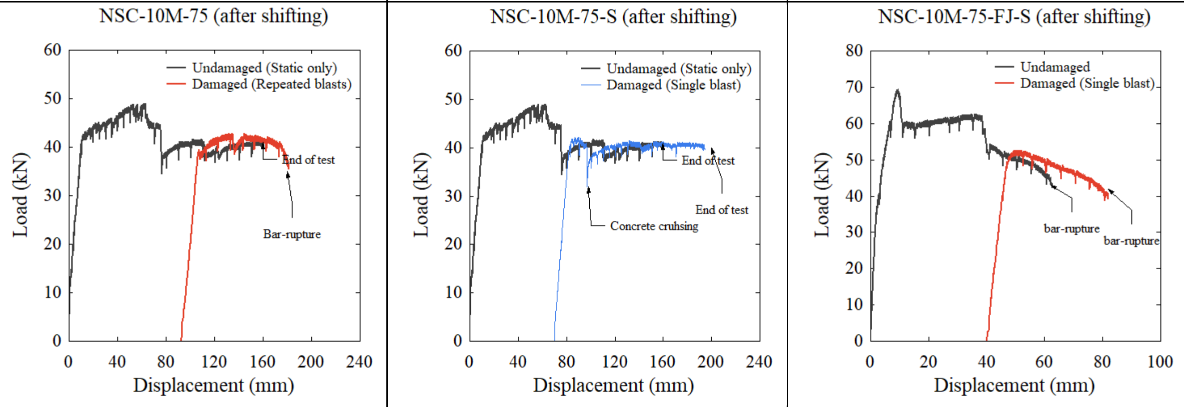

e) NSC-10M-75 – repeated blasts (after shifting by d_{res}^{cum})

f) NSC-10M-75-S – single blast (after shifting by d_{res})

g) NSC-10M-75-FJ-S – single blast (after shifting by d_{res})

Figure 7 - 13 Results from post-blast residual static tests

Specimens	Static loading	Failure mode
NSC-10M-75 (Static test)		Concrete cruhsing
NSC-10M-75 (Residual test after repeated blast)		Concrete cruhsing & Bar-rupture
NSC-10M-75-S (Residual test after single blast)		Concrete cruhsing
NSC-10M-75-FJ (Static test)		Bar-rupture
NSC-10M-75-FJ-S (Residual test after single blast)		Bar-rupture

Figure 7 - 14 Damage photographs of beams at end of static and residual static tests

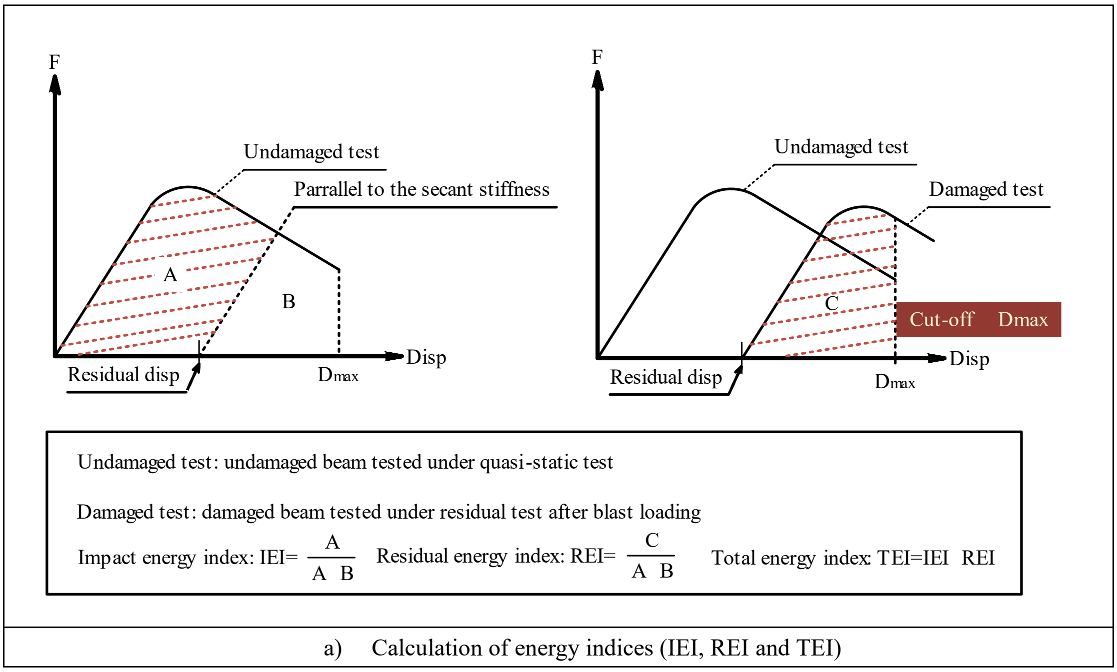

a) Calculation of energy indices (IEI, REI and TEI)

Figure 7 - 15 Definitions used in the calculation of the Total Energy Index

7.4 Finite Element Modelling

7.4.1 FE modelling of test beams

7.4.1.1 FE model and meshing

Finite element (FE) modelling was used to simulate the blast behaviour of the test beams using LS-DYNA [38], a general-purpose software which can simulate the non-linear behaviour of reinforced concrete structures under transient dynamic loading.

Figure 7 - 16 presents the 3D model used in the FE simulations. Within LS-DYNA similar functions are grouped together under the same keyword. The element formulations and cross-sectional properties are defined within keyword **SECTION*. The concrete and UHPFRC were built using eight node hexahedron elements (**SECTION_SOLID*), with a mesh size of 10 × 10 × 10 mm, and constant stress solid element formulation. The steel reinforcement was modelled using two node Hughes-Liu beam elements (**SECTION_BEAM*) with a mesh size of 10 mm. The mesh for a typical specimen consisted of 73200 solid concrete elements and 2514 beam elements. The keyword **CONSTRAINED* can be used to constrain degrees of freedom so that they move together. Perfect bond was assumed between the concrete and steel reinforcement using keyword **CONSTRAINED_LAGRANGE_IN_SOLID*, which constrains the beam elements to move with the solid elements. Perfect bond between the concrete (NSC) and UHPFRC was ensured by sharing common nodes. To closely replicate the shock-tube setup, the load transfer device (LTD) was simulated by using *Belytschko-Tsay* shell elements (**SECTION_SHELL*). The keyword **BOUNDARY* is used in LS-DYNA to define imposed motions on boundary nodes. The support conditions in the tests allowed rotation but prevented translation at the beam ends. To closely simulate the support conditions, steel beams were built at each support (using **SECTION_SOLID*) and connected with bolts using the keyword **SECTION_DISCRETE*. The boundary conditions were specified using the **BOUNDARY_SPC_SET* keyword, while the intersections between the concrete portion (Master) and LTD or steel supports (Slave) were simulated by the contact algorithm **CONTACT_AUTOMATIC_SURFACE_TO_SURFACE.*

Blast loads were simulated using idealized triangular blasts with the same reflected pressure and positive-phase impulse found in the experiments. The blasts were applied onto the load transfer device using the **LOAD_SEGMENT_SET* keyword in LS-DYNA. In the case of the specimens tested under repeated blasts, the effects of accumulated damage were considered by applying the blasts in succession with a sufficient time gap between each loading.

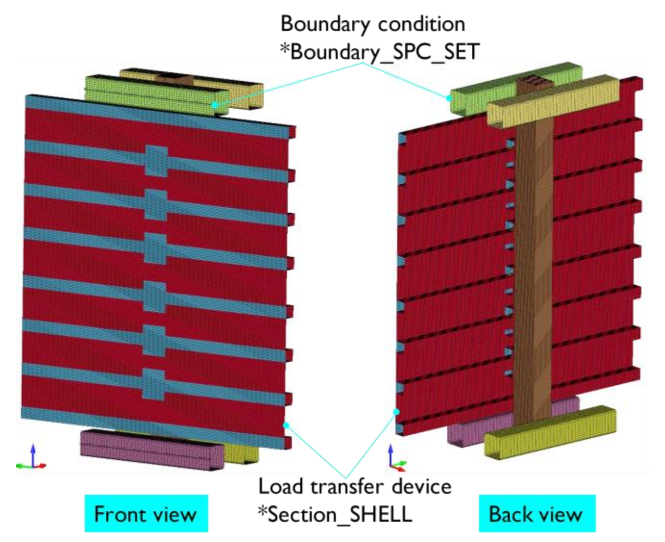

a) Modelling of shock tube

b) Concrete and steel elements

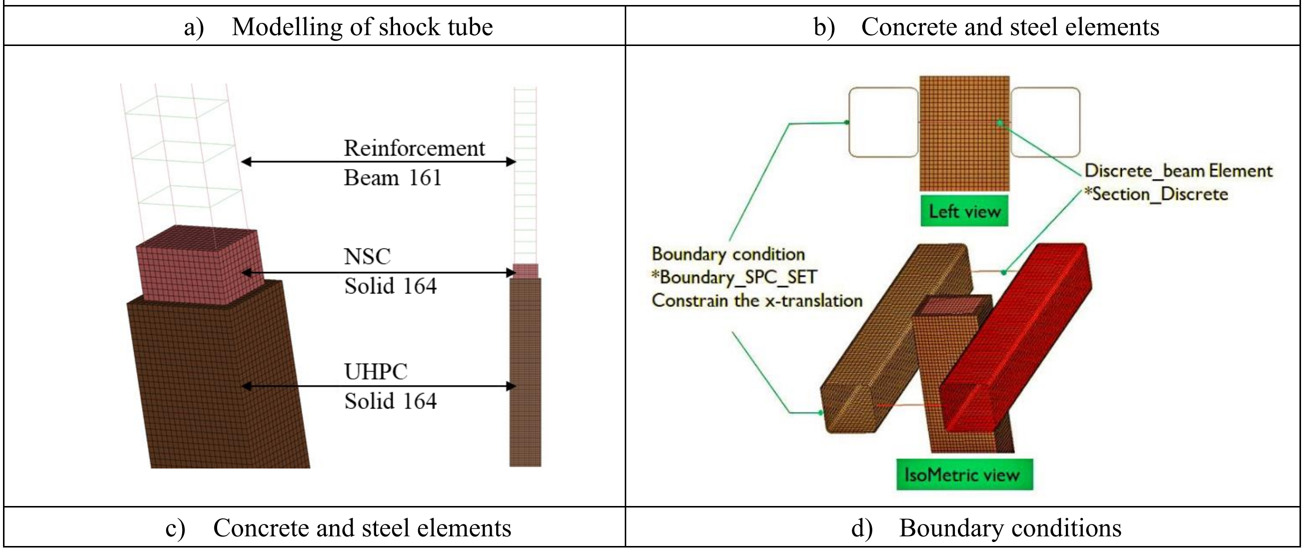

c) Concrete and steel elements

d) Boundary conditions

Figure 7 - 16 FE modelling: 3D model, concrete/steel elements and boundary conditions

7.4.1.2 Material models

LS-DYNA contains a large material library for the simulation of reinforced concrete materials. Each material is defined using the keyword *MAT* followed by a numerical or descriptive designation. In this study, the normal-strength concrete and UHPFRC were modeled using the Continuous Surface Cap Model, designated as *MAT_159* and *MAT_CSCM* [39]. This model can be used to simulate concrete-like materials and was developed specifically for structures exposed to impact loading. The ability of the model to simulate concrete structures under blast loads has also been verified in several previous studies [40, 41]. The model includes various formulations including: isotropic constitutive equations, three stress-invariant shear surface, a hardening cap, damage-based softening and rate effect formulations for high-strain rate applications [39]. For conventional concrete the model includes initialization routines for strength, stiffness, hardening, softening and rate effects which can be simply defined using the concrete compressive strength (f_c') and maximum aggregate size (*DAGG*), taken as 58 MPa and 10 mm for the normal-strength concrete. Rate effects are implemented in the CSCM model and were considered for the NSC using the equations shown in **Table 7 - 6** [39].

UHPFRC shows enhanced properties in tension and compression when compared to conventional concrete, therefore the default parameters in the CSCM model need to be adjusted. Guo et al. [42] presented a comprehensive study which calibrated the CSCM model for UHPFRC, with consideration of rate effects. Subsequently, the calibrated parameters were confirmed to well-predict the behaviour of UHPFRC and UHPFRC-strengthened structures under impact and blast loads [20, 21, 43]. Therefore, the calibrated CSCM parameters shown in **Table 7 - 6** were used to model the UHPFRC in the retrofit beams. Rate effects were considered using the revised equations proposed by Guo et al. [42] based on the formulations in Fujikake et al. [44, 45].

The longitudinal and transverse steel reinforcement were modeled using the *MAT_003* model (*MAT_PLASTIC_KINEMATIC*). This bi-linear model is suitable for modelling kinematic hardening plasticity in steel reinforcement, and includes rate effects using the Cowper and Symonds model [46]. The parameters used to define the model are obtained from the steel coupon tests.

Table 7 - 6 Constitutive models of materials used in LS-DYNA

FE models	
Normal-strength Concrete: *MAT_CSCM_CONCRETE (159) (MAT_159) Default model parameters generated with f_c' based on cylinder tests	Ultra-high performance fiber reinforced concrete (UHPFRC): *MAT_CSCM (159) (MAT_159) Material properties determined by 45 input parameters using the calibrated values presented in Guo et al (2018).
DIF formulations for concrete in tension and compression: $DIF_t = f_{t,d}'/f_t' = 1 + E\dot{\varepsilon}\,\eta_{0t}/(f_t'\dot{\varepsilon}^{N_t})$ $DIF_c = f_{c,d}'/f_c' = 1 + E\dot{\varepsilon}\,\eta_{0t}/(f_c'\dot{\varepsilon}^{N_c})$	Rate effect parameters $\eta_{ot}, \eta_{oc}, N_t, N_c$ were updated based on the following expressions in Guo et al (2018). $\eta_{0t} = 0.7912\,f_t'/E,\ N_t = 0.7087$ $\eta_{0c} = 0.311\,f_c'/E,\ N_c = 0.7817$
Longitudinal steel: *MAT-PLASTIC_KINEMATIC (MAT_003) Mass density: 7800 kg/m^3 Poisson's ratio: 0.3 Young's modulus: 200 GPa Yield stress: varies – based on coupons Failure strain: varies – based on coupons DIF: Cowper & Symonds strain rate model which scales the yield stress with the factor $1 + (\frac{\dot{\varepsilon}}{C})^{\frac{1}{p}}$	

7.4.1.3 FE model results

The results from the FE simulations are presented in **Table 7 - 7** and **Figure 7 - 17 & Figure 7 - 18**, which present a comparison between the numerical and experimental maximum displacements (d_{max}^{num} and d_{max}), displacement time-histories, and damage modes.

Considering all blast tests and beams, the mean $d_{max}^{\text{num}}/d_{max}$ ratio is 1.03, with an average error of 8.3%, and coefficient of variation of 9.36%. Considering the individual specimens, beam NSC-10M-75 shows $d_{max}^{\text{num}}/d_{max}$ ratios of 1.09, 1.19 and 0.92 under Blast 1-2-3 loading, and 0.98 under the single Blast 3 scenario. In general, the damage patterns and displaced shapes also match well with the experimental damage photos. The simulation for beam NSC-10M-75-FJ under repeated blast loads results in $d_{max}^{\text{num}}/d_{max}$ ratios of 0.99 and 0.91 under Blast 1 and 2, and captures the crack localization and bar rupture at Blast 3. Under the single Blast 3 load, the simulation results in an accurate prediction of the maximum displacement with a $d_{max}^{\text{num}}/d_{max}$ ratio of 1.10, and correctly simulates the damage mode (including crack localization), without bar rupture.

In summary the FE simulations showed good agreement with the experimental tests. In particular, the modeling was able to predict the displaced shapes, damage patterns and failure modes observed in the test beams. In the next section the validated FE models are used to further study the effects of steel ratio, jacket thickness and jacket interface location on the blast response of the UHPFRC-retrofitted beams under single or repeated blast loading.

Table 7 - 7 Results of numerical FE predictions

Beam ID	Blast ID	Shockwave Properties[1]			Specimen Response[2]			
		P_r (kPa)	t_d (ms)	I_r (kPa·ms)	d_{max} (mm)	d_{max}^{num} (mm)	d_{max}^{num}/d_{max}	Error (%)
NSC-10M-75	1	20.9	13.9	145.22	14.8	16.1	1.09	8.8%
	2	43.9	11.9	261.5	39.8	47.4	1.19	19%
	3	50.5	14.33	361.89	85.5	78.4	0.92	8.3%
NSC-10M-75-FJ	1	16.9	16	135.1	10.5	10.4	0.99	1.0%
	2	37.5	13.3	249.6	27.2	24.8	0.91	8.8%
	3	49.1	15.5	380.1	Rupture	-	-	-
NSC-10M-75-S	3	53	14.1	374.9	84.1	82.2	0.98	2.3%
NSC-10M-75-FJ-S	3	47.8	16.2	387.9	50.6	55.7	1.10	10%
Statistical analysis	Mean d_{max}^{num}/d_{max}						1.03	
	Mean error						8.3%	
	Standard deviation						0.1	
	Coefficient of variation						9.36%	

Note:

[1]: Idealized shockwave properties: P_r = Reflected pressure; I_r = Reflected impulse; t_d = positive phase duration;

[2]: d_{max} = maximum mid-span displacement from tests; d_{max}^{num}= maximum mid-span displacement obtained from FE simulation;

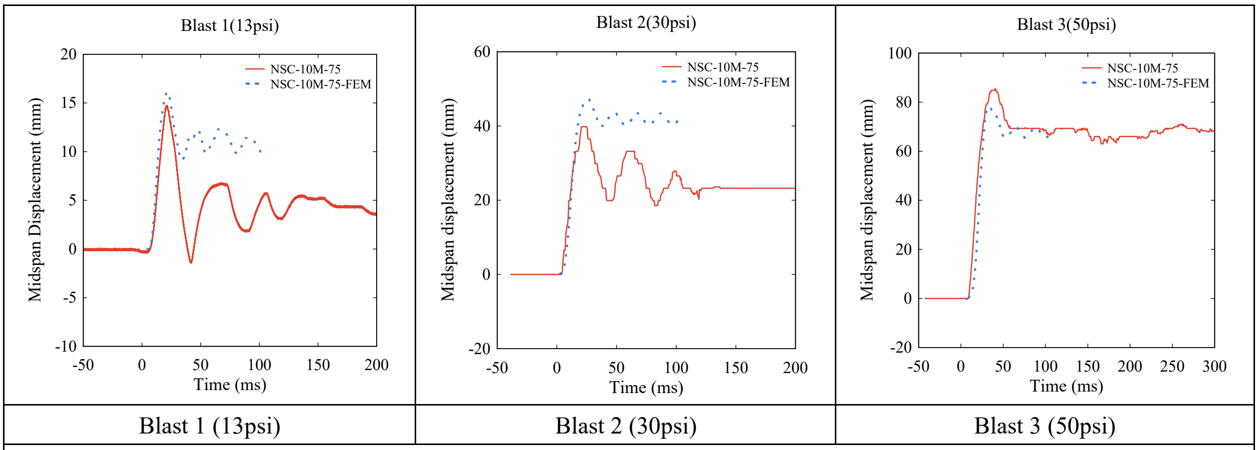

Blast 1 (13psi)

Blast 2 (30psi)

Blast 3 (50psi)

a) NSC-10M-75 (repeated blasts)

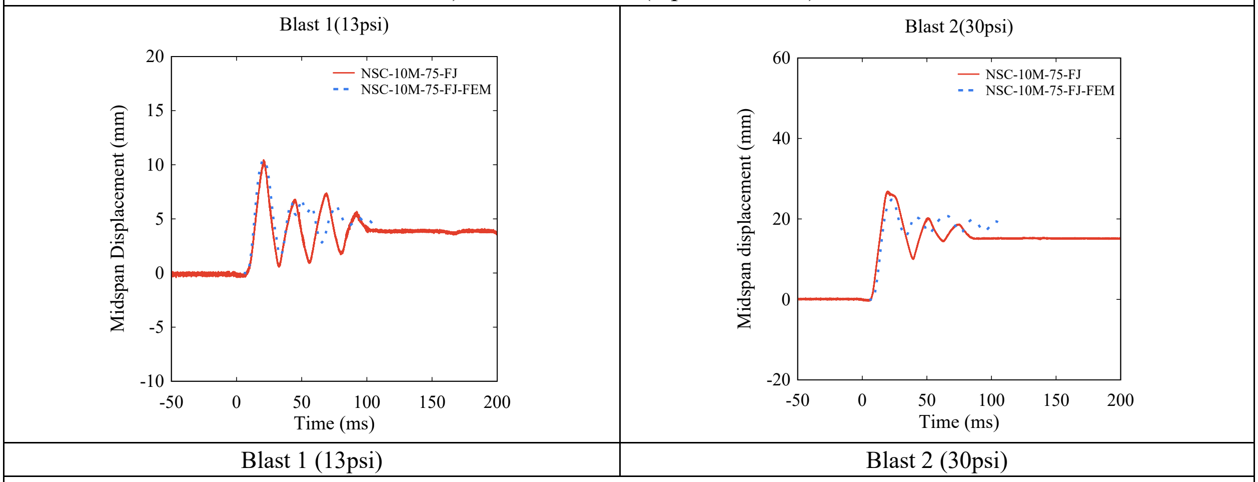

Blast 1 (13psi)

Blast 2 (30psi)

b) NSC-10M-75-FJ (repeated blasts)

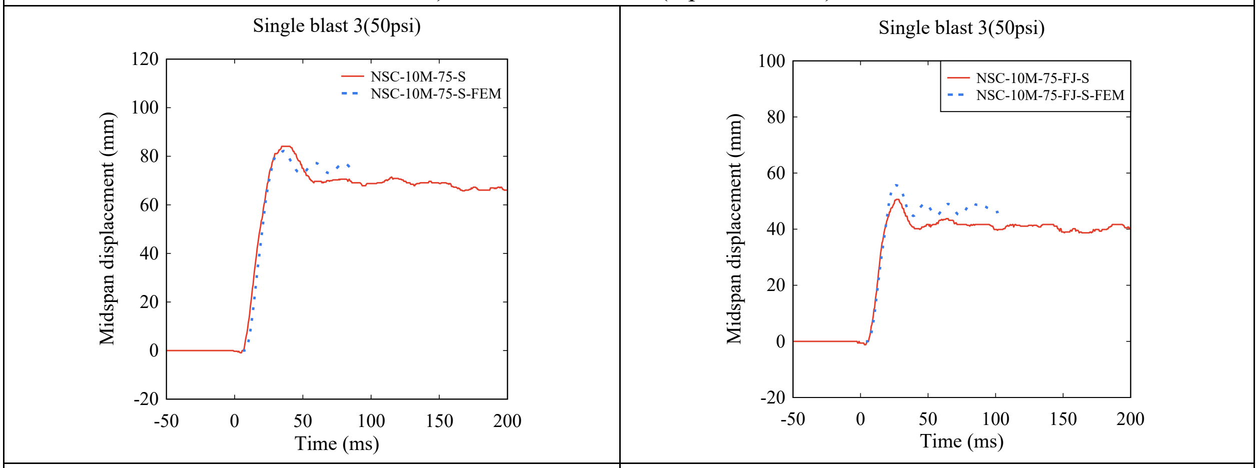

Blast 3 (50psi)

Blast 3 (50psi)

c) NSC-10M-75-FJ-S (single blast)

d) NSC-10M-75-FJ-S (single blast)

Figure 7 - 17 Sample numerical analysis results for control and retrofit beams

<table>
<tr><th colspan="2">NSC-10M-75 (repeated blasts)</th><th colspan="2">NSC-10M-75-FJ (repeated blasts)</th></tr>
<tr><td>Blast 2 (30psi)</td><td>Blast 3 (50psi)</td><td>Blast 2 (30ps)</td><td>Blast 3 (50psi)</td></tr>
<tr><td>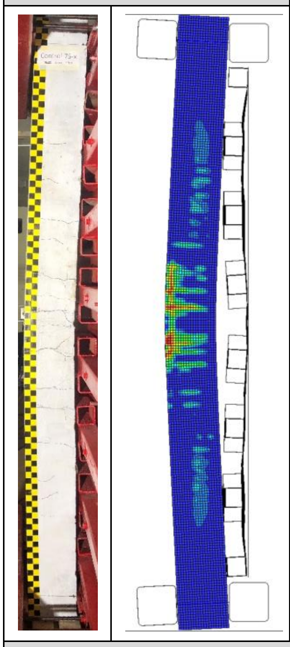</td><td>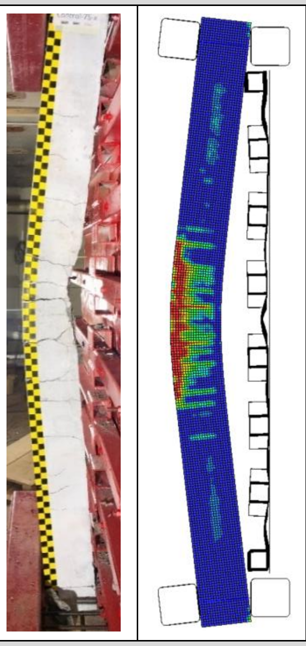</td><td>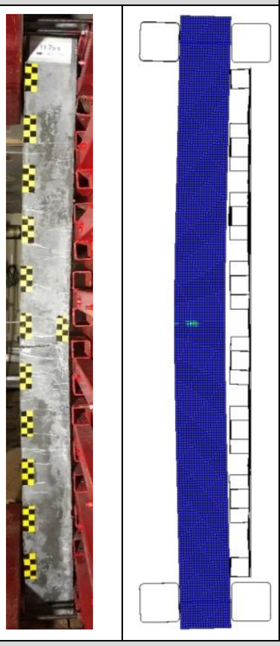</td><td>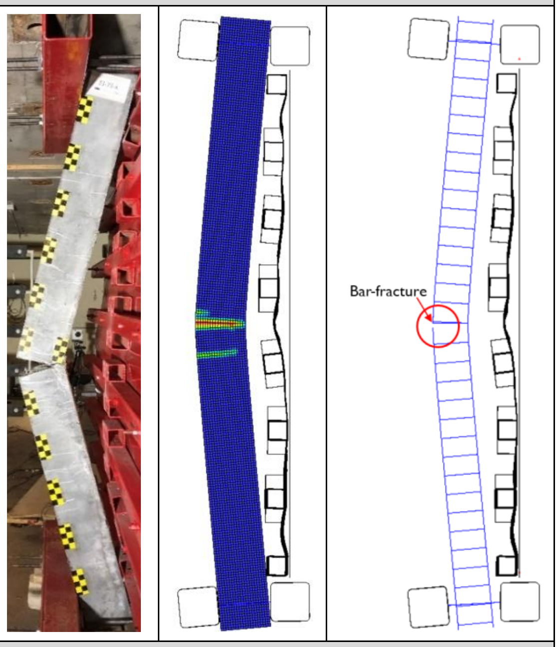 </td></tr>
<tr><th colspan="2">NSC-10M-75-S (single blast)</th><th colspan="2">NSC-10M-75-FJ-S (single blast)</th></tr>
<tr><td colspan="2">Blast 3 (50psi)</td><td colspan="2">Blast 3 (50psi)</td></tr>
<tr><td colspan="2">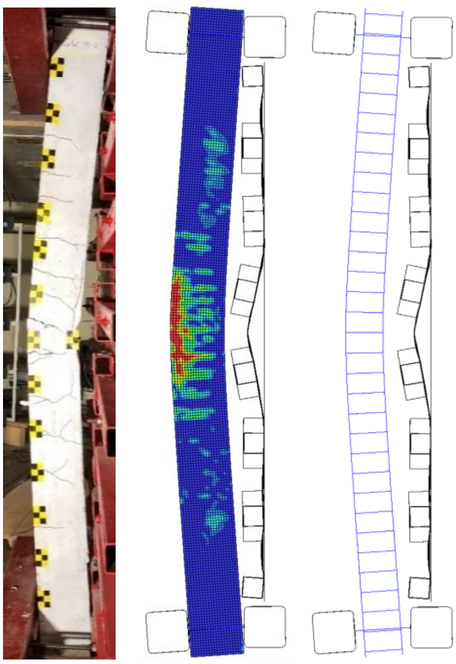</td><td colspan="2">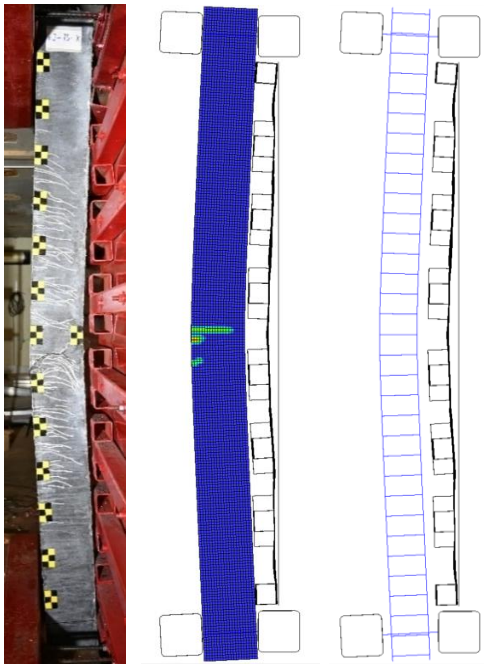</td></tr>
</table>

Figure 7 - 18 Experimental and numerical damage profiles after repeated and single blasts

7.4.2 Parametric study

Based on the validation of FE simulations, a parametric study is presented in this section. The following variables were considered: the longitudinal steel ratio (0.8, 1.6, 2.4%), jacket thickness (10, 20, 30 mm) and jacket interface location (at or away from bar interface). The properties of beam and cross section details are shown in **Table 7 - 8** and **Figure 7 - 19**.

Table 7 - 8 Properties of beam in the parametric study

Parameters	Beam ID	Blast load type	Longitudinal reinforcement (tension zone)		UHPFRC		Section dimensions
			Bar size	Steel ratio ρ (%)	Thickness (mm)	Interface	
Effect of steel ratio	NSC-10M-75	Repeated (Blasts 1-2-3)	10M	0.8%	-	-	150 × 200
	NSC-15M-75		15M	1.6%	-	-	
	NSC-20M-75		20M	2.4%	-	-	
	NSC-10M-75-S	Single (Blast 3)	10M	0.8%	-	-	150 × 200
	NSC-15M-75-S		15M	1.6%	-	-	
	NSC-20M-75-S		20M	2.4%	-	-	
	NSC-10M-75-FJ	Repeated (Blasts 1-2-3)	10M	0.8%	20	at bar interface	150 × 200
	NSC-15M-75-FJ		15M	1.6%			
	NSC-20M-75-FJ		20M	2.4%			
	NSC-10M-75-FJ-S	Single (Blast 3)	10M	0.8%	20	at bar interface	150 × 200
	NSC-15M-75-FJ-S		15M	1.6%			
	NSC-20M-75-FJ-S		20M	2.4%			
Effect of UHPC thickness and interface location	NSC-10M-75-FJ	Repeated (Blasts 1-2-3)	10M	0.8%	20	at bar interface	150 × 200
	NSC-10M-75-FJ(10)		10M	0.8%	10	10 mm away from bars	150 × 200
	NSC-10M-75-FJ(20+)		10M	0.66%	20		170 × 220
	NSC-10M-75-FJ(30+)		10M	0.56%	30		190 × 240

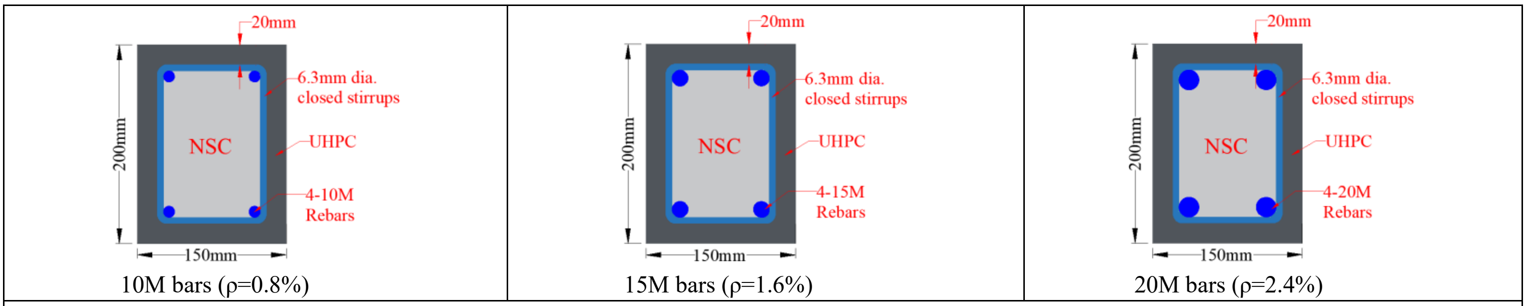

10M bars (ρ=0.8%) 15M bars (ρ=1.6%) 20M bars (ρ=2.4%)

a) Effect of steel ratio

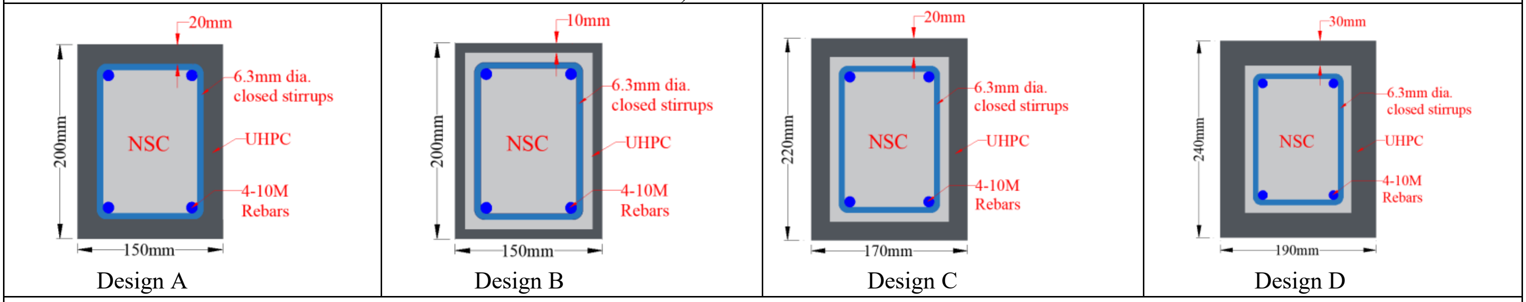

Design A Design B Design C Design D

b) Effect of UHPFRC jacket thickness and interface location

Figure 7 - 19 Cross section details of beams in parametric study

7.4.2.1 Effect of longitudinal steel ratio

The effect of longitudinal steel ratio (ρ) is examined by comparing the dynamic responses of control and UHPFRC retrofitted beams with 10M, 15M or 20M bars, corresponding to ρ = 0.8%, 1.6% and 2.4%, under repeated or single blasts. The properties of the beams are shown in **Figure 7 - 19(a)**, and the nomenclature follows the same logic presented previously (e.g. NSC-15M-75 and NSC-15M-75-FJ are control and retrofits with 15M bars tested under repeated blasts). The results of the analysis are summarized in **Table 7 - 9** and **Figure 7 - 20** to **Figure 7 - 22**.

Table 7 - 9 Results of parametric study on the effect of steel ratio

Beam ID	Blast load type	Blast ID	Numerical results			CSA S850 Response limits	
			d_{max}^{num} (mm)	d_{res}^{num} (mm)	θ_{max}^{num} (°)	Response limit	Expected Damage level
NSC-10M-75	Repeated	1	16.1	10.2	0.8	<B1	Superficial
		2	47.4	41.9	2.4	B2-B1	Moderate
		3	78.4	68.8	4.0	B3-B2	Heavy
NSC-15M-75	Repeated	1	12.7	3.5	0.7	<B1	Superficial
		2	25.4	18.7	1.3	B2-B1	Moderate
		3	44.7	40.1	2.3	B2-B1	Moderate
NSC-20M-75	Repeated	1	11.4	3.8	0.6	<B1	Superficial
		2	15.9	0	0.8	<B1	Superficial
		3	28.3	16.8	1.5	B2-B1	Moderate
NSC-10M-75-FJ	Repeated	1	10.4	4.34	0.5	<B1	Superficial
		2	24.8	19.1	1.3	B2-B1	Moderate
		3	-	-	-	-	-
NSC-15M-75-FJ	Repeated	1	9.3	2.8	0.5	<B1	Superficial
		2	16.6	3.7	0.9	<B1	Superficial
		3	27.3	17.3	1.4	B2-B1	Moderate
NSC-20M-75-FJ	Repeated	1	8.7	2.4	0.5	<B1	Superficial
		2	13	0	0.7	<B1	Superficial
		3	24.9	9.1	1.3	B2-B1	Moderate
NSC-10M-75-S	Single	3	82.2	74.6	4.2	B3-B2	Heavy
NSC-15M-75-S	Single	3	51.5	44.5	2.6	B2-B1	Moderate
NSC-20M-75-S	Single	3	34.8	19.6	1.8	B2-B1	Moderate
NSC-10M-75-FJ-S	Single	3	55.7	46.5	2.9	B2-B1	Moderate
NSC-15M-75-FJ-S	Single	3	37	27.5	1.9	B2-B1	Moderate
NSC-20M-75-FJ-S	Single	3	27.7	8.9	1.4	B2-B1	Moderate

As expected, increasing the steel ratio was effective in improving the control of displacements in both beam types. Beginning with the control set, gradually increasing the steel ratio from ρ = 0.8% to 1.6% (10M to 15M bars) led to reductions of 21% 46% and 43% in maximum displacements under repeated Blast 1-2-3 loading. The beam with 20M bars (ρ = 2.4%) shows further reductions of 29%, 66% and 64% when compared to the control with 10M bars. The same trend is observed under the singly-applied Blast 3 loading, with reductions of 37% and 58% in d_{max}^{num} for the beams with 15M and 20M bars when compared to the control with 10M reinforcement.

Increasing the steel ratio was also effective in reducing the support rotations and damage states. Under repeated Blast 2-3 loading, beams NSC-10M-75, NSC-15M-75 and NSC-20M-75 show rotations of $\theta_{max}^{\text{num}}$ of 2.0° and 4.0° (damage states: "moderate" and "heavy"), 1.3° and 2.3° ("moderate"), and 0.8° and 1.5° ("superficial" and "moderate"), with the same trend observed under single Blast 3 loading. Indeed, **Figure 7 - 21** shows that cracking and damage are better controlled with the increase in ρ. Therefore, it is confirmed that increasing the steel ratio is an effective means to reduce blast-induced displacements, support rotations and damage in conventional reinforced concrete beams with moderate detailing.

The same patterns are observed in the UHPFRC-retrofitted specimens, where the beams with 15M and 20M bars show reductions of 11% and 33%, and 16% and 48% in d_{max}^{num} under Blast 1 and 2. Importantly, while Beam NSC-10M-75-FJ (ρ = 0.8%) suffers bar rupture under the repeated Blast 3 load, beams NSC-15M-75-FJ (ρ = 1.6%) and NSC-20M-75-FJ (ρ = 2.4%) survive this blast with low support rotations of $\theta_{max}^{\text{num}}$ of 1.4° and 1.3°, and moderate damage as shown in **Figure 7 - 21**. Under the singly-applied Blast 3 load, support rotations and damage are also better controlled when increasing the bar size (seen in **Figure 7 - 22**). Thus, it is confirmed that the steel ratio is an important parameter which affects the ductility, failure mode and blast response of UHPFRC-retrofitted beams.

Yoo et al. [30] and Pokhrel and Bandelt [31] reported an increase in ductility and a delay in bar rupture in UHPFRC beams under static loading when increasing ρ from 0.53% to 1.71%, and 0.7% to 1.9%. Shao and Billington [32] further noted a change in failure mode from bar rupture to UHPFRC crushing when increasing ρ from 0.96% to 2.1%. Aoude et al. [34] also observed a delay in bar fracture in UHPFRC columns under blast loading when increasing ρ from 0.86% to 1.72%. As noted in these studies increasing the steel ratio effectively spreads steel reinforcement plasticity which delays bar fracture. Based on the results of the numerical analysis this same effect also occurs in UHPFRC-retrofitted beams under blast loading.

The numerical results can also be used to study the benefits of UHPFRC jacketing in beams with 15M and 20M bars (ρ = 1.6% and 2.4%). Under the repeated Blast 1-2-3 and single Blast 3 loading the UHPFRC in NSC-15M-75-FJ and NSC-15M-75-FJ-S decreased maximum displacements by 27-35-39% and 28% when comparing to the control NSC-15M-75 and NSC-15M-75-S beams. Likewise, in the 20M set, the UHPFRC jacketing reduced d_{max}^{num} by 24-18-12% and 20% under the same blast load scenarios. Thus, the beneficial effects of the UHPFRC jacketing on improving control of blast-displacements and damage in beams with varied steel ratios is confirmed.

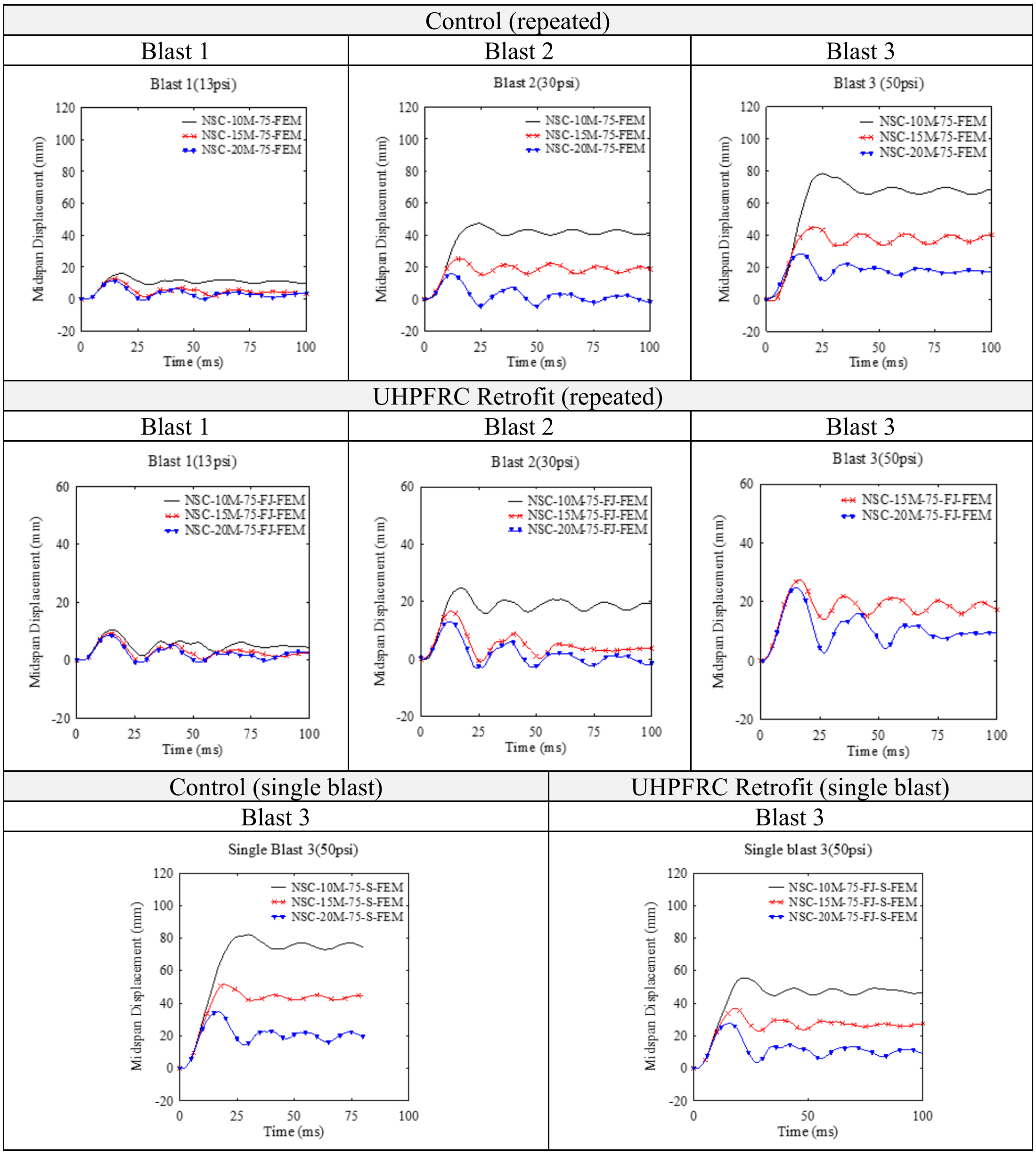

Figure 7 - 20 Effect of steel ratio on displacements under single and repeated blast loading

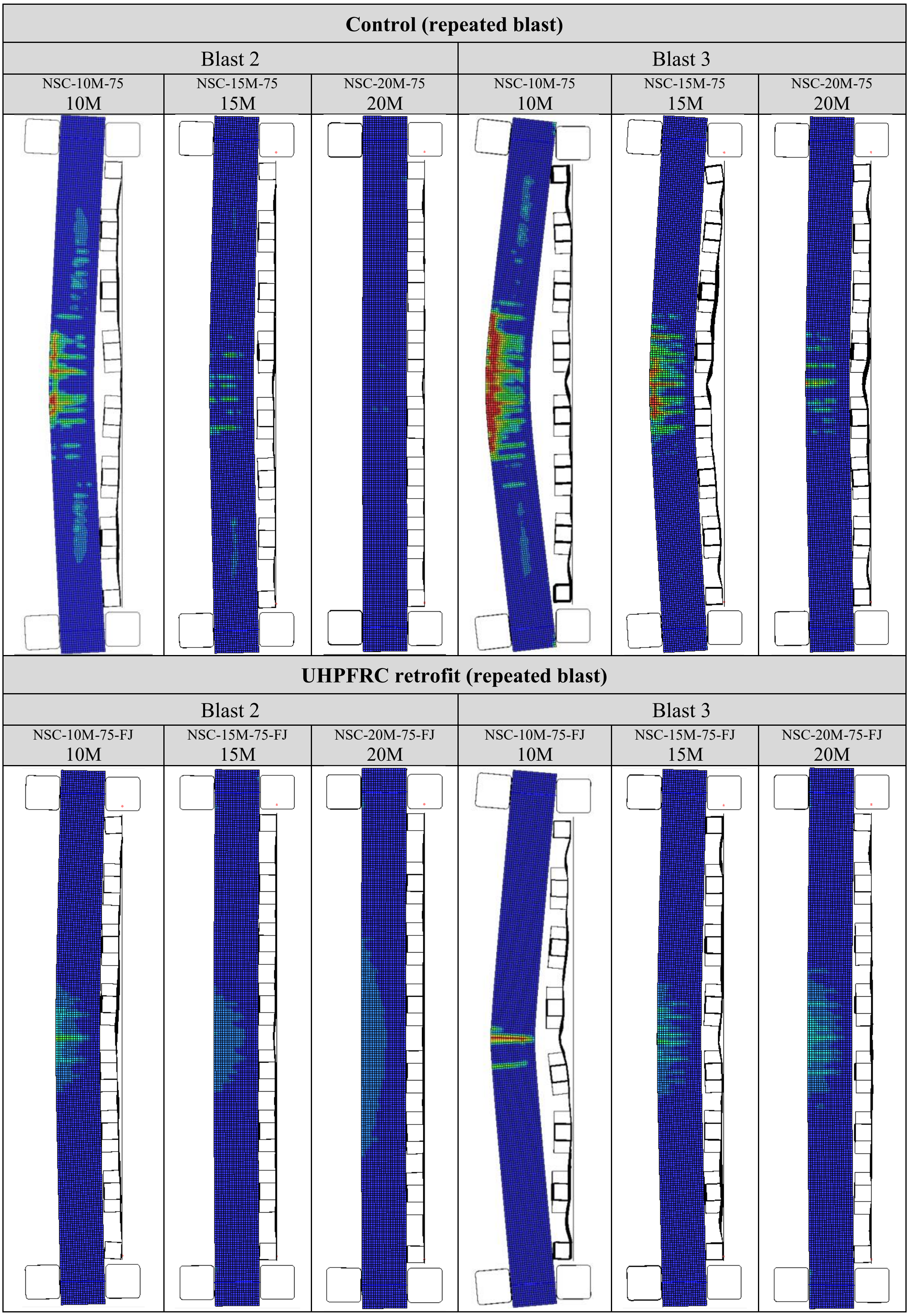

Figure 7 - 21 Effect of jacket steel ratio on damage progression under repeated blast loading

Control (single blast)			UHPFRC retrofit (single blast)		
Blast 3			Blast 3		
NSC-10M-75-S 10M	NSC-15M-75-S 15M	NSC-20M-75-S 20M	NSC-10M-75-FJ-S 10M	NSC-15M-75-FJ-S 15M	NSC-20M-75-FJ-S 20M
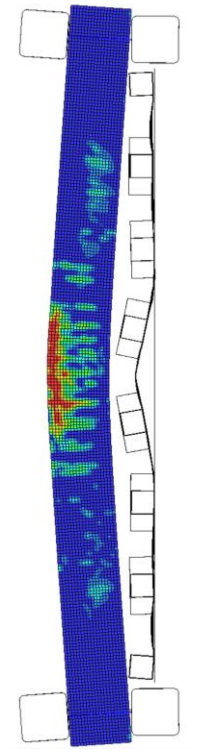	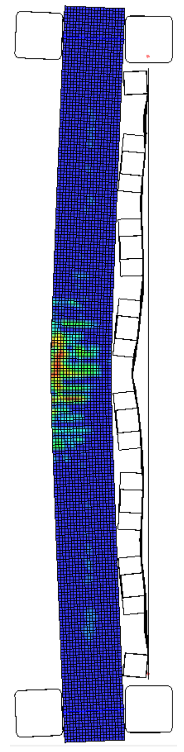	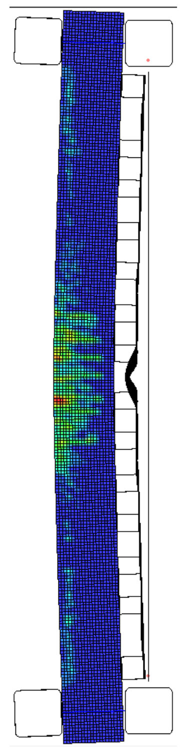	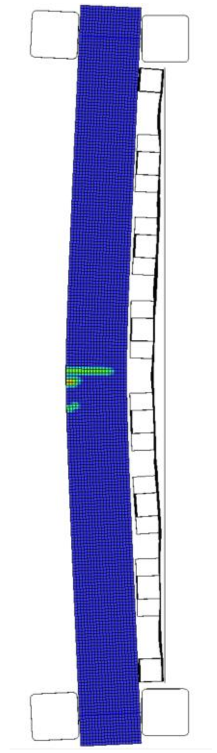	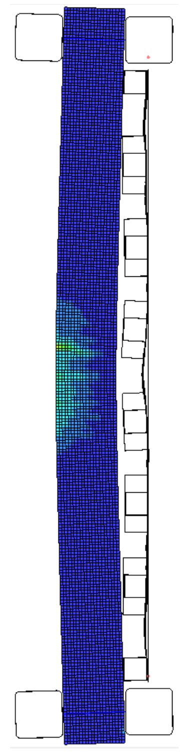	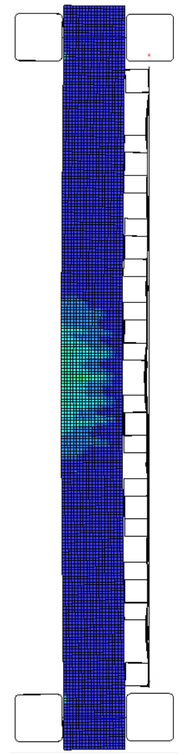

Figure 7 - 22 Effect of jacket steel ratio on damage progression under single blast loading

7.4.2.2 Effect of UHPFRC jacket thickness and interface location

The effect of interface location is investigated by comparing the blast responses of beams NSC-10M-75-FJ and NSC-10M-75-FJ-(+20) under repeated blast loading. Both beams have the same core dimensions and jacket thickness (20 mm), with the UHPFRC applied at the bar interface or 10 mm away from the bars, resulting in total dimensions of 150 × 200 mm and 170 × 220 mm, respectively (see designs A and C in **Figure 7 - 19(b)**). The purpose of the comparison is to examine whether the interface location affects the failure mode in the beams. The results of the analysis are presented in **Table 7 - 10** and **Figure 7 - 23** & **Figure 7 - 24**.

As shown in **Figure 7 - 23**, moving the interface location while keeping the jacket thickness constant in design C, reduces the maximum displacements by 20% and 32% under Blast 1 and 2. The support rotations are also reduced from 0.5° to 0.4°, and from 1.4° to 1.0° when compared to design A. The result can be explained by the slight increase in dimensions which increases the moment arm of the UHPFRC in tension and increases flexural resistance. More importantly, moving the interface location prevents the bar rupture observed in beam

NSC-10M-75-FJ under Blast 3 loading (see **Figure 7 - 24**). The damage profile for design C also shows the development of multiple flexural cracks in the UHPFRC which counters the crack localization effect. Therefore, moving the jacket interface away from the bars is a strategy to counter bar fracture failures in UHPFRC-jacketed beams with low steel ratios.

Table 7 - 10 Results of parametric study on the effect of jacket thickness/interface

Beam ID	Blast ID	Numerical results			CSA S850 response limits	
		d_{max}^{num} (mm)	d_{res}^{num} (mm)	θ_{max} (°)	Response limit	Expected Damage level
NSC-10M-75-FJ	1	10.4	4.34	0.53	<B1	Superficial
	2	24.8	19.1	1.27	B2-B1	Moderate
	3	Rupture	-	-	-	-
NSC-10M-75-FJ(10)	1	11.6	6	0.6	<B1	Superficial
	2	24.8	20.9	1.27	B2-B1	Moderate
	3	57.8	46.4	2.96	B2-B1	Moderate
NSC-10M-75-FJ(20+)	1	8.4	2.7	0.43	<B1	Superficial
	2	18.5	11.6	0.95	<B1	Superficial
	3	39	34.1	2.0	B2-B1	Moderate
NSC-10M-75-FJ(30+)	1	6.7	1.7	0.24	<B1	Superficial
	2	10.4	0.3	0.53	<B1	Superficial
	3	18.6	9	0.95	<B1	Superficial

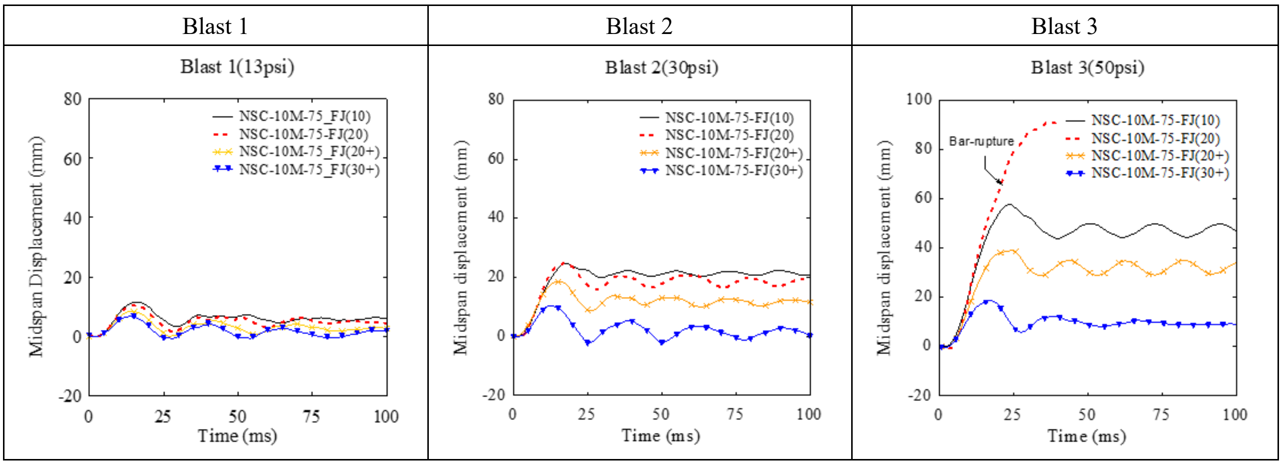

Figure 7 - 23 Effect of jacket thickness on displacements under repeated blast loading

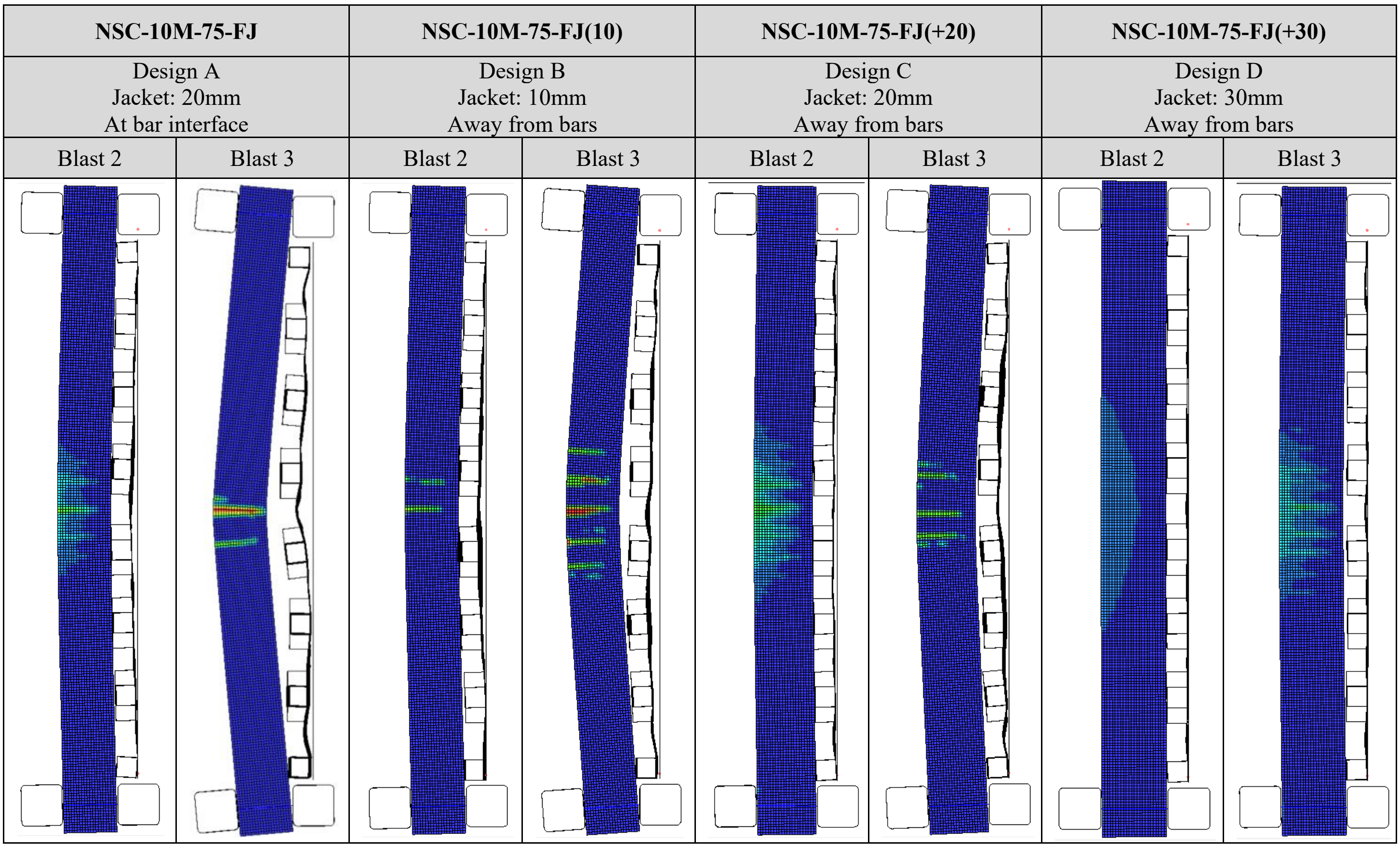

Figure 7 - 24 Effect of jacket thickness on damage progression under repeated blast loading

This effect is further confirmed by comparing the responses of beams NSC-10M-75-FJ and NSC-10M-75-FJ(10) (designs A and B in **Figure 7 - 19(b)**). The beams have the same dimensions of 150 × 200 mm, but with jacket thicknesses of 10 mm and 20 mm, applied away from and just below the bars, respectively. Despite the smaller UHPFRC jacket thickness, beam NSC-10M-75-FJ(10) shows similar displacements when compared to NSC-10M-75-FJ under Blasts 1-2 (see **Figure 7 - 23**). Importantly, this design prevents the bar rupture observed in NSC-10M-75-FJ at Blast 3. As evidenced in the damage profiles, the beam once again shows the formation of multiple wide cracks at midspan when compared to the single dominant crack in NSC-10M-75-FJ (see **Figure 7 - 24**). Comparing to the control NSC-10M-75 concrete beam, the use of the minimal 10 mm UHPFRC jacket in NSC-10M-75-FJ(10) leads to reductions of 28%, 48% and 26% under Blasts 1-2-3, without the problem of bar rupture.

Finally, the effect of jacket thickness is examined by comparing the blast responses of beams NSC-10M-75-FJ(10), NSC-10M-75-FJ(+20) and NSC-10M-75-FJ(+30) (designs B, C and D). As illustrated in **Figure 7 - 19(b)** the beams had the same core dimensions, jacket interface location (away from the bars) but jacket thicknesses of 10 mm, 20 mm and 30 mm on each face, and cross-section dimensions of 150 × 200 mm, 170 × 220 mm and 190 × 240 mm. Examining the displacement time histories in **Figure 7 - 23** it is clear that the increase in jacket thickness reduces the maximum and residual displacements. Compared to design B (10 mm jacket), design C (20 mm jacket) shows reductions of 28%, 25% and 33% in maximum displacements, while design D (30 mm jacket) shows further reductions of 42%, 58% and 68%, under Blast1-2-3 loading. Importantly, all three beams do not show bar rupture failure due to the location of the UHPFRC jacket interface which is placed away from the reinforcing bars (see **Figure 7 - 24**).

Comparing to the control beam without retrofit, design D (30 mm jacket) reduces displacements by 58%, 78% and 76% under Blast 1-2-3, with support rotations of less than 1°, with only superficial damage at the conclusion of Blast 3. The results demonstrate that increasing the jacket dimensions through slight increases of cover and cross-section dimensions is an effective means to improve blast performance.

7.5 Conclusions

This study examined the effects of UHPFRC jacketing on the static and blast performance of doubly reinforced concrete beams with top compression bars and moderately-spaced ties. The effects of the retrofit were examined under quasi-static, repeated blast and singly-applied blast loading. Finite element modelling was further used to predict the blast response of the test beams and conduct parametric studies on the influence of tension steel ratio, jacket thickness and interface location. The following conclusions can be summarized from this study:

1) Under quasi-static loading, the use of UHPFRC jacketing enhanced flexural behavior in terms of strength and stiffness when compared to the control RC beam by margins of 42% and 100%. The use of UHPFRC also led to a distinct cracking pattern, with many closely spaced fine cracks and the formation of one dominant crack at midspan. The high bond capacity of the UHPFRC and this crack localization led to bar rupture failure, which reduced the ductility and drift capacity in the retrofit beam. Based on the results, the interface location and longitudinal steel ratio may be important parameters that affect the performance of beams retrofitted with UHPFRC jacketing;
2) Under repeated Blast 1 and 2 loading, the use of UHPFRC jacketing improved control of maximum and residual displacements and reduced support rotations when compared to the control RC beam. However, the high bond capacity of UHPFRC, crack

localization, and relatively low steel ratio led to brittle bar fracture failure in the UHPFRC retrofitted beam under the subsequent Blast 3 loading. Despite the brittle failure, the UHPFRC was effective in preventing the formation of secondary blast fragments at failure;

3) Under the singly applied Blast 3 load the UHPFRC retrofit beam showed reductions of approximately 40% in maximum and residual displacements, and reductions in support rotations when compared to the control RC specimen. Damage was well controlled, with the formation of a dominant crack, but no bar rupture was observed in the test;
4) The control RC beam specimens showed similar maximum and residual displacements at Blast 3 under single versus repeated blast loading, although greater concrete damage was observed in the beam subjected to repeated testing. Conversely, the repeated blast testing was found to be an important factor in the bar fracture failure observed in beam NSC-10M-75-FJ due to the crack localization which formed at the earlier blasts;
5) The blast-damaged beams were tested under quasi-static loading to assess their residual capacity. Both control beams showed significant residual resistance (with RRI ≥ 0.86) and stiffness (with RSI = 0.7-0.85). The retrofit beam also showed high residual capacity and stiffness with an RRI = 0.76, damage index of 0.24 and RSI of nearly 1.0 (no stiffness degradation), but eventually failed by bar rupture;
6) Finite element modelling was used to simulate the blast response of the control and retrofit beams. The FE simulations resulted in accurate predictions of maximum displacements, with an average $d_{max}^{\mathrm{num}}/d_{max}$ ratio of 1.03. The modelling was also able to well predict the damage and failure modes in the control and retrofit beams;
7) Using the validated FE models, a parametric study was used to investigate the effects of steel ratio, jacket thickness and interface location on blast response. Increasing the tension steel ratio was effective in reducing displacements, support rotations and damage in the control beams under both single and repeated blasts. The same trends were observed in the retrofit beams, while the use of 15M bars (1.6%) was sufficient to prevent bar rupture under repeated blast loading. Moving the UHPFRC jacket interface slightly away from the longitudinal reinforcement was shown to prevent bar rupture, regardless of the jacket thickness (10 mm, 20 mm or 30 mm in this study). Thus, the steel ratio, interface location and jacket thickness are important parameters that should be considered in the blast design of UHPFRC-retrofitted beams.

References

[1] Habel K, Gauvreau P. Behavior of Reinforced and Posttensioned Concrete Members with a UHPFRC Overlay under Impact Loading. Journal of Structural Engineering. 2009;3:292-300.

[2] Ullah R, Qiang Y, Ahmad J, Vatin NI, El-Shorbagy MA. Ultra-High-Performance Concrete (UHPC): A State-of-the-Art Review. Materials (Basel). 2022;15.

[3] Yoo D-Y, Banthia N. Mechanical and structural behaviors of ultra-high-performance fiber-reinforced concrete subjected to impact and blast. Construction and Building Materials. 2017;149:416-31.

[4] Wu ZM, Shi CJ, He W, Wang DH. Static and dynamic compressive properties of ultra-high performance concrete (UHPC) with hybrid steel fiber reinforcements. Cement & Concrete Composites. 2017;79:148-57.

[5] Mohamed M, Ser T, Quek, Jing Z. Behavior of Hybrid-Fiber Engineered Cementitious Composites Subjected to Dynamic Tensile Loading and Projectile Impact. Journal of Meterials in Civil Engineering. 2005;17:143-52.

[6] Brühwiler E. UHPFRC is ready to revolutionize existing and new structures. IABSE Symposium Prague 2022 - Challenges for Existing and Oncoming Structures. Prague, Czech Republic: Zürich, Switzerland, IABSE; 2022. p. 67-79.

[7] Zhu Y, Zhang Y, Hussein HH, Chen G. Flexural strengthening of reinforced concrete beams or slabs using ultra-high performance concrete (UHPC): A state of the art review. Engineering Structures. 2020;205.

[8] Yuan TF, Hong SH, Shin HO, Yoon YS. Bond Strength and Flexural Capacity of Normal Concrete Beams Strengthened with No-Slump High-Strength, High-Ductility Concrete. Materials. 2020;13.

[9] Yin H, Teo W, Shirai K. Experimental investigation on the behaviour of reinforced concrete slabs strengthened with ultra-high performance concrete. Construction and Building Materials. 2017;155:463-74.

[10] Moon J, Reda Taha MM, Kim JJ. Flexural Strengthening of RC Slabs Using a Hybrid FRP-UHPC System Including Shear Connector. Advances in Materials Science and Engineering. 2017:1-7.

[11] Safdar M, Matsumoto T, Kakuma K. Flexural behavior of reinforced concrete beams repaired with ultra-high performance fiber reinforced concrete (UHPFRC). Composite Structures. 2016;157:448-60.

[12] Hussein L, Amleh L. Structural behavior of ultra-high performance fiber reinforced concrete-normal strength concrete or high strength concrete composite members. Construction and Building Materials. 2015;93:1105-16.

[13] Noshiravani T, Brühwiler E. Experimental Investigation on Reinforced Ultra-HighPerformance Fiber-Reinforced Concrete Composite Beams Subjected to Combined Bending and Shear. ACI Stuctural Journal. 2013;110:251-61.

[14] Sakr MA, Sleemah AA, Khalifa TM, Mansour WN, Beushausen H, Dehn F, Moyo P. Behavior of RC beams strengthened in shear with ultra-high performance fiber reinforced concrete (UHPFRC). MATEC Web of Conferences. 2018;199:09002.

[15] Ramachandra Murthy A, Karihaloo BL, Priya DS. Flexural behavior of RC beams retrofitted with ultra-high strength concrete. Construction and Building Materials. 2018;175:815-24.

[16] Paschalis SA, Lampropoulos AP, Tsioulou O. Experimental and numerical study of the performance of ultra high performance fiber reinforced concrete for the flexural strengthening of full scale reinforced concrete members. Construction and Building Materials. 2018;186:351-66.

[17] Tanarslan HM, Alver N, Jahangiri R, Yalçınkaya Ç, Yazıcı H. Flexural strengthening of RC beams using UHPFRC laminates: Bonding techniques and rebar addition. Construction and Building Materials. 2017;155:45-55.

[18] Al-Osta MA, Isa MN, Baluch MH, Rahman MK. Flexural behavior of reinforced concrete beams strengthened with ultra-high performance fiber reinforced concrete. Construction and Building Materials. 2017;134:279-96.

[19] Lampropoulos AP, Paschalis SA, Tsioulou OT, Dritsos SE. Strengthening of reinforced concrete beams using ultra high performance fibre reinforced concrete (UHPFRC). Engineering Structures. 2016;106:370-84.

[20] Fan W, Shen D, Yang T, Shao X. Experimental and numerical study on low-velocity lateral impact behaviors of RC, UHPFRC and UHPFRC-strengthened columns. Engineering Structures. 2019;191:509-25.

[21] Fan W, Xu X, Zhang Z, Shao X. Performance and sensitivity analysis of UHPFRC-strengthened bridge columns subjected to vehicle collisions. Engineering Structures. 2018;173:251-68.
[22] Wei J, Li J, Wu C, Liu Z-x, Fang J. Impact resistance of ultra-high performance concrete strengthened reinforced concrete beams. International Journal of Impact Engineering. 2021;158.
[23] Zanuy C, Ulzurrun GSD. Impact Resisting Mechanisms of Shear-Critical Reinforced Concrete Beams Strengthened with High-Performance FRC. Applied Sciences. 2020;10.
[24] Lee JY, Aoude H, Yoon YS, Mitchell D. Impact and blast behavior of seismically-detailed RC and UHPFRC-Strengthened columns. International Journal of Impact Engineering. 2020;143.
[25] CSA. Design and assessment of buildings subjected to blast loads. CSA S850-12. Mississauga, ON: Canadian Standards Association; 2012.
[26] ICRI. ICRI Standard 310.2 Selecting and Specifying Concrete Surface Preparation for Sealers, Coatings, Polymer Overlays, and Concrete Repair with CSP Chips. 2013.
[27] Lloyd A, Jacques E, M S, Palermo D, Nistor I, Tikka T. Capabilities of a Shock Tube to Simulate Blast Loading on Structures. ACI SP-281: Behaviour of concrete structures subjected to blast and impact loadings. 2011:1-20.
[28] Khaksefidi S, Ghalehnovi M, de Brito J. Bond behaviour of high-strength steel rebars in normal (NSC) and ultra-high performance concrete (UHPC). Journal of Building Engineering. 2021;33.
[29] Hung C-C, Lee H-S, Chan SN. Tension-stiffening effect in steel-reinforced UHPC composites: Constitutive model and effects of steel fibers, loading patterns, and rebar sizes. Composites Part B: Engineering. 2019;158:269-78.
[30] Yoo D-Y, Banthia N, Yoon Y-S. Experimental and numerical study on flexural behavior of ultra-high-performance fiber-reinforced concrete beams with low reinforcement ratios. Canadian Journal of Civil Engineering. 2017;44:18-28.
[31] Pokhrel M, Bandelt MJ. Material properties and structural characteristics influencing deformation capacity and plasticity in reinforced ductile cement-based composite structural components. Composite Structures. 2019;224.
[32] Shao Y, Billington SL. Impact of cyclic loading on longitudinally-reinforced UHPC flexural members with different fiber volumes and reinforcing ratios. Engineering Structures. 2021;241.
[33] Silfwerbrand J. Bonded Concrete Overlays. 2017, May 1;39(5):31-6.
[34] Aoude H, Frederic P. Dagenais, Russell P. Burrell, Saatcioglu M. Behavior of ultra-high performance fiber reinforced concrete columns under blast loading. International Journal of Impact Engineering. 2015;80:185-202.
[35] Li Y, Aoude H. Effects of detailing on the blast and post-blast resilience of high-strength steel reinforced concrete (HSS-RC) beams. Engineering Structures. 2020;219.
[36] Adhikary SD, Li B, Fujikake K. Residual resistance of impact-damaged reinforced concrete beams. Magazine of Concrete Research. 2015;67:364-78.
[37] Zanuy C, Ulzurrun GSD. Residual behavior of reinforced steel fiber-reinforced concrete beams damaged by impact. Structural Concrete. 2018;20:597-613.
[38] Hallquist JO. LS-DYNA theory manual. 2006.
[39] Murray YD. Users Manual for LS-DYNA Concrete Material Model 159. Cambridge, MA: Federal Highway Administration; 2007.
[40] Gholipour G, Zhang C, Mousavi AA. Loading rate effects on the responses of simply supported RC beams subjected to the combination of impact and blast loads. Engineering Structures. 2019;201:109837.
[41] Zhang C, Gholipour G, Mousavi AA. Nonlinear dynamic behavior of simply-supported RC beams subjected to combined impact-blast loading. Engineering Structures. 2019;181:124-42.
[42] Guo W, Fan W, Shao XD, Shen DJ, Chen BS. Constitutive model of ultra-high-performance fiber-reinforced concrete for low-velocity impact simulations. Composite Structures. 2018;185:307-26.
[43] Gholipour G, Muntasir Billah AHM. Nonlinear Analysis of Shear-Deficient Beams Strengthened Using UHPFRC under Combined Impact and Blast Loads. Journal of Structural Engineering. 2022;148.
[44] Fujikake K, Uebayashi K, Ohno T, Shimoyama Y, M K. Dynamic properties of steel fiber reinforced mortar under high-rates of loadings and triaxial stress states. Structures Under Shock and Impact VII. 2002:437-46.
[45] Fujikake K, Senga T, Ueda N, Ohno T, M. K. Effects of strain rate on tensile behavior of reactive powder concrete. Journal of Advanced Concrete Technology. 2006;4:79-84.

[46] Cowper G, Symonds P. Strain-hardening and strain-rate effects in the impact loading of cantilever beams. Brown Univ. Applied Mathematics Report; 1957. p. 28.

Chapter 8: Behaviour of UHPFRC-retrofitted RC beams with varying strengthening configurations under single and repeated blast loading

Paper 5: extracted from dynamic results in series 2 (submitted to journal- "Cement and Concrete Composites")

Abstract

This paper presents results from shock-tube tests on eight as-built and UHPFRC (ultra-high performance fiber-reinforced concrete)-retrofitted reinforced concrete beams under blast loading. The objective was to characterize the effects of various UHPFRC strengthening configurations on blast performance. The first group included one as-built beam and three specimens strengthened with UHPFRC in flexure using tension-sided (T), U-jacket (UJ) or full jacket (FJ) retrofits. The second group included one as-built beam and two specimens strengthened using full-jacket retrofits applied either over the full span (FJ) or in the middle hinge region (FJ-Hinge). The final beam was strengthened using a hybrid of the T-sided and FJ-Hinge schemes. The beams in Groups 1 and 2 were tested under repeated and singly-applied blast loads, respectively. In the first group, all retrofit schemes resulted in reduced displacements, damage and support rotations when compared to the as-built beam, however the repeated blasts ultimately led to crack localization and rupture of the tension steel bars. In the second group, both the full-span and localized hinge schemes led to reductions in midspan displacements and increased damage tolerance, without bar fracture. These beams further showed significant residual post-blast capacity. As part of the numerical study, finite element (FE) modelling was used to predict the blast behavior of the tested beams. After validation, the models were used to study the effects of the longitudinal steel ratio and blast load scenario (single vs repeated) on the behaviour and failure mode of the beams.

Keywords: UHPFRC; Retrofit configuration; Blast loading; Shock-tube; FE modelling.

8.1 Introduction

Recent global events such as the Beirut Explosion have highlighted the vulnerability of buildings and infrastructure to blast loads caused by accidental explosions. Events such as the Oklahoma City Bombing also highlight the need to incorporate blast protection in the design of vulnerable structures. On the other hand, many existing concrete structures are blast-deficient and lack the design and detailing required by modern blast codes [1]. These structures may also face increased vulnerability due to deterioration and ageing. Thus, there is a need to explore novel techniques and materials for the structural protection of vulnerable structures against blast loads.

Recently ultra-high performance fiber-reinforced concrete (UHPFRC) has been proposed as a novel material to rehabilitate and strengthen existing concrete structures. Indeed, the technique of flexural strengthening of reinforced concrete (RC) beams with UHPFRC has been well established in several experimental studies [2-13]. A review reveals four common forms of strengthening, including: tension or compression-sided layers (T or C-sided), side strips (SS), U-jackets (UJ) or full-jackets (FJ). In these tests the UHPFRC was either applied as a retrofit (to replace part of the existing concrete substrate) [2-7], or as an overlay (as an additional layer to increase the overall section dimensions) [5-13], with the UHPFRC applied either in-situ (casted in place, or using prefabricated strips applied using various bonding techniques.

Among these tests, a few examined the effects of strengthening configuration. Lampropoulos et al. [12] numerically studied the effects of T-sided and UJ overlays and noted that the three-sided UJ scheme resulted in the greatest increase in moment capacity and overall structural performance. Al-Osta et al. [8] presented a series of experiments on beams strengthened using three UHPFRC overlay schemes (T-sided, two-sided and UJ); all techniques were found to increase stiffness and load capacity, however the UJ scheme showed the highest strength enhancement, but with an unfavorable reduction in ductility. Yuan et al. [4] presented further tests on RC beams with various "no-slump high-strength high-ductility concrete" retrofit schemes (T-sided, T+C-sided, as well as UJ and FJ jackets) and noted superior performance for the UJ and FJ retrofits in terms of stiffness, strength, ductility and ability to change the failure from shear to flexure in the as-built beams.

The remarkable properties of UHPFRC under dynamic loading, which include high toughness and fragmentation resistance, also make it an ideal material for the impact and blast protection of structures [14-18]. Indeed, a few studies confirm the ability of UHPFRC strengthening to improve the behaviour of RC columns [14, 15], beams [16, 17] and slabs [18] under impact loading. Among them, Fan et al. [14] demonstrated the superior crash-worthiness of axially-loaded UHPFRC-jacketed columns under low-velocity impact loads using three retrofit schemes (“middle”, “two-ends” and their combination), with the “two-end” scheme proving to be most effective. Lee et al. [15] further verified the ability of UHPFRC jacketing to enhance the resistance, damage tolerance and displacement control of axially-loaded RC columns with seismic detailing under both drop-weight impact and shock-tube induced blast loads. A few other studies [16-18] also confirm the ability of T-sided UHPFRC overlays to improve the shear resistance and damage tolerance of beams and slabs under low-velocity drop-hammer impact loading.

Despite these important tests and findings, data on the blast behaviour of UHPFRC-strengthened RC members is scarce, with no previous tests on beams. The effects of strengthening scheme on blast resistance also requires further study. Accordingly, this paper presents the results of a research program which studies the blast resistance of RC beams retrofitted with UHPFRC. Various strengthening schemes (T-sided, UJ, FJ and localized hinge retrofits) are considered in two groups of beams which are tested under either repeated or singly-applied blast loads using a shock-tube. Finite element modelling is further used to study the influence of parameters not considered in the experiments, including the effects of the longitudinal steel ratio and blast load scenario (single vs repeated) on blast resistance and failure mode.

8.2 Experimental investigation

8.2.1 Description of test specimens

A total of eight specimens, including two as-built beams and six retrofits, were built and tested in this study. As shown in **Figure 8 - 1(a)**, the as-built and retrofit beams had the same dimensions of 150mm × 200mm × 2440mm and were tested under blast loads over a clear span of 2232mm. Longitudinal reinforcement in all beams consisted of 2-10M bars in tension and compression ($\rho = 0.8\%$ on both sides), with transverse ties made from 6.3 mm wire spaced as 75 mm throughout the beam span. The clear cover to the ties was 20 mm on all faces. All beams were first cast with the same 40 MPa ready-mix concrete. The strengthening involved removing the existing concrete cover using a chisel and then replacing it with UHPFRC using various strengthening schemes.

As shown in **Figure 8 - 1(b)**, Group 1 (G1) included one as-built beam and three specimens strengthened in flexure using UHPFRC applied on the tension-side (T), or using U or full jackets (UJ or FJ), over the entire span. These specimens were tested under repeated blast loads corresponding to Blast 1-2-3 (see **Section 2.3)**.

As shown in **Figure 8 - 1(c)**, Group 2 (G2) included one as-built beam and two specimens strengthened in flexure using full-jacketing applied over the entire span (FJ) or in the middle hinge region (FJ(Hinge)). The final beam was retrofitted using a hybrid of the T-sided and FJ(Hinge) schemes (T&FJ(Hinge)). The beams in this set were tested under singly-applied blast loads corresponding to Blast 3, and were subsequently tested under static four-point bending to assess their residual post-blast capacity.

Further details on the beam designs and blast load sequence are provided in **Table 8 - 1**. The beam nomenclature follows the following logic: “NSC” for normal-strength concrete, “10M” to indicate the size of the longitudinal steel bars, “75” to indicate the tie-spacing, “T, UJ, FJ, FJ(Hinge) or T&FJ(Hinge)” for the retrofit scheme, and “S” for the beams tested under single blasts. Further details on the material properties, blast loads and test setups are provided in the following sections.

Table 8 - 1 Beam test matrix and blast testing sequence

Set	Specimen ID	Concrete strength f_c' (MPa)		UHPFRC retrofit			Steel reinforcement			Blast sequence
		NSC	UHPFRC	Type	Thickness (mm)	Region	Long. Steel T/C	Tension ratio ρ (%)	Stirrup spacing (mm)	
Group 1 (G1)	NSC-10M-75	58.4	-	-	-	-	T: 2-10M C: 2-10M	0.8	75	Blast 1-2-3
	NSC-10M-75-T		174	T-sided	20	Full span				Blast 1-2-3
	NSC-10M-75-UJ		180	UJ	20	Full span				Blast 1-2-3
	NSC-10M-75-FJ		174	FJ	20	Full span				Blast 1-2-3
Group 2 (G2)	NSC-10M-75-S		-	-	-	-	T: 2-10M C: 2-10M	0.8	75	Blast 3
	NSC-10M-75-FJ-S		180	FJ	20	Full span				Blast 3
	NSC-10M-75-FJ(Hinge)-S		180	FJ(Hinge)	20	Middle*				Blast 3
	NSC-10M-75-T&FJ(Hinge)-S		174	T&FJ(Hinge)	20	FJ: Middle* T: Full span				Blast 3

*Middle = retrofit applied over the central 400 mm of the beam

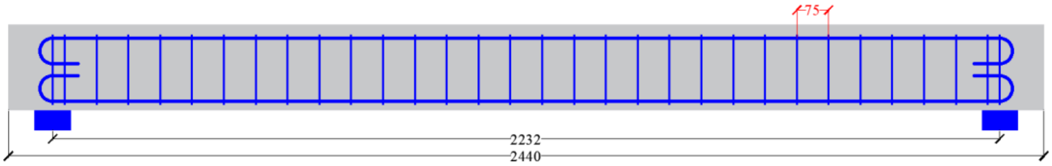

(a) Beam geometry and reinforcement (all dimensions in mm)

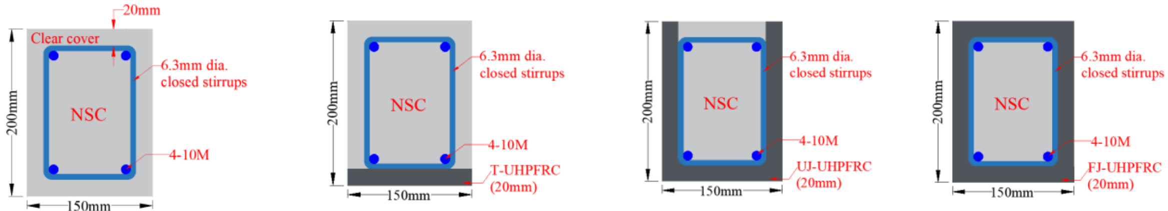

NSC-10M-75 NSC-10M-75-T NSC-10M-75-UJ NSC-10M-75-FJ

i) Cross-ssection details

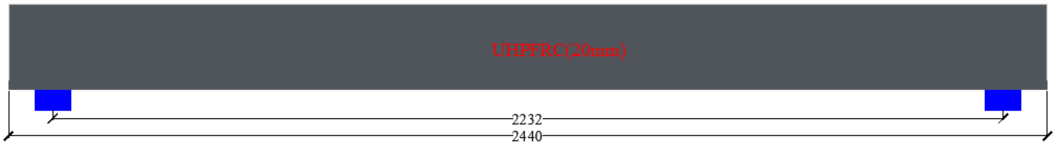

ii) FJ and UJ beams (NSC-10M-75-FJ, NSC-10M-75-UJ)

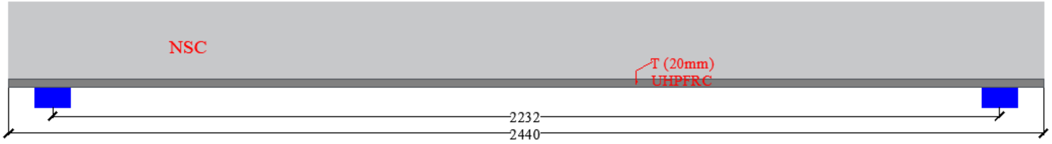

iii) T-sided beam (NSC-10M-75-T)

(b) Beam designs in Group 1 (G1)

NSC-10M-75-FJ-S: applied over full span
NSC-10M-75-FJ(Hinge)-S: applied over central 400 mm
NSC-10M-75-T&FJ(Hinge)-S: applied over central 400 mm

NSC-10M-75-T&FJ(Hinge)-S:
applied over full span outside central 400 mm

i) Cross-section details

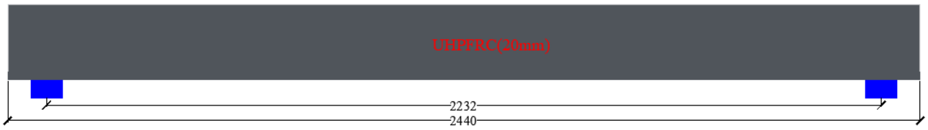

ii) NSC-10M-75-FJ

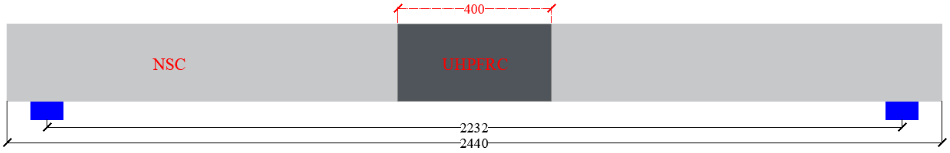

iii) NSC-10M-75-FJ(Hinge)

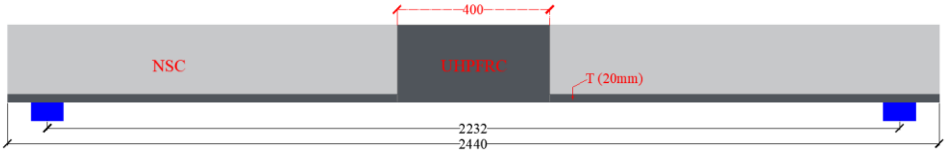

iv) NSC-10M-75-T&FJ(Hinge)

(c) Beam designs in Group 2 (G2)

Figure 8 - 1 Beam geometry and Beam designs in companion Groups 1 and 2

8.2.2 Material properties and specimen fabrication

As noted in the previous section all beams were first cast using the same ready-mixed concrete which had a specified strength of 40MPa, maximum aggregate size of 10 mm and specified slump of 120 mm. The actual compressive strength of the NSC concrete at the time of testing was determined by testing three standard 100 × 200 mm cylinders according to the ASTM C39 standard (**Table 8 - 1**). The stages in casting and preparing the specimens are illustrated in **Figure 8 - 2**. After reaching a minimum compressive strength of 25MPa, the concrete cover in the strengthening zones was removed using a concrete chisel and roughened to a concrete surface profile of CSP-10 according to the roughness grades specified by the International Concrete Repair Institute (ICRI) [19]. After cleaning and moistening the substrate surface, the beams were strengthened in-situ using UHPFRC, followed by 7 days of moist curing using wet burlap and plastic sheets. The beams were then cured under laboratory conditions until testing.

The proprietary UHPFRC used in this study was mixed using a large-capacity pan-mixer at the University of Ottawa. The mix components are illustrated in **Table 8 - 2** and consisted of a dry premix, water, straight steel fibers, and three types of liquid admixtures (A, B and C) which were added based on the proportions specified by the manufacturer. The straight steel fibers had a tensile strength of 2850MPa, length (l_f) of 13 mm and diameter (d_f) of 0.2mm, and were added at a constant volume fraction of 2.5% (195 kg/m^3). The compressive and flexural properties of the UHPFRC were obtained by testing standard 75×150mm cylinders and 75×75×280mm prisms according to the ASTM C1856 specifications. Sample results from these tests are plotted in **Figure 8 - 3(a-b)**. The workability of the UHPFRC was assessed using a flow test as specified in the same standard, with an average flow diameter of 225mm.

Two types of steel reinforcement were used in the fabrication of the specimens, and their properties were determined by testing standard coupons according to ASTM A615. The 10M steel bars, with diameter (d_b) of 11.3 mm and area (A_b) of 100 mm^2, had an average yield strength (f_y) of 484 MPa, while the 6.3mm wire used for the ties (A_b = 31 mm^2) had a yield strength of 413MPa. Sample stress-strain curves for both steel types, as well as the 15M and 20M reinforcement (A_b = 200 and 300 mm^2) which will be considered in the numerical parametric study are presented in **Figure 8 - 3(c)**.

Table 8 - 2 UHPFRC mixture components

Premix (kg/m^3)	Water (kg/m^3)	Admixture A (kg/m^3)	Admixture B (kg/m^3)	Admixture C (kg/m^3)	Steel Fibers (kg/m^3)
1930	195	15	26	28	195
					

a) Casting of NSC b) Interfacial preparation c) Moistening d) Retrofitting

e) Grades of Roughness (source: ICRI)

Figure 8 - 2 Casting and retrofit procedure

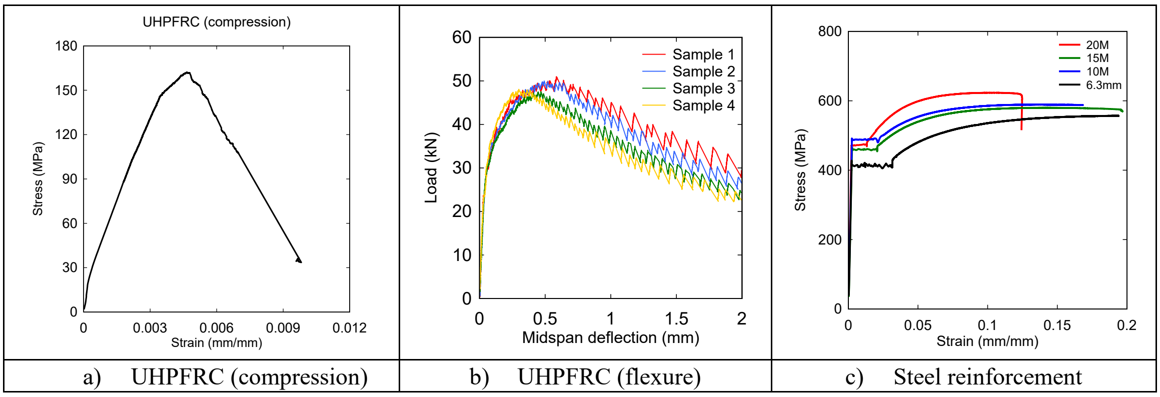

a) UHPFRC (compression) b) UHPFRC (flexure) c) Steel reinforcement

Figure 8 - 3 Material properties

8.2.3 Test setup and procedure

The beams in this study were tested under simulated blast loads using the University of Ottawa shock-tube. The pneumatically-driven shock-tube can accurately simulate the shock-waves produced by the far-field detonation of high explosives [20], and consists of four main components (see **Figure 8 - 4(a)**): 1 – a variable length driver (which generates the blast energy), 2 – a spool section (which triggers the blast), 3 – an expansion section with a length of 7 m (which generates a uniform shock-front), and 4 – a rigid end test frame with a 2m × 2m opening (where specimens are attached).

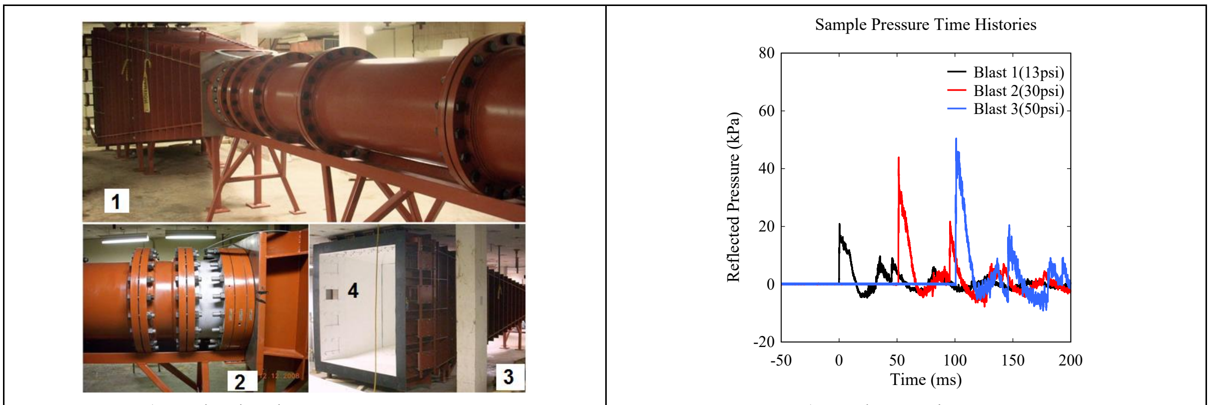

a) Shock-tube components

c) Blast testing sequence

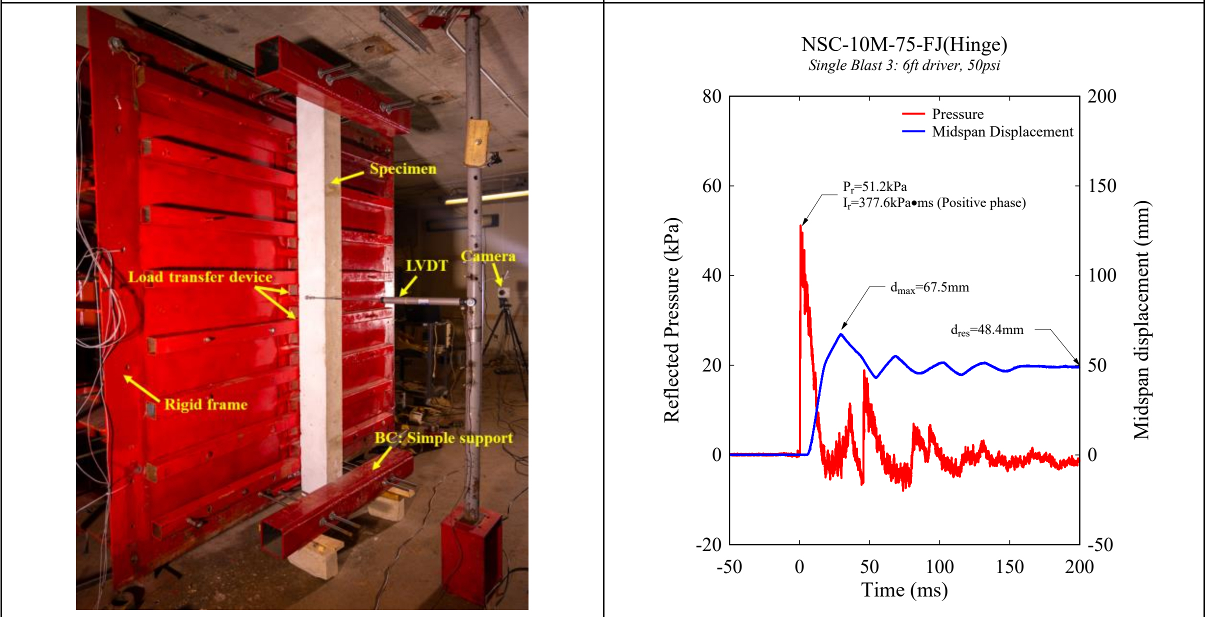

b) Blast test setup

d) Blast shockwave and response parameters

Figure 8 - 4 Details of the dynamic test setup and blast testing parameters

As shown in **Figure 8 - 4(b)**, the specimens were bolted to the shock-tube frame using steel fixtures which provided simple boundary conditions. Since the beams did not cover the entire end-frame area, a load-transfer device (LTD) was used to collect and transfer the load onto the specimens [21, 22]. The LTD consisted of a light-gauge 2m × 2.44m sheet metal which covered the entire opening, and a series of fourteen rigid hollow steel section (76× 76 × 6mm) beams which were distributed equally over the test area. Reflected pressure-time histories were captured using two piezoelectric pressure sensors attached near the end-frame, while displacements were captured using a midspan linear variable differential transducer (LVDT), and two high-speed cameras which tracked the displaced shapes of the specimens during the tests. All data was collected using a high-speed data acquisition system.

The blast loading sequence in Group 1 consisted of three gradually increasing blasts corresponding to Blasts 1-2-3, which tested the specimens under yield, inelastic and ultimate conditions. These blasts were generated by fixing the driver length at 1829mm (6ft), and gradually increasing the driver pressure from 90 to 345kPa (13 to 50psi). The beams in Group 2 were tested under a singly-applied Blast 3 load. Sample pressure time-histories for Blasts 1-2-3 are shown in **Figure 8 - 4(c)** while a typical response history is shown in **Figure 8 - 4(d)**. The average peak reflected pressures (P_r) and positive-phase impulses (I_r) for Blasts 1-2-3 were: P_r =16, 38 and 50 kPa, and I_r =125, 248 and 373 kPa-ms, respectively, with positive phase durations (t_d) which varied between 13-16 ms.

8.3 Experimental results

8.3.1 Summary of results

The experimental results for all beams in Groups 1 and 2 are presented in **Table 8 - 3**. The reported shockwave parameters include the peak reflected pressure (P_r), positive phase duration (t_d) and reflected impulse over the positive phase (I_r), while the beam response parameters include the maximum & residual displacements ($d_{max}\ and\ d_{res}$) and maximum support rotations (θ_{max}) after each test. Damage levels corresponding to the CSA S850 component damage descriptions are also reported [1]. Comparisons of displacement time-histories illustrating the effects of the test parameters are shown in **Figure 8 - 5** and **Figure 8 - 8**, while photos illustrating the damage and failure modes are presented in **Figure 8 - 6** and **Figure 8 - 9**. The effects of the UHPFRC retrofits and strengthening schemes on deflection behaviour, blast capacity and failure modes are discussed in the following sub-sections.

Table 8 - 3 Summary of Blast test results

Beam ID	Blast ID	Shockwave Properties[1]			Specimen Response[2]				CSA S850 Response limits and Component damage Failure mode[3]	
		P_r (kPa)	t_d (ms)	I_r (kPa·ms)	d_{max} (mm)	d_{res} (mm)	θ_{max} (°)	Observed damage	Response limit	Expected Damage level
NSC-10M-75	1	20.9	13.9	145.22	14.8	4.2	0.76	1st hairline cracks	<B1	Superficial
	2	43.9	11.9	261.5	39.8	23.2	2.04	Further crack opening	B2-B1	Moderate
	3	50.5	14.33	361.89	85.5	65	4.38	Concrete crushing	B2-B1	Heavy
NSC-10M-75-T	1	12.8	16.3	104.5	7.1	0.4	0.36	1st hairline cracks	<B1	Superficial
	2	34.8	13.8	240.9	28.9	14.3	1.48	Crack localization & fiber pull-out	B2-B1	Moderate
	3	46.2	15.25	352.3	Rupture	-	-	Bar-rupture	-	-
NSC-10M-75-UJ	1	14.1	16.2	114.5	5.2	0.7	0.27	1st hairline cracks	<B1	Superficial
	2	35.2	13.6	238.6	18.2	9.8	0.93	Crack localization	<B1	Superficial
	3	49.4	15.6	385.6	Rupture	-	-	Bar-rupture	-	-
NSC-10M-75-FJ	1	16.9	16	135.1	10.5	3.8	0.54	1st hairline cracks	<B1	Superficial
	2	37.5	13.3	249.6	27.2	15.2	1.40	Crack localization	B2-B1	Moderate
	3	49.1	15.5	380.1	Rupture	-	-	Bar-rupture	-	-
NSC-10M-75-S	3	53	14.1	374.9	84.1	70	4.30	Concrete crushing & fragmentation	B3-B2	Heavy
NSC-10M-75-FJ-S	3	47.8	16.2	387.9	50.6	40.2	2.60	Concrete crushing & crack localization & fiber pull-out	B2-B1	Moderate
NSC-10M-75-FJ(Hinge)-S	3	51.2	14.8	377.6	67.5	48.4	3.46	Mild concrete crushing & Fiber pull-out	B2-B1	Moderate
NSC-10M-75-T&FJ(Hinge)-S	3	52.9	14.5	382.3	55.7	39	2.86	Fiber pull-out	B2-B1	Moderate

Note:
[1]: P_r = Reflected pressure; I_r = Reflected impulse; t_d = positive phase duration;
[2]: d_{max} = maximum mid-span displacement; d_{res}= residual mid-span displacement; θ_{max} = max support rotation;
[3]: Double-reinforced beam: Blowout: $\theta \geq 10°$, Hazardous: $6° \leq \theta < 10°$; Heavy: $4° \leq \theta < 6°$; Moderate: $1° \leq \theta < 4°$; Superficial: $\theta < 1°$

8.3.2 Results from Group 1 (repeated blasts)

8.3.2.1 Effect of T-sided retrofit

The effect of the T-sided UHPFRC is examined by comparing the blast behaviors of NSC-10M-75 (as-built) and NSC-10M-75-T (with retrofit), which were tested under repeated blast loading. The results in terms of displacement histories and damage modes are studied in **Figure 8 - 5a** to **Figure 8 - 7**. In general, the application of the T-sided UHPFRC increased beam stiffness, and reduced displacements, but changed the failure mode when compared to the as-built specimen.

Blast 1, with an average reflected pressure of P_r = 16 kPa and impulse of I_r = 125 kPa-ms, was meant to bring the beams to yielding. The as-built beam shows displacements of d_{max} of 14.8 mm and d_{res} of 4.2 mm, with a support rotation θ_{max} of 0.8° ("superficial damage") after this test. In comparison, NSC-10M-75-T shows displacements d_{max} of 7.1 mm and d_{res} of 0.4 mm, corresponding to reductions of 52% and 90%. The support rotation is also reduced by half to 0.4°. Damage is indeed superficial, and is limited to hairline cracks in both specimens.

Blast 2, with an average P_r = 38 kPa and I_r = 248 kPa-ms, was meant to bring the beams into the inelastic range. The as-built beam shows displacements d_{max} and d_{res} of 39.8 mm and 23.2 mm, with a support rotation θ_{max} of 2.0° ("moderate" damage) after this test. Actual damage consists of the formation of widely spaced flexural cracks at midspan, and initiation of concrete crushing on the compression face. Beam NSC-10M-75-T shows a reduced support rotation of 1.5°, and displacements d_{max} of 28.9 mm, and d_{res} of 14.3 mm, which are reduced by 27% and 38%. Although damage is otherwise well-controlled, crack localization is evident in the UHPFRC layer in NSC-10M-75-T with a primary crack width of 5 mm, indicating the initiation of fiber pullout.

Blast 3, with an average P_r = 50 kPa and I_r = 373 kPa-ms resulted in failure of both specimens, but with different failure modes. The as-built beam shows large displacements d_{max} = 85.5 mm and d_{res} = 65 mm, with a support rotation θ_{max} of 4.4° ("heavy" damage). Indeed, the damage consists of important concrete crushing on the compression face, widening of the previously formed flexural cracks and the development of secondary blast fragments at failure. In comparison, the NSC-10M-75-T beam fails by rupture of the tension-side longitudinal bars at the previously-formed dominant crack location. The failure may be attributed to the high bond capacity of the UHPFRC [23] and low tension steel ratio of ρ=0.8%, but also to the crack localization which was intensified by the repeated blast testing. Despite the brittle failure, high-speed video shows no fragmentation or flying debris during the failure of the retrofit specimen.

8.3.2.2 Effect of U-jacket (UJ) retrofit

Next, the effect of the U-jacket UHPFRC retrofit is examined by comparing the blast responses of NSC-10M-75-UJ and the previously studied beams. The results are studied in **Figure 8 - 5b** to **Figure 8 - 7**. The UJ beam shows displacements d_{max} of 5.2 mm and d_{res} of 0.7 mm after Blast 1, which are reduced by 65% and 83% when compared to the as-built beam (**Figure 8 - 5b**), with a reduced support rotation of θ_{max} of 0.3° vs. 0.8°. The UJ retrofit also shows a 27% reduction in d_{max} when compared to the beam with the tension-side UHPFRC (**Figure 8 - 5d**), with hairline cracks observed in both specimens after this test (**Figure 8 - 6** & **Figure 8 - 7**).

Improved control of displacements is also observed for the UJ beam at Blast 2 with reductions of 54% in d_{max} (18.2mm vs. 39.8mm) and 58% in d_{res} (9.8 mm vs. 23.3 mm), and a reduced support rotation of 0.9° ("superficial") vs. 2.0° ("moderate") in the as-built specimen (**Figure 8 - 5b**). The displacements are also reduced when compared to beam NSC-10M-75-T, with reductions of 37% in d_{max} (18.2mm vs. 28.9mm) and 31% in d_{res} (9.8mm vs. 14.3mm) (**Figure 8 - 5d**). Consistent with the T-sided beam, crack localization is evident in NSC-10M-75-UJ, with a primary crack width of 5 mm after this blast (**Figure 8 - 6** & **Figure 8 - 7**). Failure of beam NSC-10M-75-UJ occurred by bar-fracture at Blast 3, and once again coincides with location of the previously formed dominant crack. High-speed video indicates no secondary blast fragments formed during failure.

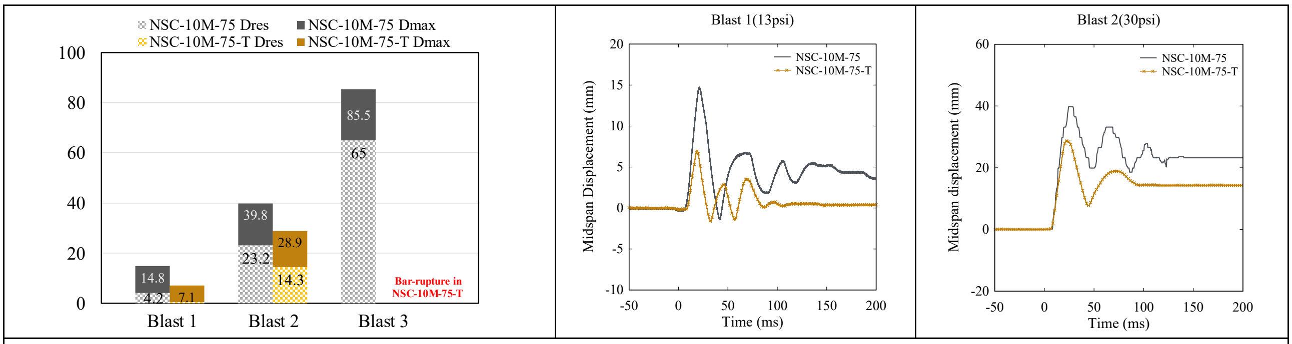

a) Effect of T-sided retrofit

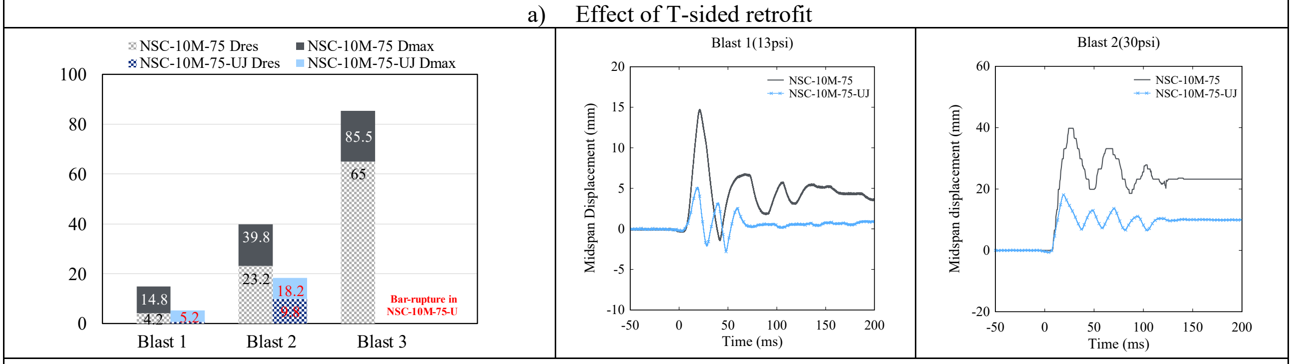

b) Effect of UJ retrofit

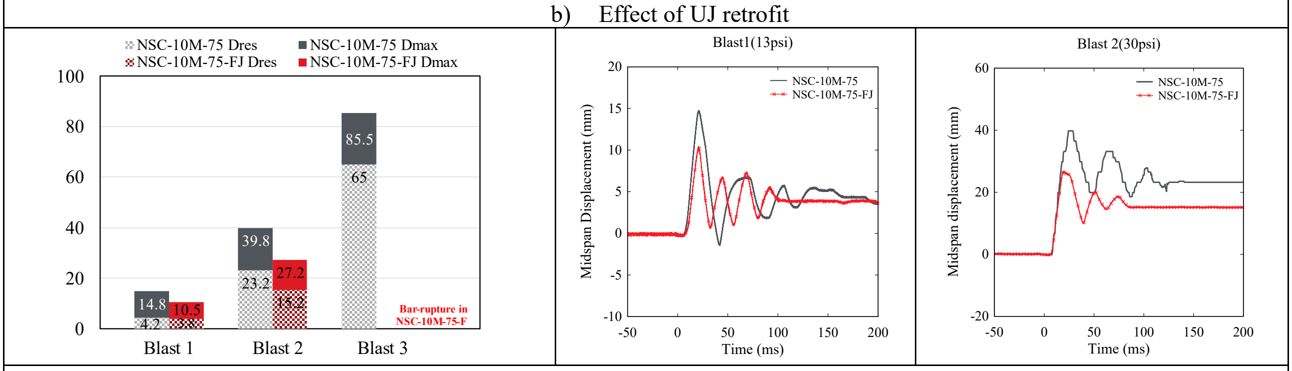

c) Effect of FJ retrofit

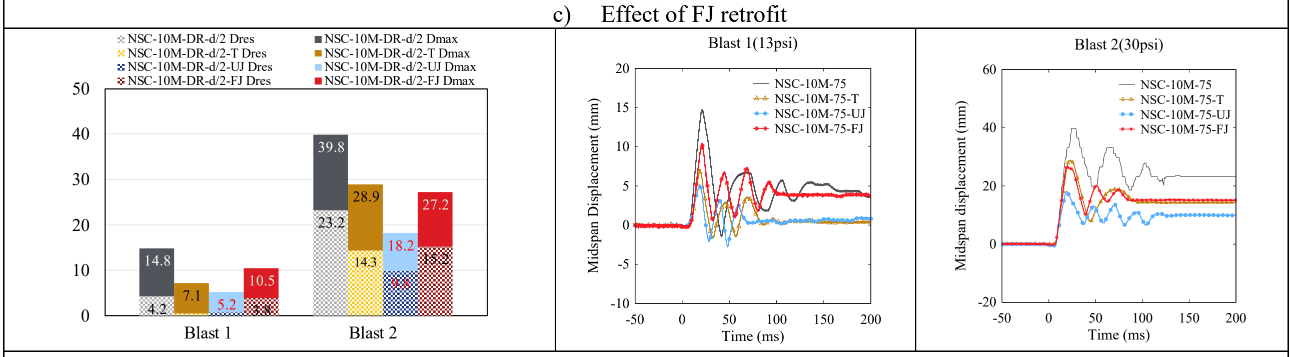

d) Effect of retrofit type

Figure 8 - 5 Effect of retrofit configurations in G1 under repeated blast loads

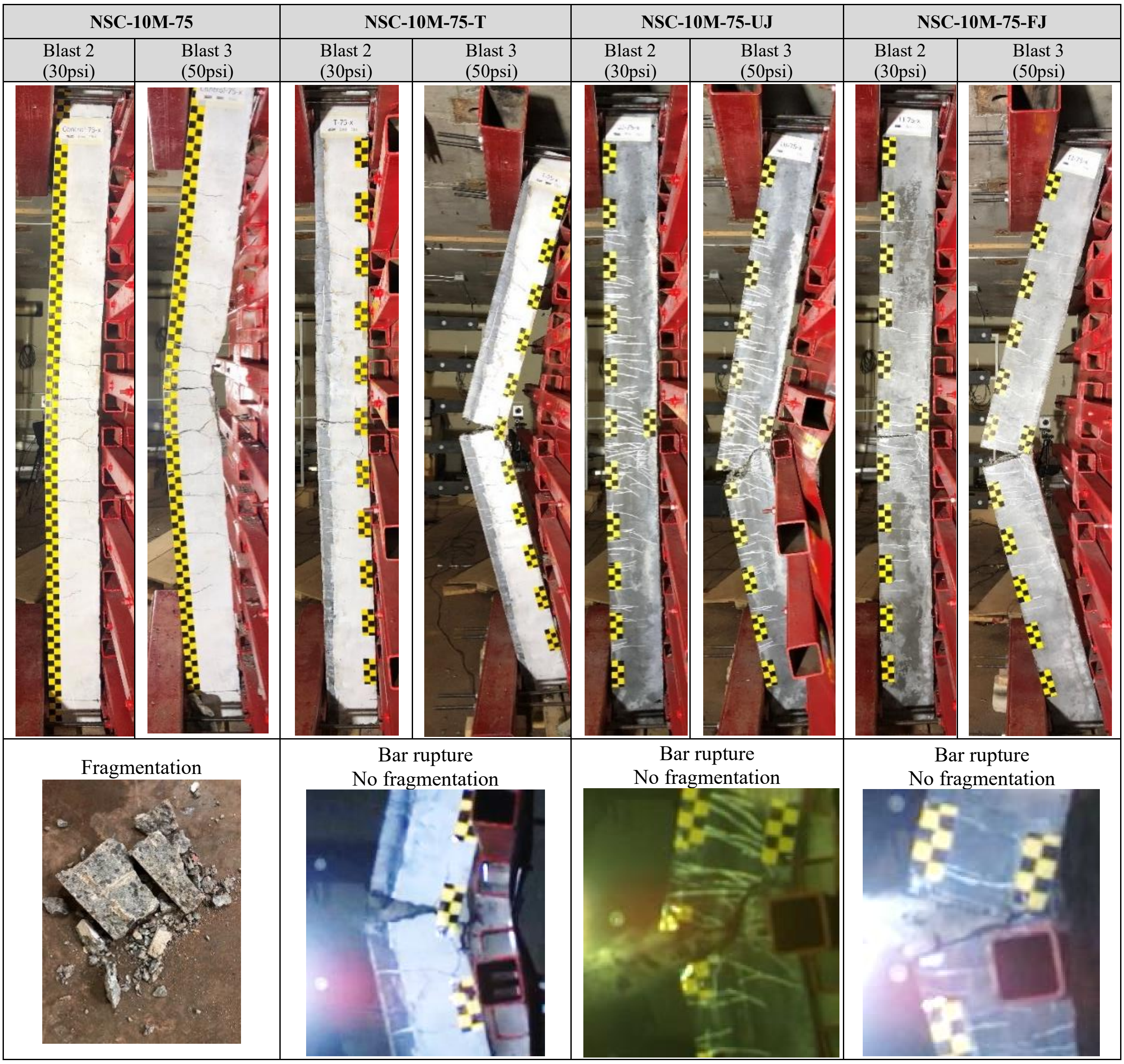

Figure 8 - 6 Progression of blast damage in G1 beams under repeated blast loads

Beam Design	Major crack at Blast 1	Major crack at Blast 2	Failure at Blast 3
As-built: NSC-10M-75	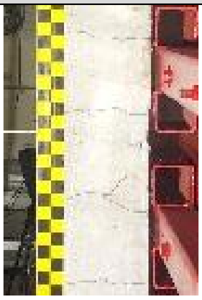 Hairline	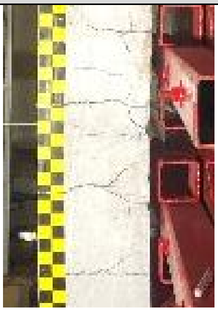 3.3mm	 Crushing and spalling
T-sided retrofit: NSC-10M-75-T	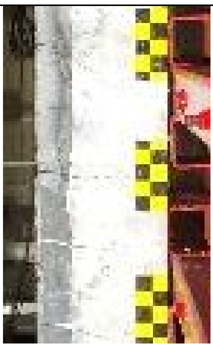 Hairline	 4.5mm	 Bar rupture
UJ retrofit: NSC-10M-75-UJ	 Hairline	 5mm	 Bar Rupture
FJ retrofit: NSC-10M-75-FJ	 1mm	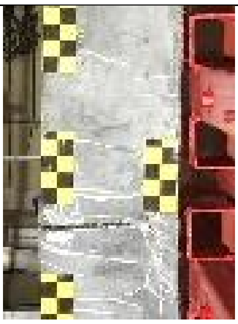 8mm	 Bar Rupture

Figure 8 - 7 Evolution of dominant crack widths in G1 beams under repeated blast loads

8.3.2.3 Effect of Full-jacket (FJ) retrofit

The effect of full-jacketing with UHPFRC is studied by comparing the blast responses of NSC-10M-75-FJ and the remaining beams in G1 (**Figure 8 - 5(c)** and **Figure 8 - 6**). Continuing the previous trend, the NSC-10M-75-FJ beam shows reductions of 29% in $\mathrm{d_{max}}$ (10.5mm vs. 14.8mm) and 10% in $\mathrm{d_{res}}$ (3.8mm vs. 4.2mm) at blast 1 when compared to the as-built specimen (**Figure 8 - 5(c)**). However, the FJ beam shows an obvious increase in displacements when compared to the T-sided and UJ retrofits (**Figure 8 - 5(d)**). Indeed, as shown in **Figure 8 - 6** & **Figure 8 - 7** crack localization (with a maximum crack width of 1mm) is already evident at midspan after this blast and is attributed to the less uniform distribution of steel fibers around the midspan tension zone.

Nonetheless, the FJ beam continues to show reduced displacements when compared to the as-built beam at Blast 2, with reductions of 32% in d_{max} (27.2mm vs. 39.8mm) and 34% in d_{res} (15.2mm vs. 23.2mm) (**Figure 8 - 5(c)**). The displacements nearly match those of the T-sided NSC-10M-75-T beam under Blast 2, while the UJ beam shows improved performance when compared to FJ counterpart (**Figure 8 - 5(d)**). While all three retrofits show crack localization, the primary crack of 8 mm (which exceeds $\mathrm{l_f}/2$) is larger for the FJ specimen, indicating complete fiber pullout after this test (**Figure 8 - 6** & **Figure 8 - 7**). Continuing the trend, the FJ beam would fail by fracture of the tension steel bars at Blast 3, with the failure coinciding with the location of the previously-formed dominant crack. Once again, despite the brittle failure, no fragmentation was observed in the FJ specimen at failure.

8.3.2.4 Comparison of retrofit types in G1

As noted in the above sections all three retrofit types in G1 resulted in improved control of displacements at Blasts 1 and 2 when compared to the as-built specimen. The most optimal performance (reductions of ~ 60% in d_{max}) was observed for the UJ specimen, while similar responses were observed for the FJ and T-sided beams (with reductions of ~ 30% in d_{max} for both beams under Blast 2). All three retrofits showed crack localization after the second blast, and eventually failed by bar fracture under Blast 3. As noted above, this failure mode is attributed to the high bond capacity of the UHPFRC, coupled with the low tension steel ratio and repeated blast testing. These effects are studied using additional FE simulations in **Section 8.4** of this paper.

8.3.3 Results from Group 2 (single blasts)

8.3.3.1 Effect of Full-jacket (FJ) retrofit under single blast loading

The effect of the full-jacket (FJ) retrofit under single Blast 3 loading is studied by comparing the responses of the as-built NSC-10M-75-S and retrofit NSC-10M-75-FJ-S beams. As seen in **Figure 8 - 8(a)**, the FJ beam presented an excellent ability to restrain the midspan displacement under the single Blast 3 load, with significant reductions of 40% and 43% in maximum (50.6mm vs. 84.1mm) and residual displacements (40.2mm vs. 70mm). The as-built and retrofit beams show support rotations of 4.3° and 2.6° which correspond to “heavy” and “moderate” damage according to the CSA S850 standard. As shown in **Figure 8 - 9**, actual damage in the as-built beam consists of concrete crushing and full depth and widely spaced flexural cracks. The retrofitted NSC-10M-75-FJ-S beam shows mild crushing, many closely spaced fine cracks, and a primary flexural crack with a width of 14 mm at midspan. Despite this crack localization, bar fracture did not occur in the FJ beam under the single blast load test.

Comparing the companion specimens tested under single and repeated blasts in **Figure 8 - 10**, the as-built NSC-10M-75-S (single blast) and NSC-10M-75 (repeated blasts) beams show nearly identical displacements and support rotations under Blast 3, although damage (in terms of crushing) is clearly greater in the specimen which was subjected to multiple blasts. On the other hand, the repeated tests had a significant effect on the retrofit FJ beams, with bar fracture negated in beam NSC-10M-75-FJ-S (single blast). Therefore, it is confirmed that the repeated blast testing was an important driver for the bar fractures observed in the G1 retrofit specimens.

8.3.3.2 Effect of localized FJ(Hinge) retrofit

In this section, the effectiveness of applying a localized FJ jacket retrofit is studied by comparing the blast responses of beams NSC-10M-75-FJ(Hinge)-S and NSC-10M-75-S under single Blast 3 loading. In this comparison the UHPFRC was applied in the middle hinge region over a length of 400mm, equivalent to two times the beam height (2h). As shown in **Figure 8 - 8(b)** the retrofit beam shows obvious reductions of 20% in d_{max} and 31% in d_{res} when compared to the control beam, indicating the ability of the localized FJ retrofit to effectively control maximum and residual displacements under blast loading. The support rotation is also reduced from 4.3° in the as-built beam (“heavy” damage) to 3.5° (“moderate”) in the retrofit specimen. Compared to the obvious crushing in the control beam, crushing is negated in the NSC-10M-75-FJ(Hinge)-S specimen which shows several closely spaced fine cracks within the retrofit zone, along with two major cracks of 6mm and 3.5mm at the interface (ends) of the retrofit zone (see **Figure 8 - 9**). An additional two major cracks (2.5mm and 2mm) are also developed outside this zone in the NSC concrete with almost the same spacing to the main cracks at the interface. Importantly, bar fracture was also negated in this specimen.

8.3.3.3 Effect of T&FJ(Hinge) retrofit

The last beam in G2 (NSC-10M-75-T&FJ(Hinge)-S) can be used to study the effect of using a hybrid of the FJ(Hinge) and T-sided retrofit approaches. This beam included a full-jacket applied in the central 400 mm hinge region, along with tension-sided UHPFRC applied over the remaining beam span. **Figure 8 - 8(c)** compares the blast responses of this beam with that of the as-built NSC-10M-75-S specimen under single Blast 3 loading.

The hybrid retrofit is shown to result in obvious reductions of 34% and 44% in maximum and residual displacements when compared to beam NSC-10M-75-S. The support rotation was also effectively reduced from 4.3° ("heavy") to 2.9° ("moderate") in the retrofit beam. The actual damage patterns in both beams can be compared in **Figure 8 - 9**. The crushing and overall damage is clearly better controlled in the retrofit specimen. It can be seen that the hybrid retrofit resulted in the formation of multiple flexural cracks in the "FJ hinge" zone with two major cracks of 5.5mm and 8mm at midspan and near the interfaces (ends) of the FJ retrofit zone. Importantly, bar fracture was once again prevented in this retrofit beam.

8.3.3.4 Comparison of retrofit types in G2

All three retrofits in Group 2 resulted in excellent blast performance and important reductions in midspan displacements when compared to the as-built specimen. Comparing the three retrofit schemes in **Figure 8 - 8(d)**, the beam with full-span FJ retrofit showed the most optimal control of maximum displacements with a reduction of 40% in d_{max}, which compares to 20% for the localized FJ(Hinge) scheme. The hybrid T&FJ(Hinge) beam shows an intermediate performance with a reduction of 34% in d_{max}. A similar trend is observed for the residual displacements which were reduced by 43%, 31% and 44% for these three specimens.

All three retrofits also showed an ability to reduce damage and fragmentation when compared to the as-built specimen. While bar fracture did not occur in all G2 retrofits, crack localization was an important driver of bar fracture in G1. It is therefore interesting to study the difference in dominant crack formation in the three G2 specimens in **Figure 8 - 9**. The beam with full span FJ retrofit developed a single dominant crack, with a large crack width of 14mm (well beyond fiber pullout) at midspan. This beam also shows mild crushing of the

UHPFRC on the compression face. In comparison, the FJ(Hinge) beam developed two dominant cracks (with lower crack widths of 6mm/3.5 mm) which formed away from midspan (near the ends of the UHPFRC jacket). A similar effect and cracking pattern is observed in the hybrid T&FJ(Hinge) retrofit. As discussed in the literature [24], the formation of multiple dominant cracks can spread plasticity over a longer length of steel reinforcement and delay bar fracture, as will also be confirmed in the next section.

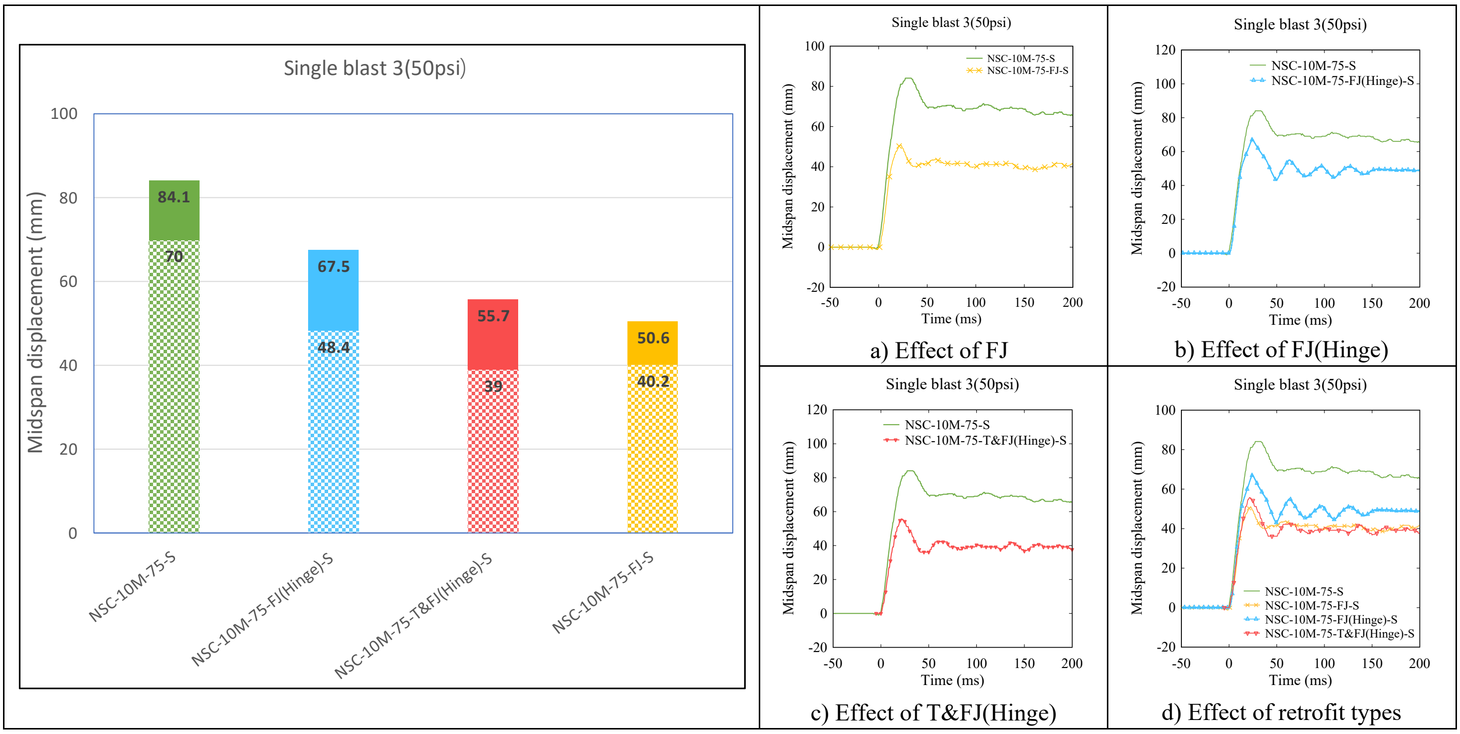

a) Effect of FJ

b) Effect of FJ(Hinge)

c) Effect of T&FJ(Hinge)

d) Effect of retrofit types

Figure 8 - 8 Effect of UHPFRC retrofit configurations in G2 under single Blast-3 load

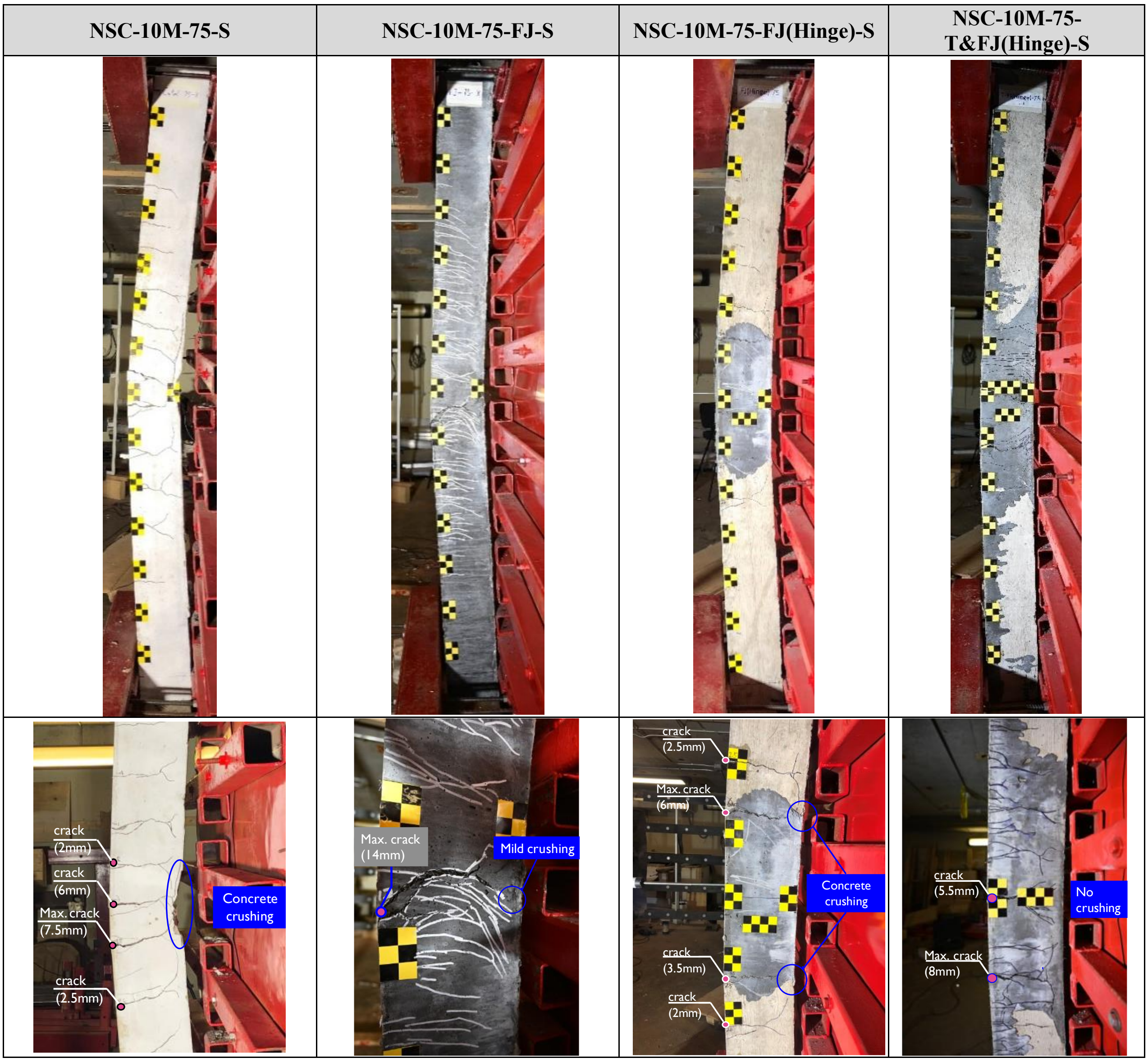

Figure 8 - 9 Progression of blast damage in G2 beams under single Blast-3 load

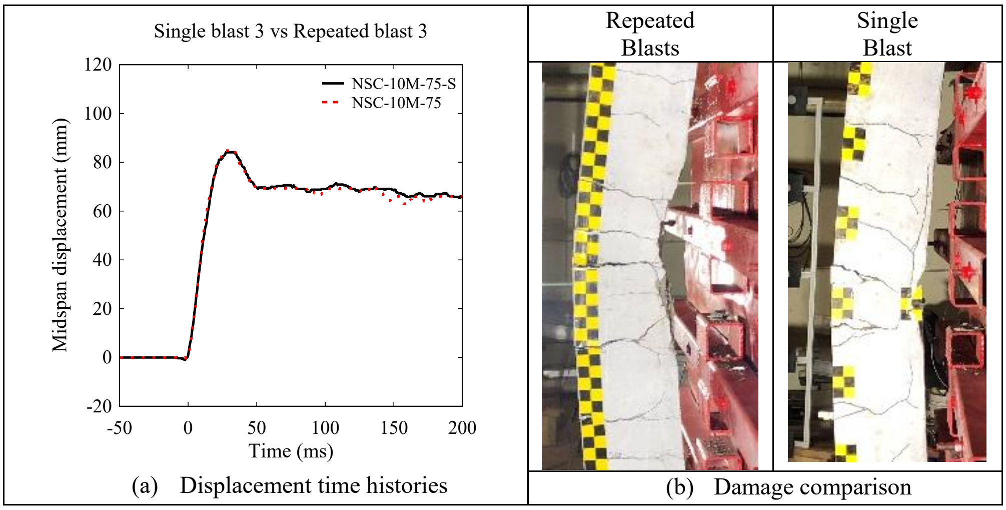

(a) Displacement time histories

(b) Damage comparison

Figure 8 - 10 Effect of repeated blast loads in as-built beams

8.3.3.5 Post-blast residual capacity of beams in G2

All beams in Group 2 survived Blast 3 and were further tested under static four-point bending to examine their residual capacity. The setup used in the post-blast static tests is shown in **Figure 8 - 11(a)**. In all cases the beams were tested over a simply-supported span of 2232mm, with two equal shear spans of 741mm and a constant moment region of 750mm, with the load and displacement at midspan captured using a load-cell and cable-transducer. The load-deflection results, and photos of the beams before and after testing, are presented in **Figure 8 - 11** and **Figure 8 - 12**. Key data from the residual static tests are reported in **Table 8 - 4**, including the maximum residual load (P_{max}^{R}), residual stiffness (k_{s}^{R}), maximum residual displacement (Δ_{max}^{R}), failure mode and toughness (T_{max}^{R}), representing the area under the residual load-deflection curves.

Table 8 - 4 Summary of post-blast residual test results

Beam ID	Condition	Blast load type	Load	Stiffness	Displacement	Toughness	Failure mode
			$P_{\max}^{R}$ (kN)	k_{s}^{R} (N/mm)	$\Delta_{\max}^{R}$ (mm)	$T_{\max}^{R}$ (kN-mm)	
NSC-10M-75-S	Damaged	Single blast	42.2	3232	124	4771	Crushing
NSC-10M-75-FJ-S	Damaged	Single blast	52.6	7351	42	1846	Bar rupture
NSC-10M-75-FJ(Hinge)-S	Damaged	Single blast	47.0	4110	65	2530	UHPFRC Crushing
NSC-10M-75-T&FJ(Hinge)-S	Damaged	Single blast	56.9	5886	79	3422	UHPFRC debonding followed by bar rupture

Note: P_{max}^{R}= Maximum residual load; k_{s}^{R}= Residual stiffness; Δ_{max}^{R}= Maximum residual displacement; T_{max}^{R}= Toughness representing the area under the residual load-deflection curve.

It is of interest to first compare the results of the "blast-damaged" as-built and FJ beams with that of companion "undamaged" beams previously tested by the authors under static loading only. As shown in **Figure 8 - 11(b)**, despite the significant displacement and rotation ($d_{\max}$ = 84 and $\theta_{\max} = 4.3^{o}$) during the blast test, the as-built NSC-10M-75-S beam retained significant post-blast load capacity ($P_{\max}^{R}$) of 42kN, representing 86% of the undamaged beam capacity. Likewise, as shown in **Figure 8 - 11(c)**, the NSC-10M-75-FJ-S beam (with full-span jacketing) which underwent $d_{\max}$ = 51 mm, retained a post-blast load capacity of $P_{\max}^{R}$ = 53kN, corresponding to 76% of the undamaged beam capacity. Both beams also retained significant residual stiffness with damaged/undamaged stiffness ratios of 85% and 96%, respectively.

Next, the load-deflection results from the four blast-damaged specimens are compared in **Figure 8 - 11(d)**. The FJ beam shows the highest residual stiffness of 7.4 kN/mm, with an increase of 127% when compared to as-built beam (3.2 kN/mm). Improved stiffness is also observed for the T&FJ(Hinge) beam, which shows an increase of 82% when compared to the as-built specimen. Due to the localized use of UHPFRC, the FJ(Hinge) beam shows a lower increase of 27% in stiffness when compared to its counterparts. The FJ and T&FJ(Hinge) retrofit beams also show larger load capacities of P^R_{max} = 53kN and 57kN, representing increases of 25% and 35% when compared to the as-built beam (P^R_{max} = 42kN), with a more modest increase of 11% for the FJ(Hinge) specimen (P^R_{max} = 47kN).

Despite the increases in residual load and stiffness, the FJ beam (with full-span jacketing) eventually failed by bar fracture during the post-blast test, whereas the failure mode consisted of concrete crushing and large opening of flexural cracks in the as-built beam (see **Figure 8 - 12**). As a result, the FJ beam shows a 61% reduction in toughness (area under the load-deflection curve) when compared to the as-built beam, with reductions of 47% and 28% for the FJ(Hinge) and T&FJ(Hinge) beams, respectively. Comparing the three retrofits it is clear that earlier bar fracture (at Δ^R_{max} = 42mm) occurred in the beam with the full-span FJ scheme. To recall, this beam showed a single dominant crack with a width of 14 mm after the single Blast 3 test. In comparison blast damage in the FJ(Hinge) beam consisted of two dominant cracks (with lower crack width of 6mm), which allowed the beam to survive up to a larger displacement of 65 mm without bar fracture (increase of 56% in Δ^R_{max}). In a similar way, bar fracture occurred in the T&FJ(Hinge) specimen, but at double the displacement recorded for the beam with full-span jacketing (Δ^R_{max} = 79mm vs 42 mm), and was preceded by partial debonding of the tension-side UHPFRC (see **Figure 8 - 12**). This beam also showed the greatest toughness when comparing all retrofits, with an increase of 85% in T^R_{max} when compared to NSC-10M-75-FJ-S.

Pokhrel and Bandelt [24] have noted that the formation of multiple dominant cracks in conventional UHPFRC beams can allow the steel reinforcement to strain over a longer length, thereby increasing member deformation capacity. In conventional UHPFRC beams this can be achieved by using a UHPFRC material with lower tensile strength (for example, by reducing the fiber content) [25]. In the current tests, the localized retrofit produced a similar effect by pushing the formation of the dominant crack from midspan, to multiple dominant cracks at the ends of the retrofit hinge region, resulting in increased member deformation capacity in the post-blast tests. In general, the results demonstrate that the localized hinge retrofits, with more efficient use of UHPFRC, allowed for excellent post-blast performance, with a delay in bar fracture when compared to the beam with full-span jacketing. Comparing all schemes, the T&FJ(Hinge) retrofit showed optimal post-blast performance with the greatest residual strength, toughness and deformation capacity, while acceptable performance without bar fracture was obtained for the FJ(Hinge) beam.

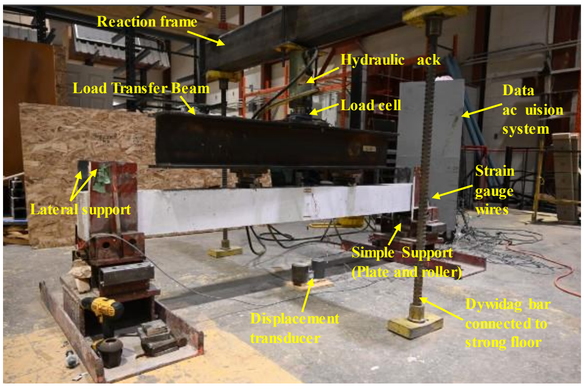

(a) Setup used in the residual static tests

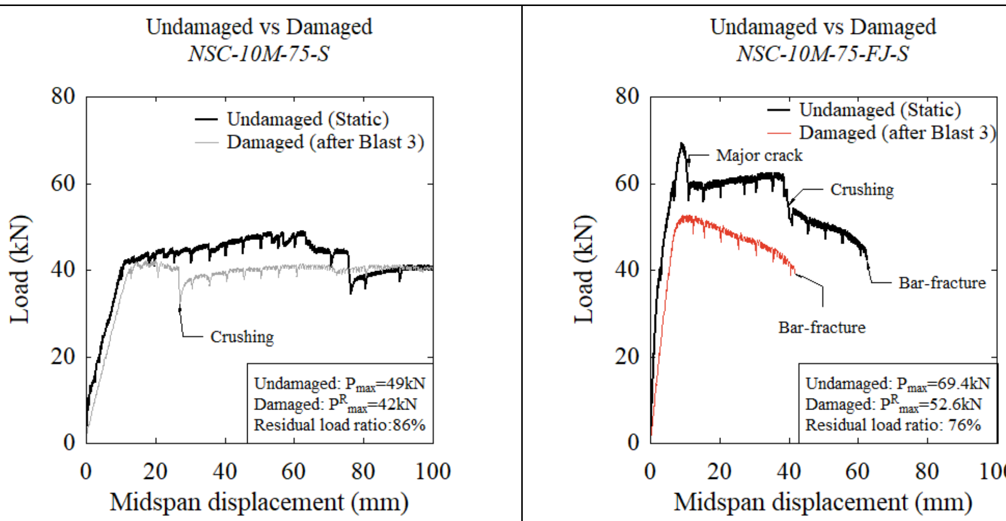

(b) Undamaged and damaged beam response under static loading: as-built beam

(c) Undamaged and damaged beam response under static loading: FJ-beam

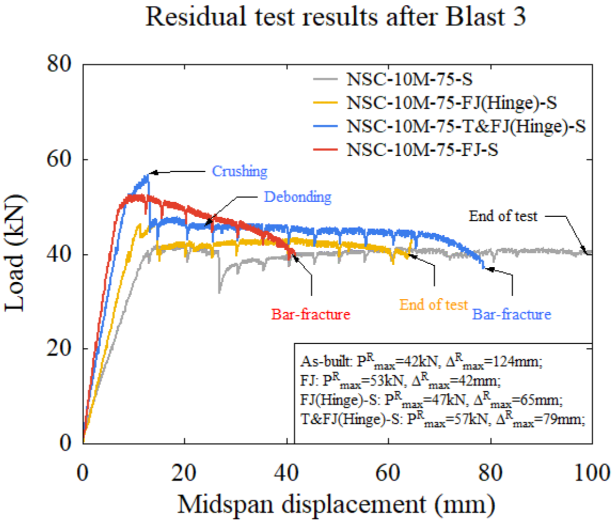

(d) Residual static test results (all blast-damaged beams)

Figure 8 - 11 Behaviour of G2 beams under 4PT static bending after single Blast-3 load

NSC-10M-75-S	NSC-10M-75-FJ-S
 At start of test	 At start of test
 At end of test (Δ^{R}_{max} = 124 mm)	 At end of test (Δ^{R}_{max} = 42 mm): Bar rupture
NSC-10M-75-FJ(Hinge)-S	**NSC-10M-75-T&FJ(Hinge)-S**
 At start of test	 At start of test
 At stage 30-40 mm: Crushing near load points	 At stage 30-40 mm: Partial debonding of UHPFRC at left interface
 At end of test (Δ^{R}_{max} = 65 mm): no rupture	 At end of test (Δ^{R}_{max} = 79 mm): Bar rupture

Figure 8 - 12 Beams in Group 2 before and after the residual static tests

8.4 Finite Element Analysis

8.4.1 Construction of FE model

8.4.1.1 FE model and meshing

Finite element (FE) analysis was used to predict the blast behaviour of the tested beams using software LS-DYNA [26]. The 3D model which includes the beam, load-transfer device (LTD) and boundary conditions is presented in **Figure 8 - 13**.

The 3D mesh for a typical reinforced concrete beam consisted of 73200 solid elements for the concrete and 2514 beam elements for the steel reinforcement. The eight-node concrete elements (**SECTION_SOLID*) had a mesh size of 10 mm, while the steel was modelled using two-node Hughes-Liu beam elements (**SECTION_BEAM*) with 10 mm length. Perfect bond was assumed between the concrete and steel reinforcement using keyword **CONSTRAINED_LAGRANGE_IN_SOLID* in LS-DYNA. UHPFRC was assigned for the concrete elements in the retrofit zones, with perfect bond ensured between the NSC and UHPFRC by sharing common nodes.

The load transfer device (LTD) was built in LS-DYNA using *Belytschko-Tsay* shell elements (**SECTION_SHELL*). In addition, the simple boundary conditions found in the experiments were assigned using the keyword **BOUNDARY* in LS-DYNA. The steel beam fixtures at the supports were built using **SECTION_SOLID* and clamped with bolts using the **SECTION_DISCRETE* keyword. Contact between the specimens, LTD and support fixtures was specified using the **CONTACT_AUTOMATIC_SURFACE_TO_SURFACE* contact algorithm in LS-DYNA.

Blast loads were idealized as triangular using the same pressure and impulse found in the experimental shock-tube tests, and applied onto the LTD device using the **LOAD_SEGMENT_SET* keyword in LS-DYNA. For the specimens tested under repeated Blast 1-2-3 loading, the blasts were applied in succession with a small time gap between each shot.

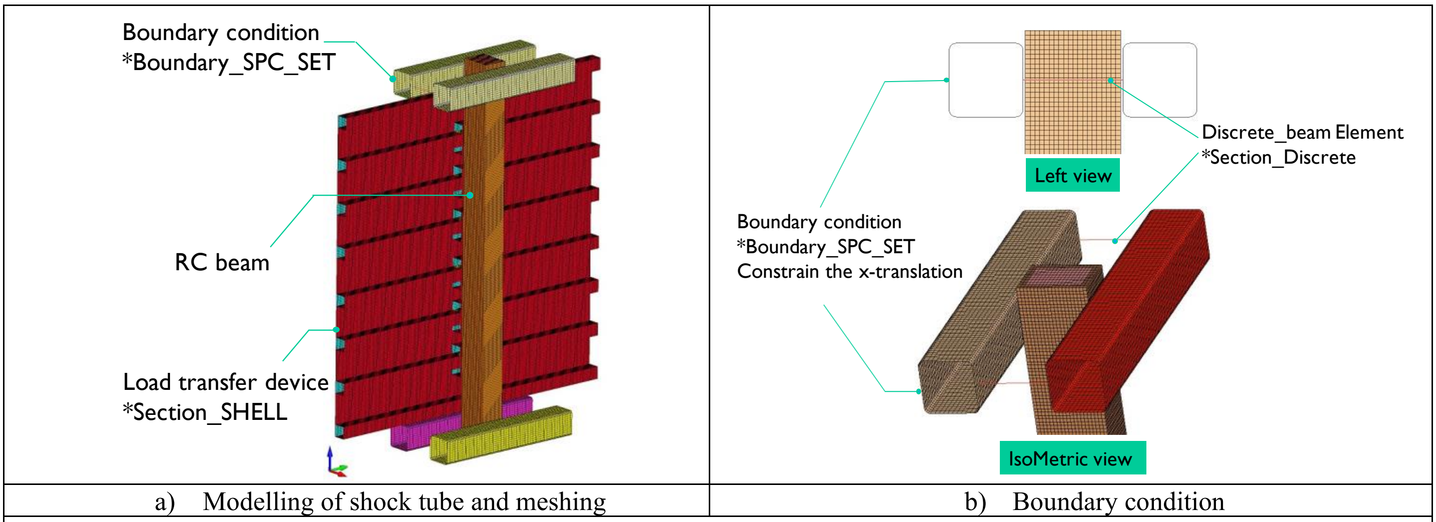

a) Modelling of shock tube and meshing

b) Boundary condition

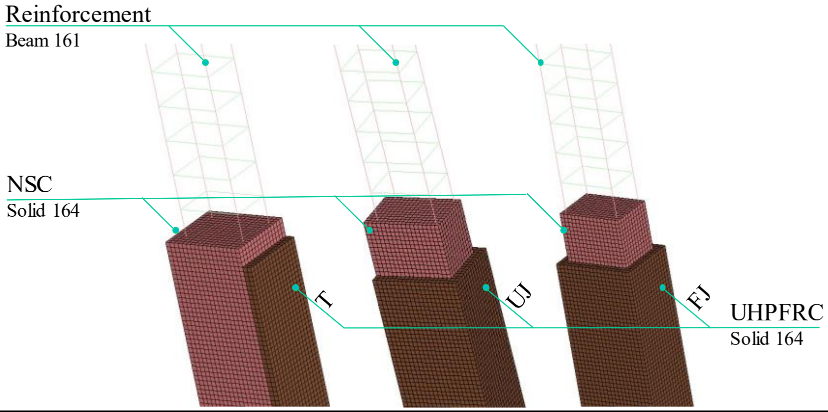

c) Concrete and steel elements

Figure 8 - 13 FE modelling: 3D model meshing, concrete/steel elements and boundary conditions

8.4.1.2 Material models

The concrete and UHPFRC materials were assigned using the Continuous Surface Cap Model (CSCM), which is designated as *MAT_CSCM* or *MAT_159* in LS-DYNA [27]. This model can simulate the response of concrete-like materials subjected to dynamic loading and has been verified in several previous impact and blast studies [28, 29]. The model is defined using isotropic constitutive equations, three stress-invariant shear surface formulations, a hardening cap, damage-based softening and rate effect equations. In the case of conventional concrete, the model can be specified using initialization routines which are defined using the compressive strength (f_c') and maximum aggregate size (*DAGG*), which were taken as 58 MPa and 10 mm for the NSC concrete. Rate effects were also considered for the NSC concrete using the equations shown in **Table 8 - 5** [27].

The enhanced properties of UHPFRC, which include increased tensile strength and post-cracking resistance, requires a modification of the default parameters in the CSCM model. In this study the calibrated formulations proposed by Guo et al. [30] were applied. This calibrated model has been shown to well predict the behaviour of UHPFRC members under both impact and blast loads [14, 31, 32]. **Table 8 - 5** shows an overview of the calibrated CSCM parameters which were used in the simulations. Rate effects were considered using updated formulations for UHPFRC proposed by Guo et al. [30] based on the work of Fujikake et al. [33, 34].

The steel reinforcement in the beams was modeled using the *MAT_003* (*PLASTIC-KINEMATIC*) model in LS-DYNA. This bi-linear hardening model is suitable for modelling the stress-strain response of Hughes-Liu steel beam elements, and includes rate effects based on Cowper and Symonds [35]. The model was defined using inputs for the modulus of elasticity (*E*), yield stress (*SIGY*) and tangent modulus (*ETAN*), based on the results from the experimental steel coupon tests.

Table 8 - 5 Constitutive models of materials used in LS-DYNA

<table>
<tr><th colspan="2">FE models</th></tr>
<tr>
<td><u>Normal-strength Concrete:</u>
*MAT_CSCM_CONCRETE (159) (MAT_159)
Default model parameters generated with f_c' based on cylinder tests</td>
<td><u>Rate effects:</u>
DIF formulations for concrete in tension and compression:
$DIF_t = f_{t,d}'/f_t' = 1 + E\dot{\varepsilon}\,\eta_{0t}/(f_t'\,\dot{\varepsilon}^{N_t})$
$DIF_c = f_{c,d}'/f_c' = 1 + E\dot{\varepsilon}\,\eta_{0t}/(f_c'\,\dot{\varepsilon}^{N_c})$</td>
</tr>
<tr>
<td><u>UHPFRC:</u>
*MAT_CSCM (159) (MAT_159)</td>
<td><u>Rate effects:</u>
Rate effect parameters $\eta_{ot}, \eta_{oc}, N_t, N_c$ were updated based on the following expressions in Guo et al (2018)
$\eta_{0t} = 0.7912\, f_t'/E,\ N_t = 0.7087$
$\eta_{0c} = 0.311\, f_c'/E,\ N_c = 0.7817$</td>
</tr>
<tr>
<td colspan="2">Material properties determined by 45 input parameters using the calibrated values presented in Guo et al (2018):
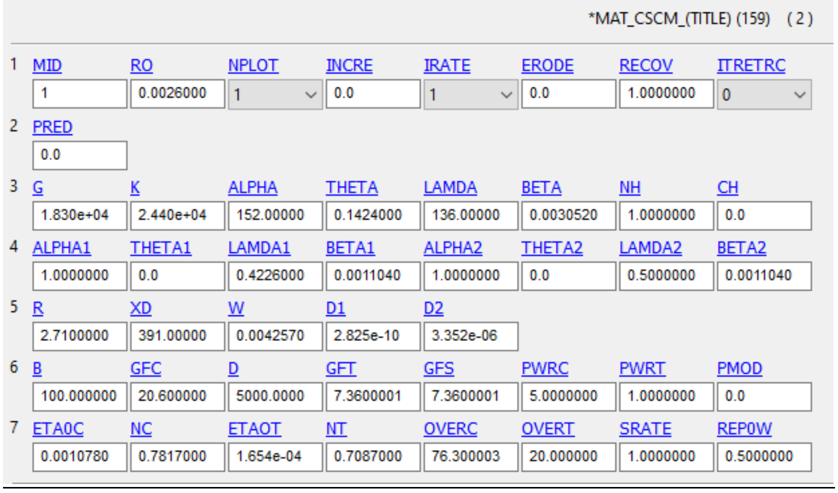

*MAT_CSCM_(TITLE) (159)   (2)
<table>
<tr><td>1</td><td>MID</td><td>RO</td><td>NPLOT</td><td>INCRE</td><td>IRATE</td><td>ERODE</td><td>RECOV</td><td>ITRETRC</td></tr>
<tr><td></td><td>1</td><td>0.0026000</td><td>1</td><td>0.0</td><td>1</td><td>0.0</td><td>1.0000000</td><td>0</td></tr>
<tr><td>2</td><td>PRED</td><td></td><td></td><td></td><td></td><td></td><td></td><td></td></tr>
<tr><td></td><td>0.0</td><td></td><td></td><td></td><td></td><td></td><td></td><td></td></tr>
<tr><td>3</td><td>G</td><td>K</td><td>ALPHA</td><td>THETA</td><td>LAMDA</td><td>BETA</td><td>NH</td><td>CH</td></tr>
<tr><td></td><td>1.830e+04</td><td>2.440e+04</td><td>152.00000</td><td>0.1424000</td><td>136.00000</td><td>0.0030520</td><td>1.0000000</td><td>0.0</td></tr>
<tr><td>4</td><td>ALPHA1</td><td>THETA1</td><td>LAMDA1</td><td>BETA1</td><td>ALPHA2</td><td>THETA2</td><td>LAMDA2</td><td>BETA2</td></tr>
<tr><td></td><td>1.0000000</td><td>0.0</td><td>0.4226000</td><td>0.0011040</td><td>1.0000000</td><td>0.0</td><td>0.5000000</td><td>0.0011040</td></tr>
<tr><td>5</td><td>R</td><td>XD</td><td>W</td><td>D1</td><td>D2</td><td></td><td></td><td></td></tr>
<tr><td></td><td>2.7100000</td><td>391.00000</td><td>0.0042570</td><td>2.825e-10</td><td>3.352e-06</td><td></td><td></td><td></td></tr>
<tr><td>6</td><td>B</td><td>GFC</td><td>D</td><td>GFT</td><td>GFS</td><td>PWRC</td><td>PWRT</td><td>PMOD</td></tr>
<tr><td></td><td>100.000000</td><td>20.600000</td><td>5000.0000</td><td>7.3600001</td><td>7.3600001</td><td>5.0000000</td><td>1.0000000</td><td>0.0</td></tr>
<tr><td>7</td><td>ETA0C</td><td>NC</td><td>ETAOT</td><td>NT</td><td>OVERC</td><td>OVERT</td><td>SRATE</td><td>REPOW</td></tr>
<tr><td></td><td>0.0010780</td><td>0.7817000</td><td>1.654e-04</td><td>0.7087000</td><td>76.300003</td><td>20.000000</td><td>1.0000000</td><td>0.5000000</td></tr>
</table>
</td>
</tr>
<tr>
<td><u>Longitudinal steel:</u>
*MAT-PLASTIC_KINEMATIC (MAT_003)
Mass density: 7800 kg/m^3
Poisson's ratio: 0.3
Young's modulus: 200 GPa
Yield stress: varies – based on coupons
Failure strain: varies – based on coupons</td>
<td><u>Rate effects:</u>
DIF formulation for steel reinforcement:
Cowper & Symonds strain rate model which scales the yield stress with the factor $1 + (\frac{\dot{\varepsilon}}{C})^{\frac{1}{p}}$</td>
</tr>
</table>

8.4.2 Validation of FE model

The test beams from Groups 1 and 2 were simulated using the FE models described in the previous section and the results are presented in **Table 8 - 6** in terms of predicted maximum displacements (d_{max}^{num}) and predicted-to-experimental displacement ratios ($d_{max}^{\mathrm{num}}/d_{max}$). Complete displacement time-histories and visual presentation of the damage modes from the FE simulations are presented in **Figure 8 - 14** to **Figure 8 - 16**, respectively.

Table 8 - 6 Results of numerical predictions

Beam ID	Blast ID	Shockwave Properties[1]			Specimen Response[2]			
		$\mathrm{P_r}$ (kPa)	$\mathrm{t_d}$ (ms)	$\mathrm{I_r}$ (kPa·ms)	$\mathrm{d_{max}}$ (mm)	$\mathrm{d_{max}^{num}}$ (mm)	$\mathrm{d_{max}^{num}/d_{max}}$	Error (%)
NSC-10M-75	1	20.9	13.9	145	14.8	16.1	1.09	8.8%
	2	43.9	11.9	262	39.8	47.4	1.19	19.1%
	3	50.5	14.33	363	85.5	78.4	0.92	8.3%
NSC-10M-75-T	1	12.8	16.3	105	7.1	8.3	1.17	16.9%
	2	34.8	13.8	241	28.9	27.3	0.94	5.5 %
	3	46.2	15.25	352	Rupture	Rupture	-	-
NSC-10M-75-UJ	1	14.1	16.2	115	5.2	6.1	1.17	17.3%
	2	35.2	13.6	239	18.2	21.2	1.16	16.5%
	3	49.4	15.6	386	Rupture	Rupture	-	-
NSC-10M-75-FJ	1	16.9	16	135	10.5	10.4	0.99	1.0%
	2	37.5	13.3	250	27.2	24.8	0.91	8.8%
	3	49.1	15.5	380	Rupture	Rupture	-	-
NSC-10M-75-S	3	53	14.1	375	84.1	82.2	0.98	2.3%
NSC-10M-75-FJ-S	3	47.8	16.2	388	50.6	55.7	1.10	10.1%
NSC-10M-75-FJ(Hinge)-S	3	51.2	14.8	378	67.5	62.7	0.93	7.1%
NSC-10M-75-T&FJ(Hinge)-S	3	52.9	14.5	382	55.7	60.7	1.09	9.0%
Statistical analysis					**Overall**	**As built**	**G1 retrofits**	**G2 retrofits**
FE analysis	Average ratio				1.05	1.05	1.06	1.04
	Average % error				10.0%	9.6%	10.9%	8.7%
	Standard deviation				0.11	0.12	0.12	0.10
	Coefficient of variation				10%	11%	12%	9%

Note:

[1] Idealized shockwave properties: P_r = Reflected pressure; I_r = Reflected impulse; t_d = positive phase duration for triangular load;

[2] d_{max} = maximum mid-span displacement from tests; d_{max}^{num}= maximum mid-span displacement obtained from FE simulation;

Considering the beams in both groups, the average $d_{max}^{\mathrm{num}}/d_{max}$ ratio is 1.05, with an error of 10%. The specimens in Group 1 were tested under repeated Blast 1-2-3 loading. Beam NSC-10M-75 shows $d_{max}^{\mathrm{num}}/d_{max}$ ratios of 1.09, 1.19 and 0.92 under these blasts and the model is able to reasonably predict the displaced shapes and concrete damage in the as-built beam after these tests. The FE simulation also results in a $d_{max}^{\mathrm{num}}/d_{max}$ ratio of 0.98 for beam NSC-10M-75-S under the single Blast 3 scenario.

Considering the retrofit specimens in Group 1 under Blasts 1 and 2, the FE models result in $d_{max}^{\mathrm{num}}/d_{max}$ prediction ratios of 0.99 and 0.91 for NSC-10M-75-FJ (full-jacket), and ratios of 1.17 & 0.94 and 1.17 & 1.16 for the T-sided and UJ specimens, respectively (NSC-10M-75-T and NSC-10M-75-UJ). Importantly the FE simulations capture the crack localization in these specimens after Blast 2, with an ability to precisely capture the bar fracture failures at Blast 3.

The retrofit beams in Group 2 were tested under single application of Blast 3. The FE simulation results in a $d_{max}^{\mathrm{num}}/d_{max}$ displacement ratio of 1.10 for beam NSC-10M-75-FJ-S. The model also results in an accurate prediction of the single crack localization at midspan, without bar fracture, which coincides with the experimental result. The beam with the localized FJ(Hinge) retrofit shows a $d_{max}^{\mathrm{num}}/d_{max}$ ratio of 0.93, and the FE model accurately captures the dual cracks which appear at the interface/ends of the FJ retrofit zone. The model is also able to predict the displacements and damage mode in the beam with the hybrid T&FJ(Hinge) retrofit.

In summary, the FE models showed an ability to well capture the displacements, damage patterns and failure modes observed in the experimental shock-tube tests. The next section presents a parametric study which examines the effects of additional parameters not considered in the experiments, including the effects of single blast loading in the G1 beams, as well as the effects of steel ratio on the response of the as-built and retrofit beams under single and repeated blasts.

Beams in G1 (repeated blasts)

Beams in G2 (single blast)

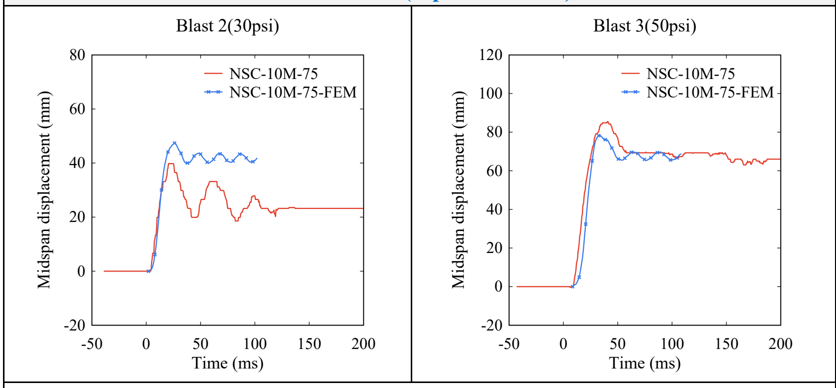

NSC-10M-75

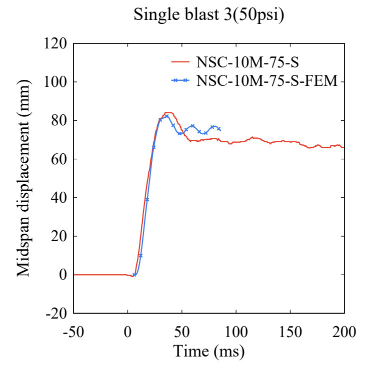

NSC-10M-75-S

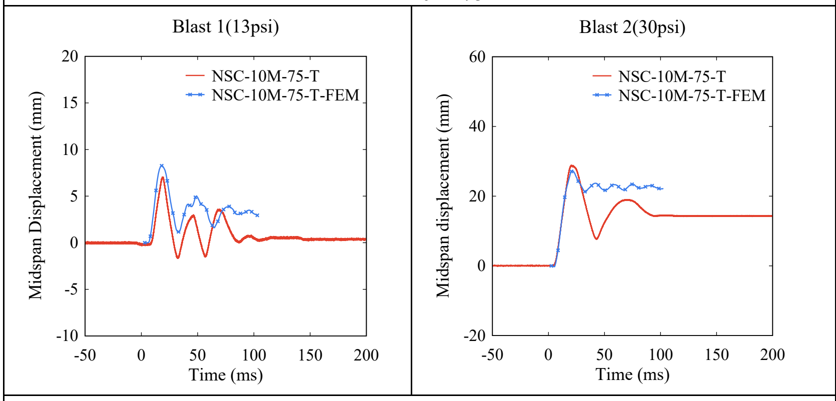

NSC-10M-75-T

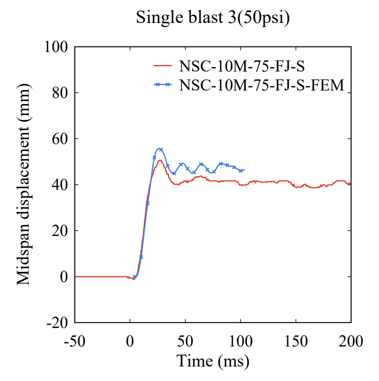

NSC-10M-75-FJ-S

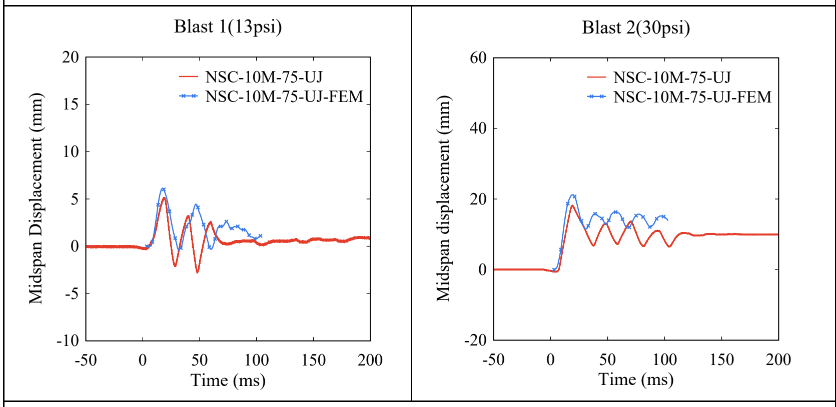

NSC-10M-75-UJ

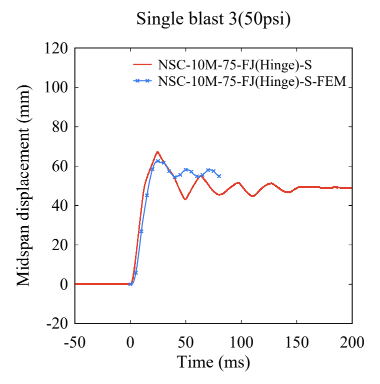

NSC-10M-75-FJ(Hinge)-S

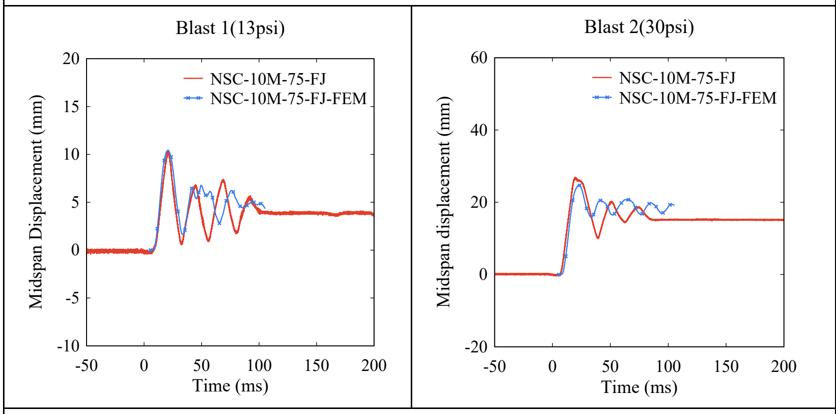

NSC-10M-75-FJ

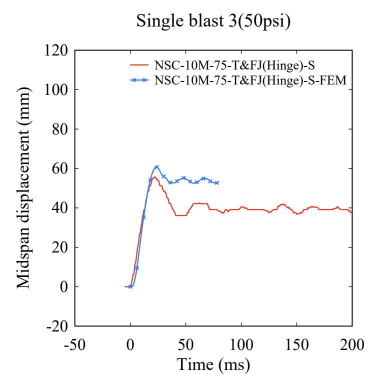

NSC-10M-75-T&FJ(Hinge)-S

Figure 8 - 14 Numerical FE analysis results of specimens in G1 and G2

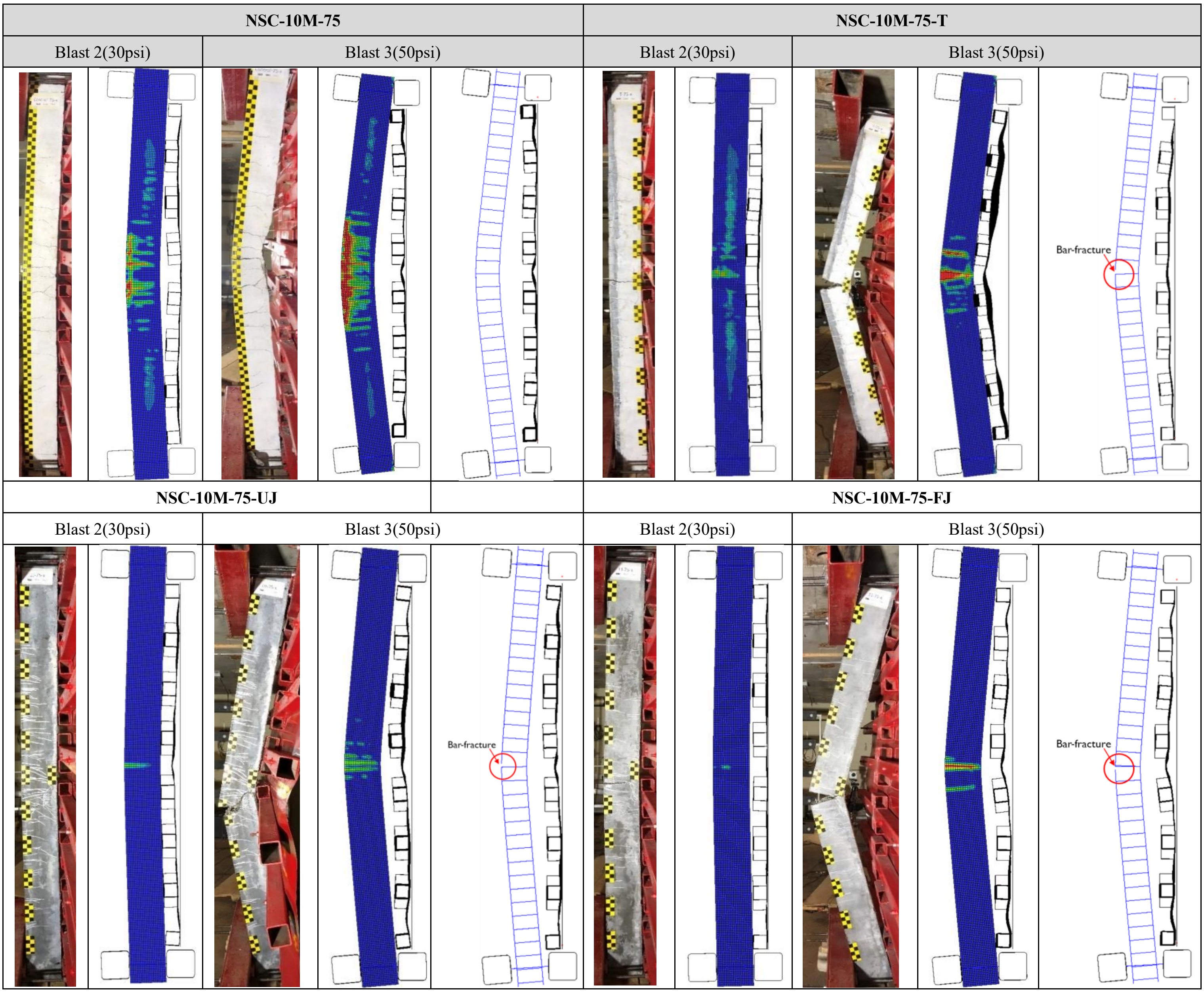

Figure 8 - 15 Numerical prediction of damage profiles in G1 beams under repeated blasts

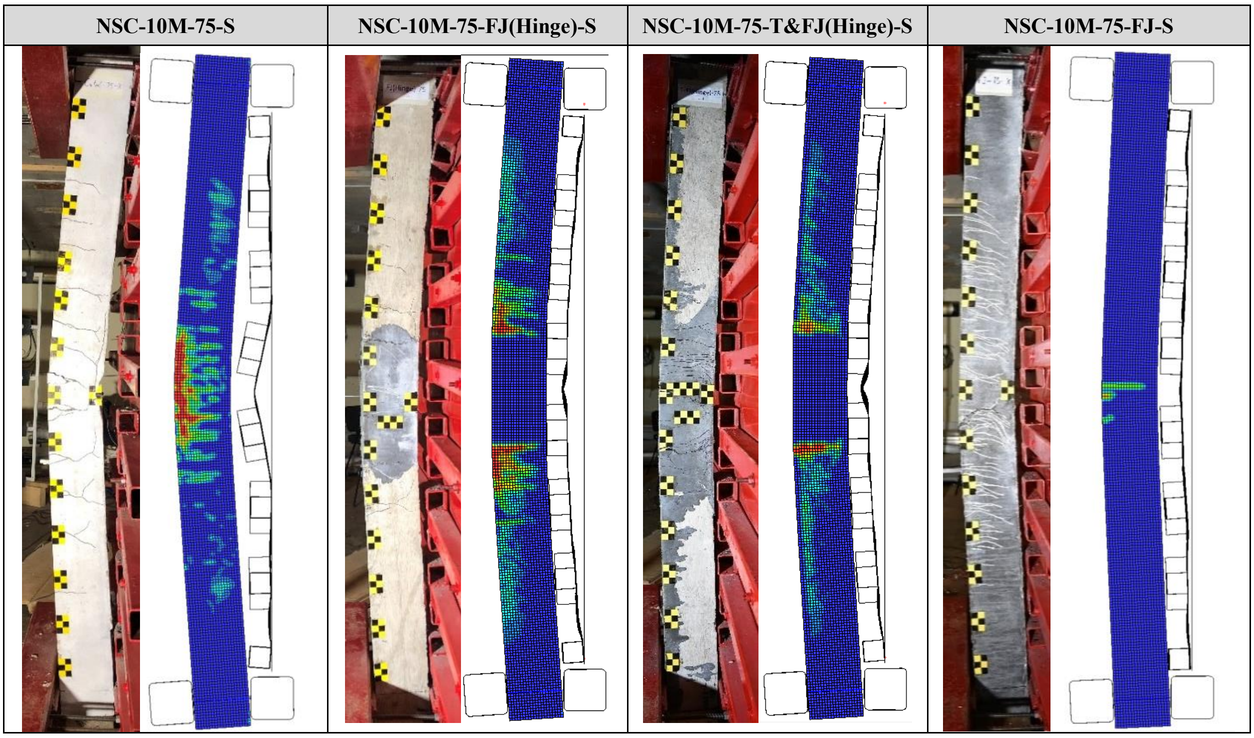

NSC-10M-75-S

NSC-10M-75-FJ(Hinge)-S

NSC-10M-75-T&FJ(Hinge)-S

NSC-10M-75-FJ-S

Figure 8 - 16 Numerical prediction of damage profiles in G2 beams under single Blast-3 loading

8.4.3 Parametric study

8.4.3.1 Effect of retrofit type (T, UJ, FJ) in G1 under single blast

The effect of retrofit configuration under single blast conditions is studied numerically by comparing the blast behaviour of the as-built and UHPFRC retrofit beams in Group 1 (T, UJ and FJ) under Blast 3 loading. The results from the simulations are presented in **Table 8 - 7** and **Figure 8 - 17** & **Figure 8 - 18** in terms of peak displacements, displacement histories and damage patterns.

The FE results confirm the ability of all three retrofits to improve control of displacements under single Blast 3 loading. When compared to the as-built beam, the T-sided, UJ and FJ retrofits result in reductions of 15%, 31% and 32% in maximum displacements (d_{max}^{num}), with corresponding reductions of 16%, 36%, and 38% in residual displacements. The UJ and FJ jacketing result in near-equal performance (displacements of 57mm and 56mm, with similar crack patterns), with larger displacements for the T-sided retrofit, which also shows greater concrete damage when compared to its counterparts. Importantly, while crack localization occurs in the UJ and FJ beams, bar fracture does not occur under the single application of Blast 3 loading. Therefore, it is confirmed that the repeated blast testing (which caused earlier crack localization) was a driver for the bar fracture failures observed in the G1 experiments.

To further study the performance of the FJ retrofit, additional FE simulations were conducted under a single application of Blast 4, with larger reflected pressure of P_r of 75 KPa and impulse of I_r of 610 KPa-ms, representing increases of 50% in P_r and 65% in I_r when compared to Blast 3. The results (see **Figure 8 - 19**) indicate that the retrofit beam fails by bar fracture under the more severe Blast 4 loading. Therefore, it is confirmed that the failure mode of the UHPFRC jacketed beams with tension steel ratio of ρ = 0.8% eventually occurs by bar fracture under sufficiently large blast loading. The effect of steel ratio on the performance of the as-built and retrofit beams under repeated and single blasting is studied in the next sections.

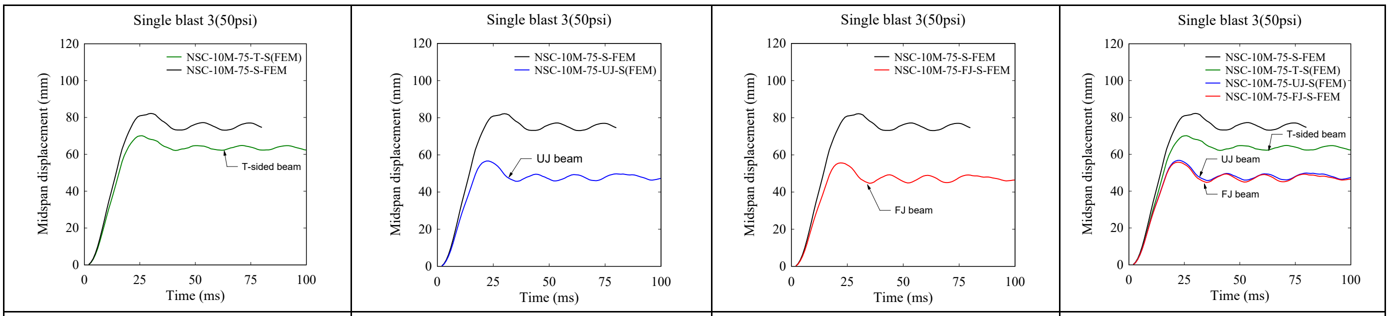

a) Effect of T under single blast b) Effect of UJ under single blast c) Effect of FJ under single blast d) Effect of retrofitting types

Figure 8 - 17 Effect of UHPFRC type under single Blast-3 loading

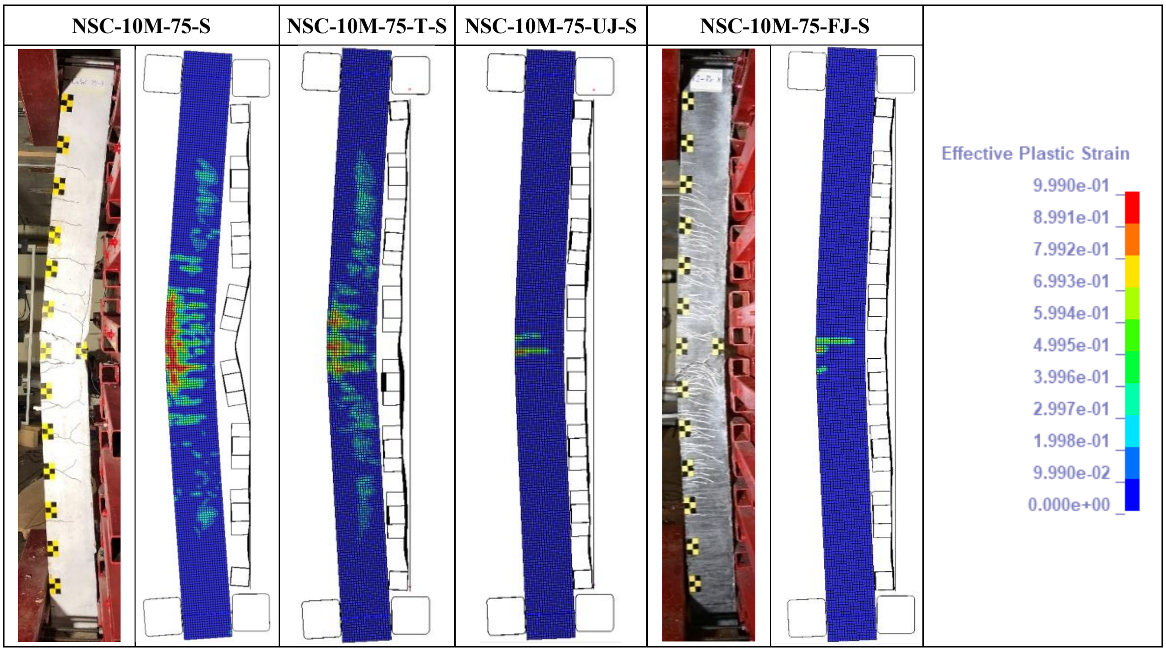

Figure 8 - 18 Effect of UHPFRC type on damage progression under single Blast-3 loading

Displacements

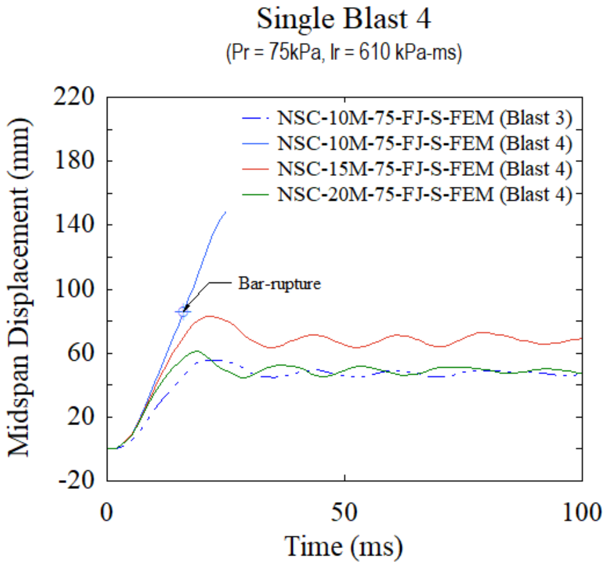

Damage and Failure mode

NSC-10M-75-FJ-S	NSC-15M-75-FJ-S	NSC-20M-75-FJ-S
10M (ρ = 0.8%) Bar rupture	15M (ρ = 1.6%) No rupture	20M (ρ = 2.4%) No rupture
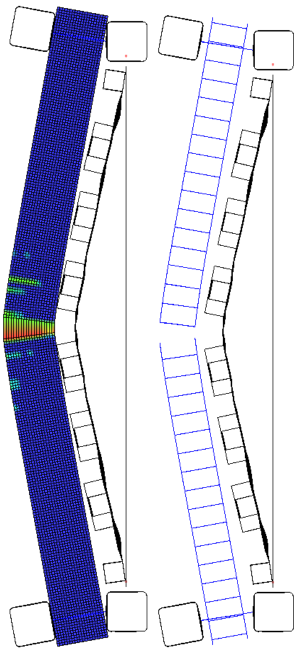	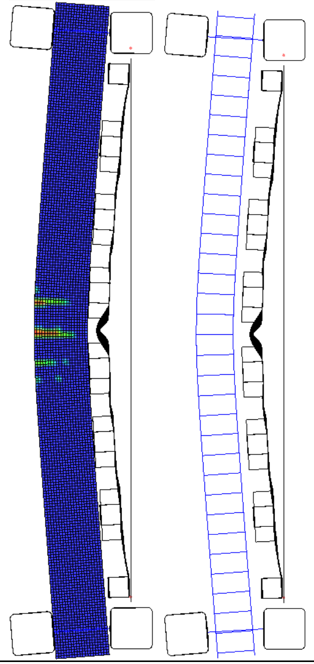	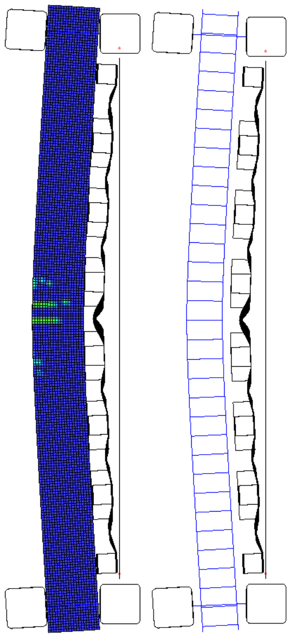

Figure 8 - 19 Effect of steel ratio in FJ beams under single Blast-4 loading

Table 8 - 7 Results of FE parametric study on the effect of steel ratios and blast load scenario

Specimen set (Blast load types)	Beam ID	Steel ratio ρ in %	Blast ID	Numerical results			CSA S850 Response limits and Component damage Failure mode[3]	
				d_{max}^{num} (mm)	d_{res}^{num} (mm)	θ_{max}^{num} (°)	Response limit	Expected Damage level
Control beams Single blast: Blast 3	NSC-10M-75-S	0.8%	3	82.2	74.6	4.21	B3-B2	Heavy
	NSC-15M-75-S	1.6%	3	51.5	44.5	2.64	B2-B1	Moderate
	NSC-20M-75-S	2.4%	3	34.8	19.6	1.79	B2-B1	Moderate
T-sided beams Single blast: Blast 3	NSC-10M-75-T-S	0.8%	3	70.1	62.3	3.59	B2-B1	Moderate
	NSC-15M-75-T-S	1.6%	3	44.6	37.1	2.29	B2-B1	Moderate
	NSC-20M-75-T-S	2.4%	3	30.9	13.4	1.59	B2-B1	Moderate
UJ beams Single blast: Blast 3	NSC-10M-75-UJ-S	0.8%	3	56.7	47.4	2.91	B2-B1	Moderate
	NSC-15M-75-UJ-S	1.6%	3	38.2	28.6	1.96	B2-B1	Moderate
	NSC-20M-75-UJ-S	2.4%	3	28.2	11	1.45	B2-B1	Moderate
FJ beams Single blast: Blast 3	NSC-10M-75-FJ-S	0.8%	3	55.7	46.5	2.86	B2-B1	Moderate
	NSC-15M-75-FJ-S	1.6%	3	37	27.5	1.90	B2-B1	Moderate
	NSC-20M-75-FJ-S	2.4%	3	27.7	8.9	1.42	B2-B1	Moderate
Control beams Repeated blasts: Blast 1-2-3	NSC-10M-75	0.8%	1	16.1	10.2	0.83	<B1	Superficial
			2	47.4	41.9	2.43	B2-B1	Moderate
			3	78.4	68.8	4.02	B3-B2	Heavy
	NSC-15M-75	1.6%	1	12.7	3.5	0.65	<B1	Superficial
			2	25.4	18.7	1.30	B2-B1	Moderate
			3	44.7	40.1	2.29	B2-B1	Moderate
	NSC-20M-75	2.4%	1	11.4	3.8	0.59	<B1	Superficial
			2	15.9	0	0.82	<B1	Superficial
			3	28.3	16.8	1.45	B2-B1	Moderate
T-sided beams Repeated blasts: Blast 1-2-3	NSC-10M-75-T	0.8%	1	8.3	2.9	0.43	<B1	Superficial
			2	27.3	22.2	1.41	B2-B1	Moderate
			3	Bar Rupture				
	NSC-15M-75-T	1.6%	1	7.4	1.2	0.38	<B1	Superficial
			2	19.6	6.4	1.01	B2-B1	Moderate
			3	39.8	32.4	2.04	B2-B1	Moderate
	NSC-20M-75-T	2.4%	1	6.9	1.8	0.35	<B1	Superficial
			2	14.5	0	0.74	<B1	Superficial
			3	23.7	9.4	1.22	B2-B1	Moderate
UJ beams Repeated blasts: Blast 1-2-3	NSC-10M-75-UJ	0.8%	1	6.1	1.3	0.31	<B1	Superficial
			2	21.2	13.4	1.09	B2-B1	Moderate
			3	Bar Rupture				
	NSC-15M-75-UJ	1.6%	1	5.7	1.5	0.29	<B1	Superficial
			2	15.3	3.4	0.79	<B1	Superficial
			3	27.5	16.4	1.41	B2-B1	Moderate
	NSC-20M-75-UJ	2.4%	1	5.5	0.7	0.28	<B1	Superficial
			2	14.1	0.8	0.72	<B1	Superficial
			3	23.9	7.7	1.23	B2-B1	Moderate
FJ beams Repeated blasts: Blast 1-2-3	NSC-10M-75-FJ	0.8%	1	10.4	4.34	0.53	<B1	Superficial
			2	24.8	19.1	1.27	B2-B1	Moderate
			3	Bar Rupture				
	NSC-15M-75-FJ	1.6%	1	9.3	2.8	0.48	<B1	Superficial
			2	16.6	3.7	0.85	<B1	Superficial
			3	27.3	17.3	1.40	B2-B1	Moderate
	NSC-20M-75-FJ	2.4%	1	8.7	2.4	0.45	<B1	Superficial
			2	13	0	0.67	<B1	Superficial
			3	24.9	9.1	1.28	B2-B1	Moderate
FJ beams Single blast: Blast 4	NSC-10M-75-FJ-S	0.8%	4	Bar Rupture				
	NSC-15M-75-FJ-S	1.6%	4	82.7	69.1	4.24	B3-B2	Heavy
	NSC-20M-75-FJ-S	2.4%	4	60.9	47.4	3.12	B2-B1	Moderate

8.4.3.2 Effect of steel ratio in the as-built beams under repeated and single blasts

The effect of tension steel ratio is first studied in as-built beams with 10M, 15M and 20M bars (steel bar areas of A_b = 100, 200 and 300 mm^2), corresponding to steel ratios of ρ = 0.8%, 1.6% and 2.4% (representing low, moderate and high steel ratios, respectively). The FE simulation results are presented in **Table 8 - 7** and **Figure 8 - 20** to **Figure 8 - 23**.

As expected, increasing the steel ratio was effective in reducing displacements in the as-built beams under repeated loading (**Figure 8 - 20**). Doubling the steel area in NSC-15M-75 (15M bars, ρ = 1.6%) reduced maximum displacements by 21%, 46% and 43% when compared to NSC-10M-75 (10M bars, ρ = 0.8%) under Blasts 1-2-3. Further reductions of 29%, 66% and 64% at these same blasts are found in NSC-20M-75 which had a steel ratio of ρ = 2.4% (20M bars). Enhanced control of displacements is also observed in the as-built beams with 15M and 20M bars under the single Blast 3 load, with reductions of 37% and 58% in d_{max}^{num} when compared to the companion with 10M bars (**Figure 8 - 21**).

Increasing the steel ratio was also effective in reducing support rotations and damage in the as-built beams. Under repeated Blast 2-3 loading, the beams with 10M, 15M and 20M bars show rotations of $\theta_{max}^{\mathrm{num}}$ of 2.4° and 4.0° (damage states: “moderate” and “heavy”), 1.3° and 2.3° (“moderate”), and 0.8° and 1.5° (“superficial” and “moderate”), with the same trend observed under single Blast 3 loading. Improved damage control is also evident when examining the damage patterns in **Figure 8 - 22** and **Figure 8 - 23**. Therefore, increasing the steel ratio is confirmed as an effective means to reduce blast-induced displacements, support rotations and damage in the as-built RC beams.

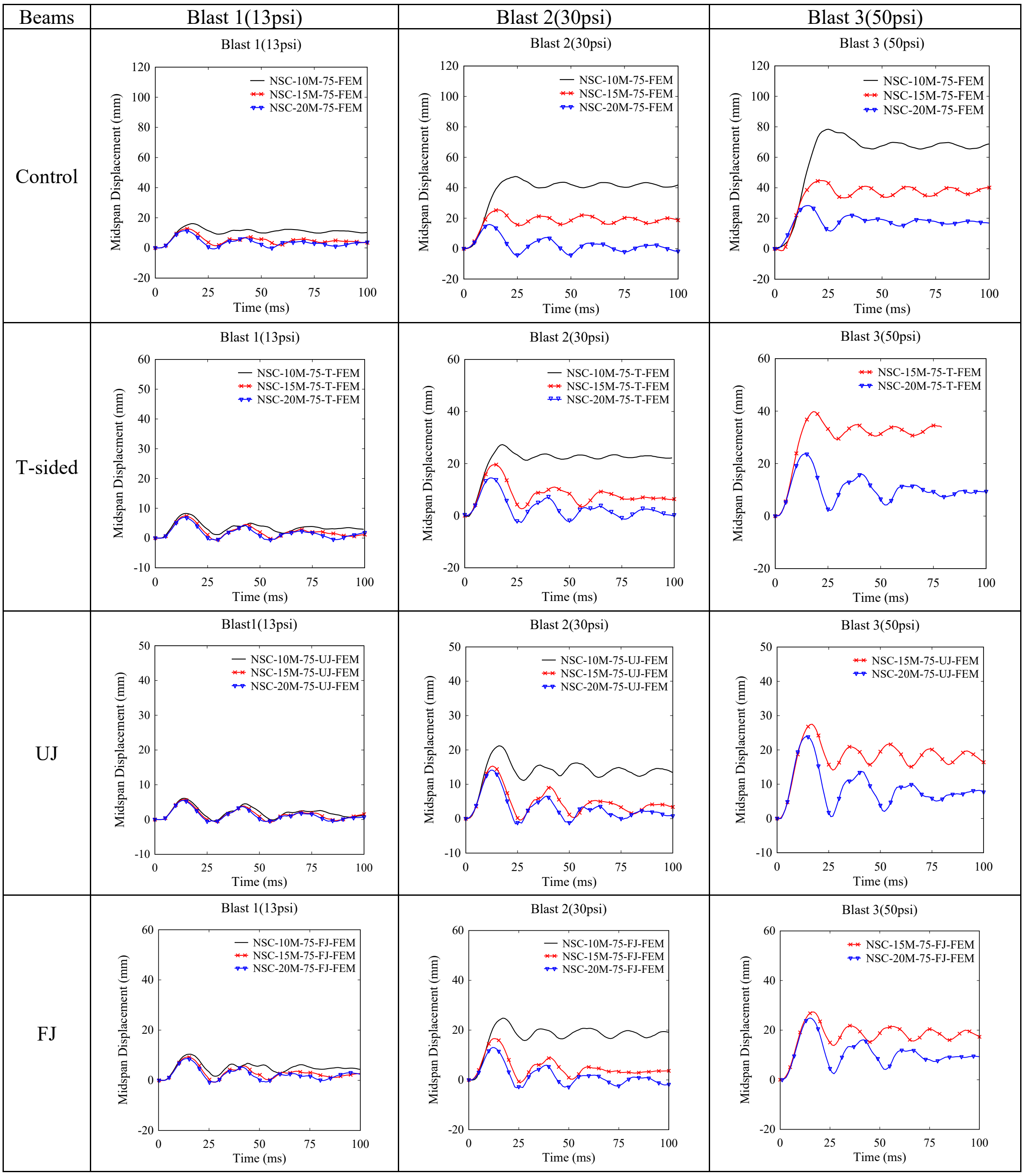

Figure 8 - 20 Effect of steel ratio on displacements under repeated blast loading

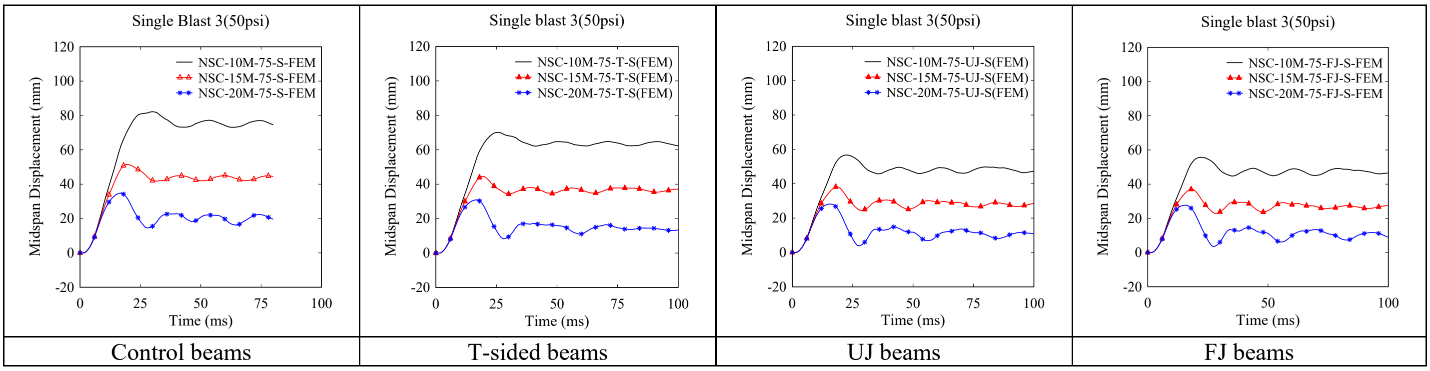

Figure 8 - 21 Effect of steel ratio on displacements under single Blast-3 loading

Beams	Blast 2				Blast 3			
	Control	T	UJ	FJ	Control	T	UJ	FJ
10M (ρ = 0.8%)	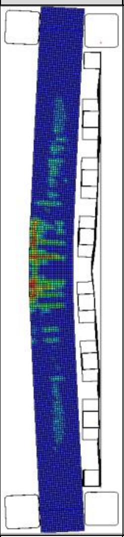	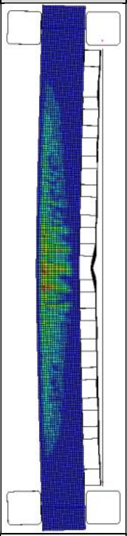	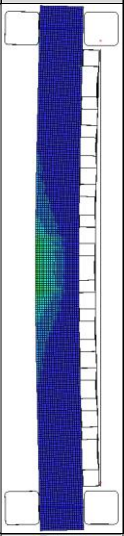	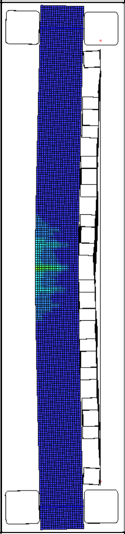	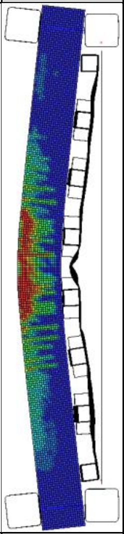	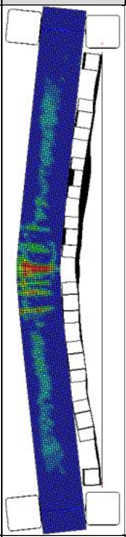	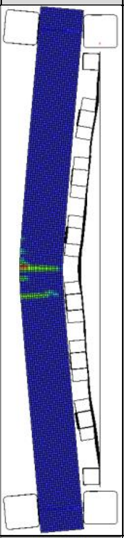	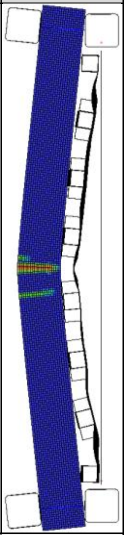
15M (ρ = 1.6%)	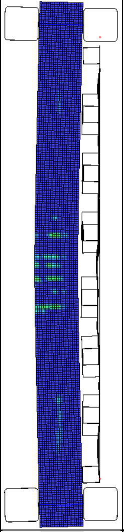	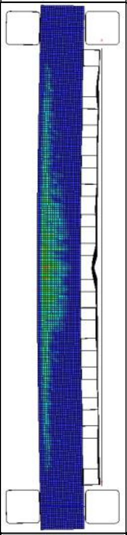	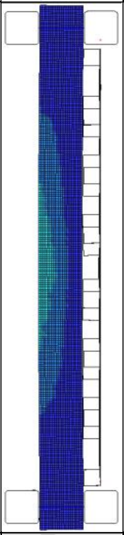	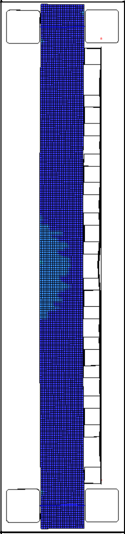	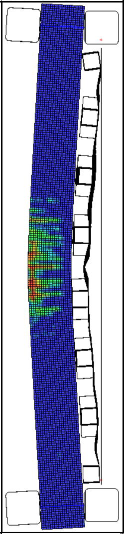	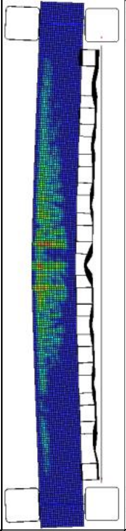	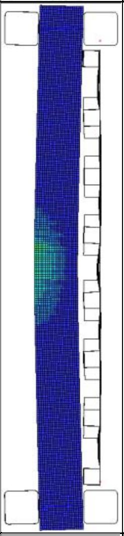	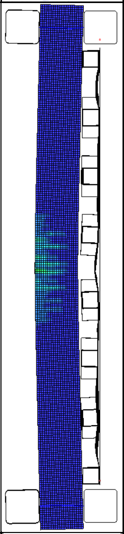
20M (ρ = 2.4%)	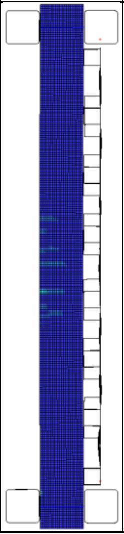	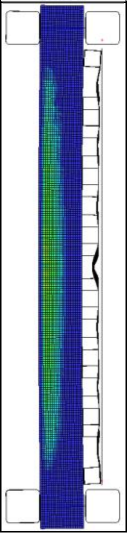	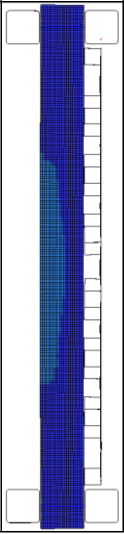	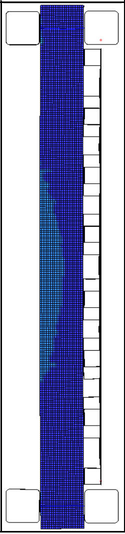	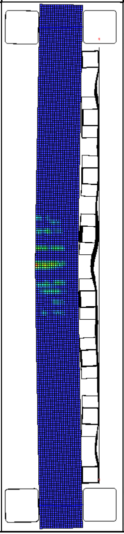	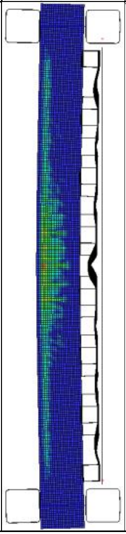	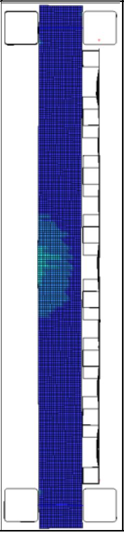	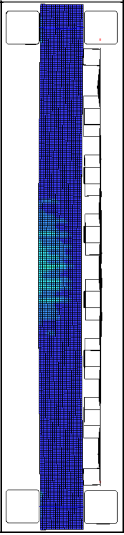

Figure 8 - 22 Effect of steel ratio on damage progression under repeated loading

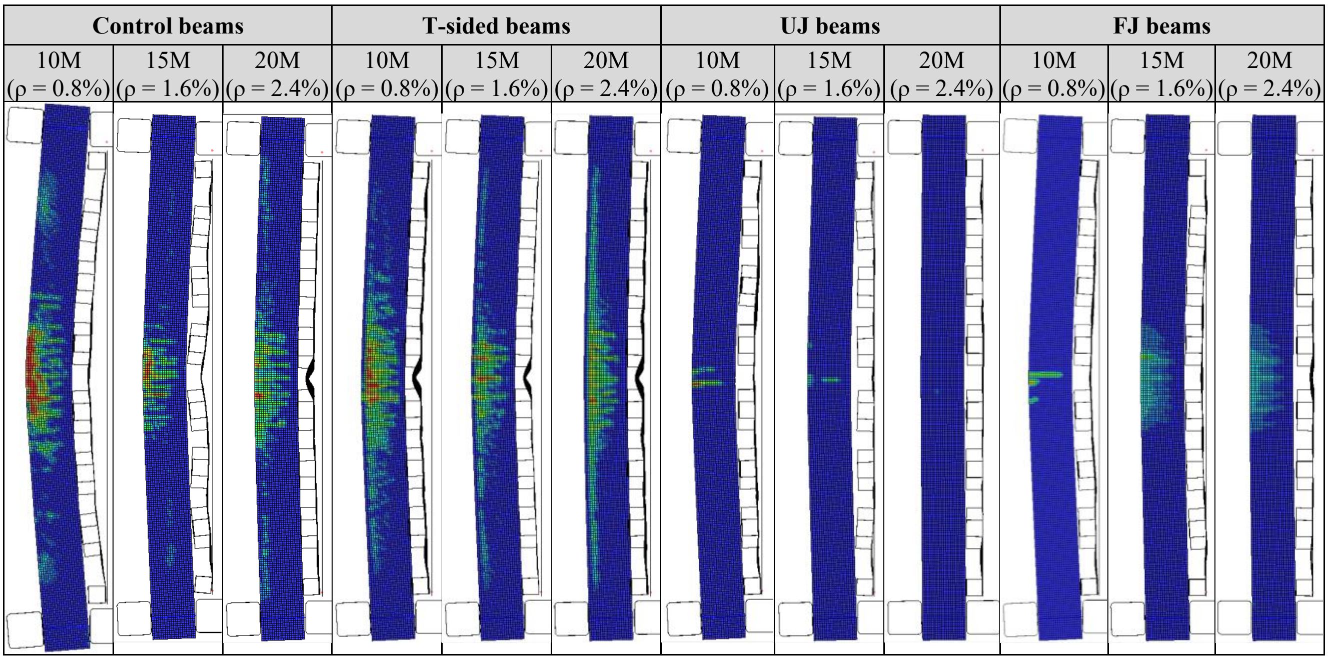

Figure 8 - 23 Effect of steel ratio on damage progression under single Blast-3 loading

8.4.3.3 Effect of steel ratio in the retrofit beams under repeated and single blasts

Next, the effect of tension steel ratio is studied in UHPFRC-retrofit beams with T-sided, UJ and FJ retrofits, and 10M, 15M and 20M bars (ρ = 0.8%, 1.6% and 2.4%), under both repeated and single blast loads. The FE simulation results are presented in **Table 8 - 7** and **Figure 8 - 20** to **Figure 8 - 23**.

Continuing the trend observed in the as-built specimens, increasing the steel ratio results in enhancements in displacement control, but with a change in failure mode under repeated blast loading. For example, the FJ beam shows reductions of 11% and 33% as ρ increases from 0.8% to 1.6% under Blasts 1-2, with further reductions of 16% and 48% as ρ increases to 2.4% (**Figure 8 - 20**). Importantly, while bar fracture occurs in the NSC-10M-75-FJ beam under Blast 3, substituting the 10M reinforcement with 15M and 20M bars effectively prevents bar fracture under repeated blast loading (**Figure 8 - 22**). The same trend is observed for the T-sided and UJ beam types, where specimens with larger steel areas show improved control of displacement and prevent bar fracture.

Next, the effect of steel ratio is considered in the same UHPFRC retrofit beams under single blast loading (**Figure 8 - 21** and **Figure 8 - 23**). All retrofit beams (regardless of steel ratio) survive the single application of Blast 3, however reduced displacements are once again obtained as the steel ratio is increased. For example, the T-sided, UJ and FJ beams with 15M bars (ρ = 1.6%) show reductions of 36%, 33% and 34% in maximum displacements when compared to the companions with 10M bars, with further reductions of 56%, 50% and 50% as the bar area increases further to 20M (ρ = 2.4%).

The effect of steel ratio in the FJ beams with varied steel ratios is further studied under single application of the more intense Blast 4 loading (P_r = 75 KPa and I_r = 610 KPa-ms) as shown in **Figure 8 - 19**. This severe blast caused bar fracture in the beam with 10M bars (ρ =0.8%), while this failure mode is prevented in the FJ beams with 15M and 20M bars (ρ =1.6% and 2.4%).

Thus its is confirmed that the steel ratio is an important parameter which affects the blast performance and failure mode of UHPFRC-retrofitted beams. Increasing the tension steel ratio is effective in reducing blast-induced displacements, and importantly, delaying bar-fracture. Conversely, the application of UHPFRC strengthening in members with low steel ratios should carefully consider the possibility of early bar fracture which can negate the possible benefits of UHPFRC on member strength and stiffness.

8.5 Conclusions

This paper presented the results of an experimental study which examined the effects of strengthening configuration on the blast behaviour of UHPFRC retrofitted RC beams tested under single and repeated blast loads using a shock-tube. The effects of steel ratio on the performance of the retrofits was also studied numerically. The following conclusions can be drawn from this study:

1) In Group 1 (G1), and under repeated blast testing, the UHPFRC retrofits improved the behavior of the RC beams prior to bar rupture. The T-sided, UJ and FJ retrofits increased member stiffness, thereby reducing displacements at equivalent Blasts 1 and 2 loads, with optimal performance recorded for the UJ specimen. However, the repeated tests eventually led to bar fracture in all three retrofits under Blast 3. This failure is attributed to the high bond capacity of the UHPFRC, low tension steel ratio of ρ = 0.8%, and repeated blast testing which intensified the crack localization in the UHPFRC.
2) In Group 2 (G2), and under single Blast 3 testing, the UHPFRC jacketing in beam NSC-10M-75-FJ-S led to a reduction of maximum and residual displacements when compared to the as-built NSC-10M-75-S specimen, without the problem of bar rupture. Improved control of displacements without bar rupture was also observed in the beam with the localized FJ(Hinge) and hybrid T&FJ(Hinge) retrofits, which also showed

unique crack patterns consisting of multiple dominant cracks, which shifted away from midspan.

3) All beams in G2 survived the blast tests and were subsequently tested under static four-point bending to assess their residual capacity. All three retrofits showed higher residual capacity when compared to the as-built specimen, with greater stiffness and strength observed for the NSC-10M-75-FJ-S and NSC-10M-75-T&FJ(Hinge)-S beams. The FJ beam eventually failed by bar rupture, while this failure was delayed or prevented in the beams with the localized T&FJ(Hinge) and FJ(Hinge) retrofits.

4) Finite element modelling was used to predict the blast behaviour of the test beams, with an excellent ability to predict the displacements and failure modes observed in the experiments. FE analysis was further used to study the effects of blast load scenario and steel ratio in the G1 beams. In the numerical simulations, the FJ, UJ and T-retrofits showed an ability to reduce displacements, with no bar rupture under the single Blast 3 scenario. Increasing the steel ratio was also shown to reduce displacements in the as-built and UHPFRC retrofit beams under both single and repeated blast loading. Importantly, retrofit beams with increased steel ratios showed an ability to delay or prevent bar rupture under both repeated and single blast loading.

References

[1] CSA. Design and assessment of buildings subjected to blast loads. CSA S850-12. Mississauga, ON: Canadian Standards Association; 2012.

[2] Noshiravani T, Brühwiler E. Experimental Investigation on Reinforced Ultra-HighPerformance Fiber-Reinforced Concrete Composite Beams Subjected to Combined Bending and Shear. ACI Stuctural Journal. 2013;110:251-61.

[3] Safdar M, Matsumoto T, Kakuma K. Flexural behavior of reinforced concrete beams repaired with ultra-high performance fiber reinforced concrete (UHPFRC). Composite Structures. 2016;157:448-60.

[4] Yuan TF, Hong SH, Shin HO, Yoon YS. Bond Strength and Flexural Capacity of Normal Concrete Beams Strengthened with No-Slump High-Strength, High-Ductility Concrete. Materials. 2020;13.

[5] Moon J, Reda Taha MM, Kim JJ. Flexural Strengthening of RC Slabs Using a Hybrid FRP-UHPC System Including Shear Connector. Advances in Materials Science and Engineering. 2017:1-7.

[6] Hussein L, Amleh L. Structural behavior of ultra-high performance fiber reinforced concrete-normal strength concrete or high strength concrete composite members. Construction and Building Materials. 2015;93:1105-16.

[7] Yin H, Teo W, Shirai K. Experimental investigation on the behaviour of reinforced concrete slabs strengthened with ultra-high performance concrete. Construction and Building Materials. 2017;155:463-74.

[8] Al-Osta MA, Isa MN, Baluch MH, Rahman MK. Flexural behavior of reinforced concrete beams strengthened with ultra-high performance fiber reinforced concrete. Construction and Building Materials. 2017;134:279-96.

[9] Paschalis SA, Lampropoulos AP, Tsioulou O. Experimental and numerical study of the performance of ultra high performance fiber reinforced concrete for the flexural strengthening of full scale reinforced concrete members. Construction and Building Materials. 2018;186:351-66.

[10] Ramachandra Murthy A, Karihaloo BL, Priya DS. Flexural behavior of RC beams retrofitted with ultra-high strength concrete. Construction and Building Materials. 2018;175:815-24.

[11] Tanarslan HM, Alver N, Jahangiri R, Yalçınkaya Ç, Yazıcı H. Flexural strengthening of RC beams using UHPFRC laminates: Bonding techniques and rebar addition. Construction and Building Materials. 2017;155:45-55.

[12] Lampropoulos AP, Paschalis SA, Tsioulou OT, Dritsos SE. Strengthening of reinforced concrete beams using ultra high performance fibre reinforced concrete (UHPFRC). Engineering Structures. 2016;106:370-84.

[13] Sakr MA, Sleemah AA, Khalifa TM, Mansour WN, Beushausen H, Dehn F, Moyo P. Behavior of RC beams strengthened in shear with ultra-high performance fiber reinforced concrete (UHPFRC). MATEC Web of Conferences. 2018;199:09002.

[14] Fan W, Shen D, Yang T, Shao X. Experimental and numerical study on low-velocity lateral impact behaviors of RC, UHPFRC and UHPFRC-strengthened columns. Engineering Structures. 2019;191:509-25.

[15] Lee JY, Aoude H, Yoon YS, Mitchell D. Impact and blast behavior of seismically-detailed RC and UHPFRC-Strengthened columns. International Journal of Impact Engineering. 2020;143.

[16] Wei J, Li J, Wu C, Liu Z-x, Fang J. Impact resistance of ultra-high performance concrete strengthened reinforced concrete beams. International Journal of Impact Engineering. 2021;158.

[17] Zanuy C, Ulzurrun GSD. Impact Resisting Mechanisms of Shear-Critical Reinforced Concrete Beams Strengthened with High-Performance FRC. Applied Sciences. 2020;10.

[18] Habel K, Gauvreau P. Behavior of Reinforced and Posttensioned Concrete Members with a UHPFRC Overlay under Impact Loading. Journal of Structural Engineering. 2009;3:292-300.

[19] ICRI. ICRI Standard 310.2 Selecting and Specifying Concrete Surface Preparation for Sealers, Coatings, Polymer Overlays, and Concrete Repair with CSP Chips. 2013.

[20] Lloyd A, Jacques E, M S, Palermo D, Nistor I, Tikka T. Capabilities of a Shock Tube to Simulate Blast Loading on Structures. ACI SP-281: Behaviour of concrete structures subjected to blast and impact loadings. 2011:1-20.

[21] Christian M. Effect of high-performance concrete and steel materials on the blast performance of reinforced concrete one-way slabs: University of Ottawa; 2016.

[22] Jackson CM, Jacques E, Saatcioglu M. Blast retrofit of one-way reinforced concrete members using externally bonded FRP and FRP anchorage. International Journal of Protective Structures.

2022;13:209-35.
[23] Khaksefidi S, Ghalehnovi M, de Brito J. Bond behaviour of high-strength steel rebars in normal (NSC) and ultra-high performance concrete (UHPC). Journal of Building Engineering. 2021;33.
[24] Pokhrel M, Bandelt MJ. Material properties and structural characteristics influencing deformation capacity and plasticity in reinforced ductile cement-based composite structural components. Composite Structures. 2019;224.
[25] Pokhrel M, Shao Y, Billington S, Bandelt MJ. Effect of Fiber Content Variation in Plastic Hinge Region of Reinforced UHPC Flexural Members. Fibre Reinforced Concrete: Improvements and Innovations2021. p. 1042-55.
[26] Hallquist JO. LS-DYNA theory manual. 2006.
[27] Murray YD. Users Manual for LS-DYNA Concrete Material Model 159. Cambridge, MA: Federal Highway Administration; 2007.
[28] Gholipour G, Zhang C, Mousavi AA. Loading rate effects on the responses of simply supported RC beams subjected to the combination of impact and blast loads. Engineering Structures. 2019;201:109837.
[29] Zhang C, Gholipour G, Mousavi AA. Nonlinear dynamic behavior of simply-supported RC beams subjected to combined impact-blast loading. Engineering Structures. 2019;181:124-42.
[30] Guo W, Fan W, Shao XD, Shen DJ, Chen BS. Constitutive model of ultra-high-performance fiber-reinforced concrete for low-velocity impact simulations. Composite Structures. 2018;185:307-26.
[31] Fan W, Xu X, Zhang Z, Shao X. Performance and sensitivity analysis of UHPFRC-strengthened bridge columns subjected to vehicle collisions. Engineering Structures. 2018;173:251-68.
[32] Gholipour G, Muntasir Billah AHM. Nonlinear Analysis of Shear-Deficient Beams Strengthened Using UHPFRC under Combined Impact and Blast Loads. Journal of Structural Engineering. 2022;148.
[33] Fujikake K, Uebayashi K, Ohno T, Shimoyama Y, M K. Dynamic properties of steel fiber reinforced mortar under high-rates of loadings and triaxial stress states. Structures Under Shock and Impact VII. 2002:437-46.
[34] Fujikake K, Senga T, Ueda N, Ohno T, M. K. Effects of strain rate on tensile behavior of reactive powder concrete. Journal of Advanced Concrete Technology. 2006;4:79-84.
[35] Cowper G, Symonds P. Strain-hardening and strain-rate effects in the impact loading of cantilever beams. Brown Univ. Applied Mathematics Report; 1957. p. 28.

Chapter 9: Effects of UHPFRC jacketing and axial loading on the blast behaviour of reinforced concrete columns

Paper 6: extracted from dynamic results in series 2 (submitted to journal- "Journal of Building Engineering")

Abstract

The objective of this study was to characterize the effects of axial loading and UHPFRC (ultra-high performance fiber-reinforced concrete) jacketing on the blast performance of reinforced concrete columns. The Test Group included two as-built and strengthened columns with UHPFRC jacketing applied over the full span (FJ). The Companion Group included three as-built and UHPFRC-strengthened beams, with jacketing applied either over the full span (FJ) or in the middle hinge region (FJ-Mid). With the exception of axial load, the specimens in both groups had the same dimensions, reinforcement properties and boundary conditions. In both groups, the UHPFRC jacketing improved control of blast-induced displacements and damage when compared to the as-built specimens. Under equivalent blasts, axial loading was also confirmed to reduce the magnitude of the displacements in both the as-built and retrofit specimens. In addition, applying UHPFRC jacketing increased the blast capacity of the columns, but ultimately led to rupture of the tension steel bars. As part of the numerical study, finite element (FE) modelling was used to predict the blast behavior of the test specimens, and to study the effects of parameters not considered in the experiments, including the effects of axial load ratio, boundary conditions, longitudinal steel ratio and jacket design on blast performance and failure mode.

Keywords: UHPFRC; Jacketing; Columns; Blast loading; Buildings; FE modelling.

9.1 Introduction

Beams and columns are critical elements which affect the blast resistance of reinforced concrete (RC) buildings. In particular, the sudden failure of axially-loaded RC columns can lead to partial or complete progressive collapse in buildings [1]. Under interior or external blast threats, beams in floor systems or at the roof level may also undergo significant upward or downward pressures [1]. On the other hand, the beams and columns in existing RC buildings may be blast-deficient since they lack the detailing required by modern blast codes [2]. These structural components may also face increased vulnerability due to deterioration and ageing. Thus, there is a need to develop novel techniques for the blast hardening of RC beams and columns in vulnerable structures.

Recently, ultra-high performance fiber-reinforced concrete (UHPFRC) has been proposed as a novel material for the blast protection of structures. Indeed, the excellent blast resistance of UHPFRC columns has been established in several experimental and numerical studies [3-6]. For example, Aoude et al. [3] noted the ability of UHPFRC to reduce displacements and increase blast resistance of comparable RC columns under shock-tube loading simulating far-field explosions. Using numerical SDOF analysis, Astarlioglu and Krauthammer [4] also verified the superior blast resistance of UHPFRC columns when compared to RC columns having either simple or fixed supports, and varied axial loads. A number of other tests confirm the remarkable blast resistance of UHPFRC columns under close-in or contact explosions [7, 8], as well as impact loads [9].

Recent studies also confirm the ability of UHPFRC strengthening to improve the impact resistance of existing RC structures [10-15]. Among them, Fan et al. [10] demonstrated the superior crash-worthiness of axially-loaded UHPFRC-jacketed columns under low-velocity impact loads (v_o= 5.4-6.9 m/s) using three retrofit schemes ("middle", "two-ends" and their combination), with the "two-end" scheme proving to be most effective. Adding UHPFRC in the "middle" contact zone increased the impact resistance, while the combined scheme triggered shear failure. Lee et al. [11] further verified the ability of UHPFRC jacketing to enhance the resistance of axially-loaded RC columns with seismic detailing, also under low-velocity impacts (v_o= 3.4-4.8 m/s). Wei et al. [12] presented further drop-hammer tests (v_o= 3.1 m/s) on RC beams with UHPFRC retrofits applied using three overlay configurations (T-sided, T-sided with a spacing gap, T and C-sided) and noted the ability of UHPFRC to eliminate "concrete shattering", with improved performance when applying a 5 mm spacing gap. Tests by Zanuy and Ulzurrun [13] and Habel and Gauvreau [14] also confirm the ability of T-sided

UHPFRC overlays to improve the shear/flexural impact resistance of beams/slabs subjected to low-velocity impacts. Wei et al. [15] presented additional drop-hammer tests on axially-loaded RC beams with UHPFRC jacketing and noted the ability of UHPFRC to shift the failure from shear to flexure at v_o= 4.95 m/s, while shear failure developed in the unstrengthened zone at v_o= 5.4 m/s. The effects of different impact locations and jacket lengths were further studied numerically; increasing the jacket length enhanced impact resistance, while the retrofit was less effective when the impact was applied outside the strengthened zones.

Despite these important studies, very limited tests exist on the blast behaviour of UHPFRC-strengthened columns. The effects of axial load, axial ratio, boundary conditions, and retrofitting scheme in blast-loaded columns also requires further study. Accordingly, this paper studies the influence of UHPFRC jacketing and axial loading on the blast resistance of RC members under shock-tube tests simulating far-field explosions. Finite element modelling is further used to study the influence of parameters not considered in the tests, including the effects of axial ratio, steel ratio, boundary conditions and jacket thickness/design on blast resistance and failure mode.

9.2 Experimental investigation

9.2.1 Description of test specimens

A total of five specimens were included in this study. As shown in **Figure 9 - 1(a)**, the as-built and strengthened specimens had the same reinforcement properties and dimensions of 150 × 200 × 2440 mm. Longitudinal reinforcement consisted of 4-10M bars (ρ = 1.3%), with equal amounts of bars in tension and compression. Transverse reinforcement consisted of square ties made from 6.3mm wire spaced as 75mm throughout the span, with a clear cover of 20mm on all faces. The tie spacing was selected to meet the requirements for “moderately ductile” columns in the CSA A23.3 standard [16]. All specimens were first cast with the same normal-strength ready-mix concrete (NSC), while strengthening in the retrofit specimens involved removing the existing concrete cover with a pneumatic-chisel and replacing it with a 20mm UHPFRC jacket (**Figure 9 - 2(a)**).

As shown in **Figure 9 - 1(b)**, the Test Group (TG) included one as-built column and one column strengthened with UHPFRC jacketing applied over the entire span (FJ: full-span jacketing). These specimens were tested under combined axial and blast loading. The axial load of 400 kN corresponded to 30% of the nominal axial capacity of the as-built column ($0.3P_o$, where $P_o = 0.85(f_{co}A_c) + A_{st}f_y$, and where f_{co} = specified strength of the NSC concrete, A_c

= net concrete area, A_{st} = steel area and f_y = steel yield strength). Blast testing consisted of applying gradually increasing blast pressures corresponding to *Blast 1-2-3*, until failure (see **section 9.2.3**).

The **Companion Group (CG)** included one as-built beam and two specimens strengthened with UHPFRC jacketing applied either over the full-span (FJ) or in the middle hinge region (FJ(Mid)). These beams were tested under a single blast load, corresponding to *Blast 1*, without axial loading. With the exception of the axial load, the specimens in both groups were tested using the same shock-tube, load-transfer device (LTD), span and boundary conditions.

Further details on the test matrix are provided in **Table 9 - 1**. The specimen nomenclature indicates the concrete type ("NSC" for normal-strength concrete), longitudinal bar size ("10M"), tie spacing in mm ("75"), strengthening scheme ("FJ" or "FJ(Mid)"), and test conditions ("S" for the beams tested without axial load, and "AL" for the columns tested under axial loading).

Table 9 - 1 Column test matrix

Group	Specimen ID	Specimen properties			UHPFRC retrofit			Blast sequence	Axial load level
		f'_c (MPa)	Longitudinal Reinf. (ρ)	Transverse Reinf. (ρ_s)	f'_c (MPa)	Thickness (mm)	Type		
Companion Group (Beams)	NSC-10M-75-S	58.4	4-10M (1.3%) [2 top, 2 bottom]	Ties at s = 75mm (2.2%)	-	-	-	Blast 1	-
	NSC-10M-75-FJ-S				180	20	FJ	Blast 1	-
	NSC-10M-75-FJ(Mid)-S				180	20	FJ(Mid)	Blast 1	-
Test Group (Columns)	NSC-10M-75-AL	58.4	4-10M (1.3%)	Ties at s = 75mm (2.2%)	-	-	-	Blast 1-2	$0.3P_o$
	NSC-10M-75-FJ-AL				180	20	FJ	Blast 1-2-3	$0.3P_o$

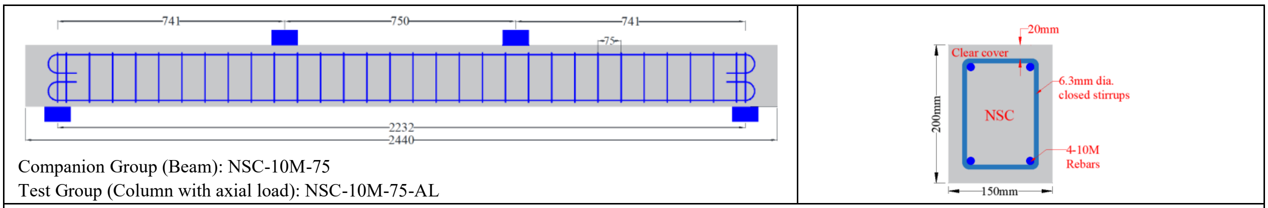

a) As-built specimens, dimensions and reinforcement details

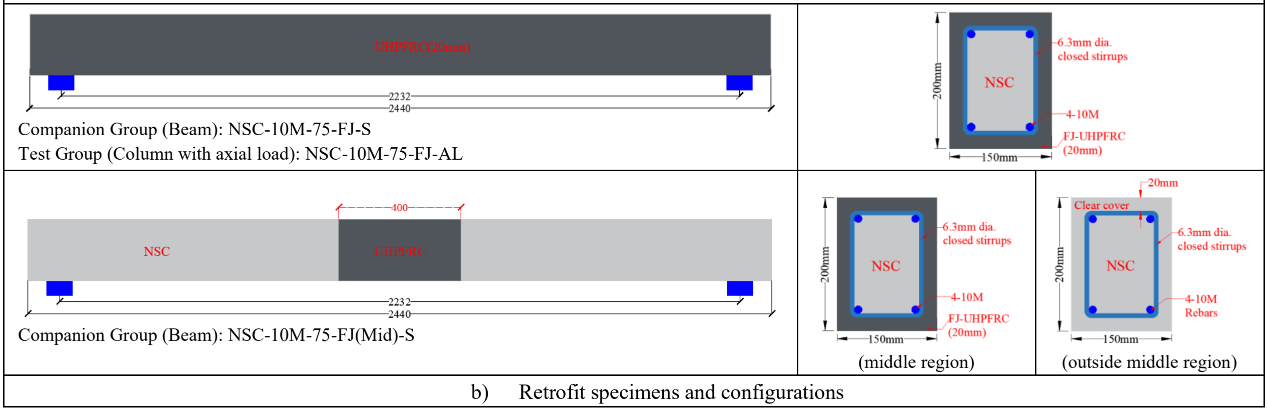

(middle region) (outside middle region)

b) Retrofit specimens and configurations

Figure 9 - 1 Specimen design details

9.2.2 Material properties

The ready-mix concrete which was used to first cast the specimens had a specified strength of 40 MPa, maximum aggregate size of 10 mm and slump of 120 mm. **Table 9 - 1** reports the compressive strength of the NSC concrete on the day of testing (f_c'), as determined from 100 × 200 mm cylinders tested according to ASTM C39. The proprietary UHPFRC used for the retrofitting had a specified strength of 140 MPa and was mixed using a large-capacity pan-mixer at the University of Ottawa. The mix components included a dry premix, water, liquid admixtures and steel fibers. The 13mm-long steel fibers had a tensile strength of 2850 MPa, and were added at a volume fraction of 2.5% (195 kg/m^3). The compressive and flexural properties of the UHPFRC were obtained by testing 75×150 mm cylinders and 75×75×280 mm prisms according to ASTM C1856. Sample results from these tests are plotted in **Figure 9 - 2(b-c)**. The steel properties were determined by testing standard coupons according to ASTM A615. The 10M bars and 6mm wire, with areas A_b = 31 and 100 mm^2, had average yield strengths (f_y) of 484 MPa and 413 MPa (see **Figure 9 - 2(d)**).

Casting of NSC   Interface preparation   Moistening   Retrofitting

a) Specimen fabrication process

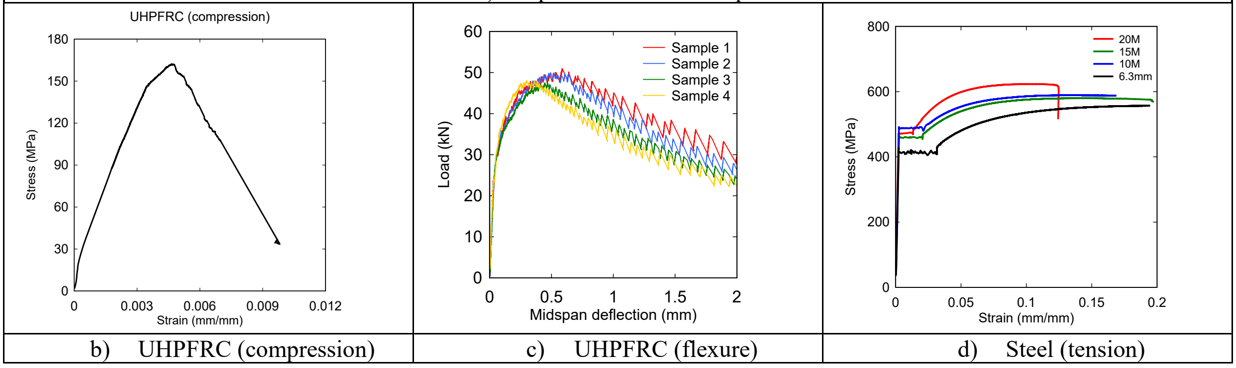

b) UHPFRC (compression)   c) UHPFRC (flexure)   d) Steel (tension)

Figure 9 - 2 Material properties and specimen fabrication

9.2.3 Test setup and procedure

All specimens were tested under blast loads using the shock-tube device shown in **Figure 9 - 3(a)** [17]. The main components of the shock-tube include: 1 – a variable length driver (which generates the shock wave using pressurized air), 2 – a spool section (which triggers the test), 3 – an expansion section (which ensures a uniform shock-front), and 4 – a rigid end-frame with 2 m × 2 m opening (where the specimens are attached). **Figure 9 - 3(b)** shows the setup used in the column tests. The column specimens had a test span of 2232 mm and were bolted to the end-frame using steel fixtures which provided simple boundary conditions. A load-transfer device (LTD) which covered the entire end-frame opening was used to collect and transfer the blast pressures onto the specimens [18]. The LTD consisted of a light-gauge 2 m × 2.44 m sheet metal, and a series of fourteen rigid hollow section beams (76× 76 × 6 mm) which were distributed equally over the test area. The axial load of 400 kN was applied using a hydraulic jack placed above the specimens, and reacted against the underside of the laboratory strong floor. With the exception of the axial load, the beams were tested using the same LTD, span and boundary conditions.

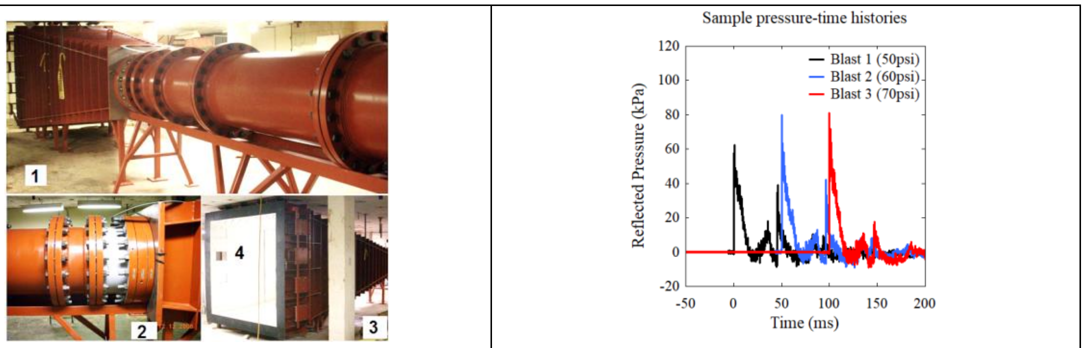

(a) Shock-tube device

(c) Blast testing sequence

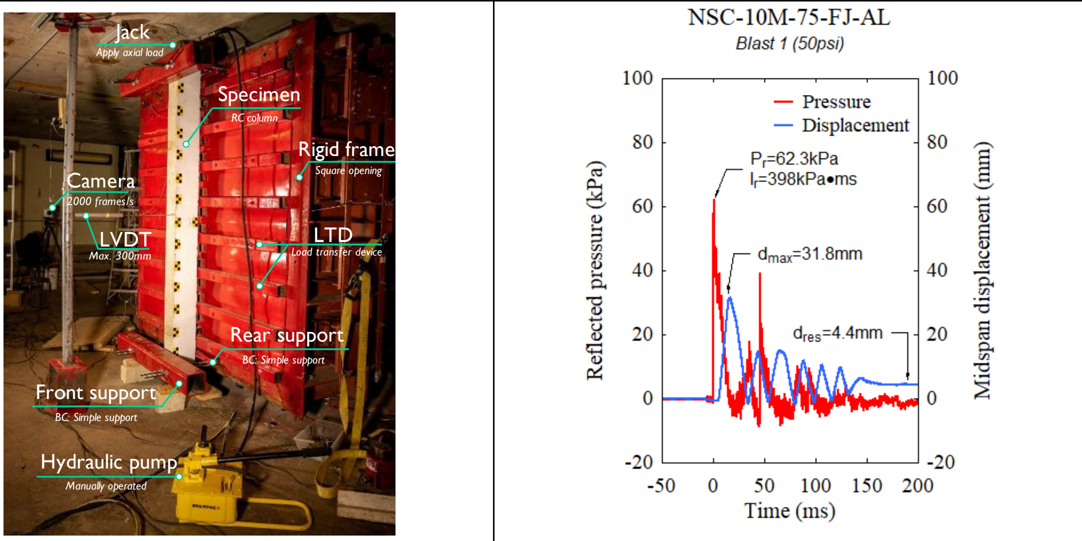

(b) Blast test setup

(d) Blast shockwave and response parameters

Figure 9 - 3 Details of the dynamic test setup and blast testing parameters

The blast loading sequence for the columns in the Test Group (TG) consisted of three gradually increasing blasts corresponding to *Blasts 1-2-3* which were meant to damage and fail the specimens. These blasts were generated by fixing the shock-tube driver length at 1829 mm (6 ft) and gradually increasing the shock-tube driver pressure from 345 to 482 kPa (50 to 70 psi). The beams in the Companion Group (CG) were tested under a single application of *Blast 1*. Sample pressure time-histories for *Blasts 1-2-3* are shown in **Figure 9 - 3(c)** and a typical shockwave and response history for one column is shown in **Figure 9 - 3(d)**. The average peak reflected pressures (P_r) and positive-phase impulses (I_r) were: 56 kPa and 383 kPa-ms for Blast 1; 82 kPa and 434 kPa-ms for Blast 2, and; 81 kPa and 474 kPa-ms for Blast 3.

9.3 Experimental results

9.3.1 Summary of results

The experimental results for the test columns and companion beams are presented in **Table 9 - 2**. The data includes the peak reflected pressure (P_r) and impulse (I_r) for each blast test, along with the specimen response in terms of maximum and residual displacements (d_{max}, d_{res}) and corresponding support rotation (θ_{max}). Comparisons of displacement-histories and damage photos illustrating the effects of the test variables are presented in **Figure 9 - 4, 9-5 and 9-7**. The effects of the UHPFRC jacketing and axial loading are discussed in the following sub-sections.

Table 9 - 2 Summary of dynamic test results

Specimen ID	Blast ID	Shockwave Properties[1]			Specimen Response[2]			
		P_r (kPa)	t_d (ms)	I_r (kPa·ms)	d_{max} (mm)	d_{res} (mm)	θ_{max} (°)	Observed damage
NSC-10M-75-S	1	53.0	14.1	375	84.1	70	4.3	Concrete crushing
NSC-10M-75-FJ-S	1	47.8	16.2	388	50.6	40.2	2.6	Crack localization and fiber pull-out (primary crack: 14mm)
NSC-10M-75-FJ(Mid)-S	1	51.2	14.8	377.6	67.5	48.4	3.5	Dual primary cracks (primary cracks: 6/3.5mm)
NSC-10M-75-AL	1	66.9	11.3	377	37.9	13.8	1.9	Mild concrete crushing
	2	83.2	10.4	431	93.5	83.1	4.8	Severe concrete crushing Bar buckling
NSC-10M-75-FJ-AL	1	62.3	12.8	398	31.8	4.4	1.6	Hairline cracks
	2	80.1	10.9	438	42.5	25	2.2	Crack localization (primary crack: 2mm)
	3	81.2	11.7	474	-	-	-	Tension Bar-rupture

Note:
[1]: P_r = Peak reflected pressure; I_r = Reflected impulse; t_d = positive phase duration;
[2]: d_{max} = maximum mid-span displacement; d_{res}= residual mid-span displacement; θ_{max} = max support rotation

9.3.2 Discussion of results

9.3.2.1 Effects of FJ retrofits in CG beams

The effect of UHPFRC jacketing is first studied in the Companion Group (CG) by comparing the results for beams NSC-10M-75-S, NSC-10M-75-FJ-S and NSC-10M-75-FJ(Mid)-S. All three beams were tested under *Blast 1*, without axial load. The FJ and FJ(Mid) beams were retrofitted with UHPFRC jackets applied over the full span and middle hinge region, respectively. The results in terms of displacement histories and damage modes are compared in **Figure 9 - 4(a) and Figure 9 - 5**.

In general, the full-span jacketing in the FJ beam increased member stiffness and reduced blast-induced displacements when compared to the as-built specimen (**Figure 9 - 4(a)**). Under Blast 1 (I_r = 380 kPa-ms) the as-built beam shows displacements of d_{max} = 84 mm and d_{res} = 70 mm, which compare to 51 mm and 40 mm for beam NSC-10M-75-FJ-S, representing reductions of 40% and 43%. The support rotation θ_{max} of 4.3°, which qualifies under "Heavy" component damage in the CSA S850 Blast standard [2], is also reduced by half to 2.6° ("moderate") in the FJ specimen. Improved performance is also noted for the FJ(Mid) beam, which shows a support rotation of 3.5° ("moderate" range in CSA S850), and displacements of d_{max} = 68 mm and d_{res} = 48 mm, corresponding to reductions of 20% and 31%, when compared to the as-built specimen.

As shown in **Figure 9 - 5**, actual damage in the as-built beam consists of crushing of concrete on the compression face, and full depth but widely spaced flexural cracks on the tension side. In comparison, the FJ beam shows a network of closely spaced fine cracks, and the formation of a single dominant crack at midspan. The width of the primary crack is 14 mm, which indicates complete fiber pullout at this location. The cracking pattern is also distinct in the beam with the FJ(Mid) retrofit, and consists of dual dominant cracks at the two ends of the UHPFRC retrofit region, with reduced primary crack widths of 6 mm and 4 mm when compared to the beam with full-span jacketing.

Subsequent to the blast tests, the beams were tested under quasi-static four-point bending to assess their residual flexural capacity (**Figure 9 - 6**). All three specimens show significant residual capacity, however the FJ beam shows a larger peak residual strength (P^R_{max}) and stiffness (k^R_s), with increases of 25% and 130%, when compared to the as-built beam. Conversely, this beam fails at an earlier displacement due to rupture of the tension steel bars at the previously formed dominant crack. The FJ(Mid) beam shows modest improvements of 10%

and 30% in residual strength and stiffness when compared to the as-built beam, however the dual crack pattern increases ductility and delays rupture of the tension steel bars when compared to the beam with full-span jacketing (increase in Δ^R_{max} from 42 to 65 mm, where Δ^R_{max} is the displacement at the end of the static test).

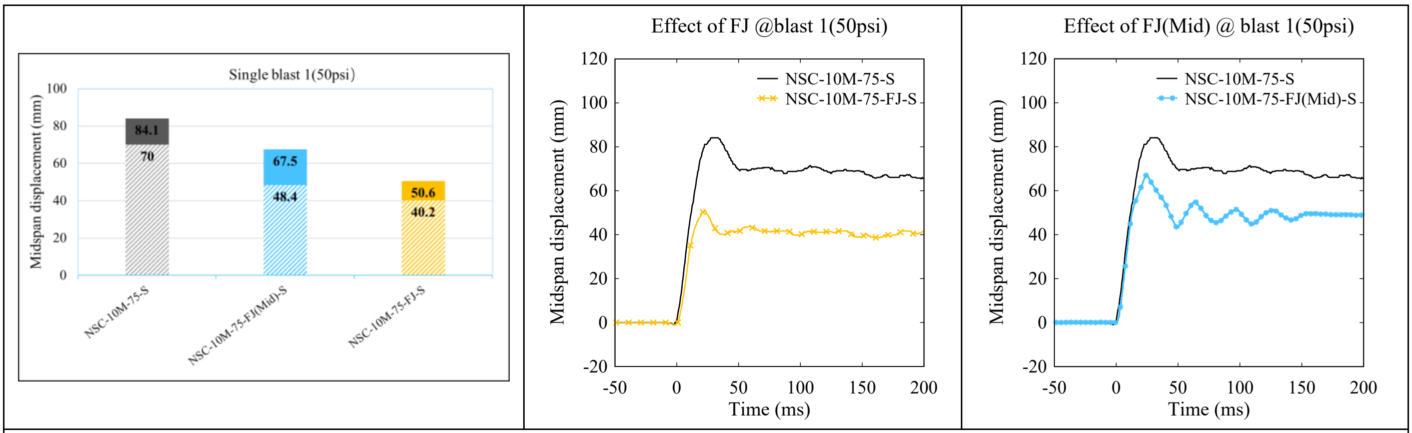

a) Effect of UHPFRC in beams under single blast loading

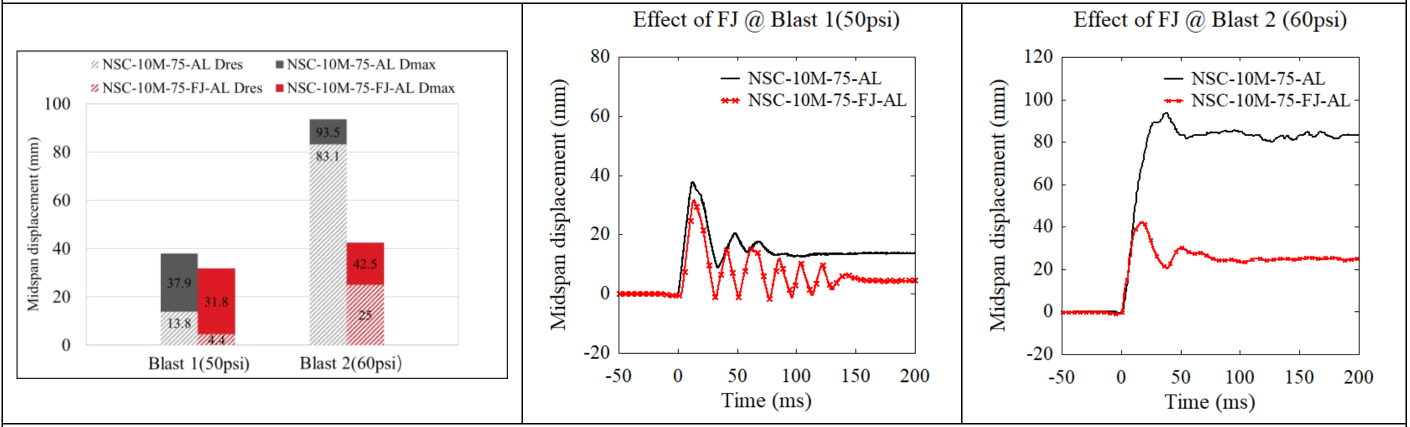

b) Effect of UHPFRC in columns under repeated blast loading

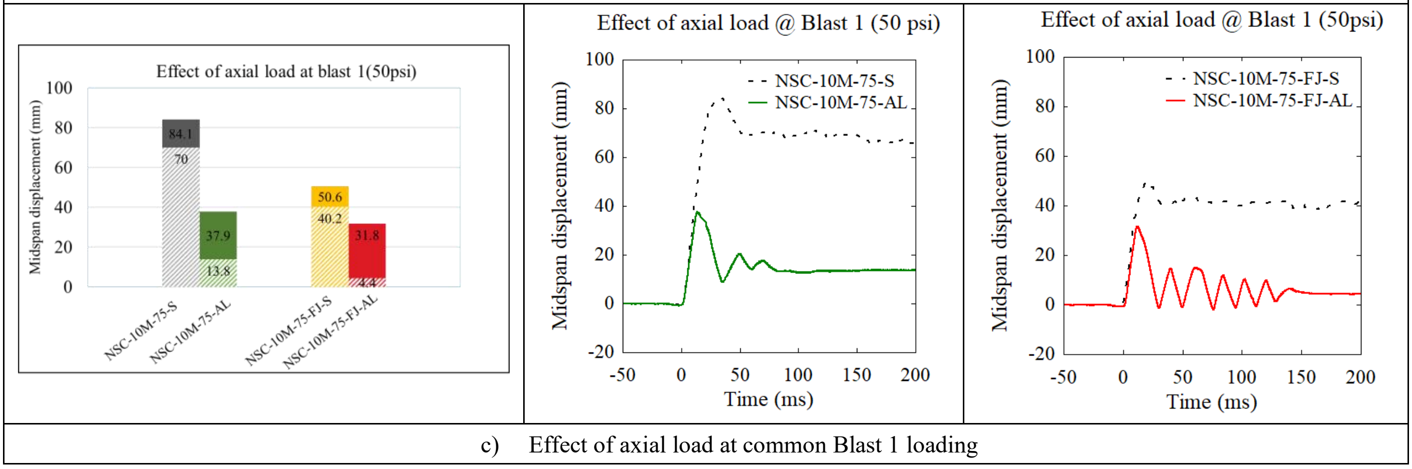

c) Effect of axial load at common Blast 1 loading

Figure 9 - 4 Effect of UHPFRC jacketing and Axial loading

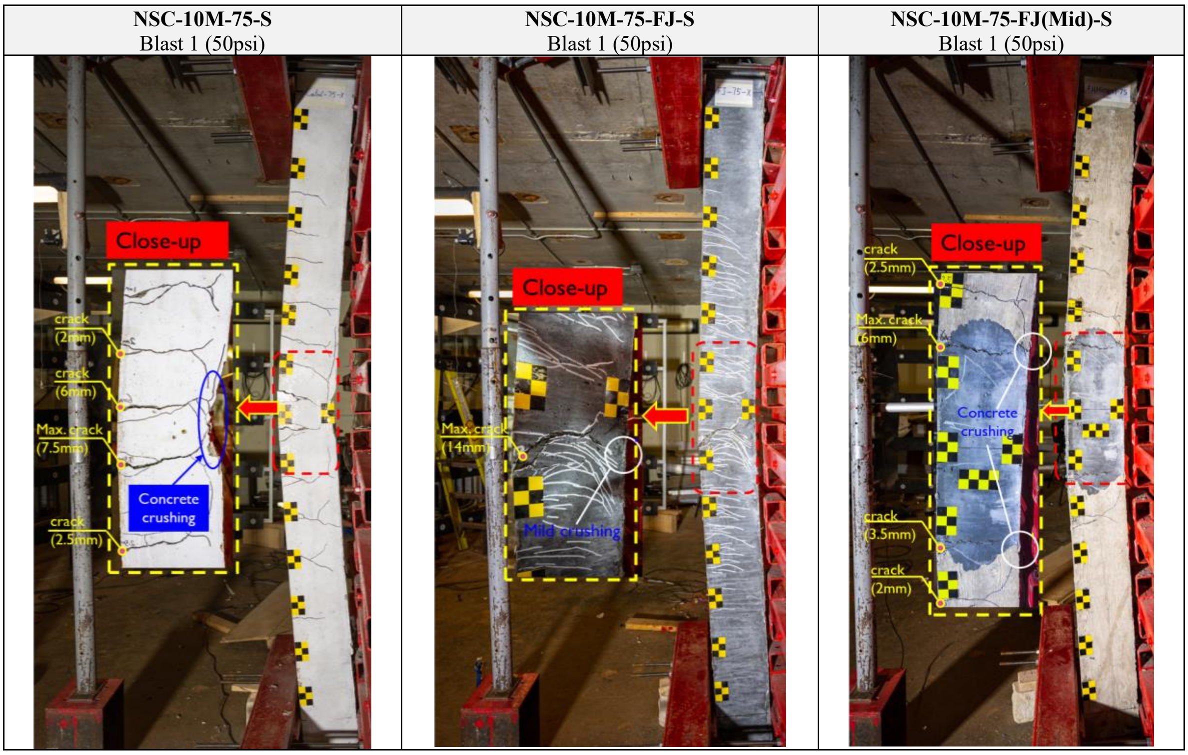

Figure 9 - 5 Progression of damage in Companion-group Beams under single Blast 1

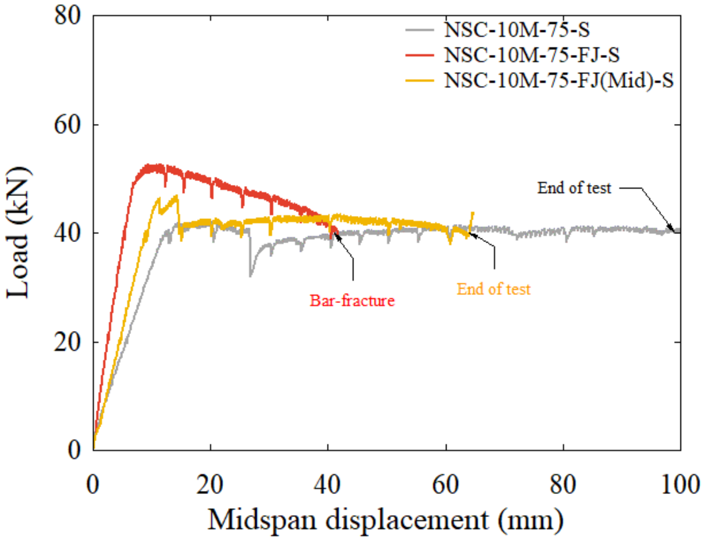

Figure 9 - 6 Results from post-blast residual static tests in the beams

9.3.2.2 Effect of FJ retrofit in TG columns

Next, the effect of UHPFRC jacketing is studied in the Test Group (TG) by comparing the results for columns NSC-10M-75-FJ-AL (retrofit) and NSC-10M-75-AL (as-built). These specimens were tested under combined axial and blast loads corresponding to *Blast 1-2-3*. The axial load was 400kN ($0.3P_o$) for each test, and only full-span jacketing was considered in this group. The results in terms of displacements and damage modes are studied in **Figure 9 - 4(b)** and **Figure 9 - 7**.

Continuing the previous trend, the NSC-10M-75-FJ-AL column shows reductions of 16% in d_{max} (32 mm vs. 38 mm) and 68% in d_{res} (4.4 mm vs. 13.8 mm) when compared to the as-built NSC-10M-75-AL specimen under *Blast 1* (I_r = 380 kPa-ms) (**Figure 9 - 4(b)**). Both columns survive this blast with moderate support rotations of θ_{max} = 1.9° and 1.6°, however damage is better controlled in the retrofit specimen (**Figure 9 - 7**). The as-built column shows full-depth flexural cracks, and suffers obvious concrete crushing after this test, while the UHPFRC jacket effectively prevented this damage. The FJ column once again shows a single dominant crack at midspan. The FJ column continued to show reduced displacements when compared to the as-built counterpart under *Blast 2* (I_r = 435 kPa-ms), with obvious reductions of 55% in d_{max} (43 mm vs. 94 mm) and 70% in d_{res} (25 mm vs. 83 mm) (**Figure 9 - 4(b)**). The support rotation is also reduced by half from 4.8° ("Heavy") in the as-built column, to 2.2° ("moderate") in the retrofit specimen. Indeed, the as-built column shows severe crushing, wide flexural cracks, buckling of the compression bars, and generates blast fragments after this test (**Figure 9 - 8**). In comparison, the column with UHPFRC jacketing only shows mild crushing, and further opening of the dominant crack at midspan. On the other hand, this primary crack now reaches 8 mm, indicating near complete fiber pullout.

Failure in the retrofit specimen eventually occurs under the third application of *Blast 3* (I_r = 474 kPa-ms), and is characterized by rupture of the tension steel bars at the previously formed dominant crack (**Figure 9 - 7**). This failure is attributed to the high bond-capacity of the UHPFRC, the crack localization effect (which was intensified by the repeated blast tests), and the relatively low tension steel ratio in the columns. Nonetheless, a study of the high-speed video indicates no secondary blast fragments, despite the brittle failure (**Figure 9 - 8**).

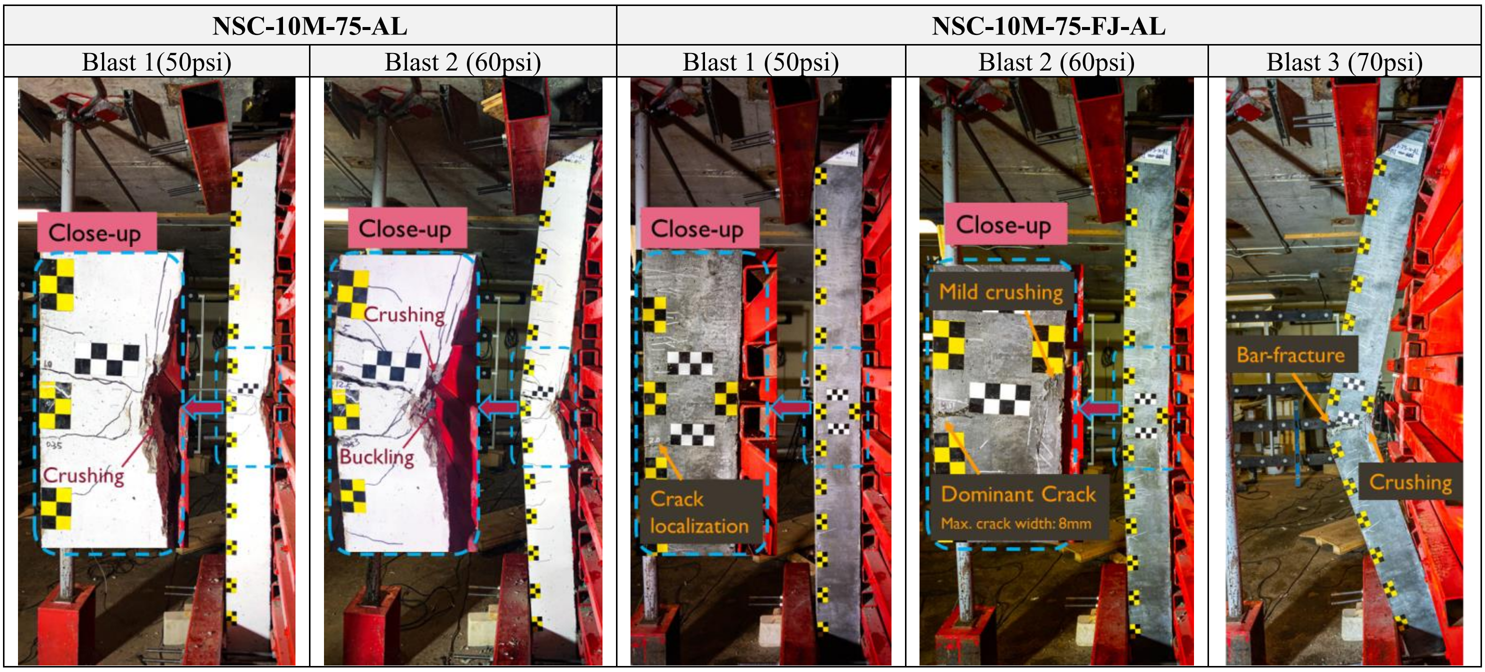

Figure 9 - 7 Progression of damage in Test-group Columns under repeated Blast 1-2-3 loading

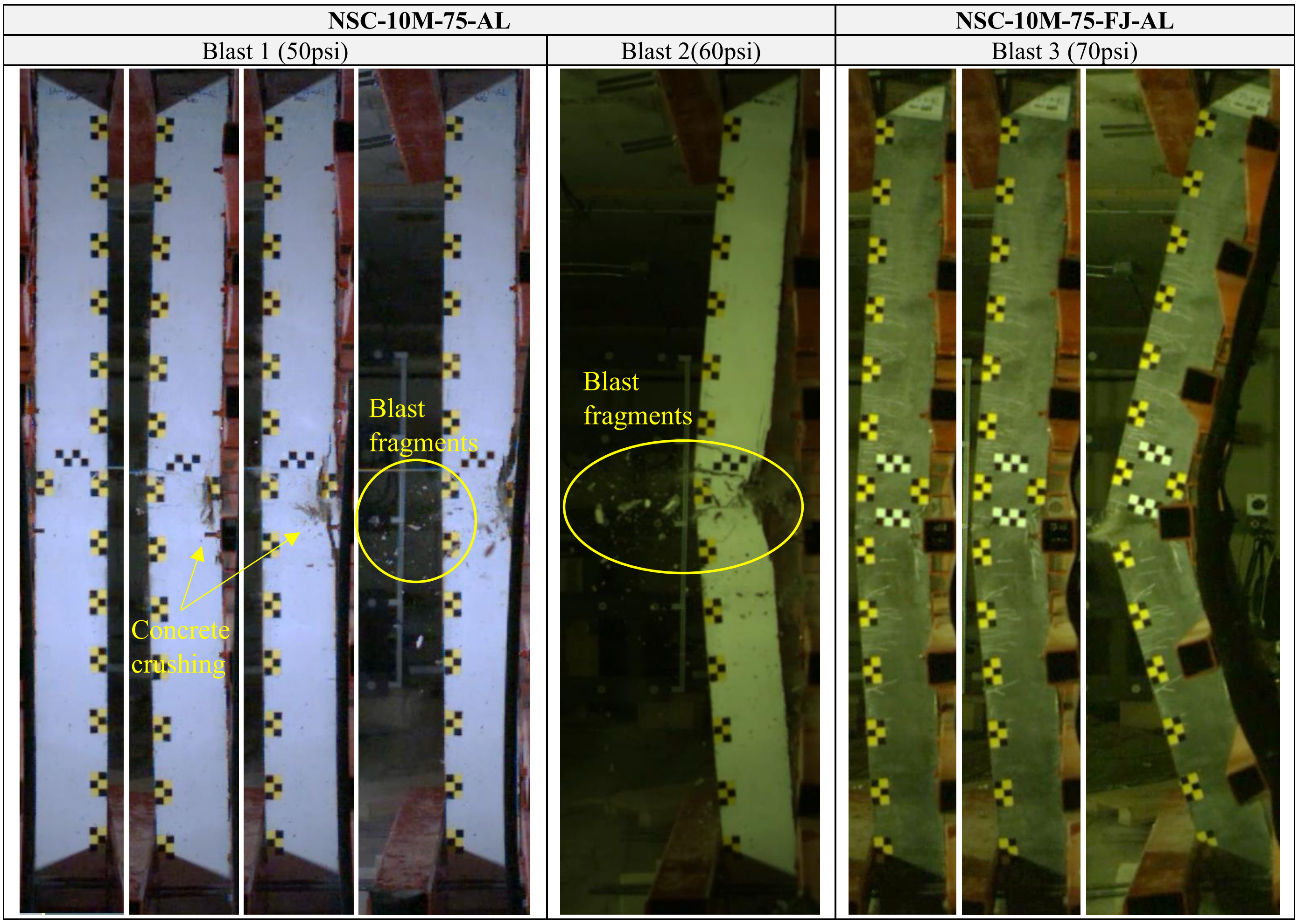

Figure 9 - 8 High-speed stills showing the failure process in as-built and retrofitted columns

9.3.2.3 Effect of axial load in the as-built and retrofit specimens

The effect of axial load is first studied in the as-built set by comparing the results of NSC-10M-75-S and NSC-10M-75-AL under the common *Blast 1* load. Both specimens were tested under the same conditions, with the exception of the axial load in the NSC-10M-75-AL test. As shown in **Figure 9 - 4(c)**, the column with axial load shows obvious reductions of 55% and 80% in d_{max} and d_{res} displacements when compared to the companion beam, which confirms the ability of axial load to effectively reduce blast-induced displacements. The support rotation is also reduced from 4.3° (in the as-built beam) to 1.9° in the column specimen. Both specimens suffered concrete crushing damage after this test, however the maximum crack width is reduced from 7.5 mm to 1.0 mm in the column specimen. The column specimen was tested under a further application of *Blast 2* loading, which resulted in severe concrete damage and buckling of the compression bars.

Both specimens were subsequently tested under static four-point bending after the blast tests and the results are presented in **Figure 9 - 9**. Owing to the increase in blast intensity and damage (from Blast 2), the column shows an obvious reduction in residual flexural strength when compared to the beam (P_{max}^{R} = 33 kN vs 42 kN); indeed, the column retains just 67% of the undamaged flexural capacity, compared to 85% for the beam which was tested under a single application of *Blast 1*.

Next, the effect of axial load is studied in the NSC-10M-75-FJ-S and NSC-10M-75-FJ-AL retrofit specimens, also under the common *Blast 1* load. Continuing the previous trend, the axial load reduces the maximum displacement d_{max} from 51 mm to 32 mm (-37%), and the residual displacement d_{res} from 40 mm to 4 mm (-90%), resulting a near elastic response in the NSC-10M-75-FJ-AL column (see **Figure 9 - 4(c)**). Both specimens show limited damage after this blast, however the width of the dominant crack is clearly reduced in the specimen with axial load (primary crack width of 2 mm vs 14 mm). Subsequent testing consisted of residual static loading for the retrofit beam, and further *Blast 2-3* loading for the retrofit column. Despite the difference in test type, failure was associated with rupture of the 10M tension bars in both specimens.

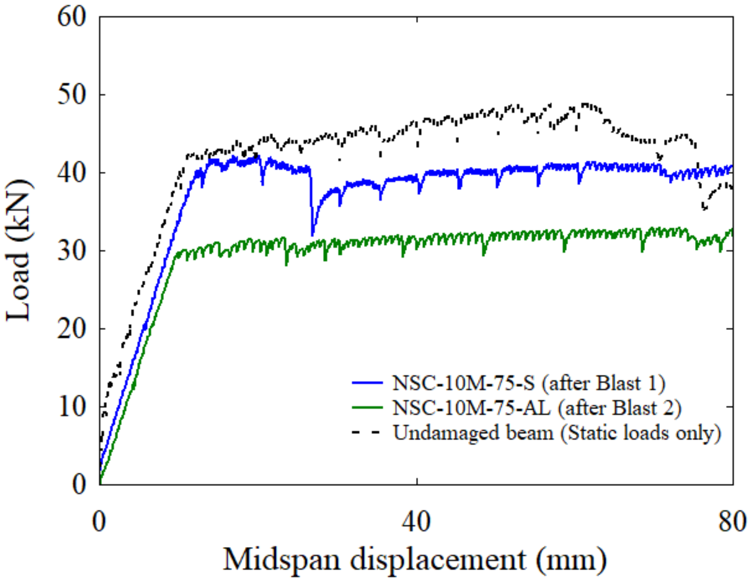

Figure 9 - 9 Results from post-blast residual static tests in the as-built beam and column

9.3.2.4 Summary

In summary, UHPFRC jacketing resulted in improved control of displacements when compared to the as-built specimens in both the beam and column groups. The application of axial load was also found to be significant on displacements in both the as-built and retrofit specimens. Conversely, the beams and columns with full-span jacketing eventually failed by rupture of the tension steel reinforcement. As noted above, this failure may be linked to the high bond capacity of the UHPFRC and low steel ratio in the specimens. In the beam tests, the localized FJ-Mid retrofit was found to be effective in improving blast performance, with an ability to delay bar fracture.

In the next section, the results from the shock-tube blast tests are used to validate numerical finite element (FE) models to gain further insight into the blast behavior of UHPFRC-retrofitted columns with varied axial load ratios, boundary conditions, steel ratios, jacket thickness and jacket designs.

9.4 Numerical Analysis

9.4.1 Validation of numerical models

9.4.1.1 Geometric and element properties

The shock-tube blast test results were used to validate numerical models for further insight into the blast behaviour of the UHPFRC-retrofitted columns. The numerical models were built using LS-DYNA, a finite element (FE) software which is commonly used to model the behaviour of RC components under impact and blast loading [19]. **Figure 9 - 10** shows a typical 3D model which incorporates the shock-tube loading device (LTD), boundary conditions and column specimen.

The 3D models were built using measured geometric properties of the as-built and UHPFRC-retrofitted members. Both beam and solid elements were used in the models. The concrete and UHPFRC elements were modelled using eight-node solid elements (with 10 mm mesh size), while the steel reinforcement was modelled with 10 mm-long two-node *Hughes-Liu* beam elements. Perfect bond was assumed between the concrete and steel reinforcement, and the substrate concrete and UHPFRC. The final models contained 73 200 solid elements for the concrete/UHPFRC and 2514 beam elements for the steel reinforcement. The loading device as well as steel beam fixtures were modelled using four-node *Belytschko-Tsay* shell elements, while the steel bolts at the supports were modelled using four discrete beam elements.

Blast loads were idealized as triangular using the same reflected pressures and impulses found in the experiments using the **LOAD_SEGMENT_SET* keycard in LS-DYNA. For the repeated blasts, the loads were applied with a small time gap between each shot. The axial load was applied on the top surface of the columns using the **LOAD_SEGMENT_SET* keycard, and was set to reduce to zero at the point of maximum displacement, which matches the conditions in the tests.

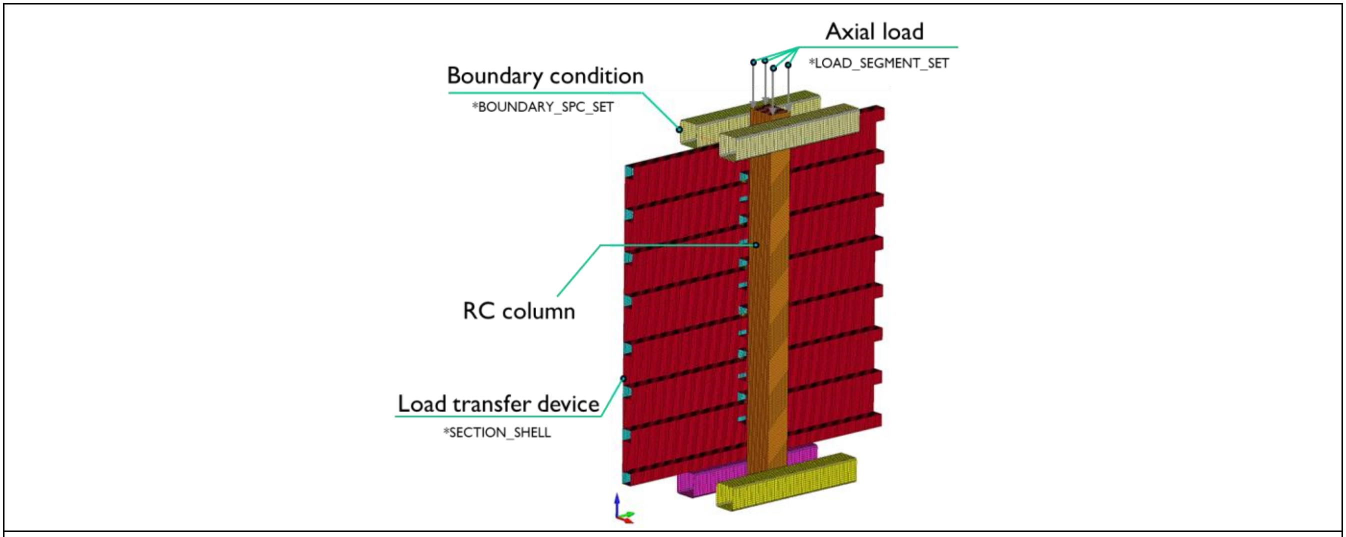

a) Modelling of shock tube

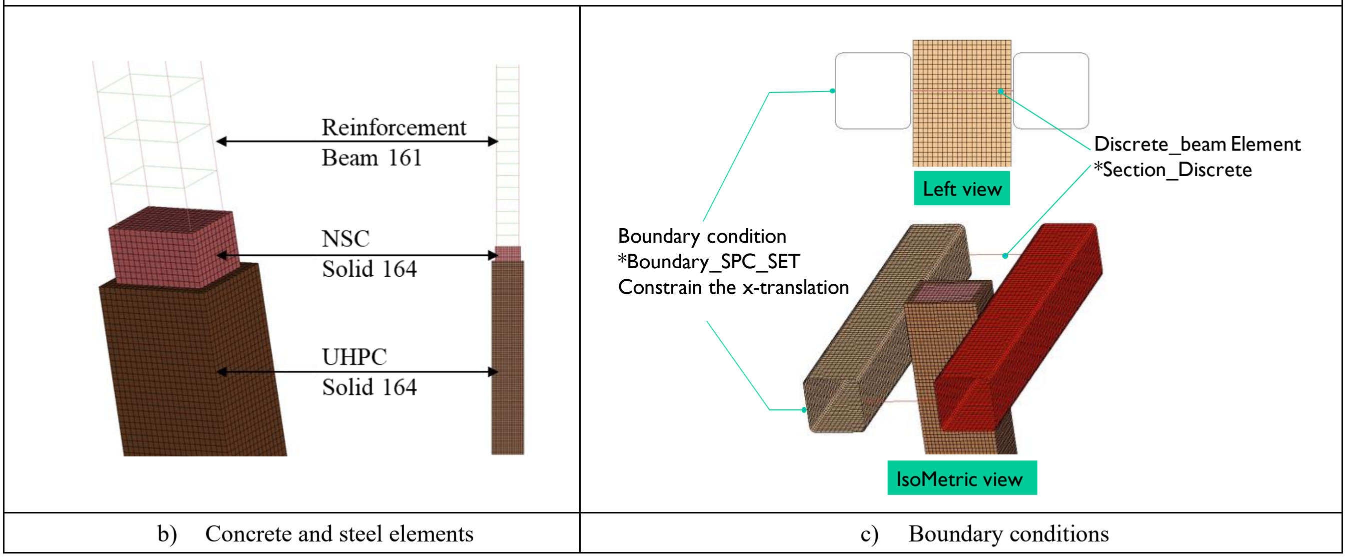

b) Concrete and steel elements

c) Boundary conditions

Figure 9 - 10 FE modelling: 3D model, concrete/steel elements and boundary conditions

9.4.1.2 Material properties

The Continuous Surface Cap Model (CSCM, *MAT_159* in LS-DYNA) was chosen for the concrete and UHPFRC elements [20]. This model includes isotropic constitutive equations, three stress-invariant shear surface formulations, a hardening cap, damage-based softening and rate effect equations. For the NSC concrete, these parameters were automatically specified using initialization routines based on the compressive strength (f_c') of 58 MPa and maximum aggregate size of 10 mm. Rate effects were considered using the equations shown in **Table 9 - 3** [20].

To better capture the UHPFRC properties, the calibrated formulations proposed by Guo et al. [21] were applied. This calibrated model which includes 45 input parameters has been shown to well predict the behaviour of UHPFRC members under impact and blast conditions [10, 22, 23]. **Table 9 - 3** lists the parameters which were considered for the UHPFRC. Rate effects were also modified using the updated formulations in Guo et al. [21] based on the equations in Fujikake et al. [24, 25].

The Plastic-Kinematic model (*MAT_003*) was chosen to model the steel reinforcement in the specimens. This bi-linear hardening model was defined based on inputs for the modulus of elasticity, yield stress and tangent modulus, as obtained from the steel coupon tests, with rate effects considered using the Cowper and Symonds model [26].

Table 9 - 3 Constitutive models of materials used in LS-DYNA

<table>
<tr><th colspan="2">FE models</th></tr>
<tr><td>Concrete model (NSC):
Continuous Surface Cap Model
*MAT_CSCM_CONCRETE (MAT_159)

Model parameters generated based on f_c' (58MPa) and maximum aggregate size (10mm).</td><td>DIF for concrete in tension and compression:
$DIF_t = f_{t,d}'/f_t' = 1 + E\dot{\varepsilon}\,\eta_{0t}/(f_t'\dot{\varepsilon}^{N_t})$
$DIF_c = f_{c,d}'/f_c' = 1 + E\dot{\varepsilon}\,\eta_{0t}/(f_c'\dot{\varepsilon}^{N_c})$</td></tr>
<tr><td rowspan="2">UHPFRC model:
Continuous Surface Cap Model, defined using
*MAT_CSCM (MAT_159)

Model defined using 45 input parameters using the calibrated values in Guo et al (2018):
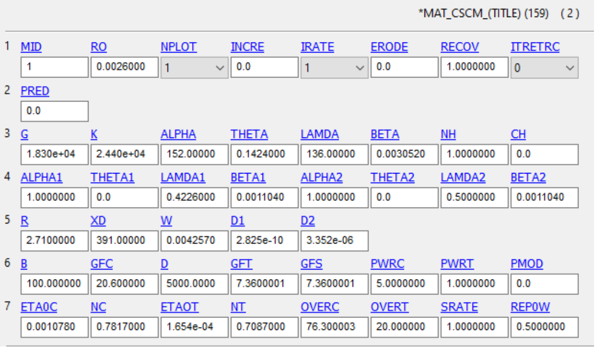
*MAT_CSCM_(TITLE) (159) (2)
<table>
<tr><td>1</td><td>MID</td><td>RO</td><td>NPLOT</td><td>INCRE</td><td>IRATE</td><td>ERODE</td><td>RECOV</td><td>ITRETRC</td></tr>
<tr><td></td><td>1</td><td>0.0026000</td><td>1</td><td>0.0</td><td>1</td><td>0.0</td><td>1.0000000</td><td>0</td></tr>
<tr><td>2</td><td>PRED</td><td></td><td></td><td></td><td></td><td></td><td></td><td></td></tr>
<tr><td></td><td>0.0</td><td></td><td></td><td></td><td></td><td></td><td></td><td></td></tr>
<tr><td>3</td><td>G</td><td>K</td><td>ALPHA</td><td>THETA</td><td>LAMDA</td><td>BETA</td><td>NH</td><td>CH</td></tr>
<tr><td></td><td>1.830e+04</td><td>2.440e+04</td><td>152.00000</td><td>0.1424000</td><td>136.00000</td><td>0.0030520</td><td>1.0000000</td><td>0.0</td></tr>
<tr><td>4</td><td>ALPHA1</td><td>THETA1</td><td>LAMDA1</td><td>BETA1</td><td>ALPHA2</td><td>THETA2</td><td>LAMDA2</td><td>BETA2</td></tr>
<tr><td></td><td>1.0000000</td><td>0.0</td><td>0.4226000</td><td>0.0011040</td><td>1.0000000</td><td>0.0</td><td>0.5000000</td><td>0.0011040</td></tr>
<tr><td>5</td><td>R</td><td>XD</td><td>W</td><td>D1</td><td>D2</td><td></td><td></td><td></td></tr>
<tr><td></td><td>2.7100000</td><td>391.00000</td><td>0.0042570</td><td>2.825e-10</td><td>3.352e-06</td><td></td><td></td><td></td></tr>
<tr><td>6</td><td>B</td><td>GFC</td><td>D</td><td>GFT</td><td>GFS</td><td>PWRC</td><td>PWRT</td><td>PMOD</td></tr>
<tr><td></td><td>100.000000</td><td>20.600000</td><td>5000.0000</td><td>7.3600001</td><td>7.3600001</td><td>5.0000000</td><td>1.0000000</td><td>0.0</td></tr>
<tr><td>7</td><td>ETA0C</td><td>NC</td><td>ETAOT</td><td>NT</td><td>OVERC</td><td>OVERT</td><td>SRATE</td><td>REP0W</td></tr>
<tr><td></td><td>0.0010780</td><td>0.7817000</td><td>1.654e-04</td><td>0.7087000</td><td>76.300003</td><td>20.000000</td><td>1.0000000</td><td>0.5000000</td></tr>
</table></td><td>Rate effect parameters η_{0t}, η_{0c}, N_t, N_c updated based on Guo et al. (2018):
$\eta_{0t} = 0.7912\,f_t'/E,\ N_t = 0.7087$
$\eta_{0c} = 0.311\,f_c'/E,\ N_c = 0.7817$</td></tr>
<tr><td>Longitudinal steel:

*MAT-PLASTIC_KINEMATIC (MAT_003)

Mass density (RO): 7800 kN/m^3
Poisson's ratio (PR): 0.3
Young's modulus (E): 200 GPa
Yield stress(SIGY) and Tangent modulus (ETAN) defined based on steel coupon test results.

DIF: Cowper & Symonds strain rate model which scales the yield stress with the factor $1 + (\frac{\dot{\varepsilon}}{C})^{\frac{1}{p}}$, where C and p are strain rate parameters.</td></tr>
</table>

9.4.1.3 Numerical modelling results

Figure 9 - 11 and **Figure 9 - 12** illustrate the results from the LS-DYNA simulations, in terms of displacement time-histories and damage modes. **Table 9 - 4** compares the peak displacements from the FE numerical models and tests, and their ratio (d_{max}^{num}/d_{max}).

Considering all tests, the average d_{max}^{num}/d_{max} ratio is 1.02, with a mean error of 9%. The as-built beam and column specimens show d_{max}^{num}/d_{max} ratios of 0.98 and 1.02 under *Blast 1*, with a ratio of 1.17 for NSC-10M-75-AL at *Blast 2*. The model also correctly captures the large displacement and failure of the column after this test.

Good predictions are also obtained for the retrofit beams and columns, with errors of less than 5mm under *Blasts 1-2*. The displacement ratio is 1.10 for the NSC-10M-75-FJ-S beam, and the model correctly captures the crack localization (without bar rupture) under the single application of *Blast 1*. Likewise, the NSC-10M-75-FJ(Mid)-S beam shows a $d_{max}^{\mathrm{num}}/d_{max}$ ratio of 0.93, and the model is able to well-capture the damage mode outside the hinge region as observed in the test.

The model for the axially-loaded NSC-10M-75-FJ-AL column results in displacement ratios of 0.83 and 1.08 (with errors of ~ 3-4mm) under *Blasts 1-2*, and accurately predicts the development of the dominant crack and bar rupture failure at *Blast 3*.

Based on these validated numerical models, additional finite element simulations studying the effects of varied axial load levels, boundary conditions, steel ratios and UHPFRC jacket designs were conducted (see **Table 9 - 5**), as presented in the next section.

Table 9 - 4 Numerical analysis results

Specimen ID	Blast ID	Shockwave Properties[1]			Comparison of peak displacements[2]			
		P_r (kPa)	t_{di} (ms)	I_r (kPa·ms)	d_{max} (mm)	d_{max}^{num} (mm)	d_{max}^{num}/d_{max}	Error (%)
NSC-10M-75-S	1	53	14.1	375	84.1	82.2	0.98	2.3%
NSC-10M-75-FJ-S	1	47.8	16.2	388	50.6	55.7	1.10	10.1%
NSC-10M-75-FJ(Mid)-S	1	51.2	14.8	378	67.5	62.7	0.93	7.1%
NSC-10M-75-AL	1	66.9	11.3	377	37.9	38.5	1.02	1.6%
	2	83.2	10.4	431	93.5	109.5	1.17	17.1%
NSC-10M-75-FJ-AL	1	62.3	12.8	398	31.8	26.4	0.83	17.0%
	2	80.1	10.9	438	42.5	45.9	1.08	8.0%
	3	81.2	11.7	474	-	-	-	-
Statistical analysis	Mean d_{max}^{num}/d_{max}						1.02	
	Mean error						9.0%	
	Standard deviation						0.11	
	Coefficient of variation						10.4%	

Note:

[1]: Idealized shockwave properties: P_r = Reflected pressure; I_r = Reflected impulse; t_{di} = duration of idealized blast load;

[2]: d_{max} and d_{max}^{num} = peak mid-span displacement from tests and numerical models.

Table 9 - 5 Properties of columns in the parametric study

Boundary conditions	Column ID	Axial load ratio (% of Po)					Blast load sequence	Longitudinal reinforcement		UHPFRC	
		0%	15%	30%	45%	60%		Bar size	ρ (%)	Retrofit Type	Thickness (mm)
Simple Boundary conditions	NSC-10M-75-AL	*	*	*	*	*	Blast 1-2	10M	1.3%	-	-
	NSC-10M-75-FJ-AL	*	*	*	*	*	Blast 1-2-3	10M	1.3%	FJ	20
	NSC-15M-75-FJ-AL			*			Blast 1-2-3	15M	2.7%	FJ	20
	NSC-20M-75-FJ-AL			*			Blast 1-2-3	20M	4.0%	FJ	20
	NSC-10M-75-FJ(10)-AL			*			Blast 1-2-3	10M	1.3%	FJ	10
	NSC-10M-75-FJ(30)-AL			*			Blast 1-2-3	10M	1.3%	FJ	30
	NSC-10M-75-FJ(Mid)-AL			*			Blast 1-2-3	10M	1.3%	FJ(Mid)	20
Fixed Boundary conditions	NSC-10M-75-AL-F	*	*	*	*	*	Blast 1-2	10M	1.3%	-	-
	NSC-10M-75-FJ-AL-F	*	*	*	*	*	Blast 1-2-3	10M	1.3%	FJ	20
	NSC-15M-75-FJ-AL-F			*			Blast 1-2-3	15M	2.7%	FJ	20
	NSC-20M-75-FJ-AL-F			*			Blast 1-2-3	20M	4.0%	FJ	20
	NSC-10M-75-FJ(10)-AL-F			*			Blast 1-2-3	10M	1.3%	FJ	10
	NSC-10M-75-FJ(30)-AL-F			*			Blast 1-2-3	10M	1.3%	FJ	30
	NSC-10M-75-FJ(Mid)-AL-F			*			Blast 1-2-3	10M	1.3%	FJ(Mid)	20
	NSC-10M-75-FJ(Ends)-AL-F			*			Blast 1-2-3	10M	1.3%	FJ(Ends)	20
	NSC-10M-75-FJ (Mid+Ends)-AL-F			*			Blast 1-2-3	10M	1.3%	FJ (Mid+Ends)	20

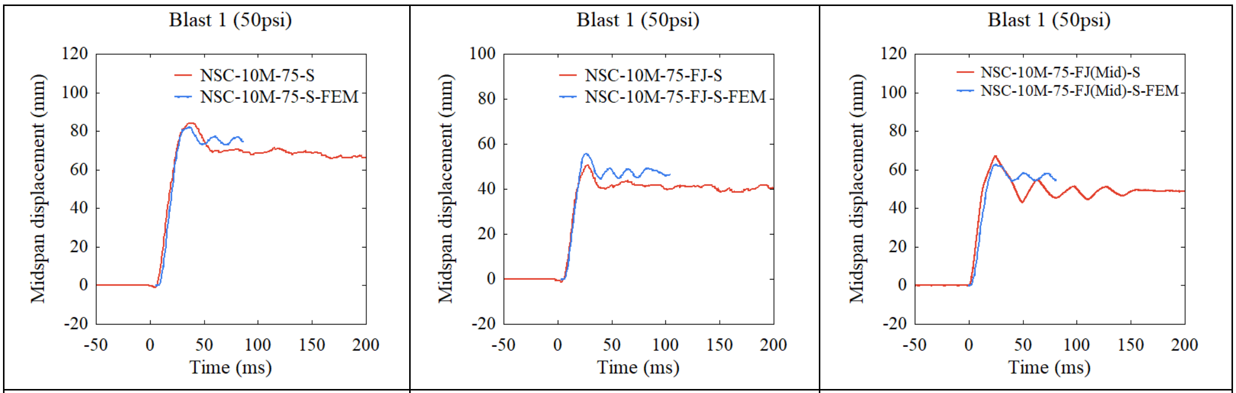

a) NSC-10M-75-S b) NSC-10M-75-FJ-S c) NSC-10M-75-FJ(Mid)-S

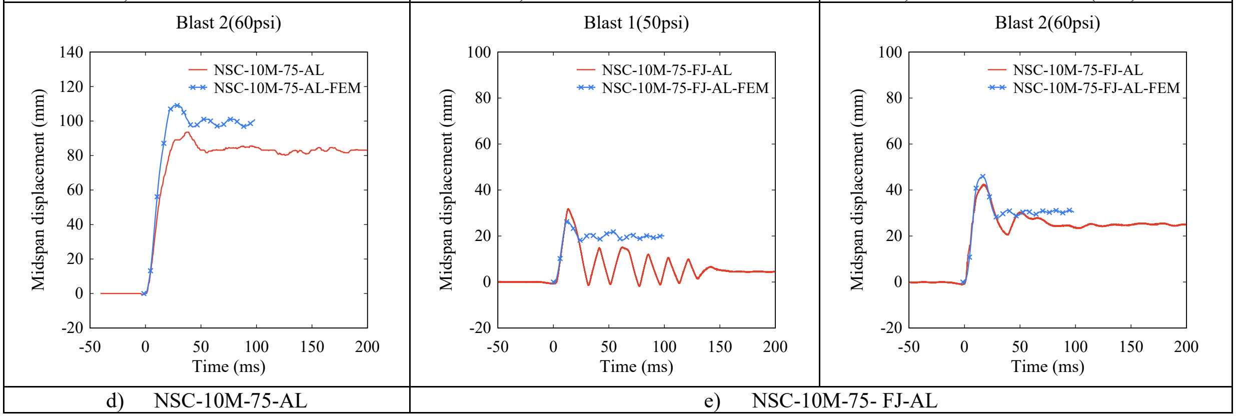

d) NSC-10M-75-AL e) NSC-10M-75- FJ-AL

Figure 9 - 11 Numerical analysis results for tested specimens

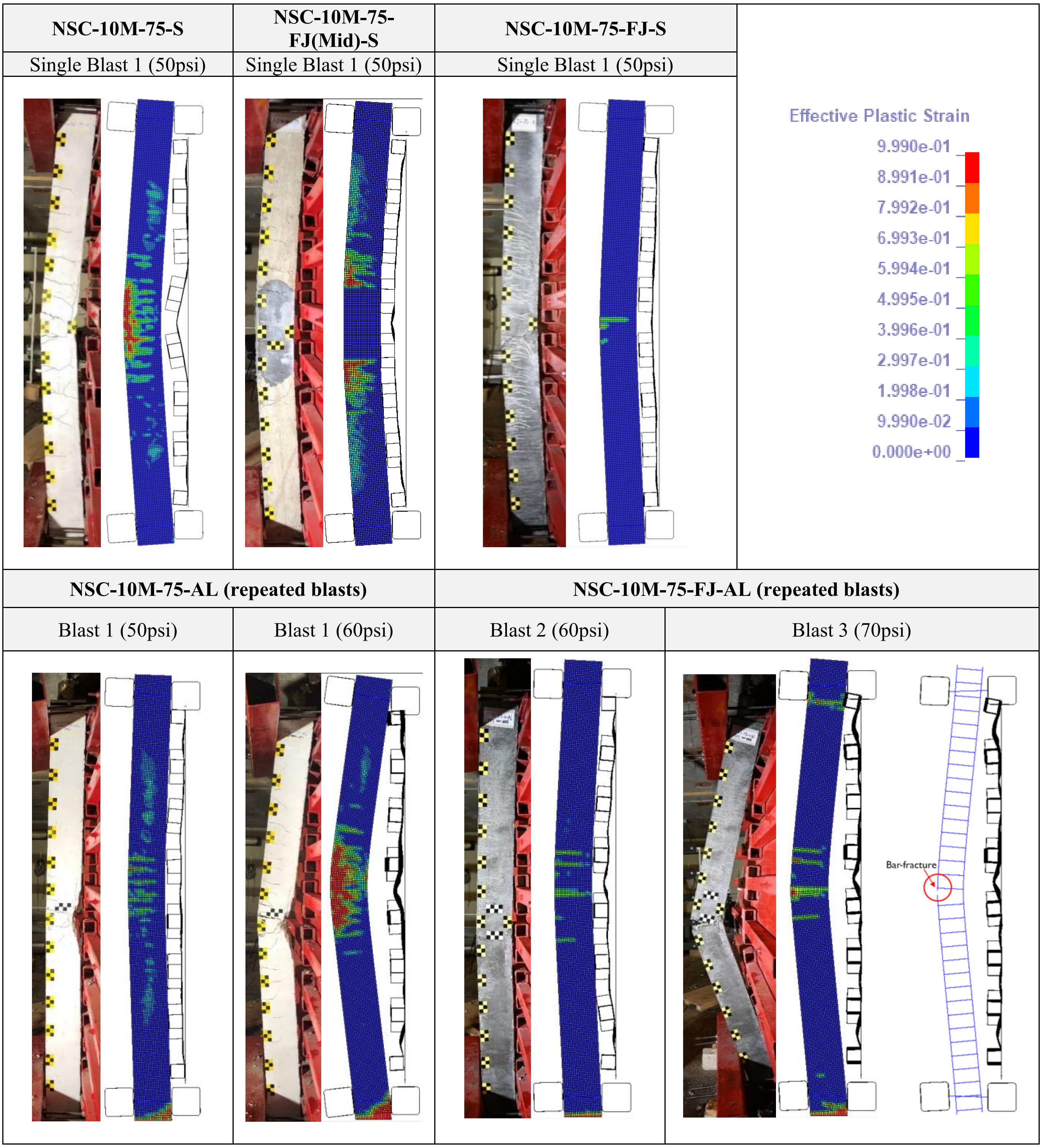

Figure 9 - 12 Experimental and numerical damage profiles for tested specimens

9.4.2 Parametric study

9.4.2.1 Effect of boundary conditions

The effect of boundary conditions (BC) is studied by comparing the numerical results of as-built and FJ columns with simple and fixed supports. In this comparison, NSC-10M-75-AL-F and NSC-10M-75-FJ-AL-F represent the columns with fixed boundary conditions ("F", in the nomenclature). The as-built models were run under *Blast 1-2*, with an axial load of $0.3P_o$, with an additional shot of *Blast 3* applied in the FJ columns. The peak displacements are summarized in **Table 9 - 6**, while **Figure 9 - 13** and **Figure 9 - 14** compare the displacement histories and damage profiles.

As expected, the magnitude of the midspan displacements were reduced as the boundary conditions were changed from simple to fixed. In the as-built case, the peak displacements reduce by 44% and 68% at *Blast 1-2*, along with reductions of 56% and 96% in permanent displacements. The column with fixed supports also shows a noticeable decrease in support rotation (from 5.6^o to less than 2^o) and a clear reduction in damage after *Blast 2*. Indeed, the as-built column with simple supports shows a rotation which exceeds 4^o, indicating heavy damage and failure, whereas the column with fixed boundary conditions survives this blast.

The effect of boundary conditions (fixed vs. simple) is also observed in the FJ-retrofit columns, with reductions of 25% and 44% in peak displacements, along with decreases of 36% and 70% in permanent deformations, under the same two blasts. Both FJ columns show crack localization after *Blast 2*, though the support rotation reduces by nearly half (from 2.4^o to 1.3^o) as the supports change from simple to fixed. Conversely, under the more intense *Blast 3* load, both retrofit columns fail by rupture of the tension steel bars, regardless of the type of support.

As in the simply-supported case, the retrofit column shows smaller displacements than the comparable as-built column with fixed supports. However, the relative decrease in displacements is more significant in the column with simple boundary conditions. Indeed, on average, the peak displacements are reduced by 45% under simple BC, which compares to only 17% for the fixed case. The trend also shows that the UHPFRC has greater effect as the blast intensity or damage in the RC column increases. For example, under fixed BC, the reduction is just 9% at *Blast 1*, compared to 25% at *Blast 2*. In a similar way, under simple BC, the displacements reduce by 31% at *Blast 1* (moderate RC damage), to more than 58% at *Blast 2* (heavy RC damage). Thus it can be concluded that the UHPFRC plays a greater role in reducing blast-induced displacements as the RC column sustains greater damage or approaches failure.

Table 9 - 6 Effects of axial load ratio and boundary conditions

Column ID	Axial load ratio	Simple BC						Fixed BC					
		Blast 1		Blast 2		Blast 3		Blast 1		Blast 2		Blast 3	
		d_{max}	d_{res}	d_{max}	d_{res}	d_{max}	d_{res}	d_{max}	d_{res}	d_{max}	d_{res}	d_{max}	d_{res}
As-built columns: NSC-10M-75-AL NSC-10M-75-AL-F	0%	82.2	74.6	-	-	-	-	37.5	24.1	47.0	16.0	-	-
	15%	50.2	46.1	103.7	97.4	-	-	26.1	18.6	30.1	12.2	-	-
	30%	38.5	34.5	109.5	101.0	-	-	21.7	15.2	34.5	3.93	-	-
	45%	29.4	25.6	112.0	103.0	-	-	18.1	11.2	38.0	16.4	-	-
	60%	24.6	18.9	96.7	86.5	-	-	15.6	8.67	38.2	24.0	-	-
FJ columns: NSC-10M-75-FJ-AL NSC-10M-75-FJ-AL-F	0%	48.9	41.2	45.6	24.1	Rupture		31.5	23.5	32.5	18.3	50.7	22.4
	15%	31.3	25.5	52.1	33.8	Rupture		23.0	16.3	25.5	9.28	39.9	17.7
	30%	26.4	20.0	45.9	30.3	Rupture		19.8	12.9	25.9	8.99	Rupture	
	45%	22.4	15.3	42.9	29.4	Rupture		16.8	9.7	28.3	12.3	Rupture	
	60%	19.9	11.7	41.9	31.8	62.4	34.9	14.9	6.7	25.8	12.2	Rupture	

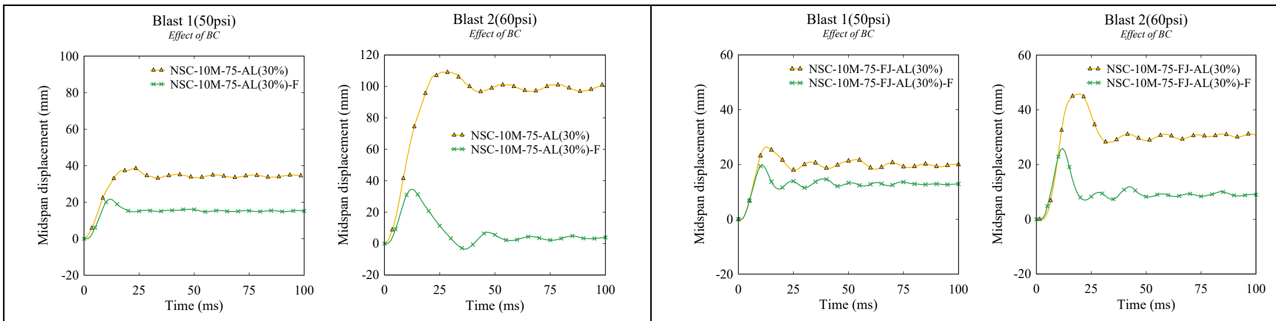

(a) Displacements (control)

(b) Displacements (FJ retrofit)

Figure 9 - 13 Effect of boundary conditions on displacements (at 0.3Pₒ)

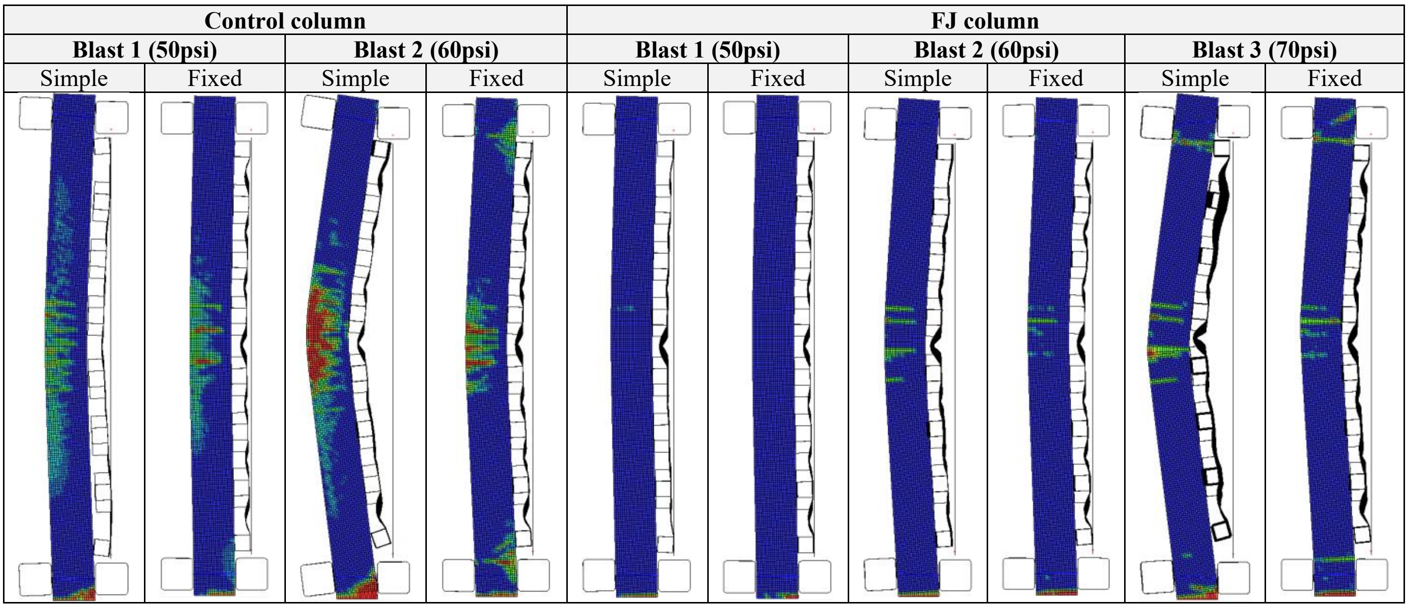

Figure 9 - 14 Effect of boundary conditions on damage profiles (at 0.3Pₒ)

9.4.2.2 Effect of axial load ratio

Next, the effect of axial load ratio is investigated by comparing the results for columns with varied axial ratios ranging from 0.15 to $0.6P_o$, consisting of low (15%), medium (30% or 45%) and high (60%), and the base case of zero axial load. **Figure 9 - 15** plots these loads on the interaction diagram of the as-built column, which was developed using the equivalent-stress block assumptions in CSA A23.3 and elastic-plastic steel properties (without applying material-reduction factors). The point of no axial load corresponds to pure bending, while the low and medium cases are realistic gravity loads for bridge and building columns, respectively. The high axial load was selected since the columns can withstand much higher gravity loads after UHPFRC retrofitting. The models were run for both the as-built and FJ columns, and both simple and fixed boundary conditions were considered. The detailed results are presented in **Table 9 - 6**, while **Figure 9 - 16** and **Figure 9 - 17** present the displacement-histories and damage profiles for all cases.

In general, increasing the axial load reduced the magnitude of displacements in the as-built and retrofit columns with simple supports under *Blast 1*. Compared to the case of zero axial load, the as-built columns with low, medium and high axial ratios show reductions of 39%, 53%-64% and 70% in peak displacements, and corresponding decreases of 38%, 54%-66% and 75% in permanent displacements. The same benefit of increased axial load is also found in the simply-supported retrofit set, with columns having low, medium and high axial loads showing reductions of 36%, 46%-54% and 59% in peak displacements, and 38%, 51%-63% and 72% in permanent displacements at this same blast.

Regardless of the axial ratio, all as-built columns with simple supports fail under *Blast 2*, with displacements of ~100mm, and rotations which exceed 4°. All retrofits show nearly-equal peak displacements ranging from 42-46mm and obvious midspan cracking at this blast, though the extent of cracking is reduced as the axial load is increased. In the end, all FJ columns with simple supports fail by bar fracture at *Blast 3*, with the exception of the $0.6P_o$ column which just survives this shot with a peak displacement of 62mm and support rotation of 3°.

Next the effect of axial ratio is studied in the columns with fixed supports. Continuing the previous trend, both as-built and retrofit specimens show reduced displacements as more axial load is applied. Comparing to the case of zero axial load, as-built specimens with low, medium, high axial ratios show consistent reductions of 30%, 42%-52%, 58% in peak displacements, and 23%, 37%-54% and 64% in residual displacements at *Blast 1*. The midspan damage is also less significant as greater axial load is applied. In a similar way, the FJ columns with low, medium and high axial ratios show consistent reductions of 27%, 37%-47% and 53% in peak displacements, and 31%, 45%-59% and 71% in residual displacements, at this same blast.

All as-built columns with fixed supports survive *Blast 2*, with lower peak displacements as axial load is applied, however the trend related to relative reductions is reversed, with decreases of 36% at $0.15P_o$, 27% at $0.3P_o$, and 19% at $0.45\text{-}0.60P_o$, when compared to the zero axial case. All columns show extensive midspan damage after this blast, however damage is more obvious in the column with zero axial load, and is reduced for columns with medium axial load ($0.3\text{-}0.45P_o$), which can partly be explained by the higher moment capacity at this axial level. Applying axial load also reduces peak displacements by ~20% in the retrofit columns when compared to the zero axial case. The permanent displacements are also reduced, though the trend between $0.15\text{-}0.6P_o$ is not clear (decreases of ~ 50% at $0.15\text{-}0.3P_o$, compared to ~30% at $0.45\text{-}0.60P_o$). However, the failure is affected, with retrofit columns having zero or low axial load ($0.15P_o$) surviving Blast 3, and columns with higher axial ratios ($0.3P_o$ and above) failing by bar rupture.

In summary, the results indicate that axial load ratio has a greater effect on reducing midspan displacement at lower blast levels, while the trend is not clear at higher blast intensities. The beneficial effect of axial load can be explained by the improvement of confinement action. In addition to confinement, arching action [10, 27] also plays an important role in restraining the deflection in the column with fixed supports during Blast 1 (see **Figure 9 - 18**). Under Blast 2, the axial load is only applied on the uncracking segment rather than whole cross-section, resulting in reduced confinement. In addition, the residual damage after Blast 1 leads to poor arching action and more obvious $P-\Delta$ effects. Therefore, less obvious reductions in displacements at Blast 2 are observed in columns with increased axial load. The results also show that the increase in axial load can result in earlier bar rupture failures in UHPFRC-retrofitted columns having fixed boundary conditions.

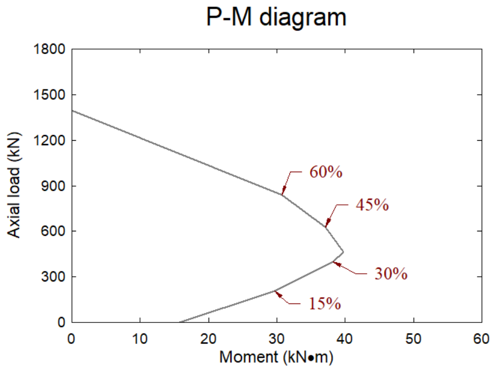

Figure 9 - 15 Column interaction diagram and axial load ratios

Boundary condition (BC)	Displacement Results		
	Blast 1	**Blast 2**	**Maximum and Residual Displacements**
Controls Simple	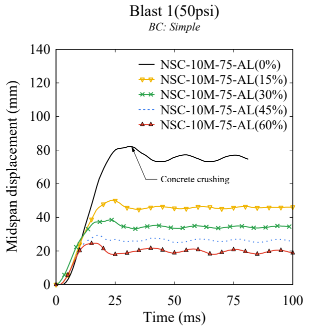	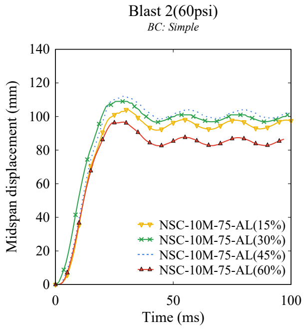	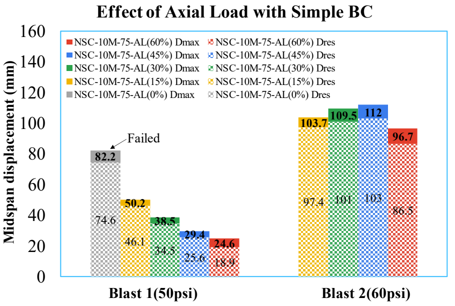
Controls Fixed	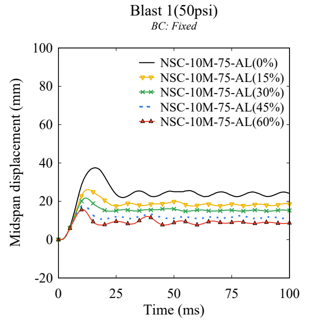	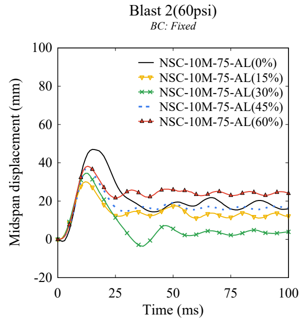	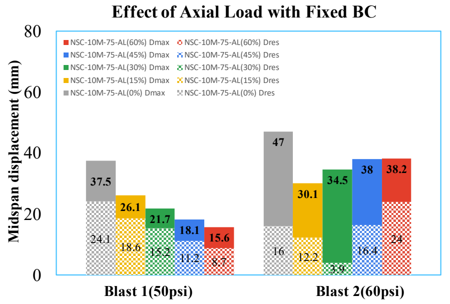
FJ Simple	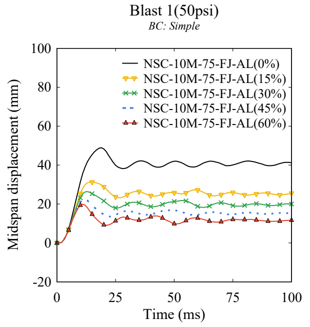	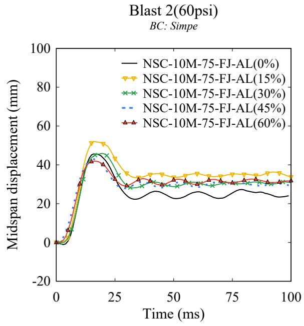	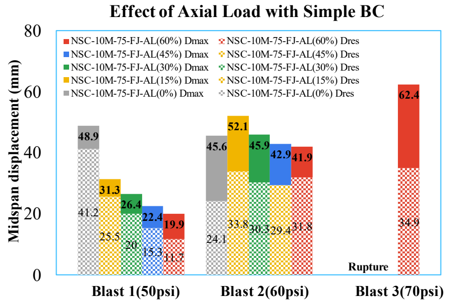
FJ Fixed	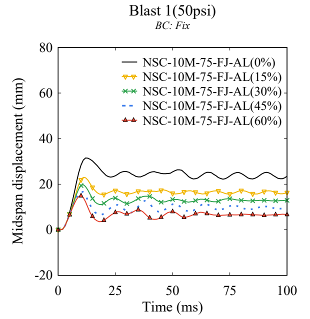	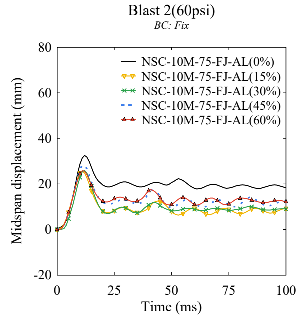	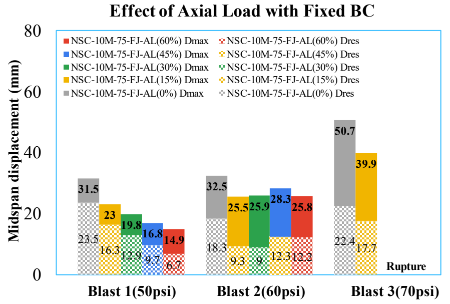

Figure 9 - 16 Effect of axial load ratio on displacements (simple and fixed BC)

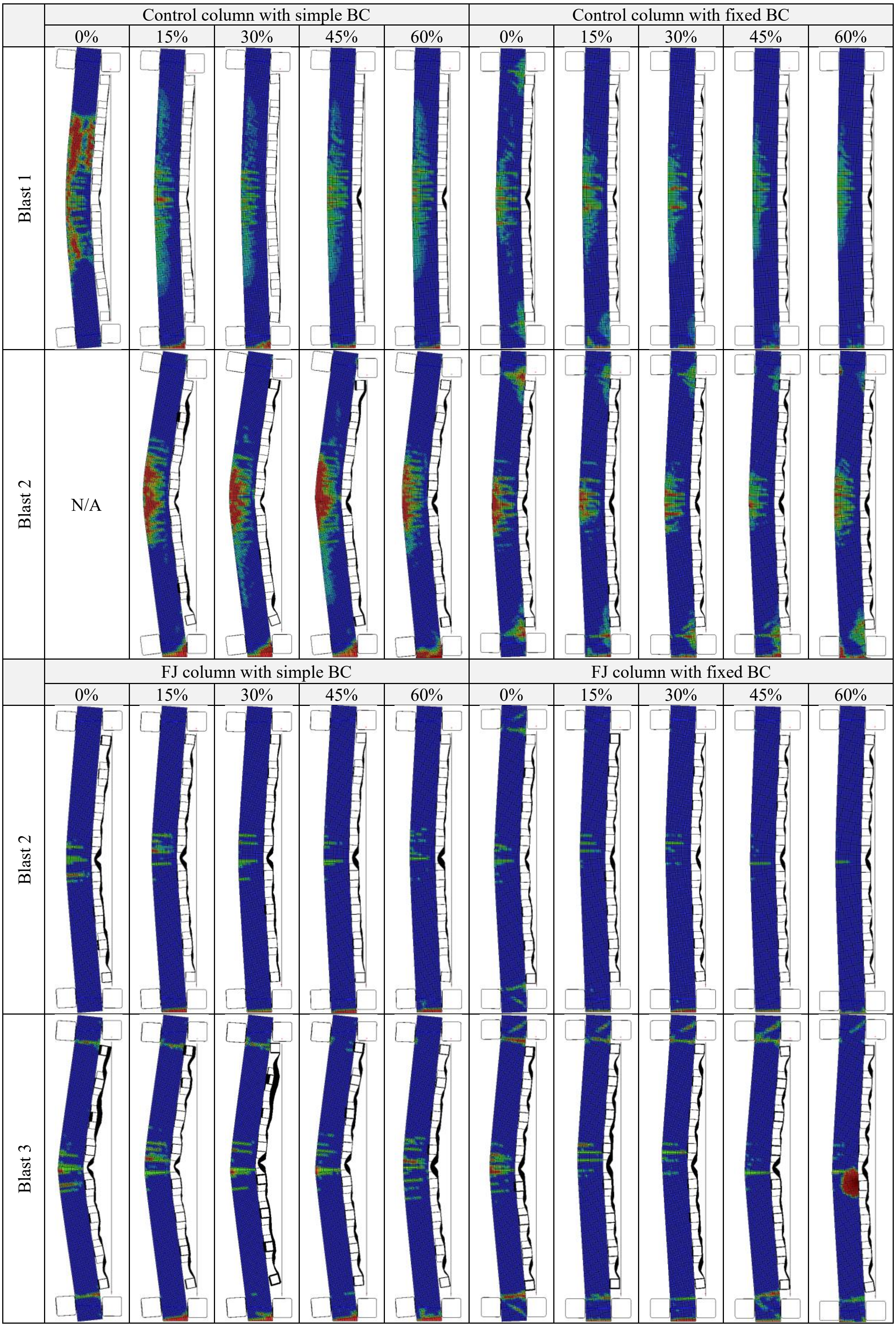

Figure 9 - 17 Effect of axial load ratio on damage profiles (simple and fixed BC)

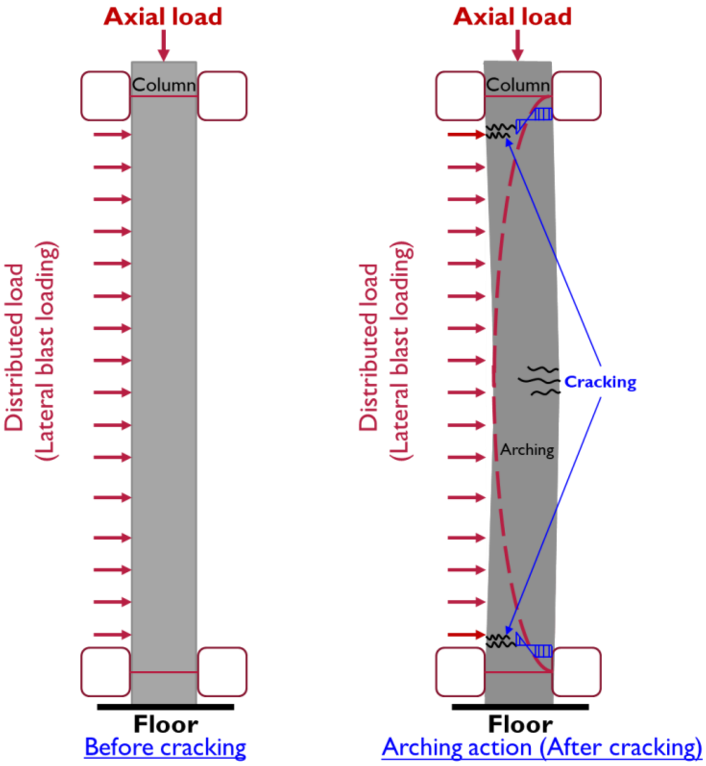

Figure 9 - 18 Arching action profile

9.4.2.3 Effect of steel ratio

The tests and previous simulations indicate that bar rupture is a common failure mode in UHPFRC- jacketed columns. This section studies the influence of the longitudinal steel ratio (ρ) on the behaviour of such columns. The simulations were conducted on columns with 10M, 15M or 20M bars, representing low, moderate and high steel ratios of ρ = 1.3%, 2.7% and 4.0% (see **Figure 9 - 19(a)**). Both simple and fixed supports were considered, with the simulations run under *Blast 1-2-3* and an axial load of $0.3P_0$. The column ID follows the same logic as before except for the use of "10M", "15M" or "20M" to indicate the bar size. The results of the analysis in terms of displacements and damage modes are summarized in **Table 9 - 7** and **Figure 9 - 20 & Figure 9 - 21**.

Beginning with the case of simple supports, the results show an obvious trend of reduced peak displacements of 17-27% at *Blast 1*, and 30-33% at *Blast 2*, as the 10M bar size transitions to 15M-20M reinforcement. Permanent displacements are also reduced by 30-59% and 25-36% for the 15M-20M columns at these same two blasts. Support rotations, and damage in terms of cracking, also gradually reduce as the steel ratio is increased (e.g. 2.4°, 1.7°, 1.6° for the columns with ρ =1.3, 2.7 and 4.0% at *Blast 2*). Importantly, the 10M column fails by bar rupture at *Blast 3*, whereas this failure mode is negated in the comparable columns with 15M and 20M bars.

The same trend is observed in the columns with fixed supports. At *Blast 1*, the columns with 15M-20M bars show declines of 15-25% and 31-59% in peak and permanent deformations, when compared to the case of 10M reinforcement. Likewise, reduced peak displacements of 20-24% are also observed for the 15M-20M columns at *Blast 2*. Once again, bar rupture occurs in the column with10M bars, while this failure mode is prevented as the bar size is increased.

Finally, it can be noted that the columns with 20M bars, and either fixed or simple supports, show reductions of ~ 30% in peak displacements, and less severe cracking, than comparable columns with 15M bars at *Blast 3*, with less remarkable differences at the earlier shots.

In summary, the results confirm that the steel ratio is a critical parameter which affects the failure mode of UHPFRC-jacketed RC columns, whereby columns with low steel ratios are more susceptible to bar rupture than comparable columns with moderate or large steel ratios.

Table 9 - 7 Effects of steel ratio, jacket thickness and jacket design in columns

Parameter	Boundary conditions	Column ID	Axial load ratio	Steel ratio	Jacket design	Blast 1		Blast 2		Blast 3	
						d_{max}	d_{res}	d_{max}	d_{res}	d_{max}	d_{res}
Effect of Steel ratio	Simple	NSC-10M-75-FJ-AL	30%	1.3%	FJ	26.4	20.0	45.9	30.3	Rupture	-
		NSC-15M-75-FJ-AL		2.7%		22.0	14.0	32.2	22.7	59.0	38.7
		NSC-20M-75-FJ-AL		4.0%		19.2	8.12	30.7	19.5	42.8	27.6
	Fixed	NSC-10M-75-FJ-AL-F	30%	1.3%	FJ	19.8	12.9	25.9	9.0	Rupture	-
		NSC-15M-75-FJ-AL-F		2.7%		16.9	8.9	20.7	9.7	31.9	9.9
		NSC-20M-75-FJ-AL-F		4.0%		14.8	5.3	19.8	10.5	20.9	9.2
Effect of Jacket thickness	Simple	NSC-10M-75-FJ(10)-AL	30%	1.3%	FJ-10mm	29.7	23.0	55.0	33.5	79.2	40.0
		NSC-10M-75-FJ-AL			FJ-20mm	26.4	20.0	45.9	30.3	Rupture	-
		NSC-10M-75-FJ(30)-AL			FJ-30mm	17.2	11.0	32.8	25.7	Rupture	-
	Fixed	NSC-10M-75-FJ(10)-AL-F	30%	1.3%	FJ-10mm	21.9	15.0	26.0	7.7	46.0	19.8
		NSC-10M-75-FJ-AL-F			FJ-20mm	19.8	12.9	25.9	8.99	Rupture	-
		NSC-10M-75-FJ(30)-AL-F			FJ-30mm	12.7	7.7	20.4	10.4	25.6	0
Effect of Jacket design (scheme)	Simple	NSC-10M-75-FJ-AL	30%	1.3%	FJ	26.4	20.0	45.9	30.3	Rupture	-
		NSC-10M-75-FJ(Mid)-AL			FJ(mid)	36.8	32.8	72.8	64.7	Rupture	-
	Fixed	NSC-10M-75-FJ-AL-F	30%	1.3%	FJ	19.8	12.9	25.9	8.99	Rupture	-
		NSC-10M-75-FJ(Mid)-AL-F			FJ(mid)	20.5	14.7	24.5	9.34	45.0	27.6
		NSC-10M-75-FJ(Ends)-AL-F			FJ(ends)	19.5	15.2	24.9	0	55.3	26.2
		NSC-10M-75-FJ(Mid+Ends)-AL-F			FJ(mid+ends)	18.3	12.9	22.8	5.98	39.1	19.1

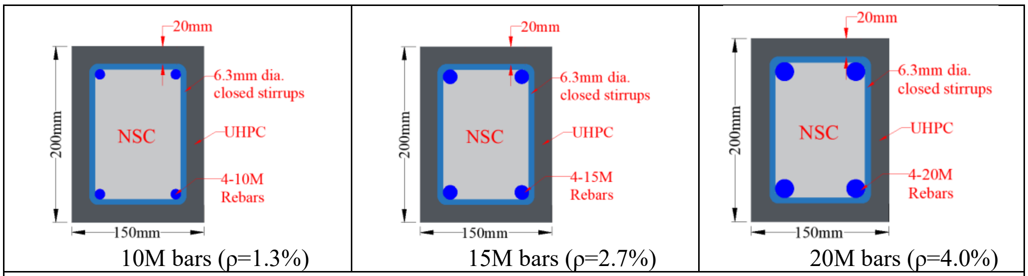

a) Effect of steel ratio

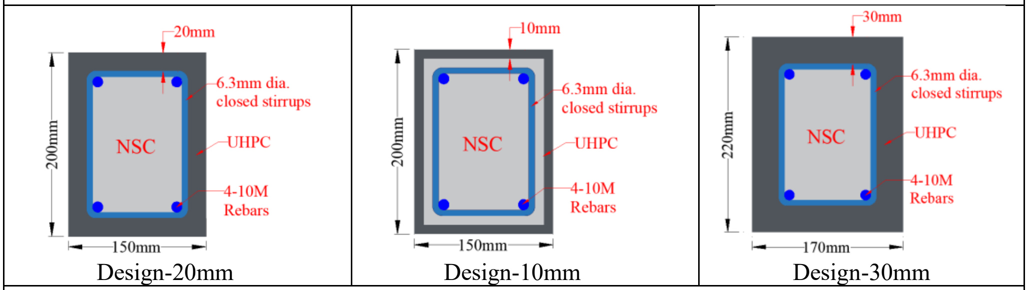

b) Effect of Jacket thickness

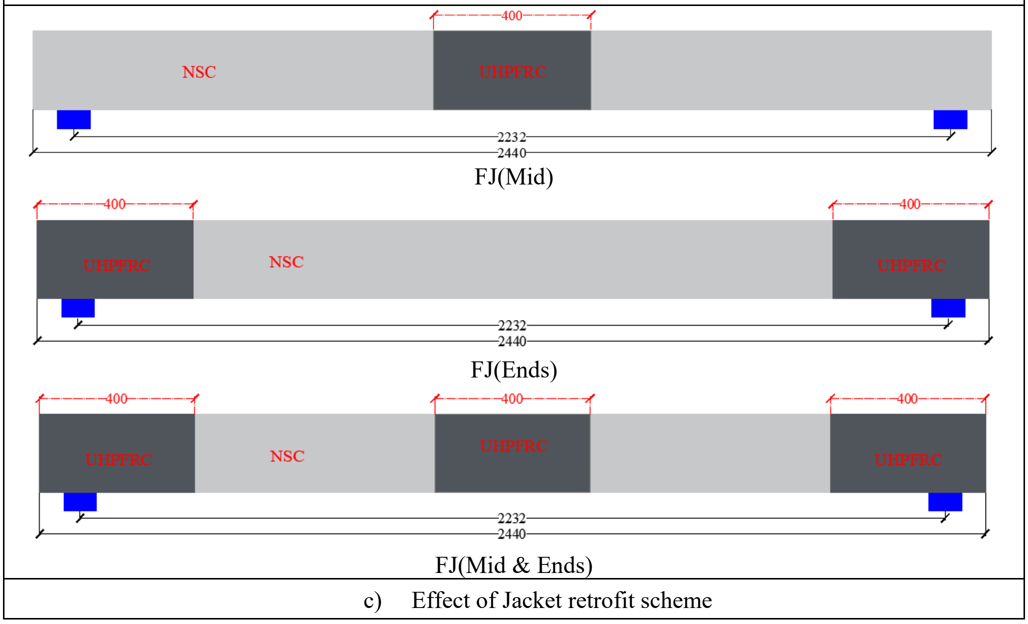

c) Effect of Jacket retrofit scheme

Figure 9 - 19 Design details of columns in parametric study

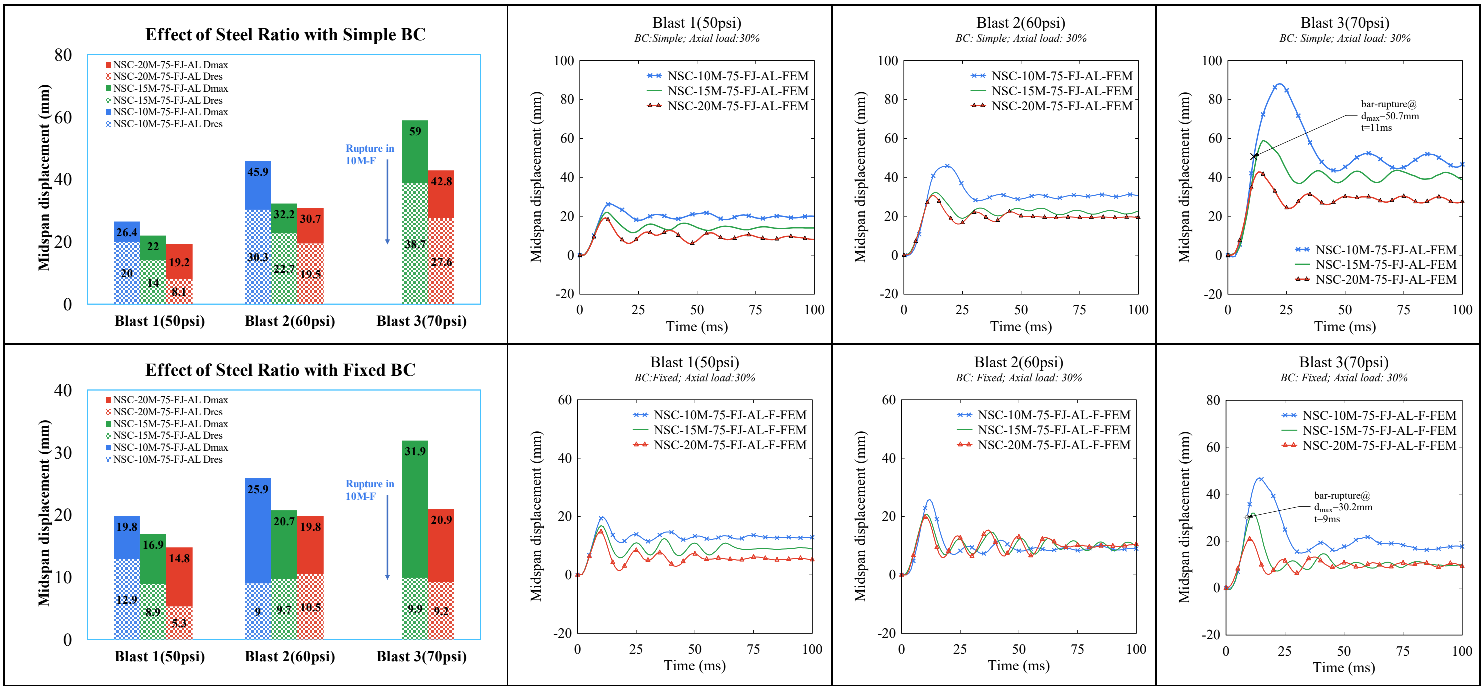

Figure 9 - 20 Effect of steel ratio on displacements (simple and fixed BC)

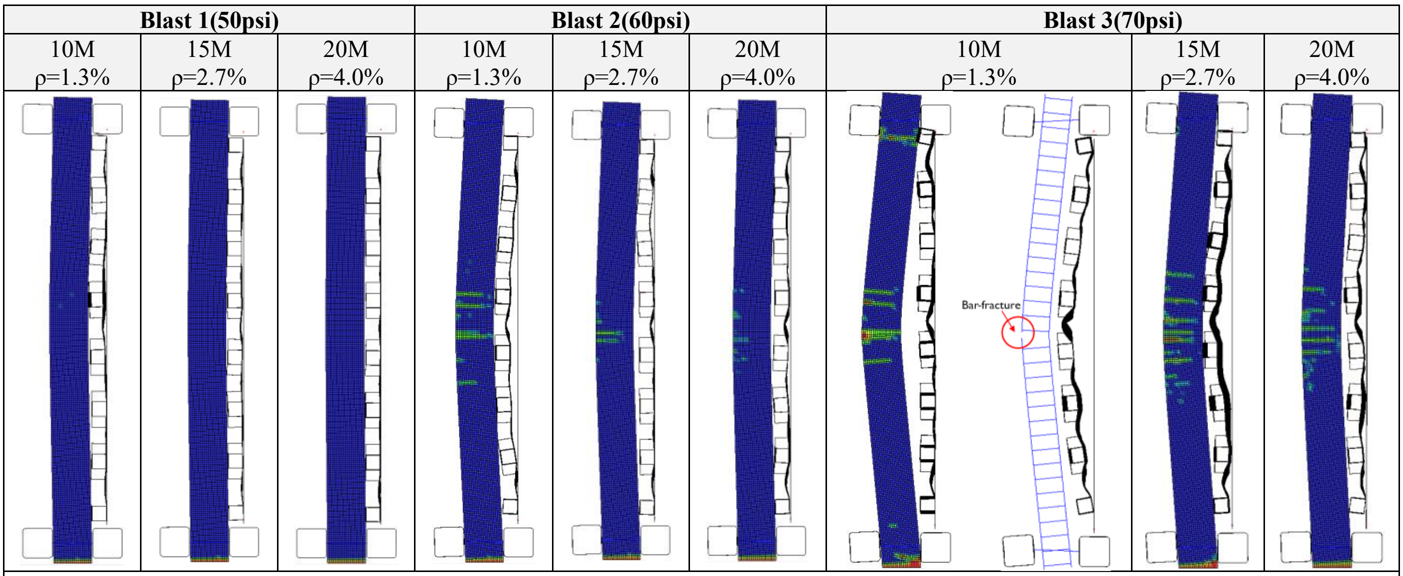

a) Simple BC

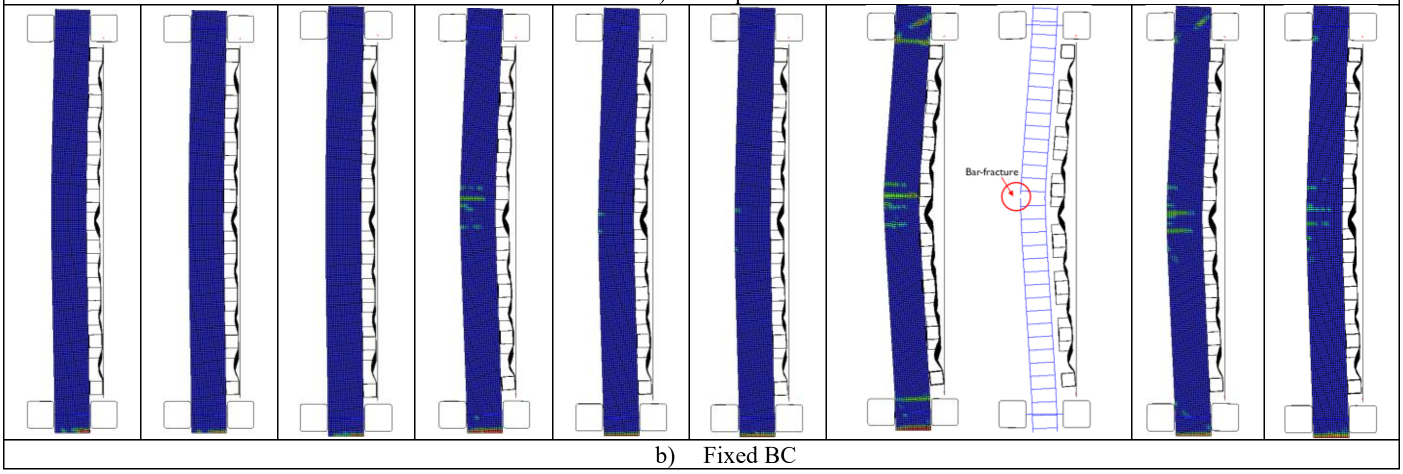

b) Fixed BC

Figure 9 - 21 Effect of steel ratio on damage profiles (simple and fixed BC)

9.4.2.4 Effect of UHPFRC jacket thickness

The effect of UHPFRC jacket thickness is studied in columns with varied jacket thicknesses of 10, 20 and 30 mm. As show in **Figure 9 - 19(b)** all columns had the same core dimensions and steel reinforcement (4-10M bars), with a cross-section of 150×200 mm for the 10 mm and 20 mm designs, and 170×220 mm to accommodate the 30 mm design. Both simple and fixed supports were considered, with the simulations run under *Blast 1-2-3* and an axial load of $0.3P_o$. The results in terms of displacements and damage modes are shown in **Table 9 - 7** and **Figure 9 - 22** & **Figure 9 - 23**.

As expected, the gradual increase in jacket thickness increased member stiffness and reduced the magnitude of displacements under both simple and fixed boundary conditions. In the simple BC case, columns with 20 mm and 30 mm jackets show decreases of 11% and 42% in peak displacements at *Blast 1*, and 17% and 40% at *Blast 2*, when compared to the 10 mm design. Permanent displacements are also reduced when doubling the jacket thickness from 10 to 20 mm, with further decreases for the 30 mm design, under the same two blasts.

However, the failure mode was also affected. While the columns with 20 mm and 30 mm jackets fail by bar rupture, this failure is not observed in the column with the 10 mm jacket design. As noted before, this failure mode can be linked to the high bond and tensile capacity of the UHPFRC which causes crack localization and the build-up of strains over a small length of tension reinforcement. In the current analysis, the 10 mm jacket shifts the UHPFRC interface away from the tension steel bars, which in turn prevents bar rupture.

The same simulations were also run under fixed boundary conditions, with similar conclusions to those discussed above; reduced displacements with the increase in jacket thickness, and reduced tendency for bar rupture as the jacket thickness is reduced and shifted away from the steel bar interface.

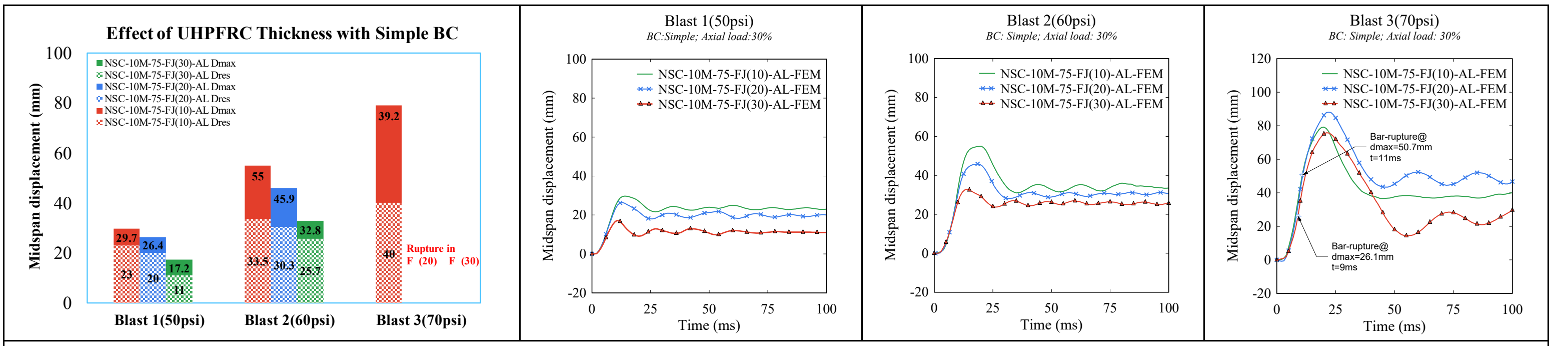

a) Simple BC

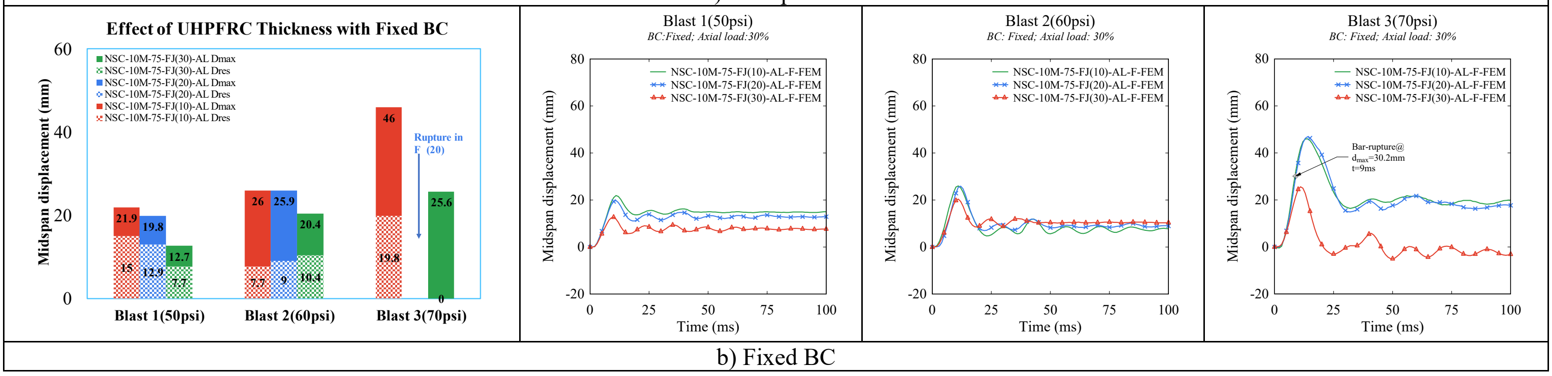

b) Fixed BC

Figure 9 - 22 Effect of UHPFRC jacket thickness (simple and fixed BC)

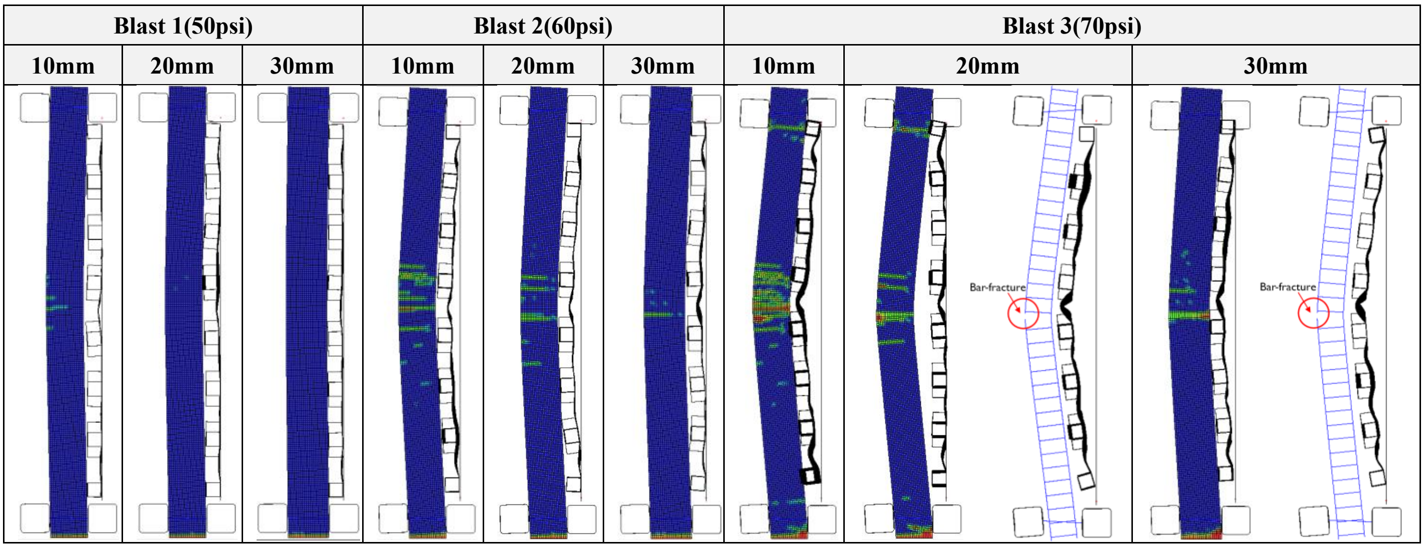

Figure 9 - 23 Effect of UHPFRC jacket thickness on damage profiles (simple BC)

9.4.2.5 Effect of UHPFRC jacket design

The effect of UHPFRC jacket design is further studied by comparing the results for columns with jackets applied either over the full-span, midspan, ends or their combination. **Figure 9 - 19(c)** illustrates the designs which correspond to the above cases, where "Mid", "Ends" and "Mid & Ends" indicate the alternative retrofit schemes. Both fixed and simple supports were considered, with the simulations run under *Blast 1-2-3* and an axial load of $0.3P_o$. The results in terms of displacements and damage modes are shown in **Table 9 - 7** and **Figure 9 - 24** and **Figure 9 - 25**.

The results for the fixed BC case indicate that the varying designs had a significant effect on damage progression and failure mode. As illustrated in **Figure 9 - 24(b-c)**, the displacements under *Blast 1 and 2* are nearly the same (regardless of the jacket design), however the damage modes are clearly affected (**Figure 9 - 25**). Damage in the case of the column with full-span jacketing consists of the formation of localized cracking at midspan at *Blast 2*, followed by rupture of the steel bars at *Blast 3*. Applying the retrofit only at the ends is clearly ineffective, with the column suffering extensive concrete damage at midspan at *Blasts 2-3*. The FJ-Mid design shifts damage to the ends of the midspan retrofit zone at *Blast 2*, and prevents bar fracture at *Blast 3*. Nearly the same damage mode occurs in the "Mid & Ends" design, with bar fracture also negated.

The effect of jacket design was further investigated in columns with simple supports. Since hinging was only expected at midspan, only the FJ and FJ-Mid schemes were considered. As shown in **Figure 9 - 24(a)**, unlike the previous case, significantly lower displacements were obtained for the full-span FJ case, with reductions of 28-37% and 39-53% in peak and residual deformations at *Blast 1-2*, with extensive damage outside the retrofit region for the FJ-Mid design. Unlike the previous case, both columns fail by bar rupture at *Blast 3*, though the location of the steel fracture shifts away from midspan in the column with the FJ-Mid design (**Figure 9 - 26**).

In summary, the results indicate that use of midspan jacketing is not as effective as full-span jacketing in columns with simple supports. Under fixed boundary conditions the FJ-Mid design shifted the failure from crack localization at a single crack at midspan, to concrete damage outside the midspan zone, thereby delaying bar fracture. The FJ-Ends retrofit was clearly ineffective, while combined "Mid & Ends" scheme proved to be quite similar to "Mid"-only design.

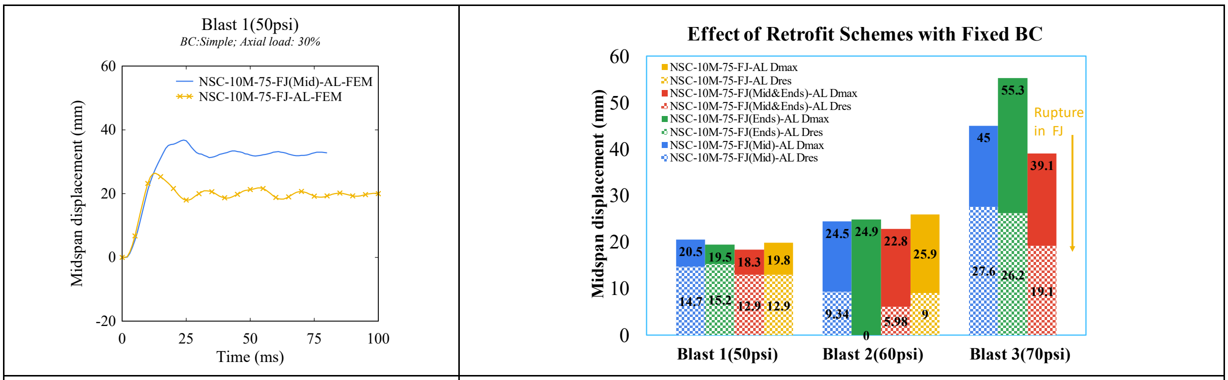

a) Displacement history (simple BC)

(b) Displacement summary (fixed BC)

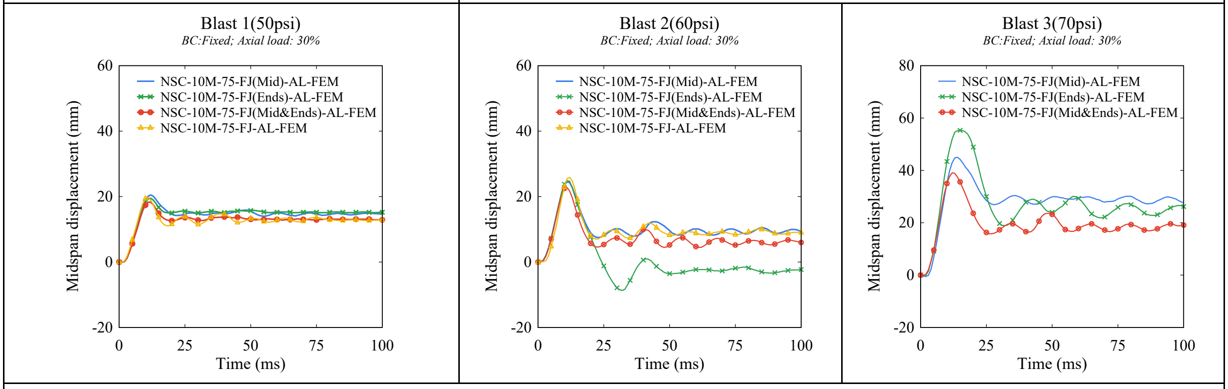

(c) Displacement histories (fixed BC)

Figure 9 - 24 Effect of UHPFRC retrofit scheme on displacements (simple and fixed BC)

Blast 1(50psi)			**Blast 2(60psi)**			**Blast 3(70psi)**		
FJ(Mid)	FJ(Ends)	FJ(Mid&Ends)	FJ(Mid)	FJ(Ends)	FJ(Mid&Ends)	FJ(Mid)	FJ(Ends)	FJ(Mid&Ends)
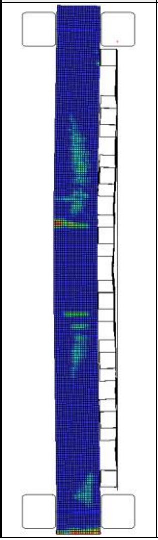	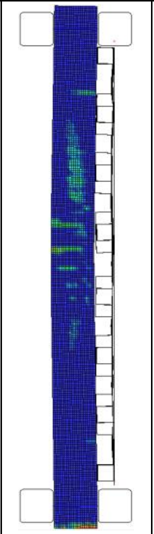	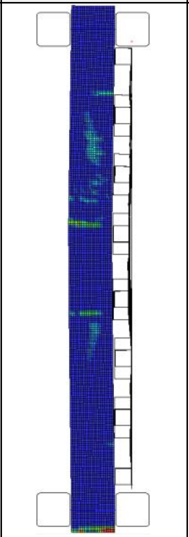	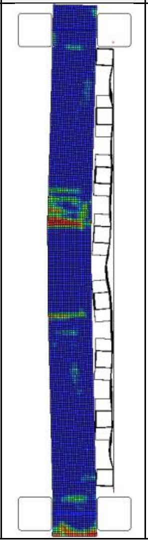	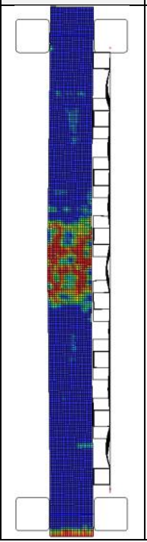	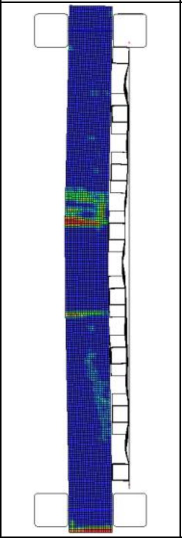	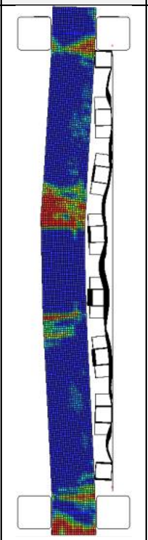	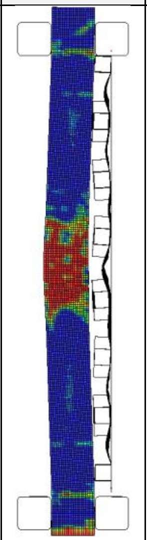	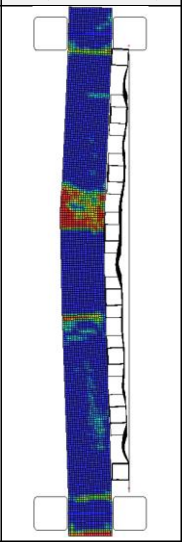

Figure 9 - 25 Effect of UHPFRC retrofit scheme on damage profiles (fixed BC)

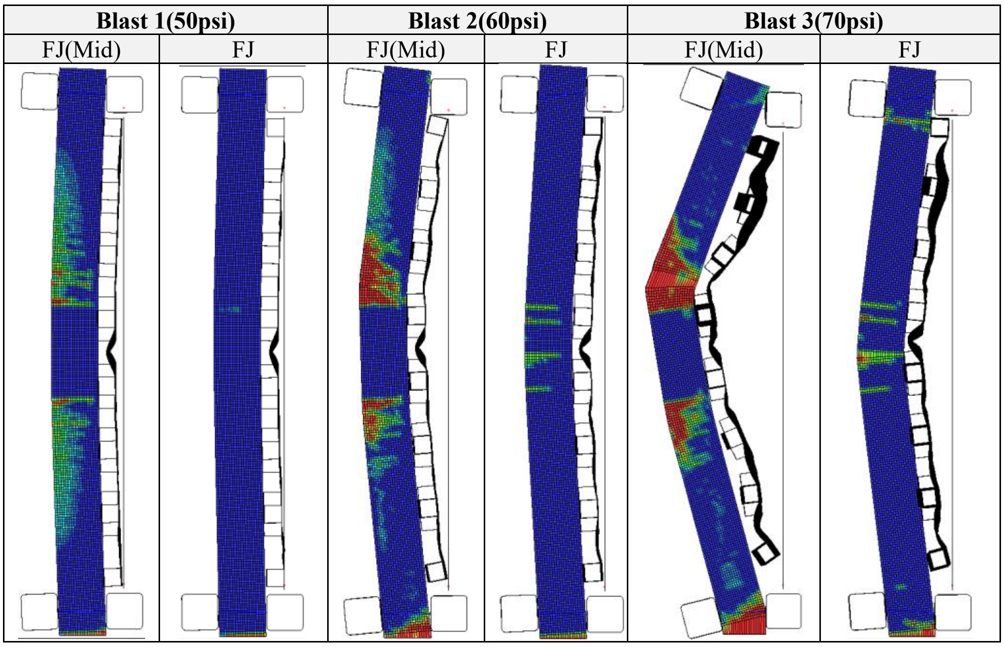

Figure 9 - 26 Effect of UHPFRC retrofit scheme on damage profiles (simple BC)

9.5 Conclusions

This paper presented the results from shock-tube tests which studied the effects of UHPFRC jacketing and axial loading on the blast behaviour of RC columns. The effects of boundary conditions, axial load level, steel ratio, jacket thickness and jacket design on blast performance and failure mode were also studied numerically. The following conclusions can be drawn from this study:

1) In the Companion Group (beams), and under single application of *Blast 1* loading, the UHPFRC jacketing increased member stiffness and reducing maximum and residual displacements when compared to the as-built specimen. Improved control of blast-displacements was also obtained for the FJ-Mid retrofit, though the improvement was not as substantial when compared to the case of full-span jacketing;

2) In the Test Group (columns), and under gradually increasing blast pressures, the UHPFRC jacketing led to a reduction of maximum and residual displacements in the columns at *Blasts 1-2*, though the retrofit specimen failed by bar rupture under Blast 3. The failure was linked to the high bond and tensile capacity of the UHPFRC, the crack localization phenomenon and the relatively low tension steel ratio in the columns;

3) Finite element (FE) modelling with software LS-DYNA was used to predict the blast behaviour of the test specimens, and showed a good ability to predict the peak displacements and failure modes observed in the experiments;

4) The validated FE models were used to gain further insights into the blast behaviour of UHPFRC-jacketed columns. It was revealed that columns with fixed boundary conditions showed lower displacements than comparable columns with simple supports. Increasing the axial load ratio generally reduced the magnitude of displacements in both the as-built and retrofit columns, though UHPFRC columns with fixed supports showed greater vulnerability to bar rupture as more axial load was applied. The steel ratio was found to be a critical parameter affecting the failure of UHPFRC-jacketed columns, with greater likelihood of bar rupture in columns with low steel ratios. Increasing the jacket thickness was found to effectively reduce peak displacements, while the use of a thinner jacket (applied away from the bar interface) reduced the likelihood of bar rupture. The effect of varying jacket retrofit schemes was also studied, with optimal performance for full-span jacketing. Damage shifted outside the retrofit zone in the FJ-Mid design, while the FJ-Ends design was found to be ineffective.

References

[1] Agnew E, Marjanishvili S, Gallant S. Concrete Detailing for Blast. STRUCTURE Magazine. 2007.

[2] CSA. Design and assessment of buildings subjected to blast loads. CSA S850-12. Mississauga, ON: Canadian Standards Association; 2012.

[3] Aoude H, Frederic P. Dagenais, Russell P. Burrell, Saatcioglu M. Behavior of ultra-high performance fiber reinforced concrete columns under blast loading. International Journal of Impact Engineering. 2015;80:185-202.

[4] Astarlioglu S, Krauthammer T. Response of normal-strength and ultra-high-performance fiber-reinforced concrete columns to idealized blast loads. Engineering Structures. 2014;61:1-12.

[5] Rong Q, Zhao Z, Hou X, Jiang Z. A P-I Diagram Approach for Predicting Dynamic Response and Damage Assessment of Reactive Power Concrete Columns Subjected to Blast Loading. Buildings. 2022;12.

[6] Stewart MG, Li J. Risk-based assessment of blast-resistant design of ultra-high performance concrete columns. Structural Safety. 2021;88.

[7] Xu J, Wu C, Xiang H, Su Y, Li Z-X, Fang Q, Hao H, Liu Z, Zhang Y, Li J. Behaviour of ultra high performance fibre reinforced concrete columns subjected to blast loading. Engineering Structures. 2016;118:97-107.

[8] Li J, Wu C, Hao H, Liu Z. Post-blast capacity of ultra-high performance concrete columns. Engineering Structures. 2017;134:289-302.

[9] Wei J, Li J, Wu CQ. An experimental and numerical study of reinforced conventional concrete and ultra-high performance concrete columns under lateral impact loads. Engineering Structures. 2019;201.

[10] Fan W, Shen D, Yang T, Shao X. Experimental and numerical study on low-velocity lateral impact behaviors of RC, UHPFRC and UHPFRC-strengthened columns. Engineering Structures. 2019;191:509-25.

[11] Lee JY, Aoude H, Yoon YS, Mitchell D. Impact and blast behavior of seismically-detailed RC and

UHPFRC-Strengthened columns. International Journal of Impact Engineering. 2020;143.
[12] Wei J, Li J, Wu C, Liu Z-x, Fang J. Impact resistance of ultra-high performance concrete strengthened reinforced concrete beams. International Journal of Impact Engineering. 2021;158.
[13] Zanuy C, Ulzurrun GSD. Impact Resisting Mechanisms of Shear-Critical Reinforced Concrete Beams Strengthened with High-Performance FRC. Applied Sciences. 2020;10.
[14] Habel K, Gauvreau P. Behavior of Reinforced and Posttensioned Concrete Members with a UHPFRC Overlay under Impact Loading. Journal of Structural Engineering. 2009;3:292-300.
[15] Wei J, Li J, Wu C, Hao H, Liu J. Experimental and numerical study on the impact resistance of ultra-high performance concrete strengthened RC beams. Engineering Structures. 2023;277.
[16] CSA. Design of concrete structures. CSA A233:19. Toronto, Ontario: Canadian Standards Association; 2019.
[17] Lloyd A, Jacques E, M S, Palermo D, Nistor I, Tikka T. Capabilities of a Shock Tube to Simulate Blast Loading on Structures. ACI SP-281: Behaviour of concrete structures subjected to blast and impact loadings. 2011:1-20.
[18] Christian M. Effect of high-performance concrete and steel materials on the blast performance of reinforced concrete one-way slabs: University of Ottawa; 2016.
[19] Hallquist JO. LS-DYNA theory manual. 2006.
[20] Murray YD. Users Manual for LS-DYNA Concrete Material Model 159. Cambridge, MA: Federal Highway Administration; 2007.
[21] Guo W, Fan W, Shao XD, Shen DJ, Chen BS. Constitutive model of ultra-high-performance fiber-reinforced concrete for low-velocity impact simulations. Composite Structures. 2018;185:307-26.
[22] Fan W, Xu X, Zhang Z, Shao X. Performance and sensitivity analysis of UHPFRC-strengthened bridge columns subjected to vehicle collisions. Engineering Structures. 2018;173:251-68.
[23] Gholipour G, Muntasir Billah AHM. Nonlinear Analysis of Shear-Deficient Beams Strengthened Using UHPFRC under Combined Impact and Blast Loads. Journal of Structural Engineering. 2022;148.
[24] Fujikake K, Uebayashi K, Ohno T, Shimoyama Y, M K. Dynamic properties of steel fiber reinforced mortar under high-rates of loadings and triaxial stress states. Structures Under Shock and Impact VII. 2002:437-46.
[25] Fujikake K, Senga T, Ueda N, Ohno T, M. K. Effects of strain rate on tensile behavior of reactive powder concrete. Journal of Advanced Concrete Technology. 2006;4:79-84.
[26] Cowper G, Symonds P. Strain-hardening and strain-rate effects in the impact loading of cantilever beams. Brown Univ. Applied Mathematics Report; 1957. p. 28.
[27] Rankin GIB, Niblock RA, Long AS. Compressive membrane action strength enhancement in uniformly loaded, laterally restrained slabs. The Structural Engineering. 1991;69.

Chapter 10: Conclusions and recommendations

10.1 Conclusions

This thesis presented the details of comprehensive experimental and numerical research programs which examined the ability of UHPFRC strengthening to improve the behaviour of reinforced concrete flexural members under static and blast loading. The experimental program included a total of twenty-one (21) specimens, organized in two different series. Series 1 included nine singly-reinforced beams built with high-strength concrete (HSC) and strengthened by UHPFRC to improve shear- and flexural behaviour under static and blast conditions. Series 2 included twelve (12) doubly-reinforced specimens built with normal-strength concrete (NSC), and strengthened by UHPFRC to improve response under blast and combined blast-axial loading.

The following conclusions can be drawn from the experimental results:

Series 1: variables investigated included UHPFRC retrofit type (FJ, UJ and T-sided), interface preparation methods (PC and BH), and steel detailing (steel ratio and presence of stirrups) in singly-reinforced HSC beams with ρ =1.6% and 2.4%:

1. Under static loading, the application of UHPFRC jacketing was effective in preventing shear failure in the shear-deficient HSC beams, with important increases in stiffness, load-carrying capacity, and overall ductility. The flexural behavior was also improved when compared to that of the HSC beams with stirrups, in terms of increased capacity, ductility and toughness.
2. Under static loading, the failure mode of the UHPFRC retrofitted beams was affected by the tension steel ratio, with the failure transitioning from bar-fracture to UHPFRC crushing in the beams with 15M and 20M bars (ρ = 1.6% and 2.4%), respectively. While bar fracture was not observed in the blast tests in Series 1, this failure mode should be considered when applying UHPFRC jacketing, especially in beams with smaller steel bar sizes or steel ratios due to the crack localization phenomenon and the high bond capacity of the UHPFRC;
3. The shear capacity of the UHPFRC retrofitted beams was estimated by combining the concrete contribution of the core section using the CSA A23.3 shear design method and the UHPFRC jacket contribution using an equation proposed by Yang et al. The analysis showed that the UHPFRC retrofitted beams had shear-to-flexure ratios of 2 and 2.97 for the beams with 20M and 15M bars respectively. The moment

capacity of the beams was also predicted by adapting a sectional analysis procedure based on a model proposed by Bae et al., with prediction ratios P_y/P_{UHPFRC} of ~ 1.0.

4. Under blast loading and regardless of retrofit type (UJ or FJ) and steel ratio (ρ = 1.6% and 2.4%), the use of UHPFRC jacketing not only improved shear resistance in the shear-deficient beams, but also allowed the beams to fail in flexure. Likewise, both UHPFRC retrofits allowed for obvious improvements in flexural behavior, in terms of displacement and damage control, and allowed for an increase in blast capacity when compared to companion unstrengthened RC beams with stirrups. Both retrofits presented multiple fine cracks, followed by the development of one or two dominant cracks and crushing of concrete, which was more obvious in the UJ beams as the steel ratio increased.
5. In the beams without stirrups, the UJ and FJ retrofits showed nearly the same displacements under Blasts 1-2-3 in the 15M group, and under Blast 1-2-3-4 in the 20M group. The benefit of full-jacketing only became evident as the 15M and 20M beams approached failure at Blasts 4 and 5, respectively. This benefit was yet more obvious as the flexural demand was increased (i.e. in the 20M beams). Indeed, eventual failure in the UJ beam with 20M bars was associated with outward buckling of the side UHPFRC jacket due to core concrete crushing, whereas such damage was negated in the beam with full-jacketing;
6. Two retrofit types (T-sided and FJ) were considered in the 20M beams with stirrups. Both retrofits showed improved displacement and damage control when compared to the as-built control beam. Similar displacements were observed under the low intensity blasts, while the benefit of FJ jacketing became more obvious at Blasts 3-4. Failure in the T-sided beam occurred at Blast 4 due to severe fracture of the HSC concrete in the midspan zone, while the FJ beam safely survived this blast, and further Blast 5 loading with limited damage;
7. Two roughening methods were considered in the tests (bush-hammer: BH and point-chisel: PC, with CSPs of 6 and 10, respectively). Regardless of roughening method, no premature debonding was found in the blast tests, indicating the effectiveness of both roughening types. Comparing the companion FJ beams with PC and BH roughening, no obvious differences in performance were observed up to Blast 3. Under Blast 4-5 the PC beam showed greater displacements and more

severe damage which was attributed to the less uniform roughness and greater substrate damage caused by the point-chisel roughening.

8. Increasing the steel ratio from 1.6 to 2.4% (15M to 20M bars) improved member stiffness which in turn led to reductions in midspan displacements and damage in the UJ and FJ retrofit beams. The existence of stirrups didn't show obvious effects on the blast responses of the FJ-retrofitted beams since the specimens failed in flexure.
9. Most beams in Series 1 survived the blast tests and were tested under quasi-static four-point bending to assess their residual capacity. In general, damaged FJ beams showed substantially higher load capacities close to that of undamaged beams when compared to damaged UJ beams. Examining all tests, limiting the blast rotation in the retrofitted beams to ~ 3° ensured adequate residual capacity after blast loading, while rotations exceeding 4° were detrimental to post-blast performance.

Series 2: variables included UHPFRC retrofit type (T-sided, UJ, FJ, FJ (hinge) and the combination of T-sided and FJ (hinge)), blast load scenarios (single vs. repeated blasts) and axial load in doubly-reinforced NSC beams with ρ =0.8%:

1. Under quasi-static loading, the use of UHPFRC jacketing enhanced flexural behavior in terms of strength and stiffness when compared to the control RC beam by margins of 42% and 100%. The use of UHPFRC also led to a distinct cracking pattern, with many closely spaced fine cracks and the formation of one dominant crack at midspan. The high bond capacity of the UHPFRC and this crack localization led to bar rupture failure, which reduced the ductility and drift capacity in the retrofit beam. Based on the results, the interface location and longitudinal steel ratio may be important parameters that affect the performance of beams retrofitted with UHPFRC jacketing;
2. In Group 1 (G1), and under repeated blast testing, the UHPFRC retrofits improved the behavior of the RC beams prior to bar rupture. The T-sided, UJ and FJ retrofits increased member stiffness, thereby reducing displacements at equivalent Blasts 1 and 2 loads, with optimal performance recorded for the UJ specimen. However, the repeated tests eventually led to bar fracture in all three retrofits under Blast 3. This failure is attributed to the high bond capacity of the UHPFRC, low tension steel

ratio of ρ = 0.8%, and repeated blast testing which intensified the crack localization in the UHPFRC.

3. In Group 2 (G2), and under single Blast 3 testing, the UHPFRC jacketing in beam NSC-10M-75-FJ-S led to a reduction of maximum and residual displacements when compared to the as-built NSC-10M-75-S specimen, without the problem of bar rupture. Improved control of displacements without bar rupture was also observed in the beam with the localized FJ(Hinge) and hybrid T&FJ(Hinge) retrofits, which also showed unique crack patterns consisting of multiple dominant cracks, which shifted away from midspan.
4. All beams in G2 survived the blast tests and were subsequently tested under static four-point bending to assess their residual capacity. All three retrofits showed higher residual capacity when compared to the as-built specimen, with greater stiffness and strength observed for the NSC-10M-75-FJ-S and NSC-10M-75-T&FJ(Hinge)-S beams. The FJ beam eventually failed by bar rupture, while this failure was delayed or prevented in the beams with the localized T&FJ(Hinge) and FJ(Hinge) retrofits.
5. The control RC beam specimens showed similar maximum and residual displacements at Blast 3 under single versus repeated blast loading, although greater concrete damage was observed in the beam subjected to repeated testing. Conversely, the repeated blast testing was found to be an important factor in the bar fracture failure observed in beam NSC-10M-75-FJ due to the crack localization which formed at the earlier blasts;
6. In Group 3 (columns), and under gradually increasing blast pressures, the UHPFRC jacketing led to a reduction of maximum and residual displacements in the columns at Blasts 1-2, though the retrofit specimen failed by bar rupture under Blast 3. The failure was linked to the high bond and tensile capacity of the UHPFRC, the crack localization phenomenon and the relatively low tension steel ratio in the columns;

As part of this research, numerical analyses of the tested beams were undertaken using the three-dimensional finite element (FE) modelling software LS-DYNA. After validation, the models were used to conduct parametric studies on parameters not considered in the experiments. The following conclusions are drawn from the numerical research program:

Series 1:

1. FE analysis was conducted to reproduce the blast response of the test beams using LS-DYNA. The numerical simulations showed a reasonable ability to predict the maximum displacements of the control and retrofit beams with an average d_{num}/d_{exp} ratio of 0.88 when considering all blasts. Importantly the FE modelling was able to capture the failure modes and damage patterns in the control and UHPFRC retrofitted specimens.

Series 2:

1. Finite element (FE) modelling with software LS-DYNA was used to predict the blast behaviour of the test specimens (in Groups 1-3), and showed a good ability to predict the peak displacements and failure modes observed in the experiments;
2. Using the validated FE models, a parametric study was used to investigate the effects of steel ratio, jacket thickness and interface location on blast response in the control and FJ beams. Increasing the tension steel ratio was effective in reducing displacements, support rotations and damage in the control beams under both single and repeated blasts. The same trends were observed in the FJ-retrofit beams, while the use of 15M bars (1.6%) was sufficient to prevent bar rupture under repeated blast loading. Moving the UHPFRC jacket interface slightly away from the longitudinal reinforcement was shown to prevent bar rupture, regardless of the jacket thickness (10 mm, 20 mm or 30 mm in this study). Thus, the steel ratio, interface location and jacket thickness are important parameters that should be considered in the blast design of UHPFRC-retrofitted beams.
3. FE analysis was further used to study the effects of blast load scenario and steel ratio in the beams with varying retrofit types. In the numerical simulations, the FJ, UJ and T-retrofits showed an ability to reduce displacements, with no bar rupture under the single Blast 3 scenario. Increasing the steel ratio was also shown to reduce displacements in the UHPFRC retrofit beams under both single and repeated blast

loading. Importantly, retrofit beams with increased steel ratios showed an ability to delay or prevent bar rupture under both repeated and single blast loading.

4. The validated FE models were used to gain further insights into the blast behaviour of UHPFRC-jacketed columns. It was revealed that columns with fixed boundary conditions showed lower displacements than comparable columns with simple supports. Increasing the axial load ratio generally reduced the magnitude of displacements in both the as-built and retrofit columns, though UHPFRC columns with fixed supports showed greater vulnerability to bar rupture as more axial load was applied. The steel ratio was found to be a critical parameter affecting the failure of UHPFRC-jacketed columns, with greater likelihood of bar rupture in columns with low steel ratios. Increasing the jacket thickness was found to effectively reduce peak displacements, while the use of a thinner jacket (applied away from the bar interface) reduced the likelihood of bar rupture. The effect of varying jacket retrofit schemes was also studied, with optimal performance for full-span jacketing. Damage shifted outside the retrofit zone in the FJ-Mid design, while the FJ-Ends design was found to be ineffective.

10.2 Design recommendations

1. The findings in this thesis showed that low-steel ratio tended to increase the vulnerability of bar-rupture in UHPFRC-retrofitted specimens; therefore, the potential for bar rupture should be carefully considered when applying UHPFRC in flexural members with low steel ratios ($\rho \leq 0.8\%$). A minimum steel ratio of 1.0% and 2.0% is recommended when applying UHPFRC in beams and columns, respectively;
2. The interface location was also shown to affect the failure mode of the UHPFRC-retrofitted flexural members. Applying the UHPFRC slightly away from the steel bar interface is recommended due to the very high bond capacity of the UHPFRC. In addition, the use of UHPFRC with lower fiber content (e.g. 1%) may also be appropriate to reduce the influence of UHPFRC tensile resistance on crack localization;
3. In this research, the use UHPFRC full-jacketing was found to be most effective in improving flexural behaviour under static and blast loads. In practice, full-jacketing is recommended in columns, whereas the use of U-jacketing is recommended in

beams where the compression face is not easily accessible (except in the case of beams without compression reinforcement). The use of tension-sided UHPFRC is recommended in panel elements such as walls.

4. In this research the smallest UHPFRC thickness used in the retrofits was 20 mm. In practice a minimum thickness equal to 1.5 x fiber length is recommended to allow for ease of construction and casting.
5. In general, the use of concrete surface profile (CSP) of CSP6 is sufficient to ensure adequate bond between UHPFRC and the substrate concrete. The use of uniform roughening pattern (as produced by the use of the bush-hammer in this study) is recommended. However, the roughening methods used in this study were labor-intensive, and therefore the use of high-pressure water-jetting is recommended in practice.
6. Based on the results in this study limiting the maximum support rotation to 3° is recommended to avoid brittle failure in UHPFRC-retrofitted flexural members.

10.3 Recommendations for future work

The following recommendations for future research are suggested:

1. Research on shear behavior of UHPFRC-strengthened beams with different shear span-to-depth ratios under both static and blast loads is recommended.
2. Research on design methods to improve the ductility of UHPFRC-strengthened structures which usually suffer crack localization; therefore, research on appropriate fiber content, use of hybrid fibers (mix of micro and macro-fibers), or other methods to improve the ductility of UHPFRC-strengthened structures is recommended.
3. Research to better characterize and quantify the effect of roughness (CSP) grade on the bond between UHPFRC and substrate concrete is needed. In addition, the effect of different interface preparation/treatment methods should be further explored. This can be accomplished through small-scale interface tests (e.g. direct shear and slant-shear tests). The performance of different interface preparation methods under northern climate conditions also requires further study.
4. The shock tube facility used in this research aimed to simulate far-field type blast loads; hence the blast behavior of UHPFRC-strengthened RC-structures under close-in or contact blast load conditions should be examined.

5. The retrofit schemes presented in this thesis focused on the use of plain UHPFRC without embedded reinforcement; the exploration of innovative retrofit methods, such as the combined use of UHPFRC, steel reinforcement, FRP and textile materials is recommended.
6. The precise calibration of 3D concrete FE models (CSCM, K&C and CDP models provided by LS-DYNA) to better simulate the behaviour of UHPFRC under blast or impact conditions should be further conducted. In addition, perfect bond was assumed in this research, however consideration of interface-bond effects in future finite element modelling is recommended.